

Accurate observations of near-infrared solar spectral irradiance and water vapour continuum

Submitted for the degree of Doctor of Philosophy

Department of Meteorology

University of Reading

Jonathan David Charles Elsey

September 2018

Declaration

I confirm that this is my own work and the use of all material from other sources has been properly and fully acknowledged.

- Jonathan Elsey

Abstract

This thesis contains analyses of the solar spectral irradiance (SSI) and near-infrared water vapour continuum from high-resolution observations by a ground-based, sun-pointing Fourier transform spectrometer in the wavenumber region 2000-10000 cm^{-1} (1-5 μm). This was performed primarily using the Langley method on observations during 18 September 2008. Particular focus was placed on a detailed assessment of the uncertainty budget for each of these analyses.

The solar spectral irradiance was found to be $\sim 8\%$ lower than the commonly-used satellite-based ATLAS3 SSI in the region 4000-7000 cm^{-1} (where ATLAS3 is most uncertain). This disagreement with ATLAS3 is in line with several other modern analyses. There is good agreement with ATLAS3 and other spectra in the 7000-10000 cm^{-1} region (where these spectra are considered more accurate).

This thesis contains the first published results of water vapour continuum absorption in the atmosphere in the 1.6 and 2.1 μm atmospheric windows (in which laboratory measurements show some significant disagreement) with robust uncertainties. The derived water vapour continuum in these windows is stronger than the widely-used MT_CKD model (v3.2) by a factor of ~ 100 and ~ 5 respectively. These results also show that MT_CKD is a reasonably accurate representation of the continuum in the 4 μm window. These results are broadly consistent with laboratory measurements of the foreign continuum, but are inconsistent with the highest such measurements of the self-continuum.

The effect of the self and foreign continuum in atmospheric conditions is assessed, with comparisons to the Langley-derived spectra from this work. These results show that the difference between MT_CKD and this work in the 1.6 and 2.1 μm windows may come primarily from the observed differences in the foreign continuum, with a smaller contribution from the self-continuum. These results show inconsistency with several sets of laboratory room temperature spectra within the experimental uncertainties.

Acknowledgements

First and most obviously is my supervisor Prof. Keith Shine, whose endless patience and insight was instrumental in getting the thesis to the state its in. I'm proud to call you my mentor; if I can be a tenth as expert and generally nice as you are I'll be doing well! I'd also like to thank Drs. Tom Gardiner and Marc Coleman at the National Physical Laboratory, with whom I worked extensively and who directed the field campaign from which most of the work in this thesis derives. I always enjoyed our meetings, and I hope to keep in contact with you after the PhD ends. The work presented in this thesis would not have been possible without the groundwork laid by Liam Tallis and Kaah Menang during their respective PhDs, and I thank Kaah in particular for our useful meetings and emails.

Additional thanks of course go to my monitoring committee, Prof. Richard Allan and Dr. Christine Chiu; your discussions in the committee meetings always helped ground and centre my work and always resulted in fruitful ideas which undoubtedly improved the manuscript. I am also indebted to Dr. Nicolas Bellouin; while the project ultimately went in a different direction to that expected our occasional meetings were always insightful, and your suggestion to use a physical method to obtain aerosol optical depth (the Mie scattering code) was an immense boost to the thesis.

There are a million other people I'd like to thank for their love and support. My family, particularly my parents have always been the most supportive people I know and have stopped at nothing to help and encourage me to get where I am today. I love you all, and hope to repay you in kind down the road. I'd like to thank my friends, particularly those who had the misfortune of sharing office space with me on Lyle 3 down the years. The endless Sporcle quizzes and lunchtime board games probably delayed my PhD by a good few weeks, but definitely contributed to keeping me sane when the work wasn't going so well! I'd also like to thank everyone who lived in House with me over the years, for putting up with me in the bad times and making the good times some of the best I've ever had.

The last few months of the PhD were definitely some of the most challenging of my life so far, and most of all I thank Sammie (she's a star) for doing so much to help me get through the thesis and viva, especially in those dark days when it felt like the chances of getting anything submitted were a million to one.

Table of Contents:

Chapter 1:	Introduction	1
1.1:	Introduction	1
1.2:	Earth's energy balance and solar radiation	2
1.3:	Absorption of solar radiation in Earth's atmosphere	4
1.4:	The water vapour continuum	8
1.4.1:	Introduction	8
1.4.2:	Theoretical and experimental perspectives on the continuum	9
1.4.3:	Impacts of the continuum for atmospheric science	12
1.5:	Objectives of this work	14
Chapter 2:	Radiative processes in the terrestrial atmosphere	17
2.1:	Molecular spectroscopy	17
2.1.1:	Rotational spectroscopy	19
2.1.2:	Vibrational transitions	21
2.1.3:	Rotational-vibrational transitions	22
2.1.4:	Line broadening	24
2.1.4.1:	Natural broadening	25
2.1.4.2:	Collision broadening	26
2.1.4.3:	Doppler broadening	27
2.1.4.4:	Voigt and Hartmann-Tran lineshape profiles	28
2.1.5:	Water vapour near-infrared spectrum	30
2.2:	Solar radiation	32
2.2.1:	Solar structure	33
2.2.2:	Sun position and distance from Earth	34
2.2.2.1:	Solar zenith angle	35
2.2.2.2:	Orbit eccentricity	35
2.2.3:	Models and observations of solar radiation	36
2.3:	Radiative transfer in the terrestrial atmosphere	38
2.3.1:	Blackbody radiation	39
2.3.2:	The Beer-Bouger-Lambert law and atmospheric transmission	40
2.3.3:	Absorption by atmospheric gases	42
2.3.4:	Rayleigh scattering	44
2.3.5:	Mie scattering and the effect of clouds and aerosols	46

2.3.6: Radiative transfer models	48
2.3.6.1: The Reference Forward Model	49
2.3.6.2: Spectroscopic line databases	52
2.3.6.3: Model atmospheric profiles	53
2.3.6.4: Mie scattering models	54
2.4: Near-IR water vapour continuum absorption	55
Chapter 3: Experimental methods in the CAVIAR field campaign	59
3.1: Introduction	59
3.2: Fourier transform infrared spectroscopy	59
3.2.1: Introduction	59
3.2.2: The Michelson interferometer	60
3.2.3: Optical path difference and interferograms	61
3.2.4: Computational methods in FTIR spectroscopy	63
3.2.4.1: Apodization	64
3.2.4.2: Zero filling	66
3.2.4.3: Phase correction	66
3.3: Retrieval methods	68
3.3.1: Radiative closure	68
3.3.2: Langley method	68
3.3.3: Advantages and disadvantages of Langley and closure methods	69
3.3.4: Calculation of Rayleigh scattering	70
3.3.5: Ångström extrapolation and Mie scattering codes	71
3.3.5.1: Ångström extrapolation	71
3.3.5.2: Mie scattering codes	72
3.3.6: Airmass correction	75
3.3.7: Monte Carlo uncertainty evaluation	76
3.4: CAVIAR field campaigns	77
3.4.1: Camborne campaign	77
3.4.2: Jungfraujoch campaign	90
3.4.3: Details of the CAVIAR FTIR	81
3.4.3.1: The Bruker 125 FTS and optical setup	81
3.4.3.2: Calibration procedure	84
3.4.3.4: FTIR uncertainty budget	88
3.4.3.5: Smoothing and filtering of FTIR data	92

3.4.4: Updates to calibration since Gardiner et al. [2012]	94
3.4.4.1: TSARS stability	94
3.4.4.2: Mirror reflectance calibration	96
3.4.4.3: Phase correction	97
3.4.5: Supplementary measurements	98
3.4.5.1: Radiosonde ascents	99
3.4.5.2: Microtops sunphotometer measurements	101
3.4.5.3: HATPRO microwave radiometer	104
3.4.5.4: FAAM aircraft data	105
3.4.5.5: Model reanalyses	105
Chapter 4: Accurate measurements of NIR solar spectral irradiance between 4000-10000 cm⁻¹	106
4.1: Introduction	106
4.2: Paper manuscript	109
4.2.1: Introduction	109
4.2.2 Current state of measurements	110
4.2.3 Analysis methods	115
4.2.3.1 Langley method	115
4.2.3.2 Radiative closure method	116
4.2.4 Experimental methods	116
4.2.4.1 Calibration	117
4.2.4.2 Spectrometer measurement uncertainty	117
4.2.4.3 Atmospheric state analyses	118
4.2.4.4 Filtering of observed spectra	118
4.2.5 Results and discussions	119
4.2.6 Conclusions	126
4.3: Additional analysis	128
Chapter 5: Observations of the near-IR water vapour continuum in the atmosphere	134
5.1: Introduction	134
5.2: Laboratory measurements and MT_CKD	135
5.2.1: CAVIAR and Tomsk continua	137
5.2.1.1: Self-continuum	137
5.2.1.2: Foreign continuum	139

5.2.2: Grenoble CRDS continua	141
5.2.1.1: Self-continuum	141
5.2.2.2: Foreign continuum	142
5.2.3: Other measurements	142
5.2.4: Synthesis	142
5.2.4.1: Self-continuum	142
5.4.2.2: Foreign continuum	145
5.2.5: Discussion of observation techniques	146
5.2.6: Temperature dependence of the observed self-continuum	147
5.2.7: Atmospheric observations of the near-IR continuum	151
5.3: Derivation of continuum using Camborne measurements	154
5.3.1: Introduction	154
5.3.2: Retrieval of continuum optical depth from observed optical depth	156
5.3.2.1: Observed optical depth	156
5.3.2.2: Optical depth from gaseous absorption	157
5.3.2.3: Optical depth from Rayleigh scattering	159
5.3.2.4: Optical depth from aerosol extinction	160
5.3.2.5: Continuum absorption	162
5.4: Uncertainty budget	164
5.4.1: Observational uncertainties	165
5.4.2: Uncertainties in the model-derived optical depth	166
5.4.3: Uncertainties in aerosol measurements	167
5.5: Results and analysis	167
5.5.1: Best estimate of the derived continuum	167
5.5.2: Comparison of Langley and closure-derived continuum absorption	173
5.5.2.1: 18 September 2008	173
5.5.2.2: 22 August 2008	176
5.6: Conclusions	177
Chapter 6: Comparison of atmospheric Langley-derived and laboratory continua	179
6.1: Introduction	179
6.2: Comparison with other atmospheric spectra	180
6.3: Temperature dependence of the self-continuum	184

6.4: Self and foreign continuum at atmospheric temperatures	190
6.4.1: Self-continuum	190
6.4.2: Foreign continuum	192
6.4.3: Combined continuum	194
6.5: Conclusions	195
Chapter 7: Conclusions and future work	196
7.1: Introduction	196
7.2: Conclusions	196
7.2.1: Solar spectral irradiance (Chapter 4)	196
7.2.2: Water vapour continuum (Chapters 5 and 6)	197
7.3: Future work	199
7.3.1: Solar spectral irradiance	199
7.3.2: Water vapour continuum	200
7.3.2.1: Laboratory experiments	200
7.3.2.2: Considerations for future field campaigns	202
7.3.2.3: Further steps and incorporation into radiation models	206
Bibliography	208

List of Acronyms:

Acronym	Definition
AOD	Aerosol Optical Depth
ATLAS3	ATmospheric Laboratory for Applications and Science 3
CAVIAR	Continuum Absorption at Visible and Infrared wavelengths and its Atmospheric Relevance
FOV	Field of View
FTIR	Fourier Transform Infrared
FTS	Fourier Transform Spectrometer
GCM	General Circulation Model
HATPRO	Humidity and Temperature PROfiler
IPCC	Intergovernmental Panel on Climate Change
LBL	Line-by-line
MT_CKD	Mlawer Tobin_Clough Kneizys Davies
NIR	Near Infrared
NPL	National Physical Laboratory
NRLSSI2	Naval Research Laboratory Solar Spectral Irradiance 2
RFM	Reference Forward Model
SIM	Spectral Irradiance Monitor
SSI	Solar Spectral Irradiance
TOA	Top of Atmosphere
TSARS	Transfer Standard Absolute Radiance Source
TSI	Total Solar Irradiance
UV	Ultraviolet

Chapter 1:

Introduction

1.1: Introduction

Weather and climate processes are driven by the absorption, scattering and emission of solar radiation by the Earth's atmosphere and surface. The difference between the incoming *shortwave* radiation emitted by the Sun and the outgoing *longwave* radiation emitted by the Earth is crucial for determining how the climate warms or cools (e.g. *Stephens et al.* [2012]). The amount of energy emitted by the Earth is dependent on how much of the incoming shortwave radiation reaches the surface and troposphere; much of it is absorbed in the atmosphere by water vapour, methane, carbon dioxide and other gases. These same gases also absorb and emit longwave radiation (see Section 2.3.1), reducing the amount which is free to escape into space. Understanding the Earth's energy budget therefore requires understanding of the spectroscopy of gases in the atmosphere.

The work in this thesis focuses on two major spectroscopic challenges in atmospheric science. The first of these is the spectral distribution of the incoming solar radiation (i.e. where in the electromagnetic spectrum this shortwave radiation lies). This spectral distribution is important; since shortwave absorption in the atmosphere is strongly dependent on wavelength; more radiation in a localised part of the spectrum can mean more of the radiation is absorbed in the atmosphere, or more of it reaches the surface to be absorbed and emitted as longwave radiation. The second challenge is in understanding components of the shortwave atmospheric absorption that are not well-understood; in this case the *water vapour continuum*, a feature of the water vapour absorption that cannot be fully explained by current spectroscopic theory, and inadequately characterised by existing observations.

1.2: Earth's energy balance and solar radiation

Central to any discussion about climate change is the Earth's *energy balance*. The energy flows into, outward and within the Earth system are shown in Figure 1.1 (from *Stephens et al.* [2012]). This Figure contains several points of note. The incoming and outgoing energy flows do not match; there is an energy imbalance at the top of atmosphere of $0.6 \pm 0.4 \text{ W m}^{-2}$. This indicates that more energy is entering the Earth system via shortwave solar radiation than is leaving it via reflected solar and emitted longwave radiation. Such an energy imbalance will cause more energy to enter the system than leaves it, which increases the temperature of the system. Thus, the Earth's energy imbalance is the key driver of anthropogenic global warming [*Von Schuckmann et al.*, 2016]. Most of this imbalance manifests as an increase in ocean heat content [*Trenberth et al.*, 2014]. Well-constrained values of the Earth's albedo and incoming solar radiation are therefore extremely important for quantification of this energy imbalance. The top of atmosphere energy imbalance (like many of the fluxes such as the sensible heat flux) is not directly measured but inferred from residuals and indirect observations (such as ocean heat uptake for the TOA energy imbalance).

The integrated values shown on Figure 1.1 do not tell the full story however. The spectral distribution of the incoming shortwave (and outgoing longwave) energy is also extremely important, since this spectral distribution determines the proportion of energy that is absorbed by greenhouse gases such as carbon dioxide and water vapour. As will be discussed in Section 1.3, water vapour is of considerable importance both in the shortwave and the longwave spectral regions, and its absorption spectrum is the primary focus of this thesis.

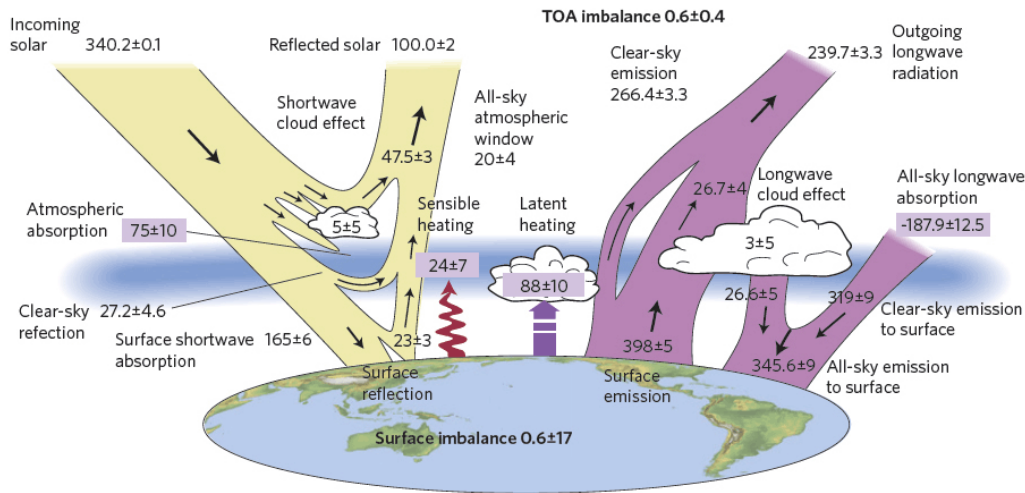


Figure 1.1: Energy flows inside the Earth system, from Stephens et al. [2012], and their associated uncertainties. All values are global and annual averages, and are presented in $W m^{-2}$ on this Figure.

The total amount of incoming solar radiation is well understood as it is strongly constrained by observations (see e.g. Dudok de Wit et al. [2017]). This is shown on Figure 1.1 by the small ($\pm 0.1 W m^{-2}$) uncertainty. However, as this energy is distributed spectrally, the amount of energy absorbed, scattered and reflected by the atmosphere and surface is dependent on where in the spectrum this energy lies (shown in more detail in Section 2.2).

Much ($\sim 40\%$) of the solar energy is emitted in the visible part of the electromagnetic spectrum ($0.4-0.7 \mu m$), which is affected less by atmospheric absorption (e.g. Petty [2005]). Most of this visible energy reaches the surface. The ultraviolet contribution from $0-0.4 \mu m$ is significantly smaller ($\sim 10\%$), but varies strongly with the *solar cycle*, an 11-year change in the Sun’s output corresponding to changes in its magnetic field e.g. Ball et al. [2014]. Additionally, UV radiation is strongly absorbed by stratospheric ozone and molecular oxygen, making it particularly important for middle-atmosphere dynamics (e.g. Zhong et al. [2008]; Ineson et al. [2011]).

Of primary interest to this thesis is the remaining $\sim 50\%$ of this radiation, which is emitted by the Sun at infrared wavelengths ($0.7 \mu m$ and longer). Specifically, this work focuses on part of the near-infrared spectrum between $1-5 \mu m$ (or $2000-10000 cm^{-1}$ in wavenumber, as is the convention hereafter). This is described more in Section 1.3 and 1.4.

Many studies (e.g. *Arvesen et al.* [1969]; *Thuillier et al.* [2003]; *Menang et al.* [2013]) have presented estimates of the near-infrared extraterrestrial solar spectrum. The region 2000-10000 cm^{-1} contains $\sim 25\%$ of the total incoming solar radiation and is strongly absorbed by water vapour in select spectral bands (see Section 1.3); it is therefore important to accurately characterise it. However, several of these studies show no agreement within their $k = 2$ (2 standard deviations) uncertainties, indicating that they cannot be reconciled. The differences in the spectra are up to 10% in the 4000-7000 cm^{-1} region, which corresponds to a difference of $\sim 16 \text{ W m}^{-2}$, which corresponds to an offset of 4 W m^{-2} in Figure 1.1 when averaged globally. This is the subject of Chapter 4 of this thesis. In practice, many applications use semi-empirical models, such as that of *Kurucz and Bell* [1995], or composite data such as the NRLSSI2 spectrum [*Coddington et al.*, 2015]. The latter of these will be discussed further in Chapter 4.

1.3: Absorption of solar radiation in Earth's atmosphere

Figure 1.1 shows several of the energy fluxes in purple boxes. These are the parts of the Earth's energy budget that have the highest relative uncertainty. The focus of this thesis is the contribution from atmospheric absorption, which has a relative uncertainty greater than 10%. This uncertainty also affects the surface absorbed radiation, since any energy that is absorbed in the atmosphere will not reach the surface directly. Gases absorbing radiation in the atmosphere will heat up and emit thermal radiation via Planck's law (see Section 2.2), leading to a heating of the atmosphere, and a cooling via emission of thermal radiation. Additional absorption in the atmosphere therefore creates temperature gradients, which drives dynamical and meteorological processes. Absorption in the atmosphere changes the rate of evaporation from the surface (via the latent heat flux shown in Figure 1.1), affecting the hydrological cycle which in turn affects energy transport in the Earth-atmosphere system [*Wild and Liepert*, 2010].

Figure 1.2 (from *Vardavas and Taylor*, [2007]) shows the solar spectrum alongside the contributors to the absorption and scatter in the clear-sky atmosphere. The

darkest grey region is the difference between the emission spectrum of a 5900 K blackbody and the observed solar emission spectrum. These are different due to the breakdown of the blackbody approximation, and extinction via gases in the solar atmosphere. The ratio of the lighter to medium grey shaded regions is an indicator of how much of the solar energy reaches the surface; where the region is darker indicates less radiation reaches the surface.

In the region of interest to this thesis ($\lambda > 1 \mu\text{m}$) the spectrum has a structure of absorption bands (where no radiation reaches the surface) and windows (where most of the radiation reaches the surface, although some radiation is still absorbed in spectral lines within these windows). This structure is predominantly due to water vapour absorption. The absorption in the band regions is very strong due to rotational-vibrational transitions of the water molecule; an increase in absorption in these regions would not cause a significant change in energy transmitted to the surface, although additional continuum absorption does increase the height in the atmosphere at which radiation is absorbed. An increase in absorption in the windows however would be much more important, since energy would be absorbed that otherwise would have been directly incident on the surface. The spectroscopic basis of the near-infrared region is covered in Chapter 2.

Water vapour absorption in the near-IR is extremely important for determining the hydrological sensitivity, i.e. the degree to which precipitation and the broader hydrological cycle change as a response to a change in temperature [Takahashi, 2009; DeAngelis *et al.*, 2015]. DeAngelis *et al.* indicate that uncertainty in the rate of change of precipitation with respect to temperature in climate models is primarily due to poor representation of shortwave absorption, of which water vapour is a significant part. This is explained in part due to the poor parameterisation of this shortwave absorption in the low-resolution wide-band radiation schemes in the GCMs, but this may also be due to lack of understanding of the underlying spectroscopy.

Additionally, a change in shortwave heating is more effective than a change in longwave heating (e.g. via CO₂ absorption) at changing the global-mean precipitation response to warming (e.g. Allen and Ingram [2002]). Allen and Ingram point out that since most tropospheric air parcels are at near saturation, an increase in

temperature leads to a direct increase in atmospheric water vapour via the Clausius-Clapeyron relation. Therefore, the effect of shortwave heating by water vapour becomes significantly more important in a warming climate.

One of the primary contributors to the near-IR absorption is the water vapour continuum, described in Section 1.4. Chapter 5 presents a derivation of this continuum in the windows at 4, 2.1 and 1.6 μm . This absorption is potentially responsible for much of the uncertainty in the shortwave absorption shown on Figure 1.1; e.g. *Rädel et al.* [2014] demonstrate that using different estimates of the near-IR continuum could result in a $\sim 3 \text{ W m}^{-2}$ difference in atmospheric absorption, with a corresponding difference (in the opposite direction) in the surface radiation. This will be discussed further in Section 1.4.

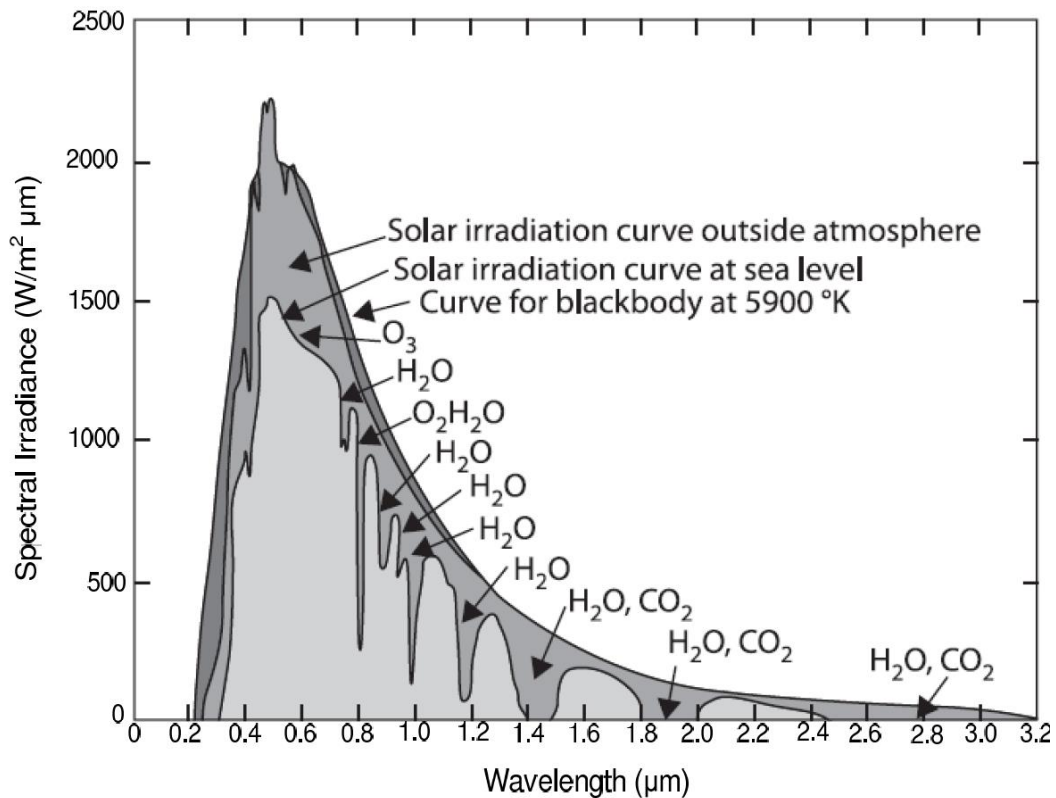


Figure 1.2: Emission spectrum of the Sun. The medium grey shaded regions indicate energy absorbed and Rayleigh scattered in the atmosphere in clear skies, the light grey regions indicate energy that reaches the surface. From Vardavas and Taylor [2007]. The dark grey regions are the difference between a 5900 K blackbody and the observed emission spectrum.

Characterising the atmospheric absorption for a given time and place is done using a radiation code, or by observations where applicable. Radiation codes vary from full line-by-line treatments, e.g. the Reference Forward Model (RFM) [Dudhia, 2017] or the Line-By-Line Radiative Transfer Model (LBLRTM) [Clough *et al.*, 2005], to the wide-band models used in most general circulation models (GCMs) (e.g. Hogan and Bozzo [2018]; Zhao *et al.* [2018]). Band models are used since they improve computational efficiency, at some decrease in their ability to accurately characterise the radiation budget. Line-by-line simulations therefore provide a benchmark for GCM radiation codes to match, such as in the Radiative Forcing Model Intercomparison Project (RFMIP, Pincus *et al.* [2015]; Forster *et al.* [2016]). In this thesis, the RFM is the preferred radiation code used to calculate atmospheric absorption. This is described in more detail in Section 2.3.6.1.

A radiative transfer code relies on a database of spectroscopic parameters, to determine how much absorption occurs at a given wavelength (for a given atmospheric profile). The most popular of these is the HITRAN database [Gordon *et al.*, 2017]; the current version is HITRAN 2016, which is used in this thesis. This is described further in Section 2.3.6.2. Such a line database model is derived via both theoretical calculations (e.g. Barber *et al.* [2008] and laboratory observations (e.g. Tashkun *et al.* [2015]).

One of the significant gaps in such databases is the representation of the water vapour continuum. Shine *et al.* [2016c] assesses the potential for inclusion of the continuum in spectroscopic databases in detail. The continuum is typically modelled in GCMs (e.g. Zhao *et al.* [2018]) and line-by-line models via the MT_CKD (Mlawer-Tobin_Clough-Kneizys-Davies, named after its creators) continuum [Mlawer *et al.*, 2012]. This is a semi-empirical model derived in part from observations. The reliance on observations comes in part from the lack of a robust theoretical framework for the continuum. This is discussed further in Sections 1.4 and 2.4.

The importance of the continuum and lack of understanding (see Section 1.4) is the primary motivation for this thesis. Chapter 5 presents observations of the continuum absorption in the 2000-10000 cm^{-1} region, which demonstrates the great uncertainty in the strength of the continuum in laboratory experiments (see Section 1.4).

1.4: The water vapour continuum

1.4.1: Introduction

The following Section describes the water vapour continuum in the infrared region. More information can be found in *Shine et al.* [2012, 2016c] and *Daniel* [2004]. As discussed in Section 1.3, the near-infrared spectrum is characterised by its spectral band-window structure, where parts of the spectrum are completely opaque to radiation and parts are mostly transparent over typical atmospheric paths. Pervading the entirety of this spectrum (and extending out into the longwave) is the *water vapour continuum*. The strength of the continuum varies smoothly with wavenumber. It is stronger in the water vapour bands and weaker in the windows, underlying the pattern of the water vapour spectral line absorption. Since the bands are saturated (from the perspective of an observer looking up from the surface), the continuum in these regions is less important. In the windows this continuum is much more significant, contributing a significant portion of the atmospheric absorption in these regions, particularly between spectral lines.

The net effect of the continuum is that more energy is deposited in the atmosphere (particularly the troposphere, where most of the water vapour lies) than would be the case without the continuum. Since weather and climate dynamics are driven in part by temperature gradients in the atmosphere, it is important to quantify this absorption. Any radiation absorbed in the atmosphere does not reach the surface, which changes the surface-atmosphere partitioning of energy and is therefore important for understanding the circulation and dynamics of the surface-troposphere system.

The continuum also impacts upon remote sensing of the Earth's atmosphere and surface. Some remote sensing platforms e.g. the Orbiting Carbon Observatory 2 (OCO-2) [*Oyafuso et al.*, 2017] have channels observing in the 2.1 and 1.6 μm windows, as does the MODIS satellite [*Platnick et al.*, 2017], which is used to measure cloud properties, surface albedo and aerosol optical depth.

Section 1.4.2 describes the mechanisms behind the continuum, and our current understanding of the situation in the near-IR. Section 1.4.3 investigates how the continuum impacts the Earth's energy budget and impact on remote sensing.

1.4.2: Theoretical and experimental perspectives on the continuum

As discussed in *Shine et al.* [2012], the water vapour continuum was first observed experimentally in the late 19th century, although it was not until *Elsasser* [1938] that this feature was explained from a theoretical perspective. These observations showed that there was additional absorption by water vapour in regions that spectral line theory did not predict, which pervaded the entire infrared spectrum and typically decreased in strength with wavenumber (following the band-window structure of water vapour absorption). *Elsasser* postulated that the continuum absorption was due to the *far wings* of broadened (see Section 2.1.4) water vapour spectral lines. This theory was successful in describing the behaviour seen in measurements at that time. *Bignell et al.* [1963] presented a continuum derived from atmospheric measurements in the mid-infrared window (at ~8-12 μm), and further into the longwave between 13-20 μm . They found that the optical depth (see Section 2.3) was proportional to the square of the vapour pressure; this is a property associated with the *self-continuum* explained in further detail in the next paragraphs. The far-wing theory was not completely robust however; it relies on an assumption about the line-shape and broadening of water vapour spectral lines that is not the case in reality.

Developments in the late 1960s led different groups to postulate that the continuum could be caused (at least in part) by *water dimers* (see Figure 1.3), bound complexes of two water vapour molecules in the atmosphere. The water vapour spectrum is already complex; the dimer spectrum adds an additional bond axis, further complicating the structure. The high density of spectral lines from the dimer manifests itself as continuous absorption at practical resolution. This contrasts with the far-wing theory, which relies on an adjustment to the water vapour *monomer* lineshape. The continuum was observed to have a negative exponential temperature dependence; this can be considered evidence of the dimer theory, as the dimers will dissociate when subject to more energetic collisions. *Varanasi et al.* [1968] demonstrated that this temperature dependence has an exponential factor close to the

dimer dissociation energy D_0 ; this temperature dependence is still practically used today (see e.g. Section 5.2).

Vigasin [1985] postulated that this dimer theory was not complete; he used a thermodynamic argument to explain that *quasi-bound* dimers (i.e. weakly bound monomer pairs) should be of roughly equal importance in atmospheric conditions. The dimer concentration in the atmosphere is ~0.06 % of the monomer concentration e.g. *Shillings et al.* [2011].

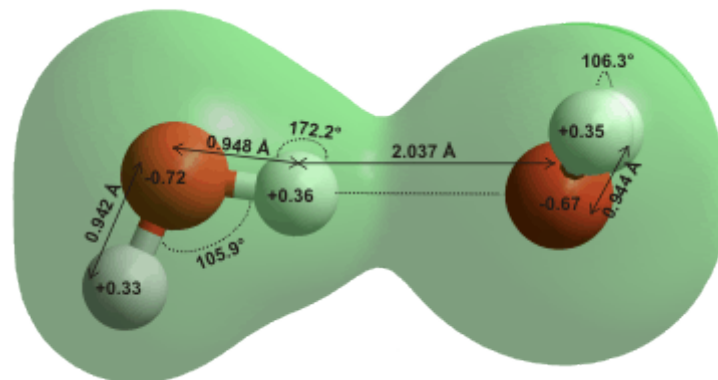


Figure 1.3: Schematic of a water dimer. The molecules are weakly bound across the middle bond axis. Figure by Martin Chaplin, London South Bank University (http://www1.lsbu.ac.uk/water/water_dimer.html).

The continuum is generally considered to have two primary components; these are the *self-continuum* (via interactions between water vapour molecules and far-wings of water monomers), and *foreign continuum* (via interactions between water vapour and other molecules in air, such as molecular nitrogen and oxygen). These have different properties; the self-continuum has negative temperature dependence and varies with the square of the vapour pressure, whereas the foreign continuum has no or very minor temperature dependence and varies with the product of the vapour pressure and overall pressure. The ratio of the self to foreign continuum depends on the spectral region in question and the ambient conditions. The case inside the near-infrared windows will be explored further in Chapter 6.

Most historical measurements (presented in *Shine et al.* [2012]) focus on the continuum in the mid and far infrared and in the microwave, which is important for climate (since it absorbs longwave radiation that would otherwise radiate out to space). The shortwave bands in the near-infrared (2000-10000 cm^{-1}) however have

had a comparative dearth of measurements. These are discussed in more detail in Section 5.2. Available measurements differ in the 1.6 and 2.1 μm spectral regions by ~ 1 -2 orders of magnitude and do not agree within their respective measurement uncertainties.

As discussed in Section 1.3, the continuum is usually represented in models using the MT_CKD (currently version 3.2, although many applications use version 2.5) semi-empirical model of *Mlawer et al.* [2012]. This spectrum is an extension of the CKD model [*Clough et al.*, 1989]. Section 2.4 goes into more detail on the formalism of MT_CKD. It includes both a lineshape parameterisation and a *collision-induced* contribution; the former dominates in the atmospheric windows, the latter in the bands. Since there have been more measurements in the longwave, MT_CKD is rather well constrained in this spectral region. The case in the shortwave is less clear, due to the lack of measurements and the disagreement between them. While there appears to be some consensus at 4 μm between measurements and MT_CKD, contemporary FTS measurements in the laboratory (e.g. *Ptashnik et al.* [2011a, 2013, 2015]) indicate absorption stronger by ~ 1 -2 orders of magnitude than MT_CKD in the 2.1 and 1.6 μm windows. Measurements using cavity ring-down spectroscopy (CRDS) by a group in Grenoble e.g. *Mondelain et al.* [2013, 2014] show much lower continuum absorption coefficients, which better agree with MT_CKD. This is described further in Section 5.2.

It is important to emphasise that MT_CKD is a semi-empirical parameterisation, rather than a physical model of the continuum. While several attempts at ab initio calculations of the water dimer spectrum exist e.g. *Salmi et al.* [2008], these have not yet proved successful in predicting the absorption strength in the windows, particularly in atmospheric conditions. Agreement with MT_CKD is therefore not an indicator of a given measurement being robust, but more an assessment of whether MT_CKD is adequately modelling the continuum absorption strength.

The laboratory (e.g. *Ptashnik et al.* [2011a, 2013]) FTS measurements are typically taken at temperatures well above typical atmospheric temperatures to obtain vapour pressures high enough to extract the continuum from baseline noise. Thus, while these observations are extremely useful for probing the physical properties of the continuum absorption, the absorption strength in atmospheric conditions cannot be

determined without making some assumption about the temperature dependence. *Ptashnik et al.* [2011b] postulate that the “temperature dependence [from observations in the mid-infrared window] is suggestive of a transition from the dominance of true bound dimers at lower temperatures to quasi-bound dimers at higher temperatures”, indicating there may be some deviations at lower temperatures (such as those found in the atmosphere) from the standard negative exponential temperature dependence.

Most of the measurements used to adjust MT_CKD are assessments of the continuum absorption coefficient in laboratory conditions, ideally at a range of temperatures (to more carefully assess the temperature dependence). There have been several (see e.g. *Grant* [1990]) sets of measurements of the longwave continuum in atmospheric conditions, but significantly fewer in the shortwave. *Reichert and Sussmann* [2016] presented a combined self and foreign near-infrared continuum taken from observations at the Zugspitze field site in the German Alps. Good measurements were obtained in the band regions. The high altitude of these measurements (above the layer where much of the atmospheric water vapour lies) meant that the observed continuum is much weaker due to the pressure-squared dependence of the self-continuum and the linear vapour pressure dependence of the foreign. In the windows, the uncertainties were larger than the continuum strength, making these measurements somewhat unreliable. These measurements are explored in more detail in Section 5.2, and in *Shine et al.* [2016a, 2016b].

Preliminary results of a near-infrared combined self + foreign continuum were presented in *Menang* [2012], consisting of analyses of Fourier transform spectrometer (FTS) measurements taken in the field. This thesis aims to update these preliminary results with a more robust uncertainty estimate, and a new calibration of the spectrometer used in this field campaign (see Sections 1.5 and 3.4).

1.4.3: Impacts of the continuum for atmospheric science

The impacts of the continuum in the longwave are many, and important in the microwave [*Payne et al.*, 2011], far-infrared [*Turner et al.*, 2012] and mid-infrared [*Paynter and Ramaswamy*, 2011]. The focus of this work is the shortwave (near-infrared) continuum; this section therefore focuses on this part of the spectrum.

As mentioned in Section 1.3, additional shortwave absorption changes the surface-atmosphere partitioning of energy, affects the hydrological cycle and has effects on dynamical processes. *Rädel et al.* [2014] present an assessment of the global radiative and climate effect of different versions of the shortwave near-infrared continuum (the CKD model and the CAVIAR continuum of *Ptashnik et al.* [2011a], see Section 5.2). Relative to the case with no continuum, the global mean absorption in clear skies is increased by ~ 1.5 and ~ 2.8 W m^{-2} respectively; using the stronger (CAVIAR) continuum results in a 3 W m^{-2} difference in the energy partition between the atmosphere and surface compared to using CKD. These values are potentially quite conservative, as the Tomsk measurements e.g. *Ptashnik et al.* [2015] show greater absorption strength than the CAVIAR continuum. The CAVIAR continuum was extrapolated from measurements at elevated temperatures (between 431 and 350 K) in the 1.6 μm window, due to the large uncertainties in the room-temperature measurements in this window. This introduces additional uncertainty into this calculation, depending on the variation of the continuum strength with temperature.

This effect is particularly important in a warming climate via water vapour feedback; while using the CAVIAR continuum only increases the overall absorption in clear skies by 0.1%, it contributes to 15% of the increase in absorption with increasing water vapour. The increased shortwave absorption in CAVIAR compared to CKD resulted in a 3% reduction in the precipitation response to warming. This occurs since an increase in atmospheric shortwave absorption reduces the amount of latent heating required to balance the surface energy budget (e.g. *DeAngelis et al.* [2015])

Paynter and Ramaswamy [2014] present a detailed study of the shortwave continuum effect on GCM climate simulations using the GFDL model. They found that the continuum reduces the temperature gradient between the surface and atmosphere, resulting in smaller convective (sensible) and latent heat fluxes and “reducing the energy transport between the surface and the boundary layer, which in turn results in decreased convection and precipitation.”

As described in Section 1.4.1, many satellite applications use these windows, such as the MODIS and OCO-2 platforms referenced in that Section. In the OCO-2 case, the continuum increases the amount of absorption in this window relative to the no-continuum case. This is considered in e.g. *Oyafuso et al.* [2017], in which the authors

could not reconcile the variation of measurements of CO₂ absorption with airmass between winter and summer. This difference could be resolved if the continuum were significantly stronger than predicted (in the MT_CKD model, see Section 1.4.2). Recent measurements, summarised in Section 1.4.2 and elaborated upon further in Section 5.2 indicate that this may indeed be the case, despite the claim in *Oyafuso et al.* that “unrealistically large multiplicative factors... for the water vapour continuum are required [to reconcile this difference]”.

Shine et al. [2012] explores the possible impact of the near-infrared continuum on cloud remote sensing in the 2.1 μm window. The authors take an increase in shortwave absorption (in this case going from MT_CKD to the CAVIAR continuum of *Ptashnik et al.* [2011a]) as a decrease in albedo (less radiation is reflected from the top of the cloud), which if unaccounted for will bias any retrieval of cloud droplet size. This effect is particularly important in the tropics, where water vapour content is higher, and for observing at large solar zenith angles (see Section 2.2); both conditions result in an increase in continuum absorption. Given these conditions, they show that the difference between MT_CKD and CAVIAR could lead to a bias in cloud drop mean effective radius of $\sim 1.5 \mu\text{m}$ (independent of droplet size). This effect could be more significant in the 1.6 μm window, where the difference between CAVIAR and MT_CKD is unknown due to the lack of room temperature CAVIAR measurements in this window.

The shortwave continuum is therefore clearly both a phenomenon which is not well understood, but also one that is potentially important for a variety of applications. These two factors were the main motivations for the work performed in this thesis.

1.5: Objectives of this work

The aim in this work is to help resolve these issues via analysis of high resolution Fourier transform spectrometer (FTS) measurements of near-infrared solar radiation through the atmosphere. These measurements were taken in Camborne, Cornwall, UK at a Met Office field site at 88 m above sea level and were taken across the course of a 2-month (July-September 2008) period. The measurements were performed by Liam Tallis (University of Reading), Tom Gardiner and Marc Coleman

(National Physical Laboratory) during the CAVIAR (Continuum Absorption at Visible and Infrared wavelengths and its Atmospheric Relevance) project.

This spectrometer was absolutely calibrated, meaning that it can directly observe spectral irradiance, from which via the use of a radiation code or the *Langley method* the top of atmosphere spectral solar irradiance can be derived. Using the Langley method (discussed in Section 3.3.2), one can also independently obtain atmospheric optical depth, which via the use of a line-by-line code and some characterisation of aerosol and Rayleigh scattering can be used to derive the water vapour continuum absorption contribution to the optical depth. The methodology used to characterise and ultimately derive SSI and continuum absorption are presented in the subsequent Chapters.

Chapter 2 focuses on fundamental spectroscopy and aims to explain the behaviour of gases and aerosols in the near-infrared when exposed to radiation. It also discusses some of the basic physics behind emission of solar radiation, and the technical details of the line-by-line radiation code used extensively throughout the thesis.

Chapter 3 focuses on the technical aspects of the Fourier Transform spectrometer, including the fundamental principles of how one works, and the specific spectrometer used in the field campaign. Work performed during this thesis is included here, regarding updates to the calibration and uncertainty budget of the measurements. This section also details the analytical methods used in the thesis, particularly the Langley and radiative closure methods used to derive the continuum optical depth and solar spectral irradiance (SSI).

Chapter 4 primarily contains a paper published in *Geophysical Research Letters* in 2017 [Elsley *et al.*, 2017], which uses the Camborne measurements to derive a new, updated version of the CAVIAR spectrum from Menang *et al.* [2013], featuring a new calibration and updated uncertainty budget. Section 4.3 of this Chapter also contains work done since Elsey *et al.* [2017], regarding additional datasets published before and since the publication of that paper.

Chapter 5 presents new observations of the water vapour continuum absorption in atmospheric conditions, featuring (to the author's knowledge) the first derivation of the continuum in the 1.6 and 2.1 μm atmospheric windows from radiometrically

calibrated observations. These are the first values that include fully characterised uncertainties. This Chapter also features a literature review of near-infrared laboratory continuum observations, particularly regarding the MT_CKD continuum model used in many radiative transfer applications.

Chapter 6 presents a comparison of these new continuum observations with the laboratory measurements and assesses the relative contribution of the self and foreign continuum to atmospheric absorption, and its implication for the MT_CKD model.

Chapter 7 presents conclusions and future work, particularly ways in which a future measurement campaign could improve the derivation of SSI and continuum.

Chapter 2:

Radiative processes in the terrestrial atmosphere

This chapter will cover various aspects of molecular spectroscopy and radiative transfer necessary for this thesis. A full treatment of many of these topics is outside of the scope of the thesis; more information is available in the References. Section 2.1 focuses on the fundamental physics of molecular spectroscopy, in particular that of the water vapour molecule. Section 2.2 focuses more on the basic physics of the Sun, to provide some background for Chapter 4. Section 2.3 looks at radiative transfer in the atmosphere and the means with which we can approximate this numerically. Section 2.4 focuses on the water vapour continuum, and the ways this is implemented into the numerical model. References will be made to the state of current observations where applicable, particularly regarding the near-infrared solar spectral irradiance (SSI) and continuum on which this thesis focuses. It is important to note that in general, spectroscopists focusing on the near-IR tend to work in spectral wavenumber $\nu = 1/\lambda$, (in units of cm^{-1}) and that convention is followed here.

2.1: Molecular spectroscopy

Molecules absorb electromagnetic radiation at specific wavelengths depending on their electronic and molecular structure. This absorption (alongside scattering) is responsible for the distribution of energy from the Sun throughout the atmosphere, which ultimately drives dynamical processes and leads to the patterns of weather we see day to day. This absorption is governed by the rules of quantum mechanics, and a full treatment is well outside of the scope of this work. Below is a basic overview of some of the principles that govern molecular absorption. More information can be found in e.g. *Banwell and McCash* [1994].

In quantum mechanics, atoms and molecules absorb radiation only at specific wavelengths, corresponding to a change in the discrete electronic, vibrational or rotational (in order of decreasing energy) energy levels of the molecule. Electronic transitions generally occur at wavelengths in the visible and UV regions of the

spectrum, and are unimportant in the scope of this thesis.¹ While there is coupling between the electronic and nuclear (vibrational, rotational) motion of a molecule, it is here assumed the Born-Oppenheimer approximation holds (i.e. the wavefunction of these two motions can be separated). In the near-infrared, the vibrational and rotational levels are of most interest. These are generally notated by the rotational quantum number J and vibrational quantum number v . While the electronic and nuclear motions are considered de-coupled, there is strong coupling between rotational and vibrational modes which cannot be neglected. Absorption spectra are generally made up of lines from a vibrational mode, surrounded by lines from corresponding rotations at that vibrational level.

In general, a molecule cannot absorb radiation unless it has an electric or magnetic dipole moment (more specifically, unless the rotation or vibration leads to a *change* in dipole moment). This dipole moment arises from the distribution of the electrons inside a molecule. For example, water vapour is very polar (i.e. has a large dipole moment), since it has a high degree of asymmetry due to the oblique angle between the two hydrogen atoms. There are a very large number of possible rotational and vibrational modes due to this (and the three possible axes of rotation). Conversely, the carbon dioxide molecule has zero dipole moment, meaning that of the three vibrations possible from the geometry of the molecule, only the asymmetric stretch mode (ν_2) and bending mode (ν_3) are infrared active², since these are the only possible vibrations which lead to a change in dipole moment. Figure 2.1 shows this graphically for water vapour. Typically a transition (absorption or emission) is notated by the vibrational quantum numbers of the transition, e.g. $010 \leftarrow 000$ denotes a transition from the ground state to the first excited state of the ν_2 mode.

The difference in structure leads to very different absorption spectra between the two molecules. While the CO_2 spectrum is relatively sparse, the water vapour spectrum has a band-window structure rich in individual rotational-vibrational lines. More specific information on the absorption by water vapour is presented in Section 2.1.5.

¹ Some electronic lines of certain species do extend into the near-IR about as far as $1 \mu\text{m}$, but are not important for this thesis.

² While the ν_2 symmetric stretch band is not conventionally infrared active, it is Raman-active.

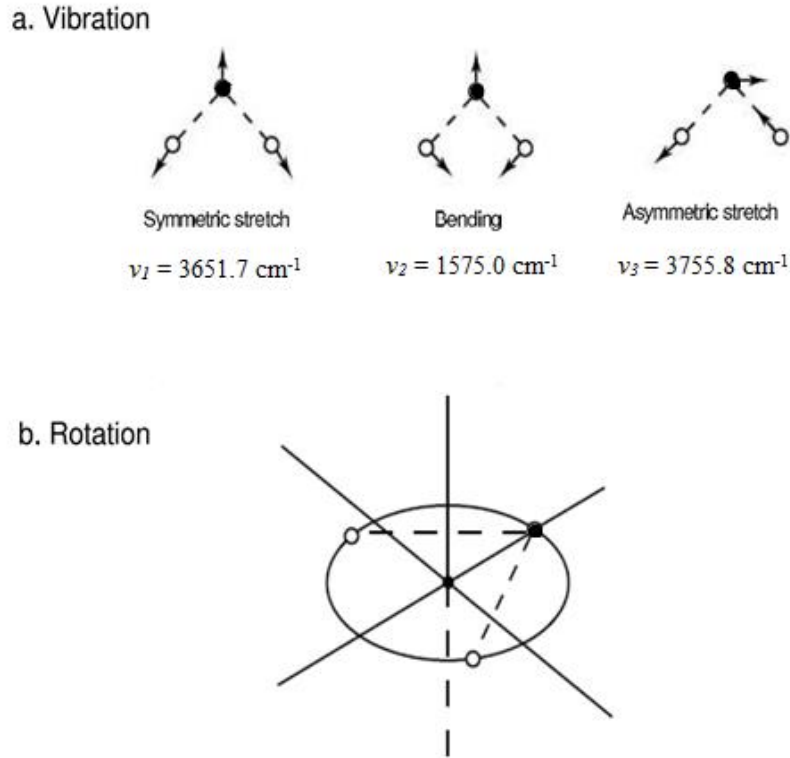


Figure 2.1: Water vapour vibration and rotation modes, adapted from Liou [2002].

2.1.1: Rotational spectroscopy

Rotational transitions occur when a photon is absorbed or emitted by a molecule. Purely rotational transitions are only relevant at low energies ($\nu < 2500 \text{ cm}^{-1}$). The concepts in this section are explained further in *Banwell and McCash*, [1994], *Atkins et al.* [2017] and *Bernath* [2005]. While a rigorous treatment involves a solution to the Schrödinger equation, a semi-classical treatment gives a close approximation and is useful for conceptualisation. Consider the simplest case (a diatomic molecule, e.g. Figure 2.1). In this case, the molecule has three axes of rotation, about the bond axis, and two rotations perpendicular to the bond axis (Figure 2.1b). The rotation of a system is dictated by its moment of inertia I , and is given by

$$(2.1) \quad I = \sum m_i r_i^2$$

where m_i is the mass of atom i and r_i is the radius from the centre of mass, and the summation is over all atoms i in the molecule. In the diatomic case, I_A is zero, and $I_B = I_C$. The energy associated with a rotation is given by:

$$(2.2) \quad E = \frac{1}{2} I \omega^2.$$

Angular momentum is classically given by:

$$(2.3) \quad L = I \omega.$$

This angular momentum on the quantum scale is discrete, and dictated by the rotational quantum number J (e.g. Liou 2002):

$$(2.4) \quad L = \frac{h}{2\pi} \sqrt{J(J+1)}$$

where h is the Planck constant. Here J is an integer, meaning this angular momentum is quantised. Combining Equations (2.2), (2.3) and (2.4) yields:

$$(2.5) \quad E = \frac{J(J+1)\hbar^2}{2I}.$$

The quantity $\frac{\hbar^2}{2I}$ is often referred to as the rotational constant B . \hbar is the reduced Planck constant, equal to $\frac{h}{2\pi}$.

To find the energy of a rotational transition, we need to look at changes in the rotational quantum number J . This can only change in accordance with specific rules, known as *selection rules* (see e.g. *Banwell and McCash* [1994]). It is found that $\Delta J = \pm 1$. Given a transition from J to $J+1$ and substituting this into Equation (2.5):

$$(2.6) \quad \Delta E = \frac{\hbar^2}{2I} ((J+1)(J+2) - J(J+1)) = \frac{\hbar^2}{I} (J+1) = 2B(J+1)$$

Given $E = hc/\lambda = h\nu$ (with ν wavenumber), B becomes:

$$(2.7) \quad \tilde{B} = \frac{\hbar}{4\pi I c}$$

Thus, we can determine the frequency spacing between individual spectral lines.

$$(2.8) \quad \nu = 2\tilde{B} (J+1)$$

Since \tilde{B} only depends reciprocally on the moment of inertia, it is apparent that molecules with high moments of inertia will have very small spacing between spectral lines, whereas molecules with lower moments of inertia will have larger spacing. As such, diatomic molecules with large differences in mass between the two atoms will have a much sparser absorption spectrum compared to those with similar masses, since the centre of gravity will tend toward the larger atom in this case and the moment of inertia will be reduced. This case considers the bond between the

atoms to be rigid; a more rigorous treatment includes a correction term to account for this not being the case, and relaxes the permitted selection rules in some cases (see Section 2.1.3).

The diatomic case is the simplest possible; while a similar treatment can be made for a linear triatomic molecule (e.g. CO₂), it is extremely difficult for cases such as water vapour (an ‘asymmetric top’) which have three separate and different moments of inertia (i.e. $I_A \neq I_B \neq I_C$).

2.1.2: Vibrational transitions

Vibrational transitions occur when an absorption or emission of a photon results in a change in the vibrational energy level of the molecule. A (non-linear) molecule has $3N$ degrees of freedom, where N is the number of atoms that make up the molecule. These degrees of freedom encompass translation, rotation and vibration. Accounting for the three translational and three rotational degrees of freedom, the remaining $3N - 6$ ($3N - 5$ in the linear case, since the rotation about the bond axis has zero moment of inertia) degrees of freedom are vibrational. For complex molecules it is the vibrational spectrum which leads to much of the spectral structure. For example, water vapour has 3 vibrational modes ($9 - 6$). These vibrational modes are shown in Figure 2.1, along with their characteristic wavenumbers.

A pure vibration can be conceptualised using the simple harmonic oscillator. Since we are dealing with quantised energy levels, this particular case can be modelled using the quantum harmonic oscillator (see e.g. *Atkins et al.* [2017]).

A vibration can be thought of as like the displacement of a mass on a spring. Any change from the equilibrium position r_{eq} will be met by a restoring force via Hooke’s Law:

$$(2.9) \quad F = -k(r - r_{eq})$$

with k the spring constant. The time-independent Schrödinger equation can be written:

$$(2.10) \quad -\frac{\hbar}{2m} \frac{\partial^2 \psi}{\partial x^2} + V(x)\psi = E\psi$$

Here m is the mass of the system, x the position vector, ψ the wavefunction, E energy and V the potential energy. In this case, it can be found that, using a quadratic potential:

$$(2.11) \quad E_n = \left(n + \frac{1}{2}\right) h\nu$$

with n the vibrational quantum number and ν wavenumber. The difference between energy levels n and $n+1$ is therefore $h\nu$.

This case is an approximation: in reality Hooke's Law does not hold. A more sophisticated treatment using an anharmonic quantum oscillator can be found in e.g. *Banwell and McCash* [1994] or *Bernath* [2005].

2.1.3: Rotational-vibrational transitions

The spectrum of water vapour (and other gases) in the near-IR is made up of a combination of rotational and vibrational transitions. Figure 2.2 shows a typical structure of a combination rotation-vibration band, in this case the ν_1 and ν_3 bands of water vapour (dominated by the ν_3 band). Typically, a vibrational transition ($\Delta v = 1$ with $v =$ vibrational quantum number) is associated with what is known as a *P-branch* and an *R-branch*, i.e. transitions of $\Delta J = -1$ and $=1$ respectively. Some transitions where the rigid rotor approximation breaks down also have a "Q-branch", where $\Delta J = 0$. This Q branch is typically stronger than the P and R branches. The vibrational mode on Figure 2.2 shows a transition where this Q branch is suppressed. Since water vapour has a complex rotational spectrum (due to the 3 axes of rotation), this structure is less clear than in a simpler molecule (e.g. CO₂).

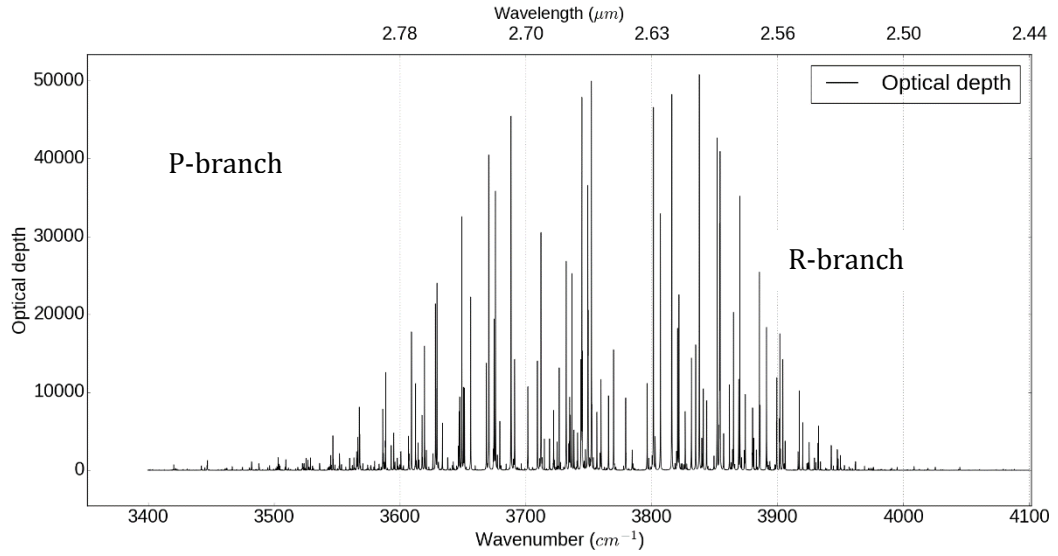


Figure 2.2: Plot of P and R branches of the ν_3 water vapour absorption band at $\sim 3700 \text{ cm}^{-1}$. Model run generated from the RFM using HITRAN 2016, for path from top of atmosphere to surface in the US standard atmosphere.

These branches are typically asymmetric in strength, since the energy levels of particles in a semi-classical gas follow the Boltzmann distribution:

$$(2.12) \quad N_i = g_i N_0 e^{\frac{-E_i - E_0}{k_B T}}$$

Here N_i is the number of particles at energy level E_i , N_0 is the number at the ground state energy E_0 , k_B is the Boltzmann constant and T is the temperature of the gas. As temperature increases the number of molecules in higher states increases relative to the ground state. g_i is a term that arises from degeneracy; in most cases particles with the same energy level can exist with different orientations of their angular momentum vector, which increases the number of possible particles within a given energy level.

This degeneracy is important, since it means that the ground state is often not the most populated state, so that the spectrum is not dominated by $J = 0$ to $J = 1$ transitions. Figure 2.3 shows the population of a gas at 300 K ignoring (left) and including (right) degeneracy. This second distribution looks similar to the envelope of the H_2O R branch in Figure 2.2; more available molecules in a given state means more molecules that can make transitions of $\Delta J = \pm 1$ and thus a stronger absorption line.

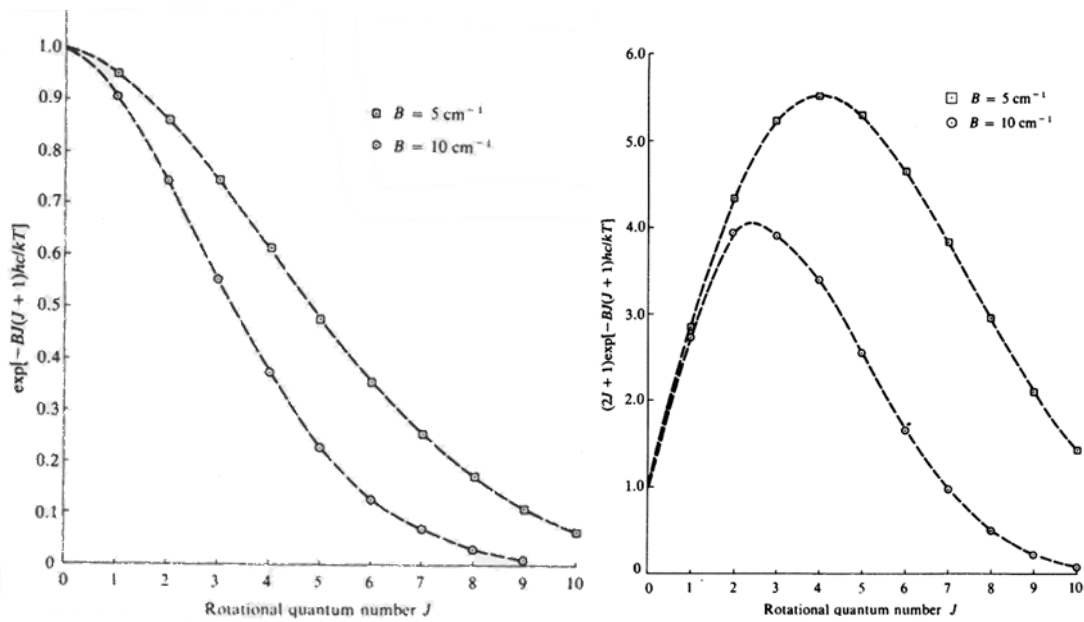


Figure 2.3: Relative population as a function of J calculated not including (left) and including (right) degeneracy. This degeneracy leads to the absorption structure observed in e.g. Figure 2.2. From Banwell and McCash [1994]

2.1.4: Line broadening

A given spectral line is associated with a particular wavenumber. In a real spectrum however, these lines do not resemble δ -functions; the absorption is spread out over a wider spectral region. At a given wavenumber ν , the absorption coefficient k is given by:

$$(2.13) \quad k(\nu) = S f(\nu - \nu_0)$$

where ν_0 is the transition wavenumber of a given spectral line, and S is the line intensity. $f(\nu - \nu_0)$ is a *lineshape function*, which determines how a line is broadened out from its central wavenumber to those around it. This function is a result of a combination of several physical factors, the most important of which are natural broadening, collision broadening and Doppler broadening. To ensure that line strength and broadening are decoupled, the lineshape is normalised to unit area:

$$(2.14) \quad \int_0^\infty f(\nu - \nu_0) d\nu = 1$$

which substituting into (2.13) and integrating over all wavenumbers gives S as the line intensity as expected. This lineshape function is generally symmetric and peaked at the transition wavenumber ν_0 .

It is important to note that due to line broadening, the absorption at a given wavenumber is not just dependent on molecular transitions at that wavenumber, but also the combined contributions of the *wings* of transitions at all wavenumbers around it. This broadening can be very significant; for closely spaced lines at high pressure broadening can completely mask this line structure, as in Figure 2.4 (from Petty [2005]). Even when measuring in micro-windows between spectral lines (as will be shown later on in the thesis), it is important to model the spectral lines within several wavenumbers either side to account for this effect.

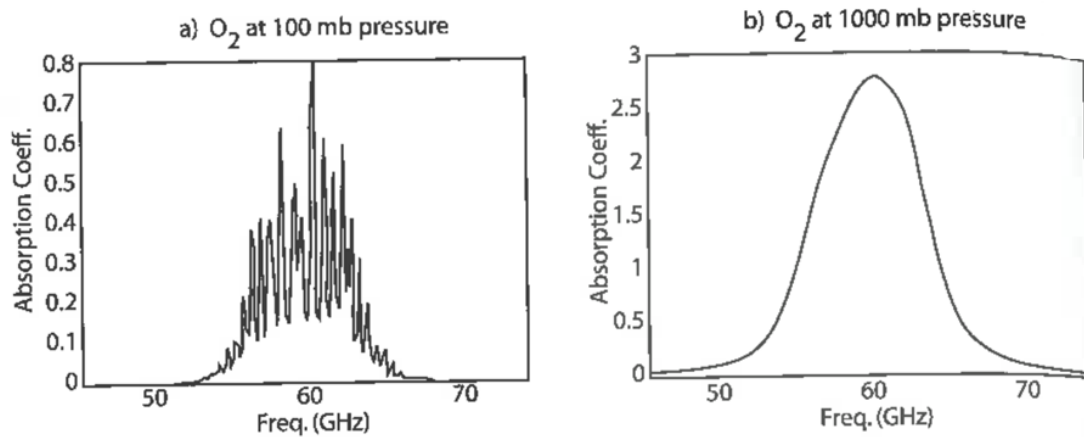


Figure 2.4: Plot demonstrating the effect of line broadening with several closely spaced lines. As the lines become more broadened, the spectral features become more difficult to discern. In this case, the broadening is collision broadening (see Section 2.1.4.2) at 100 mb (left) and 1000 mb (right). From Petty [2005]

More information on line broadening is available in e.g. Liou [2002], Pett [2005] and Banwell and McCash [1994]

2.1.4.1: Natural broadening

Heisenberg's uncertainty principle states that:

$$(2.15) \quad \Delta E \Delta t \geq \frac{\hbar}{2}$$

here ΔE is the uncertainty in the energy of a process and Δt is the uncertainty in the time of this process. The inference here is that neither the energy and time (or

equivalently position and momentum) of a particle can be known to arbitrary precision. As such, if a process (e.g. the absorption of a photon by a molecule) has a short (and precise) lifetime, there must be a corresponding increase in the uncertainty of the energy of that process. Since via $E = h\nu$ energy and wavenumber are linked, increasing the uncertainty in energy increases that in wavenumber, causing a broadening in the absorption.

This effect is typically negligible in atmospheric conditions due to the dominance of collision broadening in the troposphere and Doppler broadening in the high atmosphere but is useful as an introduction to collision broadening since it also operates using this mechanism.

2.1.4.2: Collision broadening

Collision broadening is a term which refers to any type of line broadening caused by the proximity of particles in a gas to one another. Molecules can affect the energy levels (and thus line positions) of other molecules by this proximity, and interaction between molecules can interrupt radiative processes, which causes the inherent uncertainty in the energy of this process to increase (c.f. natural broadening). The reduction in radiative lifetime caused by pressure broadening is much greater than that of natural broadening in the atmosphere.

Collision broadening and natural broadening are (generally, although not necessarily rigorously) described using a Lorentzian lineshape:

$$(2.16) \quad f_L(\nu - \nu_0) = \frac{\alpha_L/\pi}{(\nu - \nu_0)^2 + \alpha_L^2}$$

Here $f_L(\nu - \nu_0)$ is the Lorentzian lineshape function, and α_L is the Lorentzian half-width parameter, often referred to as the line-width (units cm^{-1}). In simple terms, α_L gives the wavenumber at which in a given spectral line the absorption strength is half that at line centre. Since the amount of broadening is determined by the number of collisions between molecules, α_L depends on the pressure and temperature of the gas. It is typically modelled via:

$$(2.17) \quad \alpha_L = \alpha_0 \left(\frac{p}{p_0}\right) \left(\frac{T_0}{T}\right)^n$$

with α_0 a reference linewidth for that particular line (e.g. from HITRAN, see Section 2.3.6.2) taken at a reference pressure and temperature p_0 and T_0 respectively. n is an

empirically defined exponent that dictates the temperature dependence of the line broadening. It is possible to further separate α_L into foreign and self-broadening coefficients (i.e. the degree to which the line is broadened by collisions with air and with other molecules of the same type respectively).

Conservation of energy dictates that as a line is broadened, the absorption strength in the centre of that line must decrease correspondingly. The increase in the far-wing absorption (and the decrease in the absorption at line centre) scales with pressure and temperature as indicated by Equation (2.17). This lineshape is an approximation; it is not necessarily accurate outside of the limit where $\alpha_L \ll \nu_0$. Since α_L is generally much smaller than 1 cm^{-1} , any inaccuracy from the Lorentzian lineshape will not affect lines in the near-IR significantly (although as will be discussed later in the thesis, this does not apply to the continuum).

2.1.4.3: Doppler broadening

Doppler broadening refers to line broadening where a radiative process undergoes a Doppler shift, since molecules in a gas travel with some velocity V relative to an observer. This velocity is dependent on temperature; the probability $p(V)$ of such a molecule within a gas traveling at this velocity is given by the Maxwell-Boltzmann distribution:

$$(2.18) \quad p(V_s) = \frac{1}{V_0 \sqrt{\pi}} e^{-\left(\frac{V}{V_0}\right)^2}$$

Here V_0 is the root mean squared velocity of molecules in this gas ($V_0 = \sqrt{\frac{2k_B T}{m}}$), where m is the mass of a given molecule in the gas. A photon is Doppler shifted by a wavenumber proportional to the velocity of the molecule V (assuming a stationary source):

$$(2.19) \quad \nu' = \nu (c - V)$$

with ν' the Doppler shifted frequency and c the speed of light. When the molecule has some relative velocity, a photon can absorb at a frequency different to the transition frequency ν_0 . Combining (2.18) and (2.19) yields the Doppler lineshape function f_G for the resultant line broadening:

$$(2.20) \quad f_G(v - v_0) = \frac{1}{\alpha_D \sqrt{\pi}} \exp\left(-\frac{(v-v_0)^2}{\alpha_D^2}\right)$$

Here $\alpha_D = v_0 \sqrt{\frac{2k_B T}{mc^2}}$. The initial probability distribution is a Gaussian, as is the resulting lineshape function. As the temperature of the gas increases, the spread in velocities also increases and thus the lineshape function becomes wider. Physically, as the spread becomes wider there are fewer molecules at a velocity which is (relatively) stationary to the observer. This lineshape has less pronounced line wings than the Lorentzian lineshape, but has a wider central peak.

2.1.4.4: Voigt and Hartmann-Tran lineshape profiles

Collision broadening is dependent on atmospheric pressure, since higher pressure reduces the mean free path between molecules. Its influence is therefore most seen in the absorption spectra of tropospheric species such as water vapour, and is the most important source of line broadening in the model simulations in this thesis (see Section 2.3.6.1 and 3.4.5.2). Doppler broadening is (relatively) more important in the upper atmosphere, as it is only dependent on temperature. This relative importance is strongly wavenumber dependent.

A typical α_0 (see Eq. 2.17) for water vapour at $\sim 6600 \text{ cm}^{-1}$ is $\sim 0.05 \text{ cm}^{-1}$ (taken from HITRAN, neglecting self-broadening effects since $p \gg e$, where e is the vapour pressure). The pressure dependence dominates over the temperature dependence, so the latter is not considered in this calculation (although is considered in the more detailed model calculations used later in this thesis). Assuming $p = 200 \text{ hPa}$ gives $\alpha_L \sim 0.01 \text{ cm}^{-1}$; this value increases with increasing pressure. A water vapour line at 6600 cm^{-1} has a α_D of $\sim 10^{-4} \text{ cm}^{-1}$ (assuming a temperature of $\sim 250 \text{ K}$); therefore in these conditions collision broadening dominates ($\frac{\alpha_L}{\alpha_D} \sim 100$).

Figure 2.5 shows a) a schematic of a Gaussian and a Lorentzian line with the same half-width (from Petty [2005]), and b) the relative half-widths of idealised water vapour lines at different wavenumbers with altitude. This schematic indicates the region of the atmosphere at which pressure broadening begins to become important relative to Doppler broadening.

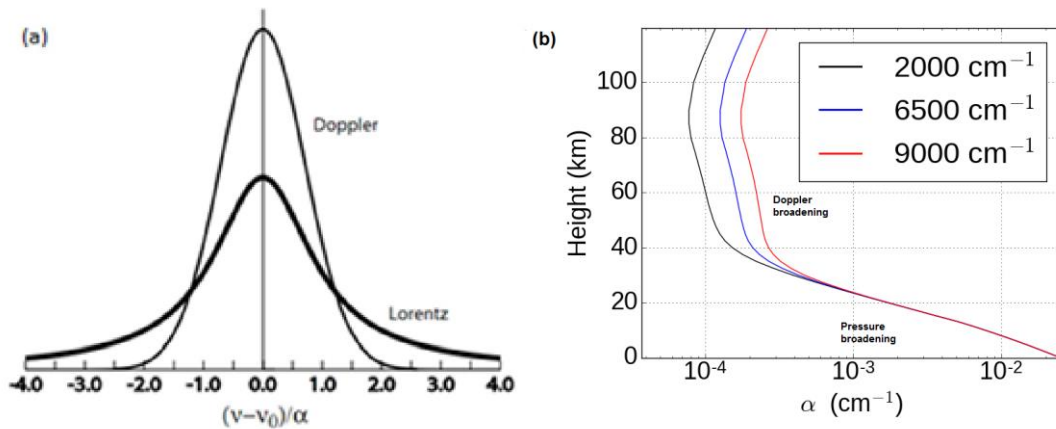


Figure 2.5: Schematic of an absorption line with Gaussian and Lorentzian broadening (a, from Petty [2005]), and the broadened width of idealised NIR ($\alpha_0 = 0.05$) water vapour lines as a function of height for a US standard atmosphere (b). The Voigt half-width was calculated using the approximation of Olivero and Longbothum [1977].

Since collision broadening generally dominates in the lower atmosphere and Doppler broadening in the upper atmosphere (although this varies with wavenumber), it holds that at intermediate points the two both contribute significantly to broadening and a combination lineshape must be used. This is commonly done using the Voigt lineshape; simply a convolution of the Lorentzian and Gaussian lineshapes, i.e.:

$$(2.21) \quad f_v(\nu - \nu_0) = \int_{-\infty}^{\infty} f_L(\nu') f_G(\nu - \nu') d\nu'$$

Most atmospheric radiative transfer models use this convention. Water vapour absorption is dominated by pressure broadening; as such most of the broadening is in the limit where the Voigt lineshape is mostly Lorentzian in nature.

There have been several attempts to construct more sophisticated lineshapes, to represent more of the physics involved in molecular transitions in the atmosphere. The IUPAC [Tennyson *et al.*, 2014] recommends the adoption of the Hartmann-Tran profile. A lineshape function is a function of many physical variables; in the case of the Voigt profile simply the Lorentzian and Gaussian half-widths, and the line shift from pressure broadening (alluded to in Section 2.1.2). The Hartmann-Tran lineshape however includes more physics, including for example a parameterisation of soft collisions, where the velocity of two molecules (and thus the broadening) after a collision depends on the speed of the collision, and can cause line narrowing (the

Dicke effect). This is primarily important at band centre rather than at the wings, and should not be important for measuring continuum absorption.

Adding additional variables improves the accuracy of the lineshape, which in the case of the Voigt profile can be ~10% inaccurate [Tran *et al.*, 2007], at the expense of computation time. The IUPAC report recommends the use of Hartmann-Tran due to a relatively small increase in computation time relative to the increase in accuracy. This is not yet applicable for all atmospherically relevant lines, since the required data is not available for all of the lines within the HITRAN database. This increase in accuracy is important in detailed spectroscopy, but detailed assessments of its relevance in atmospheric applications are not yet available.

2.1.5: Water vapour near-infrared spectrum

The near-infrared spectrum of water vapour is complex and includes thousands of spectral lines (see e.g. Barber *et al.* [2006]). These lines follow a band-window structure, as shown in Figure 2.6. This band-window structure arises from the rotational-vibrational structure of the water vapour molecule. The fundamental ν_1 and ν_3 modes of water vapour (see Figure 2.1 and Figure 2.2) have almost the same central wavenumber ($\sim 3700\text{ cm}^{-1}$). The ν_2 bending mode has a wavenumber around half ($\sim 1500\text{ cm}^{-1}$) of the ν_1 and ν_3 modes. The band-window structure is a consequence of these bands and their overtones, along with combination bands (where several transitions occur at once, e.g. $101 \leftarrow 000$ where the ν_1 and ν_3 vibrations occur simultaneously) and *hot bands*, where transitions occur from states other than the ground state (e.g. the transition $202 \leftarrow 101$ would be a combination hot band). These vibrational bands cluster around certain wavenumbers as a result of this, as shown in Figure 2.6. Each of these vibrational transitions in turn has a series of rotational transitions, exhibiting P, Q (depending on the selection rules of that particular transition) and R structure as shown in Figure 2.2.

Also present in the NIR spectrum on Figure 2.6 is absorption from isotopologues of H_2O , such as HDO. The absorption feature at $\sim 2800\text{ cm}^{-1}$ for example is the ν_1 fundamental of HDO, which is shifted relative to H_2O due to the doubled mass of one of the hydrogen atoms. While HDO makes up a very small fraction of the total water vapour in the atmosphere (0.2 % according to HITRAN), the presence of strong absorption bands in a spectral region that is otherwise mostly transparent

results in the absorption features being prominent. It is important to note here that HITRAN assumes a constant isotopologue concentration; in reality however the relative concentration changes, as evaporation and condensation change the amount of HDO present. Analysing the relative fraction (e.g. using FTIR) is a novel tool for determining the source and dynamics of water vapour (e.g. *Schneider et al.* [2006]).

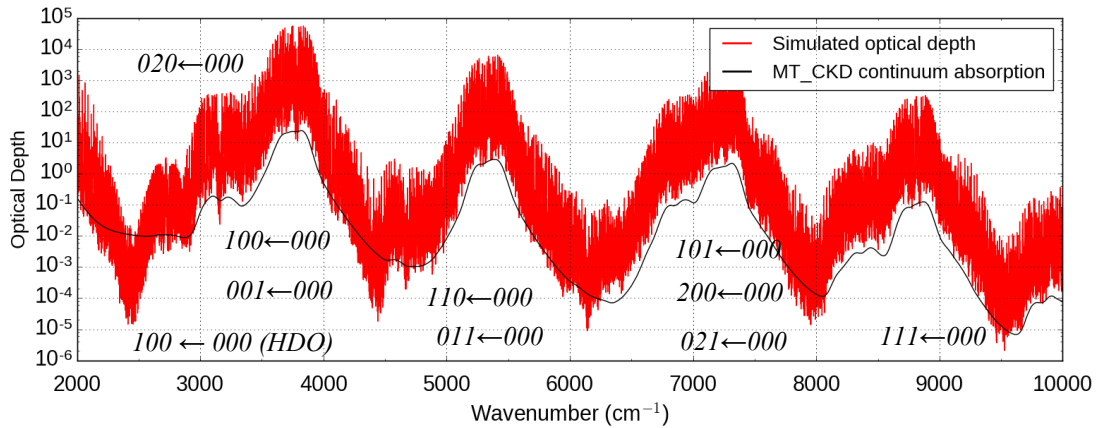


Figure 2.6: *Near-infrared water vapour spectrum, shown here as optical depth on a logarithmic scale for a vertical path from top of atmosphere to the surface using the US Standard atmosphere. The regions above ~5 optical depths are completely saturated; no solar radiation entering the top of the atmosphere reaches the surface. Also included is the MT_CKD 2.5 continuum absorption: this will be expanded upon later in this Chapter. Model run taken from the Reference Forward Model with HITRAN 2016.*

These lines follow the physical principles presented previously in this Chapter, including line broadening. Figure 2.7 shows the effect of different pressures on the line strength and broadening. Additional to these lines (as shown on Figure 2.6) is the water vapour continuum, a phenomenon not represented solely by spectral line theory and is the subject of this thesis. This will be explained further in Section 2.4.

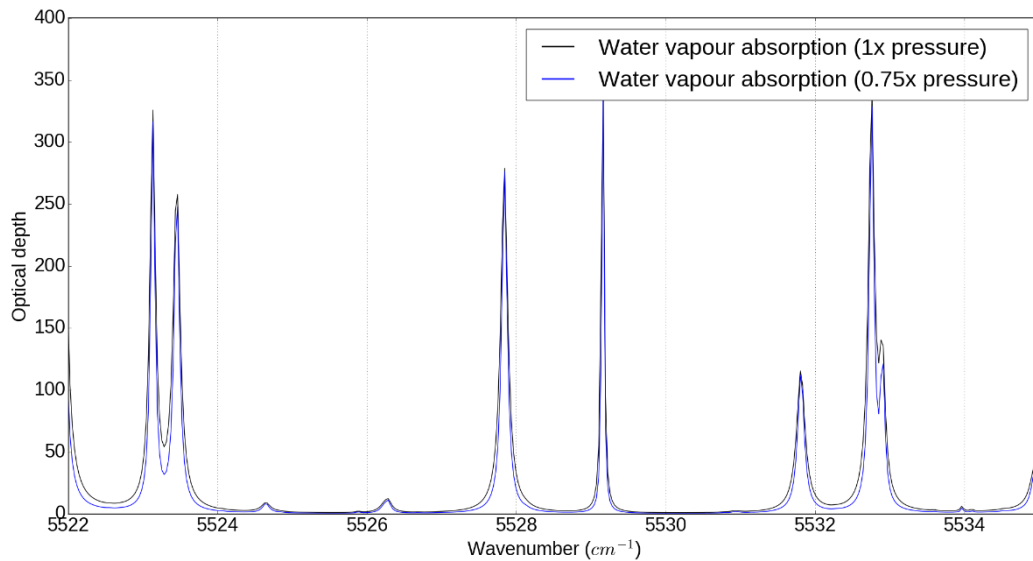


Figure 2.7: Effect of reducing atmospheric pressure at each level by 25% on RFM + HITRAN-modelled line widths, for a small region on the edge of the $2\ \mu\text{m}$ water vapour band, using a vertical path from the top of atmosphere to the surface using the US Standard atmosphere.

2.2: Solar radiation

The primary energy input into the Earth is radiation from the Sun. This energy input drives dynamics and meteorological processes in the atmosphere, and gives rise to weather and climate. It is also absorbed and re-emitted by the Earth's surface at lower wavenumbers, which is re-absorbed by the atmosphere. Understanding solar radiation is therefore vital for studies of weather and climate using models.

Solar radiation is emitted at different wavelengths in the electromagnetic spectrum, which are absorbed and scattered by gases, aerosols and clouds in the atmosphere based on their spectroscopic and bulk properties. It is therefore also important to understand the spectral variation of solar radiation, often referred to as the *solar spectral irradiance* (SSI). This will be discussed in more detail in Chapter 4.

The Sun emits radiation approximately according to the blackbody distribution. The spectral radiance of a blackbody B_ν at frequency ν is given by the Planck function:

$$(2.22) \quad B_\nu(\nu, T) = \frac{2h\nu^3}{c^2} \frac{1}{e^{\frac{h\nu}{k_B T}} - 1}$$

where T is the temperature of the blackbody. The visible disk (i.e. the photosphere) of the Sun is a blackbody of $T \sim 5800\text{K}$; the blackbody spectrum of an emitted at 5800 K roughly equates with the observed spectrum of the Sun (see Figure 2.8). More information on this section is available in e.g. *Liou* [2002].

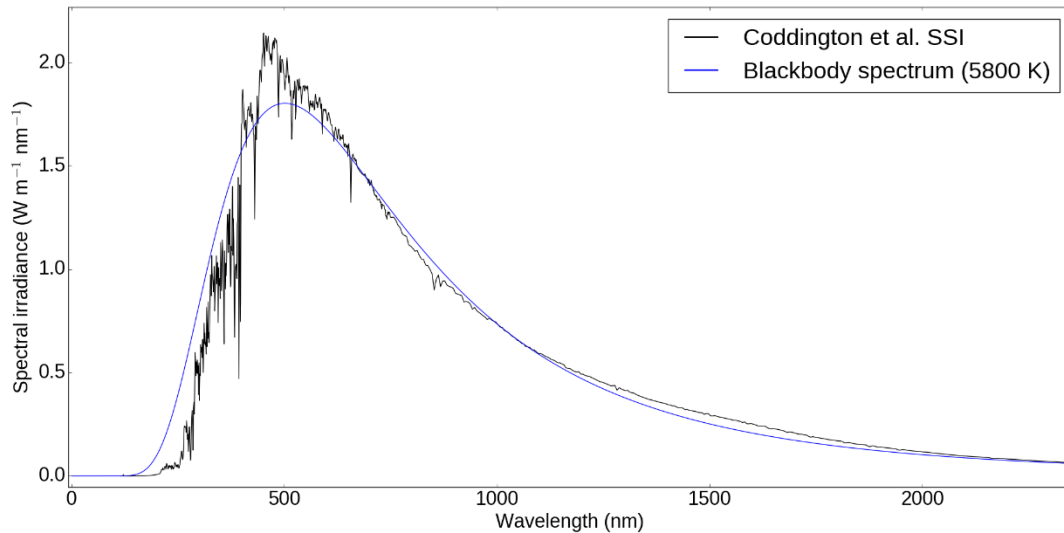


Figure 2.8: Schematic of radiation observed at the top of atmosphere (from Coddington et al. [2015]) compared with a 5800 K blackbody scaled to the Earth-Sun distance. Deviations from this blackbody spectrum are partly due to absorption and emission processes within the solar atmosphere above the photosphere. The observational spectrum is taken at solar minimum (see Section 2.2.1).

2.2.1: Solar structure

Figure 2.9 shows a schematic of the different regions of the Sun. Most of the mass is concentrated at the core, with energy transported from the core to the surface predominantly via radiation (in the radiation zone) and convection (in the convection zone). Radiation that reaches Earth comes predominantly from the photosphere, although this is subject to absorption by gases within the corona and chromosphere of the solar atmosphere.

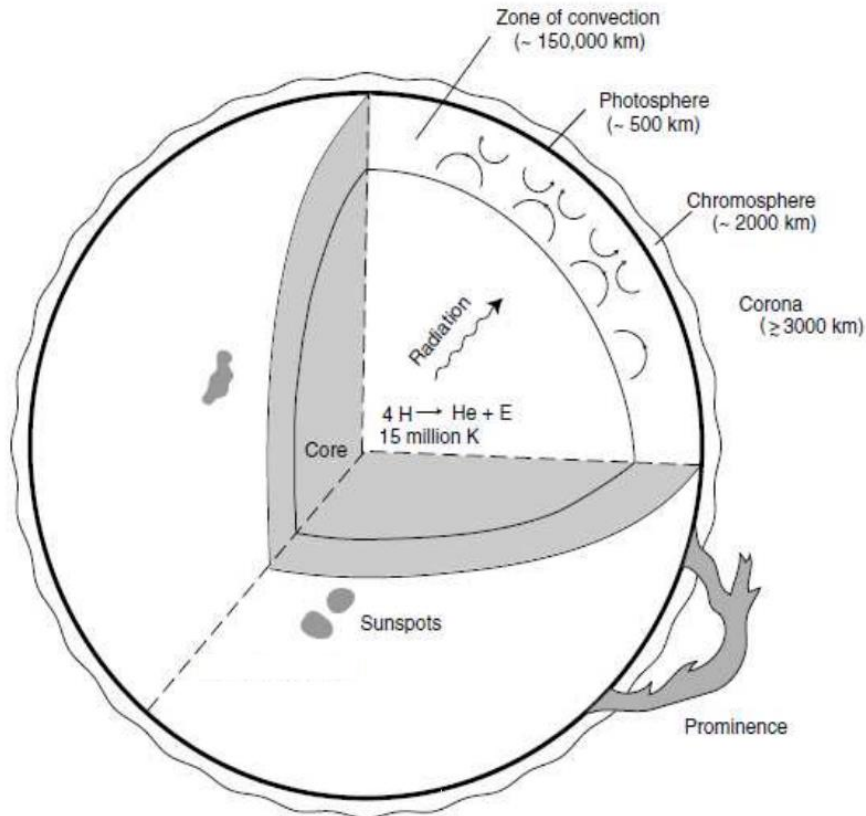


Figure 2.9: Schematic of the interior structure of the Sun. Taken from Liou [2002].

The photosphere varies in temperature; its effective temperature is $\sim 5800\text{K}$ but is significantly variable, particularly during periods of strong magnetic activity. Regions where the Sun is cooler appear as dark sunspots when observing it. These generally tend to undergo an 11-year cycle; this cycle has a small effect on the observed total solar irradiance (see Section 2.2.3). The period where there are fewest sunspots is referred to as the *solar minimum*.

2.2.2: Sun position and distance from Earth

Solar radiation emitted by the photosphere is emitted isotropically; the amount of radiation incident at a given point depends on the distance of that point to the Sun. The Earth orbits the Sun at a mean radius $r_0 = 1.496 \times 10^8$ km (known as 1 Astronomical Unit or AU).

The total power emitted by the Sun is determined by integrating over frequency and solid angle, and the power P per unit area A is given by the Stefan-Boltzmann law:

$$(2.23) \quad \frac{P}{A} = \sigma T^4$$

where σ is the Stefan-Boltzmann constant. The Earth is at a mean radius $r_0 = 1.496 \times 10^{11}$ m from the Sun; the energy incident on the Earth's surface is therefore diluted by the inverse square law. Given the radius of the Sun is $\sim 7 \times 10^8$ m, the total power received by the surface of the Earth S_0 is $\sim 1368 \text{ W m}^{-2}$. The Earth's surface area is 4x larger than the cross-sectional area of the Earth from the Sun, meaning the mean energy per unit area incident on the Earth is $\sim 342 \text{ W m}^{-2}$.

2.2.2.1: Solar zenith angle

Since the Earth rotates, and has an axial tilt relative to the Sun, observers at latitudes and different times of day will see the Sun at different positions in the sky, and is measured using the *solar zenith angle*, defined as:

$$(2.24) \quad \cos \theta = \sin \Phi \sin \delta + \cos \Phi \cos \delta \cos h$$

where Φ is the latitude of the observer, δ is the *solar declination angle* (i.e. the axial tilt of the Earth relative to the Sun, which varies from 23.44° at the Summer solstice to -23.44° at the Winter solstice). h is the *hour angle*, which is time-dependent and relates to the position of the observer relative to the meridian; it is 0 at Solar noon and varies from -180° to 180° , changing by 15° per hour. The zenith angle is defined from a path directly above the observer, thus $\theta = 0$ means an overhead Sun. This is important for measurements of solar radiation, since at a high zenith angle radiation must pass through more atmosphere than radiation coming in at a zenith angle of 0.

2.2.2.2: Orbit eccentricity

The distance between the Sun and Earth is not constant due to the Earth's eccentric orbit, varying from ~ 1.017 AU to 0.983 AU throughout the year. The mechanisms causing this are well-documented in the literature; what is important for this work is how to model this change. In this case, the correction (from *Liou* [2002]) is:

$$(2.25) \quad S_v = \frac{S_v(d_n)}{1 + 0.0334 \cos(2\pi((d_n - 3)/365))}$$

Here S_v is the corrected top of atmosphere (TOA) solar irradiance, $S_v(d_n)$ is the uncorrected TOA solar irradiance observed on a given day number d_n . The subscript v in this instance indicates that the TOA irradiance is spectrally dependent; this

method works for measuring total solar irradiance (TSI) as well. This correction has an uncertainty of $\sim 0.1\%$.

2.2.3: Models and observations of solar radiation

As seen in Figure 1.1, the incoming solar radiation is a well-characterised component of the Earth-atmosphere energy budget, with an uncertainty of $\sim 0.1 \text{ W m}^{-2}$.

Contemporary measurements of the total solar irradiance from space by the Total Irradiance Monitor (TIM) show a value of $\sim 1360 \pm 0.5 \text{ W m}^{-2}$ [Kopp and Lean, 2011; Kopp, 2016; Dudok de Wit et al., 2017] during the 2008 solar minimum. This value has been steadily decreasing as instrument technology and methodology becomes more sophisticated. Reanalyses of older datasets at the TSI Radiometer Facility [Kopp et al., 2007] have shown that, when corrected for, these older, higher measurements are consistent with the newer TIM data, as shown in Figure 2.10 and Figure 2.11 (updated to present-day versions via Greg Kopp's webpage).

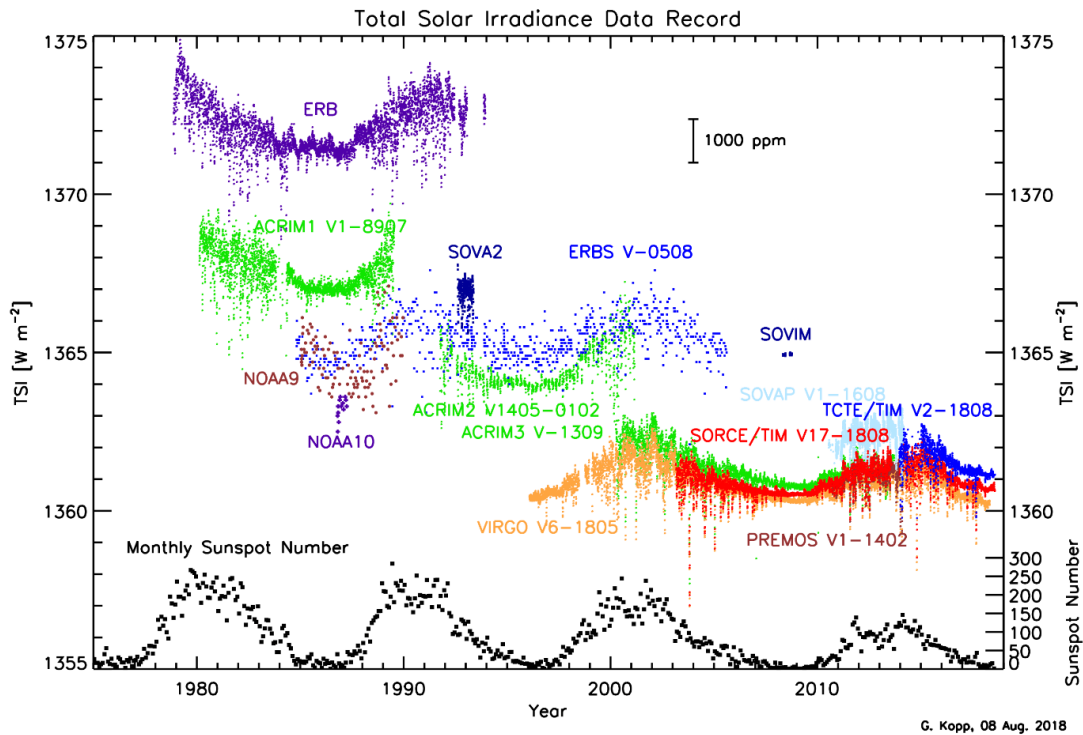


Figure 2.10: Plot of total solar irradiance measurements over time, showing the downward trend in observed TSI over time. The oscillating variation in these measurements is related to sunspot number. (Figures originally from Kopp et al. [2012], updated to present-day from <http://spot.colorado.edu/~kopp/TSI/index.html>)

Other datasets of TSI do exist, which show a slightly larger value (e.g. *Dewitte and Nevens* [2012]) of 1362 W m^{-2} . However, the 1360 W m^{-2} figure appears to be an accepted value in the literature (e.g. *Coddington et al.* [2016]).

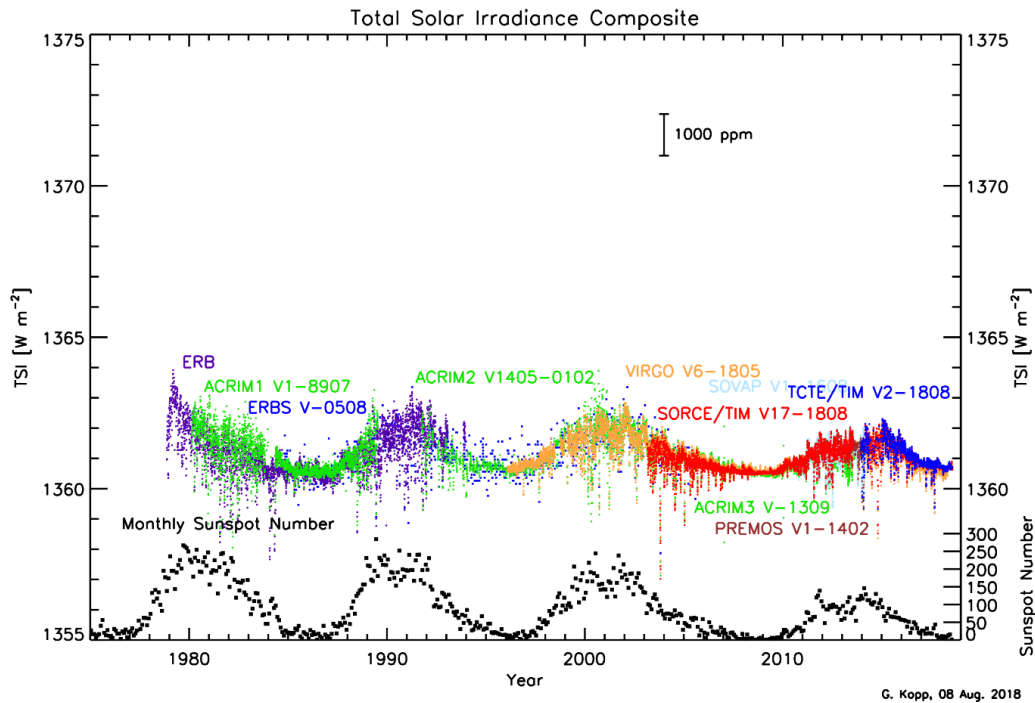


Figure 2.11: As above, but this time accounting for the reanalysis, showing much better agreement between the datasets. (Originally from *Kopp et al.* [2012], present-day version from <http://spot.colorado.edu/~koppg/TSI/index.html>)

Constructing a climate data record of TSI is important, as the natural variability from the 11-year cycle has a net radiative forcing; the IPCC Fifth Assessment Report [IPCC, 2014] estimates a forcing of $\sim 0.12 \text{ W m}^{-2}$. The TSI is highest at solar maximum, i.e. where there are most sunspots, despite these being regions of lower surface temperature. This is due to the presence of faculae, bright spots which have a larger net effect on the emitted irradiance than sunspots. At solar maximum, the TSI is estimated $\sim 0.1\%$ higher than at solar minimum [Coddington et al., 2015], although variations on the order of $\sim 0.3\%$ can take place over shorter timescales, e.g. during solar storms [Woods et al., 2004].

While a total solar irradiance climate data record exists; constructing one for the spectral solar irradiance (SSI) is more challenging. Measurements of solar spectral irradiance are myriad in the visible and UV, but in the near-infrared they are relatively sparse. Additionally, these measurements are not of the required resolution

to fully resolve many solar absorption lines, which are necessary for use of such a data record in high-resolution line-by-line calculations as is the case in this thesis. While high resolution solar irradiance models and observations exist (e.g. *Kurucz [2005]*, *Fontenla et al. [2011]*), these are not of the required resolution for line-by-line radiative transfer modelling.

The spectral distribution of solar radiation is important; additional radiation in spectral regions which are comparatively opaque (e.g. within a water vapour band) will result in that energy being absorbed higher in the atmosphere than if that radiation were in a more atmospherically transparent region of the spectrum.

Chapter 4 presents a detailed description of measurements of near-infrared SSI, focusing on the discrepancy between space-based measurements (e.g. *ATLAS3*, *Thuillier et al. [2003]*) and ground-based (e.g. *Bolsée et al. [2014]*). These measurements present SSI that do not agree within their respective measurement uncertainties between 4000-7000 cm^{-1} : the integrated difference between these measurements amounts to 16 W m^{-2} , significantly larger than any observed solar variability. Chapter 4 presents a reanalysis of the CAVIAR SSI of *Menang et al. [2013]* and indicates a lower SSI than that of *ATLAS3*, but better agreement with more recent analyses of SSI.

In practice, many weather and climate models (e.g. the UK Met Office Unified Model) use a semi-empirical spectrum to model the near-IR (e.g. *Walters et al. [2014]*) in this case the spectrum of *Kurucz and Bell [1995]*. This and other semi-empirical spectra are calculated using a physical model of the Sun's photosphere and are tied to observations. For example, the spectrum of *Kurucz and Bell [1995]* has similar spectral irradiance values to *ATLAS3*. Thus, the use of such spectra warrants caution, since more recent observations may supersede the one used to calculate the strength of the SSI.

2.3: Radiative transfer in the terrestrial atmosphere

Key to understanding the Earth's energy flows is knowledge of how solar radiation is distributed in the atmosphere. This is primarily through extinction by gases, aerosols and clouds. In this work, the atmospheric extinction is measured using a spectrometer and calculated using a line-by-line radiative transfer code with

supplementary aerosol and Rayleigh scattering calculations. More information on the technical details of this is presented in Chapter 3. More information on the principles explained in this section is available in e.g. *Petty* [2005] and *Liou* [2002].

2.3.1: Blackbody radiation

As stated in section 2.2, an object with temperature T will radiate blackbody radiation. Figure 2.12 shows the blackbody curves from the Sun (~ 5800 K) and the Earth (effective temperature ~ 255 K) respectively. These two emission curves demarcate *shortwave* radiation (from the Sun), and *longwave* radiation (emitted by the Earth's surface). The spectral region relevant to this work ($2000\text{-}10000\text{ cm}^{-1}$) therefore comes under the shortwave category. While gases in the atmosphere radiate like blackbodies, this is typically not important in the near-IR. The two have been scaled here so that the area under the curves is (roughly) equal, by multiplying the solar blackbody spectrum by the Earth's albedo, distributing the energy over all $4\pi r^2$ of the Earth's surface area and accounting for the Earth-Sun distance. Any difference between these curves in reality is indicative of an energy imbalance at the top of the atmosphere. If there is such an imbalance, the Earth's blackbody curve will adjust to resolve it, i.e. the effective temperature of the Earth will decrease if there is more outgoing longwave radiation, or increase if there is more incoming solar radiation.

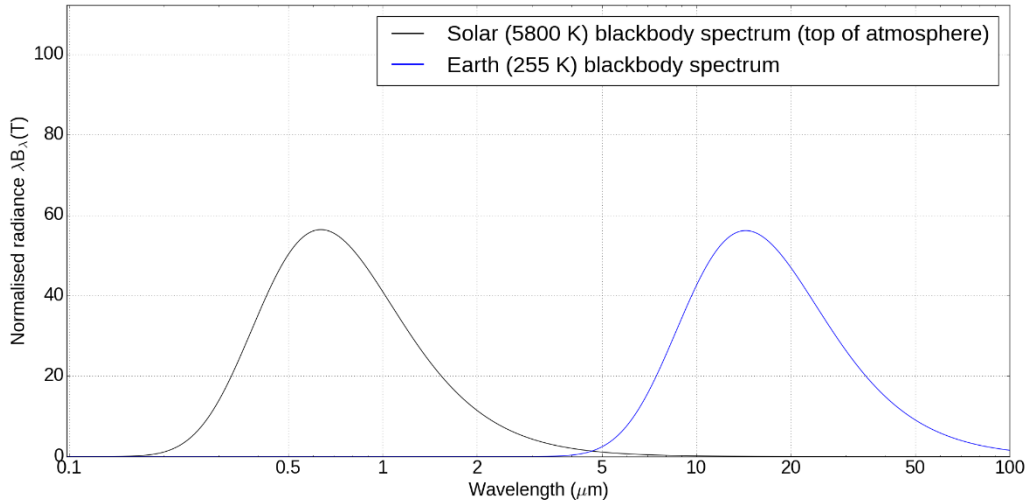


Figure 2.12: Blackbody spectra for the Sun (5800 K) and the Earth (255 K), with the solar spectrum scaled by the Sun-Earth distance, Earth’s albedo and a factor of $\frac{1}{4}$ to reflect the distribution of Earth’s energy over its surface area. The y-axis has been scaled by wavelength. The edges of the two at $\sim 4 \mu\text{m}$ denotes the transition from shortwave to longwave.

2.3.2: The Beer-Bouguer-Lambert law and atmospheric transmission

This work measures solar radiation reaching the surface through the atmosphere. A thorough understanding of how the atmosphere transmits radiation is necessary to characterise this radiation. A beam of electromagnetic radiation travelling through a medium (non-vacuum) is attenuated by the medium; the irradiance I observed after travelling through it is described using the Beer-Bouguer-Lambert law:

$$(2.26) \quad I_{\lambda}(x) = I_{0,\lambda} \exp(-\beta_{\lambda}x).$$

Here x is the distance travelled through that medium, I_0 is the incident radiation and β is the *extinction coefficient*, a function of the physical properties of the medium. From this point on the wavelength dependence subscripts will be dropped.

In the atmosphere this extinction coefficient is usually broken up into two terms $\beta_s + \beta_a$, which are the scattering and absorption extinction coefficients respectively:

$$(2.27) \quad \beta = \beta_s + \beta_a$$

Absorption in this case relates to the spectroscopic absorption of radiation, in the spectral region of interest mostly by water vapour, clouds and aerosols. Scattering refers to the redirection of radiation by clouds, gases and aerosols. For the purposes

of this thesis the scattering component is broken down into a Mie scattering component (primarily due to aerosols) and a Rayleigh scattering component (primarily by atmospheric gases). These will be discussed further in Section 2.3.4 and 2.3.5 respectively. The effect of clouds is removed entirely, as observations were made in clear-sky conditions (see Section 3.4.3.1).

This case also assumes that there is no scatter *into* the direct beam, i.e. that the observed signal is entirely due to the incident beam of radiation (which includes the sharp aerosol forward scattered peak). This case holds for the purposes of this work, since the field-of-view (FOV) of the optics used to observe the Sun is small; the FOV does not cover the entire solar disc, and the scattering phase function for aerosols is strongly forward peaked. This is explained in more detail in Section 3.4.5.2.

The relative amounts of absorption and scattering are important for many radiative transfer applications, in this case it is important for characterising the aerosol type; this is discussed further in Section 2.3.5. This quantity is referred to as the *single scattering albedo*, and is defined as:

$$(2.28) \quad \omega = \frac{\beta_s}{\beta}$$

A single scattering albedo of zero implies entirely absorption, whereas a single scattering albedo of 1 implies that all the radiation is scattered.

In practice, it is more appropriate to determine absorption via quantities such as number density of a given gas (such as that measured by the radiosonde used in this work, see Section 3.4.5.1). We can define a volume extinction coefficient σ such that:

$$(2.29) \quad \beta = N\sigma$$

where N is the number density of the gas in question. As with the extinction coefficient, σ is wavelength dependent.

When radiation travels through the atmosphere, it travels through the atmosphere at an angle θ relative to the zenith. We can define an *airmass factor* m :

$$(2.30) \quad m = \frac{1}{\cos(\theta)}$$

This airmass factor determines the additional proportion of the atmosphere relative to the zenith (i.e. the path directly upwards) that a beam of radiation must travel through in order to reach an observer, assuming that the atmosphere is homogeneous. Putting this together, one can obtain the radiation observed at a height z_0 travelling through the atmosphere:

$$(2.31) \quad I = I_0 \exp\left(-\int_{z_0}^{\infty} mN\sigma(z) dz\right)$$

Here I_0 is the top of atmosphere solar radiation. In the case of observing at the surface and integrating from infinity (i.e. the top of atmosphere) to 0, this gives the Beer-Bouguer-Lambert law as a function of *optical depth* τ :

$$(2.32) \quad I = I_0 \exp(-m\tau)$$

In this case, the optical depth does not include scatter into the FOV of the instrument, e.g. from aerosols. This optical depth is the quantity that will be looked at when deriving the continuum in Chapter 5. This optical depth can be explicitly broken down into its constituent components:

$$(2.33) \quad \tau = \tau_{H_2O} + \tau_{gas} + \tau_{aerosol} + \tau_{Rayleigh} + \tau_{clouds} + \tau_{continuum} + \tau_{other}$$

Here τ_{H_2O} denotes water vapour line absorption, τ_{gas} absorption by other gases, $\tau_{aerosol}$ aerosol absorption and scattering, $\tau_{Rayleigh}$ Rayleigh scattering, τ_{clouds} absorption and scattering by clouds, $\tau_{continuum}$ continuum absorption (particularly by water vapour) and τ_{other} other radiative processes, such as Raman scattering which generally do not contribute significantly to the overall optical depth. Optical depth is useful for many reasons; it gives an idea of how much the atmosphere transmits radiation, but can also be used as a vertical coordinate in radiative transfer calculations. Taking the ratio of I and I_0 in Equation 3.32 gives the atmospheric *transmission*, i.e. the proportion of radiation that has been removed from the beam by the atmosphere.

2.3.3: Absorption by atmospheric gases

The spectrum of water vapour was presented in Section 2.1. While it is the main contributor to near-infrared absorption, it is not the only one. Figure 2.13 shows the contributions to near-infrared absorption between 2000-10000 cm^{-1} by four major gases: water vapour, methane (CH_4), carbon dioxide (CO_2) and molecular oxygen

(O₂). Water vapour is responsible for the overall structure of this region. In the window regions, e.g. at 2.1 and 1.6 μm (the regions of most interest for this work), the clear-sky atmosphere is mostly transparent aside from Rayleigh scatter, aerosol scatter, weak absorption lines and continuum absorption.

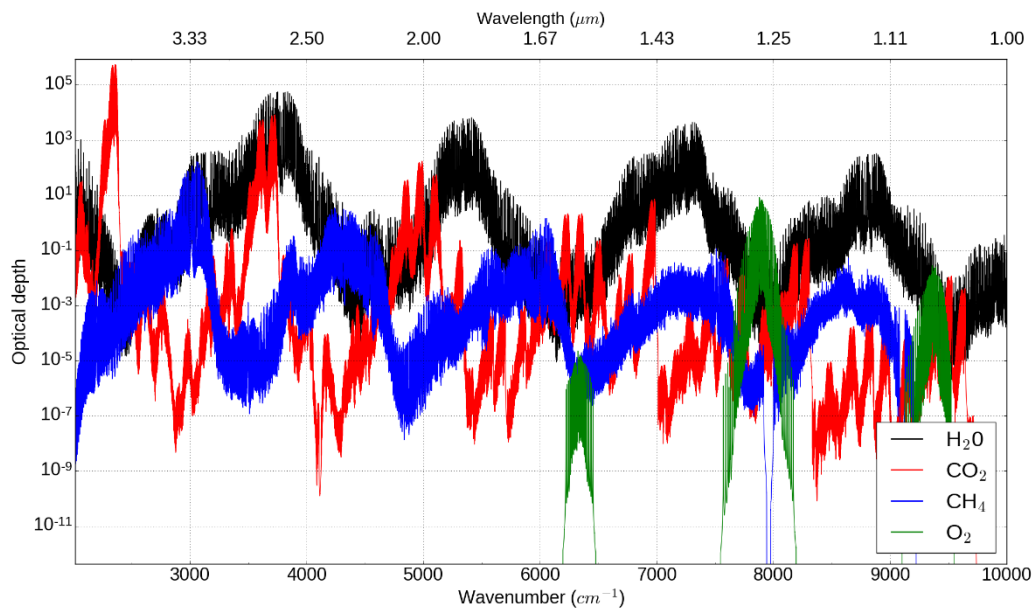


Figure 2.13: Contribution to atmospheric absorption by water vapour (black), carbon dioxide (red), methane (blue) and molecular oxygen (green), taken for a mid-latitude summer atmosphere from surface to top of atmosphere. These optical depths were generated using the Reference Forward Model [Dudhia, 2017] and the HITRAN 2016 spectroscopic database [Gordon et al., 2017].

There are some regions within these windows and on the edge of the windows where other gases contribute significantly, for example the CO₂ band at 1.6 μm , the methane band on the edge of the 1.6 μm window and the oxygen absorption band at $\sim 8000 \text{ cm}^{-1}$.

In this work, absorption by these four gases alongside carbon monoxide (CO), nitrous oxide (N₂O), ozone (O₃) and molecular nitrogen (N₂) is considered. Water vapour mixing ratios are determined from radiosonde observations (see Section 3.4.5.2). The CO₂ volume mixing ratio is determined from measurements at Mace Head Atmospheric Research Station, the closest CO₂ monitoring station to the field site used to take the FTS measurements. CH₄ volume mixing ratios are taken from

the Earth System Research Laboratory of the National Oceanic and Atmospheric Administration (*Ed Dlugokencky, NOAA/ESRL, www.esrl.noaa.gov/gmd/ccgg/trends_ch4/*). Mixing ratios for other gases are taken from climatology, e.g. from the US Standard atmosphere. These values are then fed into a line-by-line radiation model (see Section 2.3.6) to calculate the optical depth from atmospheric absorption.

An additional feature of the near-infrared spectrum (not shown on Figure 2.13) is the water vapour continuum absorption; this will be discussed in more detail in Section 2.4 and Chapter 5. As discussed in Chapter 1, water vapour and the continuum absorption are extremely important in determining the near-infrared radiation budget.

2.3.4: Rayleigh scattering

Scattering processes can be demarcated by a *size parameter* x where:

$$(2.34) \quad x = \frac{2\pi r}{\lambda}$$

where r is the radius of the scattering particle and λ is the wavelength of the incoming radiation. Figure 2.14 (from *Petty [2005]*) shows the regimes which scattering can fall under based on this parameter. For larger particles such as aerosols (with sizes ~ 0.1 - $1 \mu\text{m}$), near-IR radiation falls under the Mie regime, whereas molecular scattering (with sizes on the order of several nanometres) falls under the simpler Rayleigh regime. The reasoning behind this is that particles of sufficiently small size can be taken to be experiencing the same electric field when undergoing a scattering process.

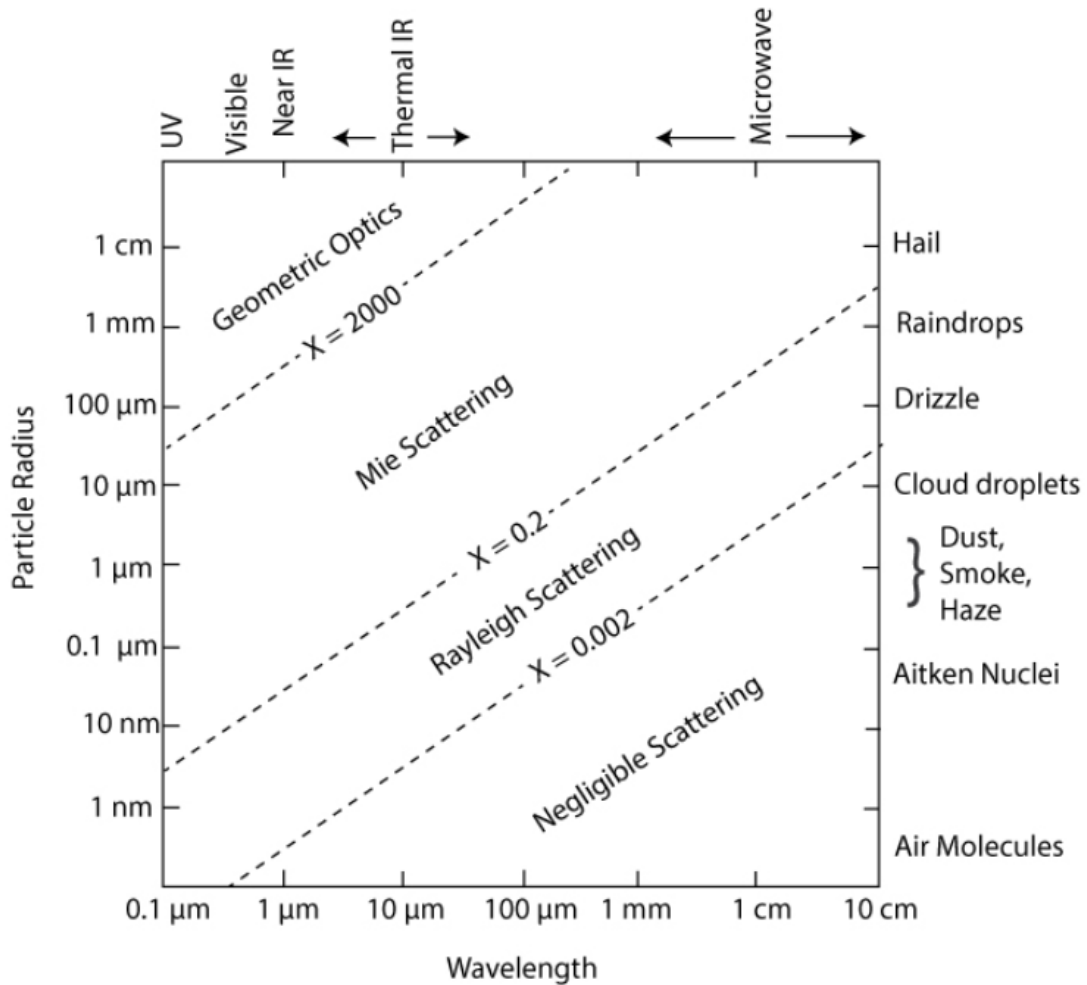


Figure 2.14: Schematic (from Petty [2005]) of scattering regimes for particles with radius r (y-axis) and radiation at wavelength λ (x-axis). For this work, most of the scattering is in the Mie regime (from aerosols), with some scattering in the Rayleigh regime (from gases, but this is mostly dominated by absorption).

A more detailed treatment of Rayleigh scattering is available in e.g. Petty [2005].

The Rayleigh scattering cross section σ_R for a particle of cross section πr^2 is given by:

$$(2.35) \quad \sigma_R \propto \frac{\pi r^6}{\lambda^4}$$

For the purposes of this work, the Rayleigh scattering optical depth is small, but still significant compared to the weak continuum absorption. Iqbal [1983] gives the transmission T_R due to Rayleigh scattering for dry air at standard temperature and pressure as:

$$(2.36) \quad T_R = \exp(-m0.008735 \lambda^{-4.08})$$

where m is the airmass factor = $1/\cos(\theta)$, and λ is in μm . This gives an optical depth of 0.008735 at 1 μm , and 1.2×10^{-5} at 5 μm . These values are significantly smaller than the expected continuum absorption in these regions. More detailed studies such as *Bucholtz* [1995] shows that for a midlatitude summer atmosphere (comparable to the conditions in this work), the Rayleigh scattering optical depth is 8.67×10^{-3} at 1 μm , reducing to 1.315×10^{-3} at 1.6 μm .

2.3.5: Mie scattering and the effect of clouds and aerosols

Larger particles undergo Mie scattering, which is more complex than the Rayleigh case. This regime is where the assumption that the entire (spherical) particle experiences the same electric field breaks down. Mie theory is derived by solving the Maxwell equations to obtain a wave equation in 3D space, with boundary conditions applied based on the coordinates of the homogeneous sphere. A detailed description of this is available in e.g. *Liou* [2002].

Solving these differential equations yields the scattering and extinction efficiencies for Mie scattering Q_S and Q_E respectively, which are expressed as an infinite sum over n terms:

$$(2.37) \quad Q_S = \frac{2}{x^2} \sum_{n=1}^{\infty} (2n + 1) (|a_n|^2 + |b_n|^2)$$

$$(2.38) \quad Q_E = \frac{2}{x^2} \sum_{n=1}^{\infty} (2n + 1) \text{Re}(a_n + b_n)$$

Here a_n and b_n are the Mie scattering coefficients. These are mathematically complex variables and are not reproduced in full here. What is important is the fact that they are dependent on the properties of the scattering medium. The complexity of these terms is such that generally the sum to infinity has to be significantly truncated in practical terms to derive Q_S and Q_E .

The scattered radiation is strongly directionally dependent. This is dependent on the size parameter (among other things) of the scattering particle, as shown in Figure 2.15.

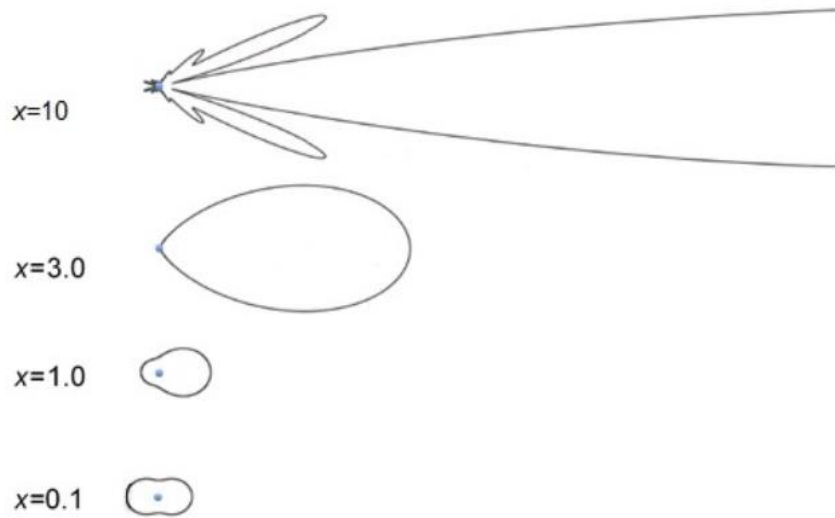


Figure 2.15: Schematic of radiation scattered by a particle with size parameter x , adapted from Petty [2005].

The isotropy of the scattered radiation is determined by a *phase function* p . Consider a beam of radiation approaching a particle from direction Ω . This radiation is scattered by the particle into a direction Ω' . By integrating over solid angle ϕ , and normalising the phase function to 1, we get:

$$(2.39) \quad \frac{1}{4\pi} \int_{4\pi} p(\Omega', \Omega) d\phi = 1$$

This can be conceptualised as a probability distribution, i.e. the probability that a photon will be scattered from Ω into Ω' . The normalisation condition ensures this condition satisfies conservation of energy (ignoring absorption in this case).

For spherical or randomly oriented particles (such as those found typically in the atmosphere), this can be simplified as being dependent on the angle between Ω and Ω' , i.e.

$$(2.40) \quad \cos(\theta) = \Omega' \cdot \Omega$$

which reduces the phase function normalisation to:

$$(2.41) \quad \frac{1}{2} \int_{-1}^1 p(\cos(\theta)) d \cos(\theta) = 1$$

In the case of isotropic scattering, this phase function $p(\cos(\theta)) = 1$, i.e. the likelihood of scatter in all directions is the same. In many radiative transfer

applications (not including this work), this is overly complex; a simpler treatment using the *asymmetry parameter* g is more computationally efficient:

$$(2.42) \quad g = \frac{1}{4\pi} \int_{4\pi} p(\cos(\Theta)) \cos(\Theta) d\omega$$

This parameter varies between 1 and -1, and determines the proportion of backscattered to forward scattered photons. For isotropic scattering, $g = 0$, as it does for Rayleigh scattering, where the forward and backward scattering are equal (despite not being isotropic scattering).

These parameters are used to generate the aerosol optical depths from the Mie scattering codes described in Section 2.3.6.2. However, a reference optical depth is necessary in this case; the Mie code calculates the spectral dependence rather than the absolute optical depth, since this would require information on the aerosol number concentration and size distribution which was not available. This reference optical depth is obtained from the sunphotometer measurements described in Section 3.4.5.2.

In the visible and near-visible, and in the shorter wavelengths in the NIR, cloud droplets are often in this Mie regime. However, due to the difficulty and complexity of measuring cloud optical depth, the need for consistent conditions for the Langley method and the need to measure a (comparable to cloud optical depth) small component of the atmospheric optical depth this was not done here. It is therefore necessary to restrict measurements to conditions where clouds are not present (and where sub-visible clouds have little effect, see Section 3.4.3.1).

2.3.6: Radiative transfer models

Radiative transfer models aim to model the physics of radiation travelling through the atmosphere for a given set of conditions, including scattering and absorption processes by gases, aerosols and clouds. Of particular interest to this work are *line-by-line* radiative transfer models, which solve the radiative transfer equation at a given spectral resolution for each spectral line of a mixture of gases, and output transmittances or radiances. In this case, it is the atmospheric optical depth that we wish to obtain. Note that these codes are generally incapable of handling scattering (without coupling to other codes); it is the optical depth due to *absorption* in clear skies that is obtained from these models.

There are many models capable of this (e.g. the LBLRTM (Line-by-line Radiative Transfer Model) of AER), or the code of *Mitsel and Firsov* [1995]. In this thesis, the Reference Forward Model (RFM) of *Dudhia* [2017] is preferred. This is due to the ease of use, the modular nature of the code (allowing for changes in the continuum absorption parameters for example), and the detailed documentation available.

2.3.6.1: The Reference Forward Model

The RFM takes as input a spectroscopic line database (e.g. HITRAN, see Section 2.3.6.2) and temperature, pressure and gas volume mixing ratios from a model atmosphere (see Section 2.3.6.3), to calculate the absorption cross-section at each wavenumber. Each spectral line is subject to Doppler and collision broadening; the Voigt profile is applied to transitions within 25 cm^{-1} of line centre. Absorption outside of this region is considered continuum absorption (Section 2.4). Explicitly, for a gas with partial pressure e :

$$(2.43) \quad k(\nu, p, T, e) = \sum_i S_i(T) f(\nu - \nu_0, p, T, e, \dots)$$

where S_i is the intensity of a given line i , and f the lineshape function (typically Voigt, unless otherwise specified in the model). The lineshape function is dependent on air pressure, temperature and partial pressure, but also on several other quantities found within the HITRAN spectroscopic database.

Resolving the Voigt lineshape for every spectral line within 25 cm^{-1} would be computationally expensive; instead a fine mesh grid and a wide mesh grid are specified. Figure 2.16 (from *Dudhia* [2017]) shows this schematically. The fine mesh grid determines the spectral resolution of the calculations, while the wide mesh grid divides this fine mesh grid into 1 cm^{-1} intervals. For a given spectral line, all of the transitions within this 1 cm^{-1} interval (and the two intervals adjacent) are considered. For remote lines (within 25 cm^{-1}), this calculation is only performed at the centre and edges of the relevant 1 cm^{-1} interval. Lines outside of this region are ignored entirely, and assumed to be included within the continuum terms.

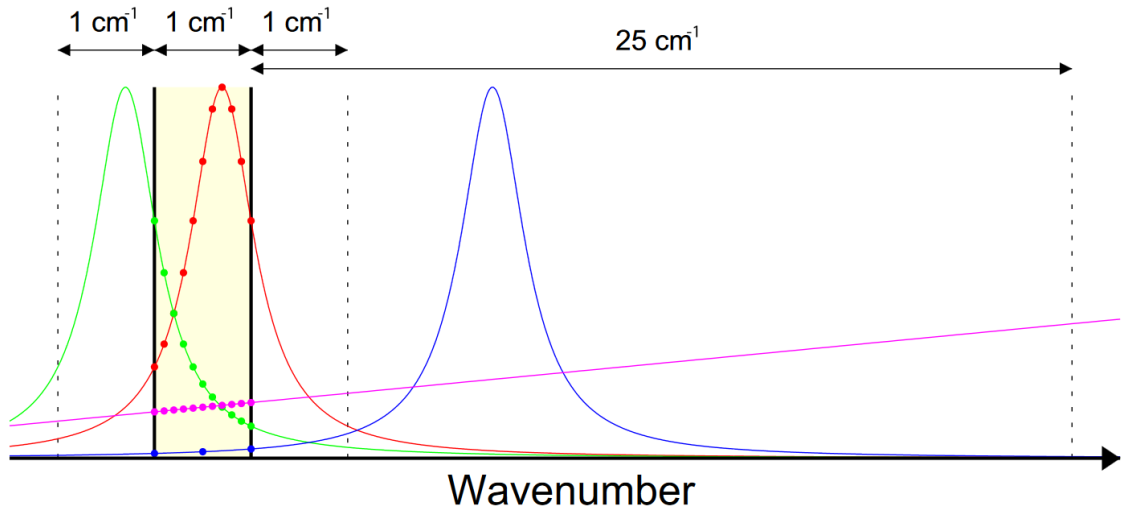


Figure 2.16: Schematic of the RFM line calculation algorithm. The wavenumber grid is split into 1 cm^{-1} intervals. A spectral line within this interval, or in the two intervals either side (which the red and green lines fall into) are calculated at each fine mesh point (the red and green dots in the yellow shaded region). The blue line is outside of these intervals, but is within 25 cm^{-1} . It is thus included but only calculated at the edges of this interval and in the centre and interpolated across. Finally, the pink line shows continuum absorption; this is calculated and interpolated across the fine mesh grid in this 1 cm^{-1} region. From Dudhia [2017].

The optical depth at a given wavenumber in a given layer i is a summation of the absorption coefficients of each gas (at that wavenumber, including broadening, within that layer) multiplied by the path the radiation takes through the atmosphere:

$$(2.44) \quad \tau_i(\nu) = \sum_{gas} \int_i k_i(\nu, p, T, e) \nu n dz$$

with ν the mixing ratio of the gas and n the number density. The RFM uses the Curtis-Godson approximation, i.e. assumes that the optical depth of a given layer is the same as that of a homogeneous layer with the same mixing ratio of absorption, with average values of p , T and e .

These cross-sections are then used to solve the equations of radiative transfer to calculate transmittance or radiance for a given viewing geometry. For this work, this is simple, since only the optical depth is considered; the output from the model is multiplied by the airmass factor m to account for the changing solar zenith angle across the day (Equation 3.31).

Figure 2.17 shows a zoomed-in version of the atmospheric optical depth as modelled from the top of the atmosphere to the surface for CO₂ lines in the 1.6 μm window. This is shown for two different resolutions, 0.03 cm⁻¹ (the resolution used in this work) and at 1 cm⁻¹. This shows the loss of spectral structure obtained when running such a model at a resolution coarser than the width of the spectral line (typically ~0.1 cm⁻¹).

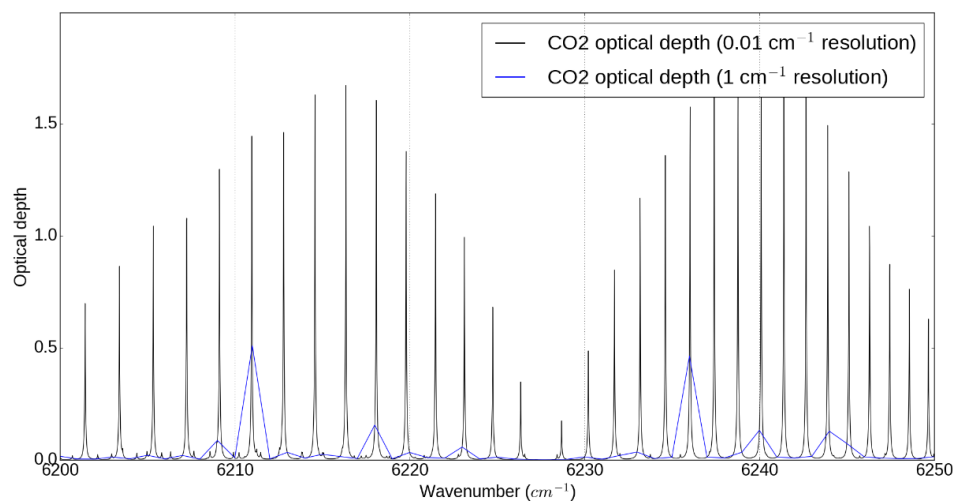


Figure 2.17: Plot of RFM modelled absorption by CO₂ at two spectral resolutions, using a vertical path of the US Standard atmosphere. Note how the peak absorption strength appears much weaker for the low resolution lines; in this case the absorption is “blurred” out into the neighbouring wavenumbers. Much of the spectral structure is lost in this case.

Figure 2.18 shows water vapour lines in the band at 1.7 μm at the same spectral resolution as one another but using two different atmospheres (a mid-latitude summer atmosphere and a sub-arctic Winter atmosphere). This shows the difference in optical depth that large differences temperature, humidity and water vapour partial pressure lead to.

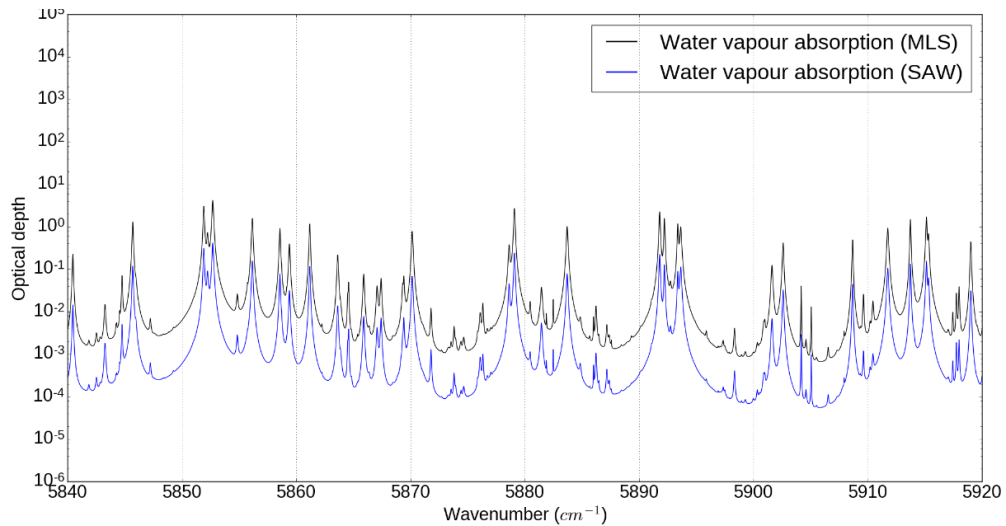


Figure 2.18: Plot of RFM-modelled absorption by water vapour lines at 0.03 cm^{-1} at the edge of the $1.6 \mu\text{m}$ window from the top of atmosphere to the surface in two atmospheres, a humid midlatitude summer atmosphere and a dry sub-arctic winter atmosphere. Note the logarithmic scale: the actual difference between the absorption is a factor of 10.

The RFM contains the MT_CKD 2.5 continuum absorption model (see Section 2.4); additionally for this work the water vapour continuum of MT_CKD 3.2 was edited into the code. This is modelled within RFM as the contribution of lines beyond 25 cm^{-1} of their line centre, plus an additional non-Lorentzian term (referred to as a χ -factor), which modifies the lineshape. When including the continuum absorption, the contribution from lines beyond 25 cm^{-1} of their line centre have to be subtracted from the derived absorption cross-section, since this is included within MT_CKD.

The RFM also includes collision-induced absorption (e.g. that of O_2 at 7800 cm^{-1}); however, this is not completely accurate in atmospheric conditions, as it does not include the O_2 continuum from MT_CKD, which contributes significantly to the absorption in the window at $\sim 8000 \text{ cm}^{-1}$ (e.g. Figure 5.20). The desired parameters are read into the model via a driver file, specifying the chosen physics, gases, model atmosphere, spectral range and viewing geometry.

2.3.6.2: Spectroscopic line databases

The RFM takes input from a spectroscopic line database in order to calculate the absorption cross-sections. This is typically (and in this case) using the High Resolution TRANsmission or HITRAN (latest version HITRAN 2016, *Gordon et al.*

[2017]) spectroscopic database, although others such as GEISA [Jaquinet-Housson *et al.*, 2017] also exist. These databases have information on millions of observed and modelled spectral lines for 39 gases (and many of their isotopologues and isotopomers), and include a wide range of parameters (see Gordon *et al.* [2017] for details). These parameters are obtained through both *ab initio* theoretical calculations and laboratory measurements. Each has an associated “uncertainty parameter”, which provides rough bounds of the uncertainty in the position and strength of each spectral line. These are not rigorously defined, and are more an indicator of the efficacy of the experiment or model used to derive the parameters.

In particular (assuming local thermodynamic equilibrium), the RFM uses the transition wavenumber ν and intensity S , the air-broadened and self-broadened linewidths γ_{air} and γ_{self} , the lower state energy E^L , the temperature dependence of the air-broadened linewidth n , and the air pressure-induced line shift s .

2.3.6.3: Model atmospheric profiles

The other primary input into the RFM is a model atmosphere. This contains information on temperature, pressure, and volume mixing ratios for various atmospheric gases. These are not necessarily limited to Earth’s atmosphere; this can be specified for any clear-skies atmosphere in which these parameters are known, provided the atmosphere is made up of at least one of the 39 gases included within HITRAN.

Standard profiles of various atmospheres exist in the literature; for example the US Standard Atmosphere and the mid-latitude Summer atmosphere (e.g. Petty [2005]). These are based on climatology rather than based on measurements of specific conditions, and are not used when modelling atmospheric optical depth in Chapter 5.

For this work, the model atmosphere is generally taken from measurements using a radiosonde (see Section 3.4.5.1). This provides temperature, water vapour and pressure; the remaining components (mixing ratios for carbon monoxide, methane, nitrous oxide, molecular oxygen, molecular nitrogen, carbon dioxide and ozone) are taken from climatological values. These model atmospheres have 64 vertical levels, each with specified temperature, water vapour etc.

2.3.6.4: Mie scattering models

The atmosphere contains particles which lie within the Mie scattering regime; primarily aerosol particulates residing in the lower troposphere. For any applications requiring well-resolved radiative transfer in the atmosphere, it is necessary to calculate extinction from Mie scattering. Due to the complexity in calculating Mie scattering coefficients, this is done using specialised models. This code requires the real and imaginary parts of the refractive index (which provides an output single scattering albedo) and a size distribution for the aerosols. This size distribution is typically a bimodal distribution, split into “fine” and “coarse” mode aerosols. This is shown schematically in Figure 2.19 (from *Lee et al.* [2015]). These distributions have associated standard deviations, means and weights, which are included in the calculation of aerosol optical depth. These were included in the Mie scattering calculations used in this work (see Section 3.4.5.2)

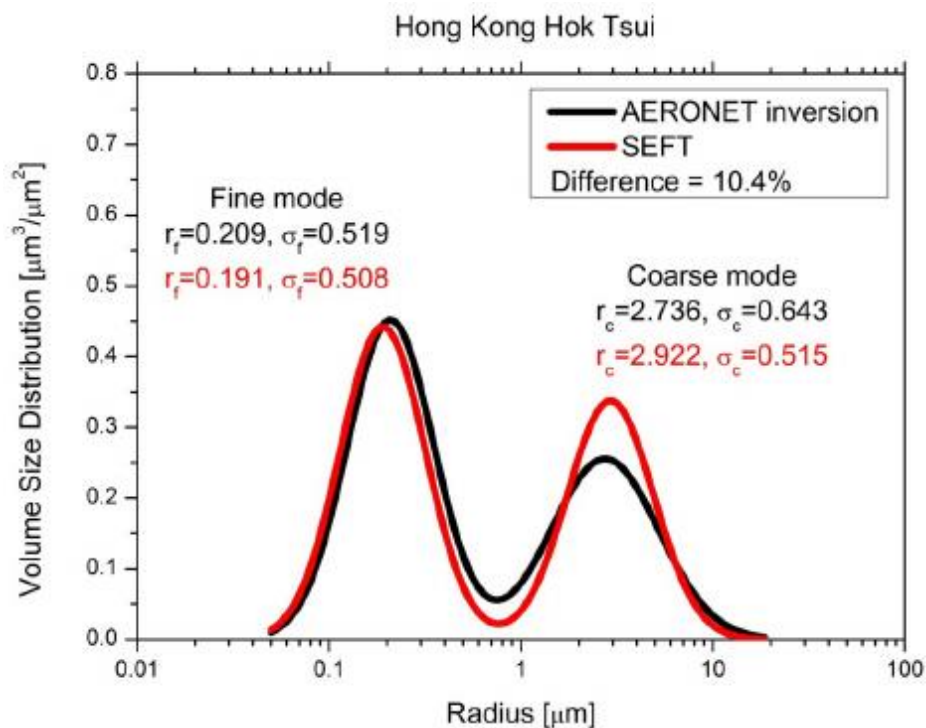


Figure 2.19: Schematic of a bimodal aerosol size distribution, from *Lee et al.* [2015], showing retrieved fine and coarse mode aerosols above Hong Kong using two different retrieval methods.

2.4: Near-IR water vapour continuum absorption

The near-IR water vapour continuum is the main subject of this thesis, particularly Chapter 5. As such, some theoretical background is necessary. There have been some recent attempts to characterise the near-IR continuum; a detailed literature review is presented in Chapter 5. A more general review of the history and impacts of the continuum was presented in Chapter 1. This section describes the theoretical basis of the continuum, and how it is incorporated into radiative transfer models.

The majority of applications (e.g. the UK Met Office Unified Model) include the CKD (Clough-Kneizys-Davies) or MT_CKD (Mlawer-Tobin-Clough-Kneizys-Davies) continuum models *Mlawer et al.* [2012]. This is a semi-empirical model which provides continuum from the microwave to the visible ($0\text{-}20000\text{ cm}^{-1}$). This model is based on observations, particularly in the microwave and far-infrared regions. In the $2000\text{-}10000\text{ cm}^{-1}$ spectral region there is a comparative dearth of observations, and disagreement between the observations that do exist. Figure 2.20 (from *Shine et al.* [2016c]) shows the MT_CKD 2.5 self-continuum (the version used in most applications) against other spectra, primarily recent laboratory spectra. The most recent version of MT_CKD (3.2) shows slightly stronger absorption in the 2.1 and $1.6\text{ }\mu\text{m}$ windows (see Chapter 5).

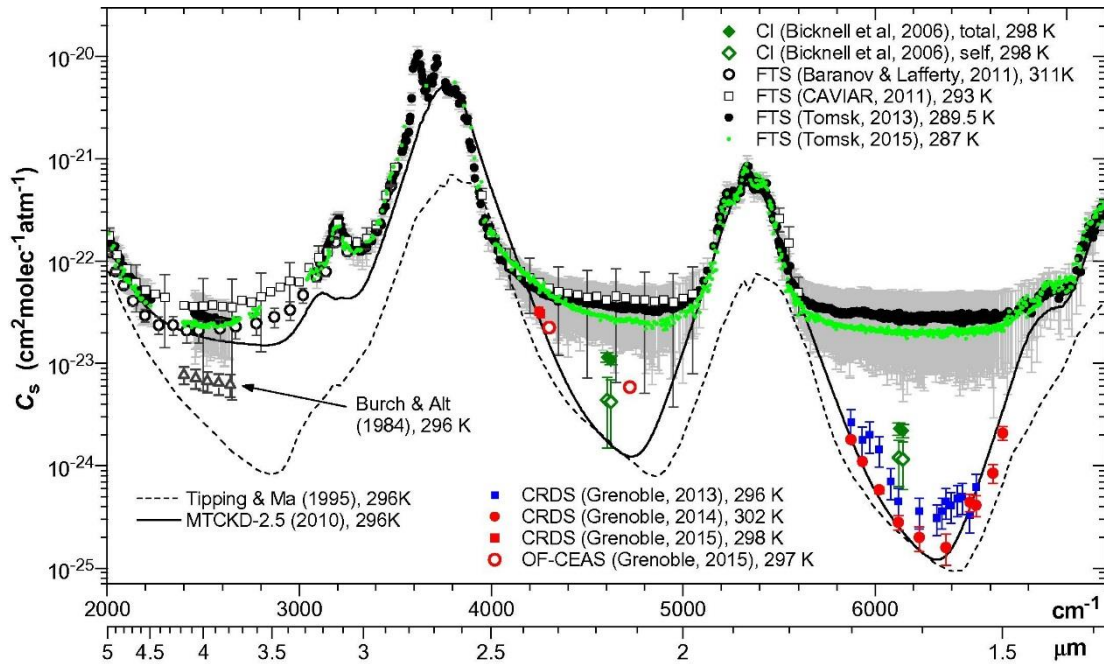


Figure 2.20: Comparison of recent observations of near-IR water vapour self-continuum and MT_CKD 2.5 (from Shine et al. [2016c]).

The MT_CKD continuum is fundamentally a contribution from two sources; a component from the exponentially decaying far-wing contribution (not explained by the standard Lorentzian lineshape), and a collision-induced component relating to interactions between water vapour and another molecule. In the atmospheric window regions, the dominant contributor is the far-wings, and vice versa in the bands. The older CKD continuum only includes a contribution from line wings. This was modelled in CKD by adjusting the lineshape by a χ -factor, which adjusts the lineshape of water vapour monomer lines. This χ -factor is typically greater than one in the band regions (where the absorption is too weak in the Lorentzian formulation, i.e. the lines become super-Lorentzian) and smaller than one in the windows (where the absorption is too strong relative to the Lorentzian, i.e. the lines become sub-Lorentzian).

Practically, this is modelled by line contributions beyond 25 cm^{-1} of a water vapour line. This includes the value at 25 cm^{-1} across the line, known as the “plinth”, as shown in Figure 2.21 (from Ptashnik et al. [2011a]).

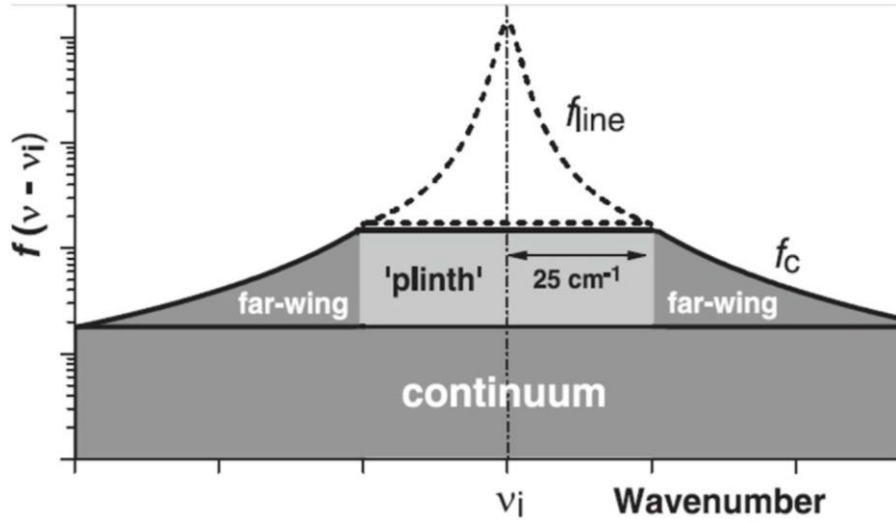


Figure 2.21: Schematic showing the contribution to continuum absorption strength. The continuum is the values in the dark shaded regions. The far-wing contributions are taken outside of 25 cm^{-1} : the value inside this region is taken as the value at the edge: i.e. at 25 cm^{-1} . From Ptashnik *et al.* [2011a].

The continuum lineshape L_{cont} is given by (e.g. *Mlawer et al.*, [2012]):

$$(2.45) \quad L_{cont}(v \pm v_i) = \begin{cases} \frac{1}{\pi} \frac{\alpha_i}{25^2} & , |v \pm v_i| \leq 25 \text{ cm}^{-1} \\ \frac{1}{\pi} \frac{\alpha_i}{(v \pm v_i)^2} & , |v \pm v_i| \geq 25 \text{ cm}^{-1} \end{cases}$$

This lineshape is Lorentzian, with the central peak removed within 25 cm^{-1} (i.e. including the plinth). This is then adjusted by the χ -factor such that:

$$(2.46) \quad f_{cont}(v - v_0) = L_{cont} \chi(v - v_0)$$

χ is a function which is derived empirically, and follows a negative exponential. To fit the observed features (stronger continuum in bands, weaker in windows), this function drops off sharply with wavenumber. As observations became more sophisticated however, adjustments had to be made in specific spectral regions to fit these. This led to a reformulation of the model, into what is now known as the MT_CKD continuum.

The MT_CKD model is also semi-empirical in nature, and includes this lineshape formalism. It also introduces another component, which relates to an interaction between water vapour and another molecule. This term is referred to in *Mlawer et al.*

[2012] as a “weak interaction term”. This term is separated into a foreign component and a self-component, and in both cases is of the form:

$$(2.47) \quad f_{WI} = \sum_i \frac{S_i \alpha_{WI} / \pi}{\alpha_{WI}^2 + (\nu - \nu_i)^2} \left\{ \zeta_{WI} \exp \left(- \left(\frac{\nu - \nu_i}{\gamma_{WI}} \right)^2 \right) \right\}$$

Here i is a sum over all lines with intensity S and position ν . ζ_{WI} is the “relative strength of interaction term”, which varies depending on the energy levels and rotational quantum numbers of the transitions being summed over. While this term can be interpreted as collision-induced absorption, it is important to note that this is not a physical formalism; it is instead a formalism adopted to fit the experimental data without the χ -factor of the original CKD model.

It is important to note that in the region of interest here, MT_CKD is (mostly) not based on observations. The most recent update to MT_CKD (3.2) adjusts absorption in the 2.1 and 1.6 μm windows to fit the observed absorption from *Bicknell et al.* [2006], but does not agree with other contemporary observations. In addition, the temperature dependence of MT_CKD is in question (see Chapter 5). Measurements of continuum temperature dependence are obtained from *Burch* [1982] from 296-338 K and extrapolated to 260 K. This extrapolation is heavily reliant on assumptions, and particularly assumes that the temperature dependence is consistent across the spectrum, since these measurements do not cover the near-infrared region beyond 2300 cm^{-1} .

The uncertainties in both the continuum strength and the temperature dependence in the near-IR are strong motivation for the work performed in this thesis, given the potential impacts described in Chapter 1. This will be explored further in Chapters 5 and 6.

Chapter 3:

Experimental methods in the CAVIAR field campaign

3.1: Introduction

This chapter contains information on the experimental setup of the field campaigns and the methods used in analysing the Fourier transform infrared (FTIR) spectra for the solar spectral irradiance measurements presented in Chapter 4 and the observations of the water vapour continuum presented in Chapter 5.

3.2: Fourier transform spectroscopy

3.2.1: Introduction

The spectral measurements presented in this thesis are obtained using the FTIR (or interchangeably Fourier Transform Spectroscopy (FTS)) technique. This technique is described here, but a more rigorous assessment can be found in e.g. *Griffiths and de Haseth* [1986], from which most of the information described in this Section was obtained. *Banwell and McCash*, [1994] provide a more accessible introduction to the topic. This technique has many advantages over other infrared spectroscopic techniques; primarily the ability to sample over a wide range of wavenumbers very quickly. This is important for measurements in the atmosphere, particularly using the Langley method (Section 3.3.2). This is because the atmosphere is a changing system; a long measurement time could lead to interference from e.g. clouds passing over or changes in atmospheric water vapour, which may mask the desired signal.

A signal can be separated into its constituent frequencies, using a technique known as *Fourier analysis*. This separates the signal into a possibly infinite sum of sine and cosine waves:

$$(3.1) \quad f(x) = a_0 + \sum_{n=1}^N \left(a_n \cos \frac{n\pi x}{L} + b_n \sin \frac{n\pi x}{L} \right).$$

By treating the function as continuous rather than discrete and using the limit $L \rightarrow \infty$, we define the *Fourier transform*. One can therefore use information about the frequency components of a signal to recover the original signal (or vice versa); this is exploited in FTIR spectroscopy (for this thesis) using a Michelson interferometer.

3.2.2: The Michelson interferometer

The Michelson interferometer works via splitting a beam of radiation into two, and obtaining a spectrum from the interference pattern obtained when these beams are recombined and observed by a detector. Figure 3.1 shows a schematic of a Fourier transform spectrometer, with a Michelson interferometer at point a). The incident beam is split into two by a beam splitter, which reflects ~50% of the input beam into two “arms”, each of which have a mirror at one end. One of these mirrors is fixed, whereas the other is attached to a rail, allowing it to move up and down the arm. These beams recombine at the beam splitter and fall upon the detector, which measures the intensity of the incoming radiation. The two beams interfere constructively or destructively depending on the position of the moving mirror and the frequencies of the incoming light.

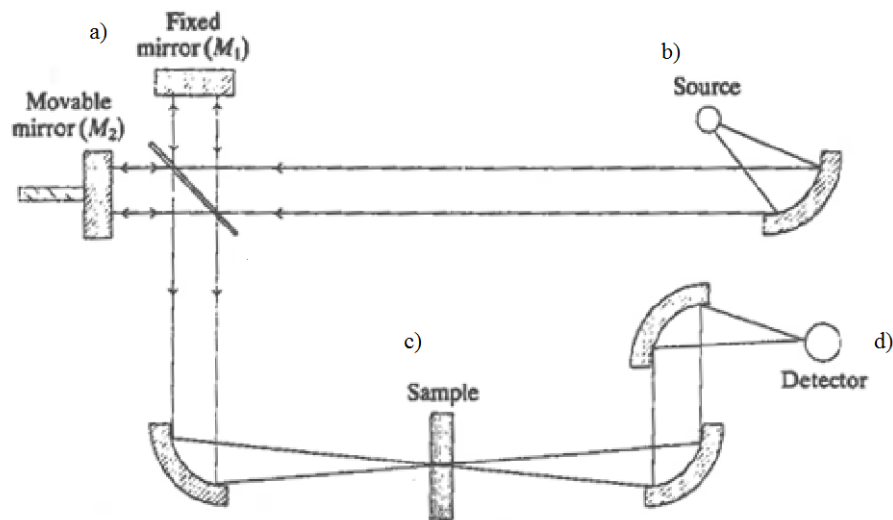


Figure 3.1: A schematic example of a Fourier transform spectrometer, with a Michelson interferometer at a), the input radiation source at b), and a sample at c), with the detector at d). Note that for the work done in this thesis, the sample is the entire atmosphere, and the source is the Sun. The sample therefore is located in between the source and the beam splitter. In this case, the beam is collimated going through the sample, rather than at a focus like in this Figure. Adapted from Banwell and McCash [1994]

3.2.3: Optical path difference and interferograms

The observed radiation can be defined in terms of the *optical path difference* δ between the two moving mirrors, given by:

$$(3.2) \quad \delta = 2(x_1 - x_2).$$

Here x_1 is the distance between the beam splitter and the translating mirror, and x_2 is the difference between the beam splitter and the fixed mirror. This optical path difference is typically observed using the interference fringes of a helium-neon laser, with wavelength much smaller ($0.633 \mu\text{m}$) than those used in the measurements ($1\text{-}5 \mu\text{m}$).

The signal observed by the detector $I(\delta)$ is dependent on the incoming radiation $I_0(\nu)$ and δ , and can be given by integrating over all of the incoming wavenumbers in the beam:

$$(3.3) \quad I(\delta) = \frac{1}{2} \int_{-\infty}^{\infty} I_0(\nu) \cos(1 + 2\pi\nu\delta) d\nu$$

This of course gives the overall intensity as a function of the path difference; this does not provide any spectral information on its own. Figure 3.2 shows an example interferogram, and the spectrum resulting from it. Notable here is the centreburst centred around $\delta = 0$ (the location of the black lines in Figure 3.2(b)); this is where the radiation (of all incident wavenumbers) is interfering constructively, and the intensity of the beam is measured by the detector in full. Either side of the centreburst, the signal drops and oscillates; the intensity and oscillation of this signal is dependent on the interference pattern (i.e. the frequencies of the observed radiation).

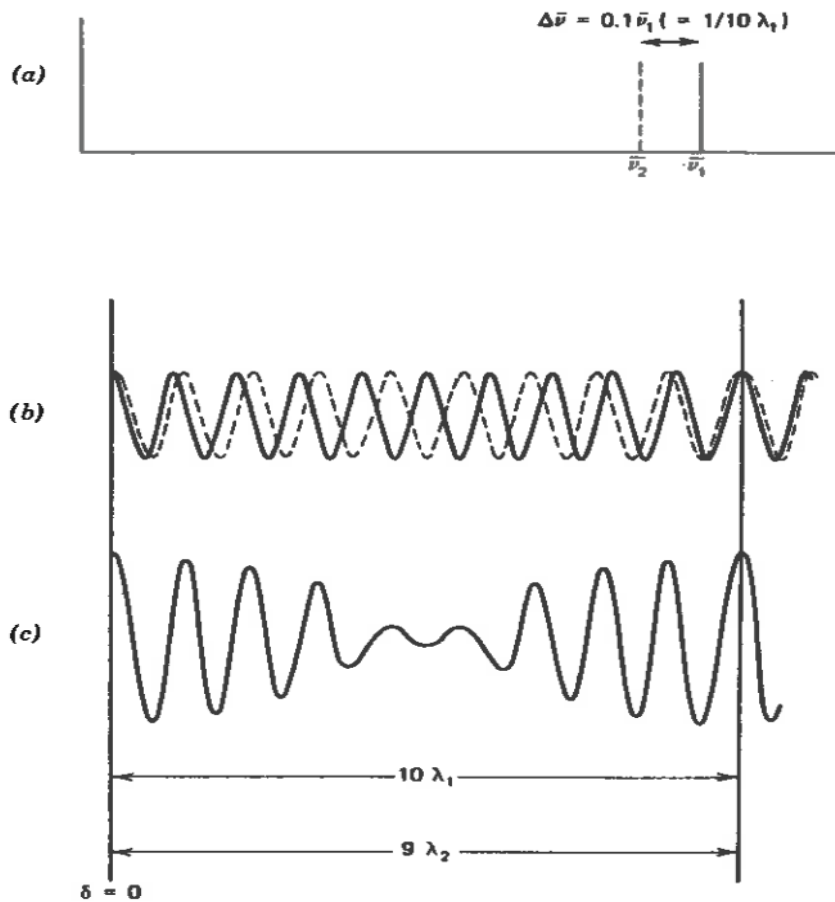


Figure 3.2: Sample spectrum showing two spectral lines of equal intensity at different wavelengths (a), with the individual interferograms (b) and combined interferogram (c). The black lines in (b) and (c) show the zero path difference, where the radiation interferes constructively. From Griffiths and de Haseth [1986],

Considering only the component that varies with δ (the non-varying component is not generally important for FTIR spectroscopy since it is simply equal to $0.5I(\nu)$) and taking the cosine Fourier transform yields B , the intensity of the observed *spectrum* (potentially including any corrections from mirror reflectivities < 1 etc.):

$$(3.4) \quad B(\nu) = 2 \int_0^{\infty} I(\delta) \cos(-2i\pi\nu\delta) d\delta$$

Here the integral is performed over one half of the domain and doubled, since this function is even (symmetric about 0). This gives the desired information about the spectral distribution of the incoming energy. In practice, this integral is instead a large sum, and the Fourier transform is performed numerically (e.g. using a Fast Fourier Transform (FFT) algorithm, see *Griffiths and de Haseth* [1986] for more information).

In the example shown in Figure 3.1 the radiation is absorbed after passing through the beam splitter, whereas for the work in this thesis the atmosphere absorbs the radiation before it is recombined. Figure 3.3 shows an interferogram observed during the experiment detailed in this thesis, alongside the corresponding spectrum.

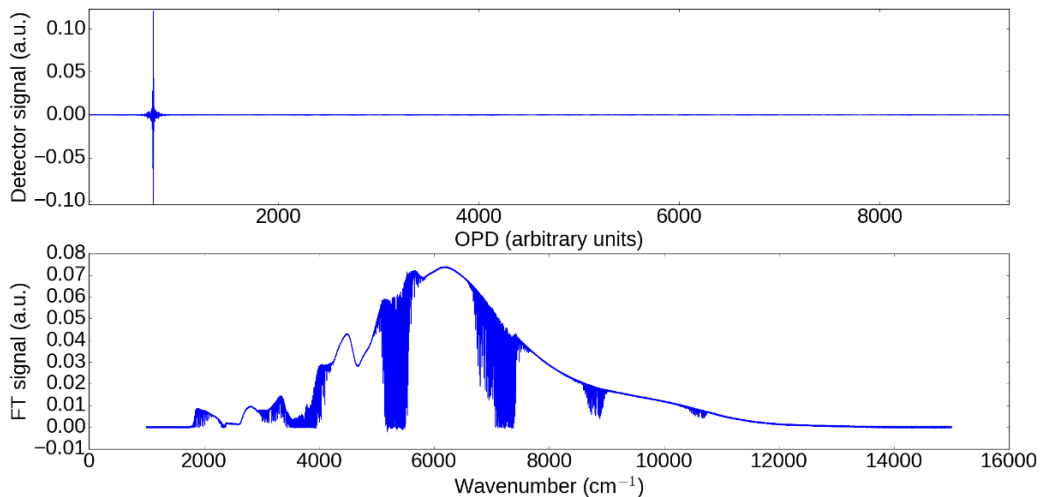


Figure 3.3: *Observed interferogram (a) and spectrum (b) from an FTIR observation taken using the TSARS radiance source. The interferogram has been truncated to show the centreburst more clearly; more data points exist up to $x = \sim 80000$.*

In many laboratory applications, this procedure is followed twice; once with the sample present and once without. This allows the absorption structure of the sample to be observed via the difference of the two observed spectra. In the case of this

thesis, this was not possible since observations were taken through the atmosphere. It was therefore necessary to perform an absolute radiometric calibration to convert the observed FT signal (in arbitrary units) into the spectral irradiance (in $\text{W m}^{-2} (\text{cm}^{-1})^{-1}$). This procedure is detailed in Section 3.4.3.2.

The resolution of the observed spectrum is inversely proportional to the maximum distance travelled by the moving mirror, i.e.

$$(3.5) \quad \Delta\nu \approx \frac{1}{\delta_{max}}$$

where δ_{max} is the maximum path difference between the mirrors. This arises from the interference of the input beam; two cosine waves with separation $\Delta\nu$ will become completely out of phase and then in phase again (i.e. can be resolved) every $\frac{1}{2\Delta\nu}$ path differences. A more rigorous derivation of this is available in *Griffiths and de Haseth* [1986].

3.2.4: Computational methods in FTIR spectroscopy

In practice, the information obtained from the FT spectrometer is never perfect. It is extremely difficult to e.g. ensure that the mirror position is determined exactly when measuring the interference pattern (particularly at high resolution, where the path differences and therefore measurement time are larger), and to determine the exact point where $\delta = 0$ (zero path difference or ZPD). These problems can however be mitigated by computational means.

3.2.4.1: Apodization

Apodization refers to the truncation of the interferogram in order to calculate the Fourier transform. In Equation (3.4), the integral is performed over infinite δ . In practice, δ limited by the physical distance travelled by the moving mirror in the interferometer (the path length). The FTS used in this work has a path length of ~ 2.85 m. While this is large (and allows a very high spectral resolution), an apodization factor is still necessary.

In this case, a boxcar apodization was used. This is defined as:

$$(3.6) \quad F(\delta) = \begin{cases} 1, & \delta < \delta_{max} \\ 0, & \delta \geq \delta_{max} \end{cases}$$

i.e. 1 for the range of possible δ for the spectrometer and 0 outside. This is the simplest type of apodization, and is useful since this does not limit the resolution of the spectrum, unlike more complex apodization functions.

Taking the Fourier transform of this function gives the *instrument line-shape*, which determines the behaviour of this apodization function on the observed spectrum. In this case:

$$(3.7) \quad f(\nu) = 2\delta_{max} \text{sinc}(2\pi\nu\delta_{max})$$

where $\text{sinc}(x) = \sin(x)/x$. This function in both interferogram and spectral space are shown in Figure 3.4 (for arbitrary x). The shape of a given spectral line is obtained via convolution of this sinc function with the “true” spectrum. This results in side lobes where the absorption can become negative. This is not an issue in this work here due to the ability to measure in microwindows which are sufficiently distinguishable from strong lines, minimising the effect of these side lobes.

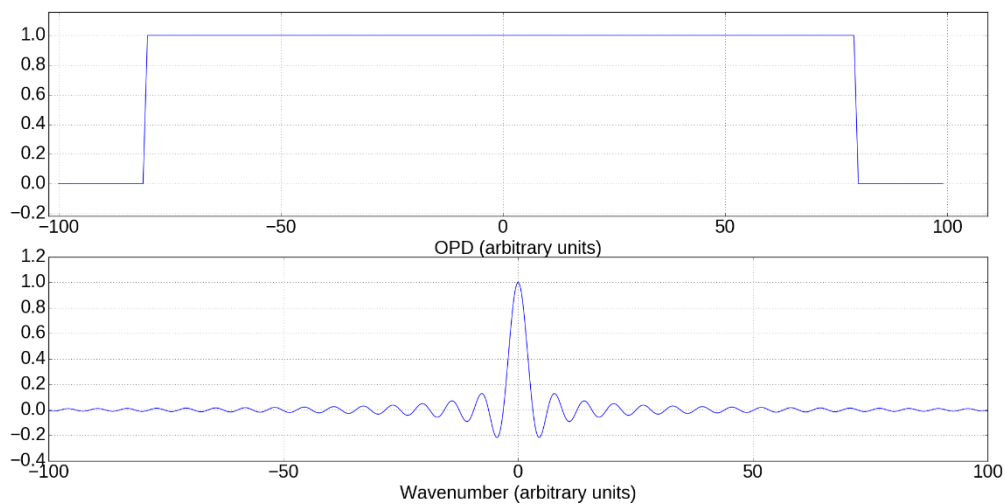


Figure 3.4: Apodization function used in this work in interferogram (a) and spectral (b) domains.

Alternative apodization functions are available, which aim to minimise these side lobes. A triangular function, i.e.

$$(3.8) \quad F(\delta) = \begin{cases} 1 - \delta/\delta_{max}, & \delta < \delta_{max} \\ 0, & \delta \geq \delta_{max} \end{cases}$$

has a Fourier transform of the form

$$(3.9) \quad f(\nu) = 2\delta_{max} \operatorname{sinc}^2(\pi\nu\delta_{max})$$

This function has the advantage of minimising the side lobes; however the resolution of the spectrum is reduced, since the FWHM (full width at half maximum) of the function is increased.

A more comprehensive account of apodization functions is available in *Griffiths and de Haseth* [1986]. *Norton and Beer* [1977] present a comprehensive list of apodization functions available, all of which provide some trade-off between resolution and lobe size.

3.2.4.2: Zero filling

Before an interferogram is Fourier transformed to produce a spectrum, it is common practice to extend the interferogram by adding zeros to the end, since the FFT algorithm requires the array size to be a factor of 2. An additional number of zeros N can be added, often equal to the array size ($N = 2$). This has the effect of smoothing the data in the observed spectrum, by increasing the number of points (by adding points that lie in between the non-zero-filled data). This improves the appearance of the spectrum when observed by eye, since it is unlikely that a spectral line centre will lie exactly on a point observed by the spectrometer. While this increases the number of points in the spectrum, it does not increase its optical resolution.

3.2.4.3: Phase correction

The *phase angle* $2\pi\nu\delta$ determines the behaviour of the interferogram (e.g. Equation 3.3). This equation relies on the assumption that the interferogram is symmetrical about ZPD ($\delta = 0$). In practice, this is often not the case. For example, if an observation is taken at some offset ϵ to the ZPD, the phase angle is therefore $2\pi\nu(\delta - \epsilon)$. Alternatively, electronic or optical filters used in removing high frequency noise may produce some offset via a phase lag θ , changing the cosine term in Equation 3.3 to $\cos(2\pi\nu\delta - \theta_\nu)$. This phase offset can be conceptualised as

adding a sine term to Equation (3.3), and is visible as asymmetry in the interferogram. Since a sum of real cosine and sine terms can be expressed in the form of an exponential, Equation 3.3 becomes:

$$(3.10) \quad I(\delta) = \frac{1}{2} \int_{-\infty}^{\infty} I_0(\nu) \exp(-2\pi i \nu \delta) d\nu$$

with the inverse Fourier transform yielding the desired spectrum:

$$(3.11) \quad B(\nu) = \frac{1}{2} \int_{-\infty}^{\infty} I_0(\nu) \exp(-2\pi i \nu \delta) d\delta$$

with a complex spectrum $B'(\nu)$:

$$(3.12) \quad \begin{aligned} B'(\nu) &= i \operatorname{Im}(\nu) + \operatorname{Re}(\nu) \\ &= r e^{i\phi_\nu} \end{aligned}$$

where r is the *magnitude spectrum*, equal to $|B(\nu)| = \sqrt{(\operatorname{Re}(\nu))^2 + (\operatorname{Im}(\nu))^2}$. By applying a correction of $e^{i\phi_\nu}$ to this complex spectrum, the desired spectrum can be obtained. ϕ_ν can be thought of as the angle posed by r in the complex plane in polar coordinates, and r the magnitude of the vector. Therefore, using trigonometry:

$$(3.13) \quad \phi_\nu = \arctan \frac{\operatorname{Im}(\nu)}{\operatorname{Re}(\nu)}$$

Rearranging Equation 3.12 (ignoring the imaginary term, since the output spectrum must be real) gives:

$$(3.14) \quad B(\nu) = \operatorname{Re}(\nu) \cos(\phi_\nu) + \operatorname{Im}(\nu) \sin(\phi_\nu)$$

so multiplying the imaginary part of the Fourier transform by the sine of the phase angle and the real part by the cosine of the phase angle gives the true spectrum, a procedure known as *phase correction*.

There are two main methods of phase correction (see e.g. Chase [1982]), which work either in spectral space (Mertz, as demonstrated above), or in interferogram space (Forman; any multiplication in spectral space is a convolution in interferogram space). The FTIR spectra analysed in this work were phase corrected using the Mertz method. Assuming that the phase angle varies slowly with wavenumber, the phase information can be obtained by taking a small region around the centreburst, to save computational time.

This procedure was handled by the OPUS (OPTics User Software) provided with the spectrometer. Section 3.4.4.3 details some of the additional work undertaken during this thesis on the effect of this phase correction.

3.3: Retrieval methods

This section details the different methods used to convert the FTIR spectra and the supplementary data (see Section 3.4.2) into spectral irradiance and continuum optical depth. The majority of the FTIR methods rely on the Beer-Bouguer-Lambert law described in Equation 2.33.

3.3.1: Radiative closure

From Equation 2.33:

$$(3.15) \quad I(\nu) = I_0(\nu)\exp(-m\tau(\nu))$$

where I is the observed spectral irradiance as a function of wavenumber, I_0 is the incoming top of atmosphere radiation, m is the airmass factor (approximately $1/\cos(\theta)$ after accounting for refraction effects) with θ the solar zenith angle, and τ is the total atmospheric optical depth. It is therefore possible to derive both the top of atmosphere irradiance and the optical depth from I , provided one has knowledge of the other, which is referred to here as the *closure method*. In this work, both I_0 (see Chapter 4) and τ (Chapter 5) are uncertain to $\sim 10\%$ and 2-3 orders of magnitude respectively in parts of the spectral region of interest. Thus, it is preferable to obtain them without assuming a value for the other, which is possible via the Langley method.

3.3.2: Langley method

The Langley method (e.g. *Liou*, [2002]) exploits observations at multiple solar zenith angles to determine τ and I_0 independently at any given ν , using the gradient and y-intercept of a linear fit respectively. Taking the logarithm of Equation (3.15) yields:

$$(3.16) \quad \ln(I) = -m\tau + \ln(I_0)$$

which by putting into the form of a linear equation with $\ln(I)$ as the y-axis and m as the x-axis yields $-\tau$ (via the gradient of the slope) and $\ln(I_0)$ via the y-intercept. An idealised Langley plot is shown in Figure 3.5. In this case, the uncertainties on the

data points are zero and they all fit (almost) perfectly in a straight line. In reality, this is not the case, and the uncertainty in τ and I_0 need to be computed accordingly. This is explained in Section 3.3.7.

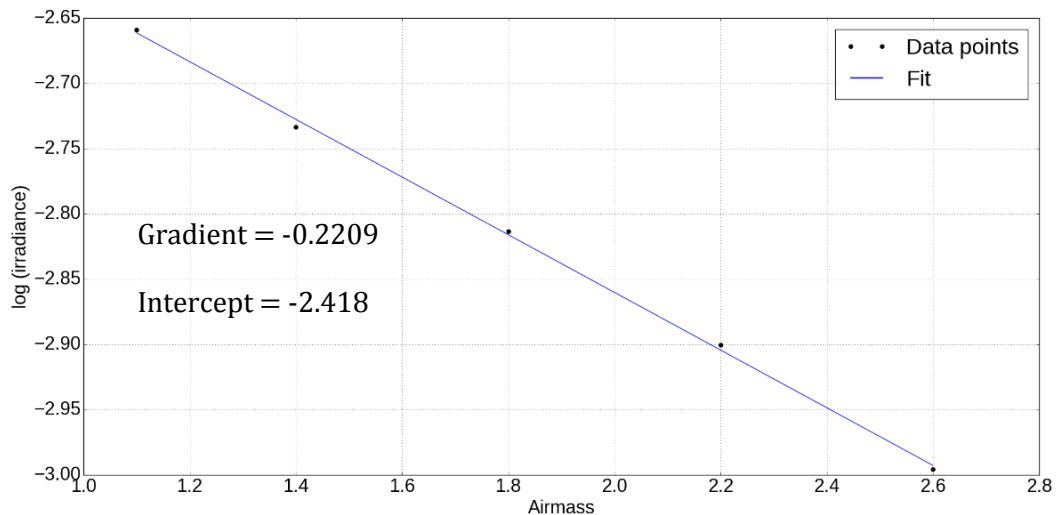


Figure 3.5: *Idealised Langley plot for observations taken at different zenith angles, the gradient and slope.*

The Langley method relies on several assumptions; the most important being that the atmospheric state must remain relatively constant. Changes in temperature, pressure, water vapour or aerosol concentrations would cause different absorption from one observation to another, causing deviations from the straight line and therefore skewing I_0 and τ . It is also important to measure in clear skies, since clouds will scatter and absorb radiation which will make it difficult to extract the desired signal.

3.3.3: Advantages and disadvantages of Langley and closure methods

Both methods have advantages and disadvantages. The Langley method has the advantage of using more data (increasing the reliability of the estimate), does not rely on prior knowledge of either I_0 or τ , and removes the effect of systematic uncertainty (when determining τ) or mitigates the random uncertainty (when determining I_0). However, it is reliant on being able to obtain observations across the course of a day, and those observations being over a period when the atmosphere is sufficiently constant. The closure method does not rely on this being the case; I_0 and τ can be obtained from a single spectrum. This does however require an assumption to be made about the value of the other. A large ($\sim 10\%$) uncertainty in τ has a small effect

on the irradiance observed at the surface, but even a small uncertainty in I_0 has a considerable effect on the uncertainty on I . In the limit of low optical depth and assuming a zenith viewing, Equation 3.15 can be approximated via a first-order Taylor expansion:

$$(3.17) \quad I = I_0 (1 - \tau)$$

Differentiating this equation with respect to both I_0 and τ gives:

$$(3.18) \quad I_0 \frac{dI}{dI_0} = I_0(1 - \tau)$$

and

$$(3.19) \quad I_0 \frac{dI}{d\tau} = -I_0\tau.$$

Assuming τ of around 0.1, it would take an uncertainty in τ of around 10% to match a corresponding 1% uncertainty in I_0 . It is therefore much more important to understand I_0 to measure τ than vice versa, which is important for the work presented in Chapter 4.

The evidence presented in Chapter 4 seems to indicate increasing consensus in I_0 in this spectral region; this I_0 was therefore used for the closure calculations performed in Chapter 5. The closure experiments in Chapter 4 provided more of a supporting role, due to the large uncertainty in the water vapour continuum in this region. This uncertainty was included in the uncertainty budget. This was also the case for the work in Chapter 5, since the closure method must account for the uncertainty in SSI when deriving optical depth, which led to an increased uncertainty estimate relative to the Langley method in which this uncertainty was not included.

In general, for this work, the advantages conferred by the Langley method make it the most reliable way of determining I_0 and τ , and the Langley derived spectra are therefore considered the best estimate. This is explained further in Section 3.4.3.

3.3.4: Calculation of Rayleigh scattering

Rayleigh scattering is a second-order effect in the 2000-10000 cm^{-1} region since it scales with $1/\lambda^4$. It is still necessary to include a contribution from this effect however, since the continuum is also a relatively weak effect. In this instance, optical depths obtained for a standard atmosphere from *Bucholtz* [1995] were used. These

vary from 8.6×10^{-3} at $1 \mu\text{m}$, 1.3×10^{-3} in the centre of the $1.6 \mu\text{m}$ window, 3.7×10^{-3} in the centre of the $2.1 \mu\text{m}$ window, and 3.3×10^{-3} at $4 \mu\text{m}$. These values are mostly insensitive to water vapour; the difference between a tropical and winter atmosphere at $1.6 \mu\text{m}$ is 0.6%. It is assumed in this case that all scattered radiation is removed from the direct beam observed by the FTIR, as the asymmetry parameter (see Section 2.3.4) is 0 in the Rayleigh regime. Therefore, using these optical depths is reasonable due to the low values and the small field of view of the FTS; very little of the forward scattered radiation enters the spectrometer. Figure 3.6 shows the Rayleigh scattering contribution to optical depth assumed in this work.

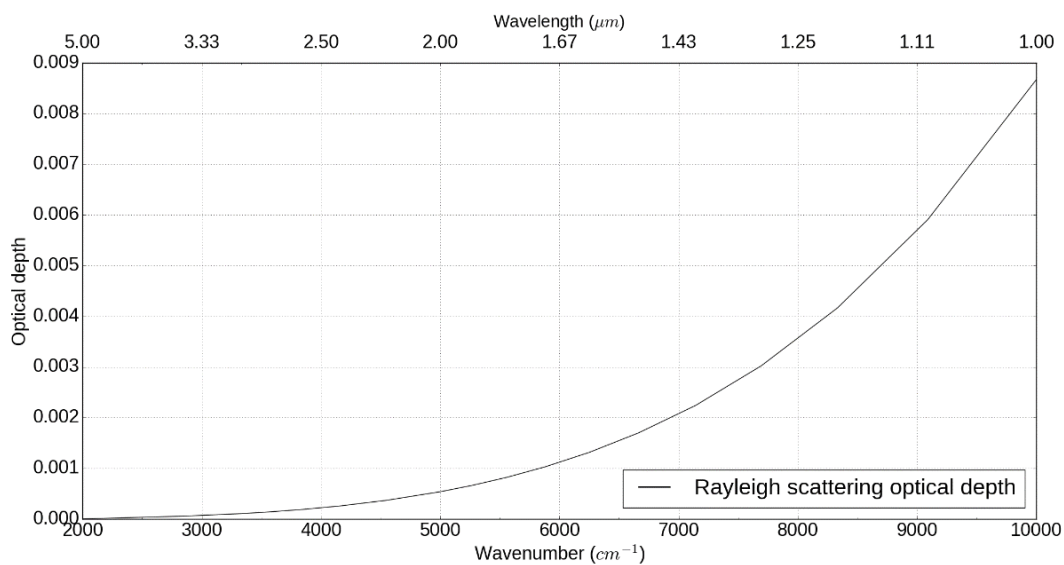


Figure 3.6: Rayleigh scattering optical depth derived for the US Standard atmosphere from Bucholtz [1995].

3.3.5: Ångström extrapolation and Mie scattering codes

As will be discussed in Section 3.4.5.2., the measurements of aerosol extinction used in this field campaign are obtained in a different part of the spectrum to that of interest to this work. There are two methods used in this thesis to extend this aerosol extinction out into the near-infrared, which are explained below.

3.3.5.1: Ångström extrapolation

The Ångström exponent (see e.g. Toledano *et al.* [2007]) is one of the most widely-used methods of extrapolating (or interpolating) aerosol optical depth (AOD) into different spectral regions. This method typically exploits observations in several channels in the visible part of the spectrum (since water vapour absorption is mostly

negligible). At least two different wavelengths are required. Observations show (see e.g. *Schuster et al.* [2006]) that aerosol spectral behaviour generally obeys a simple power law formula:

$$(3.20) \quad \tau(\lambda) = \beta\lambda^{-\alpha}$$

Here τ is the aerosol optical depth at wavelength λ , β is the aerosol optical depth at 1 μm and is sometimes referred to as the *turbidity coefficient*. This gives an indicator of the amount of aerosol present in the atmosphere. α is the *Ångström exponent*. α determines the spectral behaviour of the aerosol and can be used as a qualitative indicator of aerosol size distribution. Typically for urban-industrial and mixed aerosol, as is the case for this work, α is between ~ 1.2 and 2.1 , indicating a significant drop-off of AOD with increasing wavelength (decreasing wavenumber).

In this case, it is AOD that is of particular interest, since this is assumed to be removed from the direct beam observed by the FTS. α can be obtained by dividing Equation 3.20 (renaming τ to τ_1 and λ to λ_1) by $\tau_2(\lambda) = \beta\lambda^{-\alpha_2}$, i.e. an observation at a different wavelength. This cancels the turbidity term, and after taking the natural logarithm leaves:

$$(3.21) \quad \alpha = -\frac{\log\left(\frac{\tau}{\tau_2}\right)}{\log\left(\frac{\lambda_1}{\lambda_2}\right)}$$

Thus, with observations of β , one can obtain the spectral behaviour at any other wavelength. This is of course a simplistic treatment, and does not account for e.g. absorption bands in aerosols with low single scattering albedo etc. It is however a useful technique in this case, where it is assumed that aerosols are mostly scattering (see Section 3.4), the overall absorption is quite low, and the property we wish to retrieve is smoothly-varying. In addition, if there is absorption, this is not a problem in this case since any radiation removed from the optical beam is considered the same regardless of its nature. The Microtops sunphotometer (see Section 3.4.5.2) cannot discern between scattered radiation within the forward peak and unscattered radiation.

In this work, observations of AOD were made in 5 wavelength channels. To use all of this data simultaneously, and to obtain β , a linear fit was constructed. Taking the natural logarithm of Equation 3.20, it is found:

$$(3.22) \quad \log(\tau) = -\alpha \log(\lambda) + \log(\beta)$$

By taking a linear fit of $\log(\tau)$ on the y-axis and $\log(\lambda)$ on the x-axis, $\log(\beta)$ and $-\alpha$ can be obtained via the y-intercept and gradient of this fit respectively. This method also allows for the uncertainty in the aerosol scattering to be easily obtained. This is first done using a Monte Carlo method (see Section 3.3.7) to find the observed spread in $\log(\beta)$ and $-\alpha$, using the uncertainties (see Section 3.4.5.2) of each data point in the sunphotometer data. $\log(\beta)$ and $-\alpha$, with their respective upper and lower limits are then used to obtain τ , with the upper and lower uncertainties in τ obtained by using the upper and lower limits of $\log(\beta)$ and α .

3.3.5.2: Mie scattering codes

The alternate method used in this thesis to obtain aerosol spectral properties in the NIR is through the use of a Mie scattering code. The physics involved in such a code is discussed in more detail in Section 2.3.5. This section details some of the sensitivity to the assumptions necessary to perform the calculations, and how the uncertainty budget was obtained. In this case, a code based on the Wiscombe Mie scattering code was used. This code takes in refractive indices n and k (real and complex respectively), volume concentrations C_n , mean particle size r_n and standard deviations σ_n for the size distribution (here using a bimodal distribution with a coarse and fine mode). The code assumes an optical depth at 1 μm , this was in this case input using the 1.02 μm observations from the sunphotometer.

Since in situ measurements of these parameters were not obtained in the measurement campaign, these are instead taken from standard values for urban-industrial and mixed aerosols (from *Dubovik et al.* [2002]). The range of parameters is shown below in Table 3.1. The values from the Greenbelt measurements on the US eastern seaboard were assumed typical of a site like Camborne [*N. Bellouin, pers. comm.*].

TABLE 1. Summary of aerosol optical properties retrieved from worldwide AERONET network of ground-based radiometers.

Urban–industrial and mixed	GSFC, Greenbelt, MD (1993–2000)	Crete–Paris, France (1999)
Number of measurements (total)	2400	300
Number of measurements (for ω_0, n, k)	200 (Jun–Sep)	40 (Jun–Sep)
Range of optical thickness; $\langle \tau \rangle$	$0.1 \leq \tau(440) \leq 1.0$; $\langle \tau(440) \rangle = 0.24$	$0.1 \leq \tau(440) \leq 0.9$; $\langle \tau(440) \rangle = 0.26$
Range of Ångström parameter $\langle \alpha \rangle$ (440/670/870/1020)	$1.2 \leq \alpha \leq 2.5$	$1.2 \leq \alpha \leq 2.3$
$n; k$	$0.68/0.59/0.54/0.53 \pm 0.08$	$0.68/0.61/0.58/0.57 \pm 0.07$
$\omega_0(440/670/870/1020)$	$1.41 - 0.03\tau(440) \pm 0.01$; 0.003 ± 0.003	1.40 ± 0.03 ; 0.009 ± 0.004
$r_{\text{ref}} (\mu\text{m}); \sigma_r$	$0.98/0.97/0.96/0.95 \pm 0.02$	$0.94/0.93/0.92/0.91 \pm 0.03$
$r_{\text{vc}} (\mu\text{m}); \sigma_r$	$0.12 + 0.11 \tau(440) \pm 0.03$; 0.38 ± 0.01	$0.11 + 0.13 \tau(440) \pm 0.03$; 0.43 ± 0.05
$C_{\text{vc}} (\mu\text{m}^3/\mu\text{m}^2)$	$3.03 + 0.49 \tau(440) \pm 0.21$; 0.75 ± 0.03	$2.76 + 0.48 \tau(440) \pm 0.30$; 0.79 ± 0.05
$C_{\text{v}} (\mu\text{m}^3/\mu\text{m}^2)$	$0.15 \tau(440) \pm 0.03$	$0.01 + 0.12 \tau(440) \pm 0.04$
$C_{\text{vc}} (\mu\text{m}^3/\mu\text{m}^2)$	$0.01 + 0.04 \tau(440) \pm 0.01$	$0.01 + 0.05 \tau(440) \pm 0.02$

Table 3.1: Parameters used in the Mie scattering code, taken from Dubovik et al. [2002].

Since the parameter space was very large, it was not possible to sample the whole range. Figure 3.7 shows several examples of aerosol optical depth derived using the Mie code for different input parameters. The Mie code does not provide absolute optical depth, therefore in this case the model runs are tied to the Microtops observations (Section 3.4.5.2) at $1.02 \mu\text{m}$, since these are the most relevant to the spectral region of interest. The data from these Figures was used to determine an estimate of the uncertainty, by looking at the spread of the data and obtaining rough minima and maxima. While this is not an especially rigorous assessment, the lack of data and the large parameter spread makes a more rigorous treatment not possible. In all cases, the AOD drops off with decreasing wavenumber; this is consistent with the range of Ångström parameters observed.

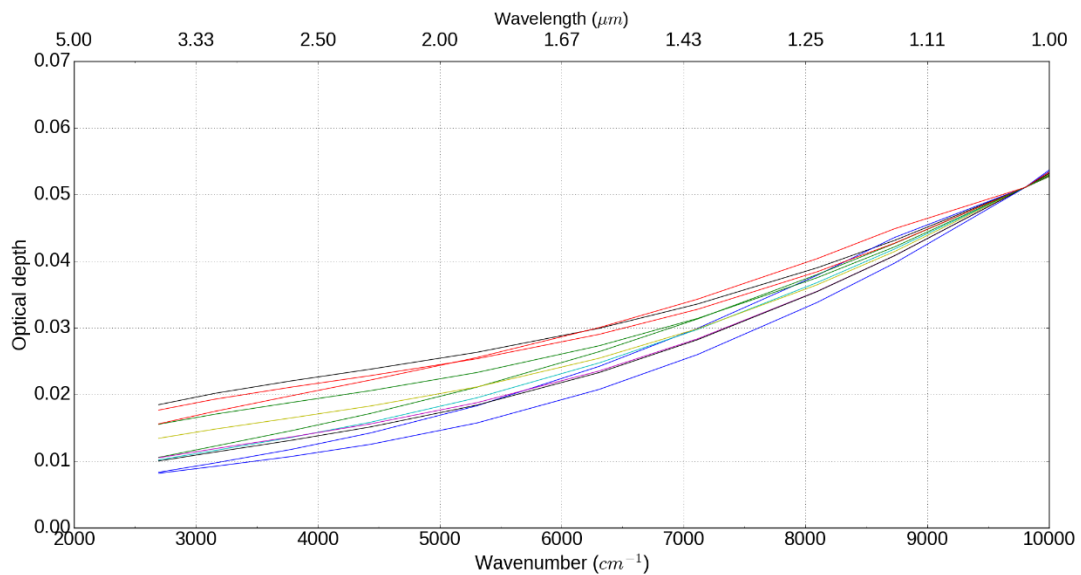


Figure 3.7: Various sensitivity tests of the Mie scattering code for different input parameters. These are for heuristic purposes only, but give an indication of the plausible range of spectral behaviour within the parameters in Table 3.1.

In this work, the Mie scattering code is preferred, since it provides a physical derivation of the aerosol extinction rather than a mathematical one. It is also a more conservative estimate, which increases the uncertainty in the final value. This is necessary, since the aerosol is by far the largest source of uncertainty and it is unclear whether the Ångström extrapolation sufficiently quantifies this uncertainty without more robust measurements. The Ångström extrapolation does provide some physical information however, since it uses all of the available spectral data from the measuring system used.

3.3.6: Airmass correction

While m is usually defined as $\sec(\theta)$, this is not strictly true. The atmosphere refracts radiation as it travels through, diverting the solar zenith angle by a small amount. This is not usually important for zenith angles below 80° [Iqbal, 1983], but is nevertheless corrected for in this work. This is done using the PyEphem Python library, which is in turn a Python wrapper for the libastro module in the XEphem library of astronomical software (<http://www.clearskyinstitute.com/xephem/>). The solar position calculation is specified in Reda and Andreas [2008] and Meeus [1999] and includes (surface) pressure-dependent (1013 mb if unspecified) corrections for

atmospheric refraction. The stated uncertainty in the sun position is 0.0003%; the uncertainty in the airmass is therefore small enough to be negligible.

3.3.7: Monte Carlo uncertainty evaluation

A given measurement has two types of uncertainty; random and systematic. Random uncertainties vary ostensibly from measurement to measurement e.g. from noise. Systematic uncertainties remain the same from measurement to measurement, e.g. uncertainty in the original instrument calibration. Systematic errors can in some cases be corrected for (e.g. signal loss due to mirror reflectivity <100%), but this correction has an associated uncertainty. Section 3.4.1.4 goes into more detail about how these uncertainties are calculated in this case. Section 4.2.5 goes into some more detail about how this is used in practice in measuring SSI.

This difference is important in the case of the Langley method; since the final values are derived from multiple data points, the systematic uncertainty should remain the same for each data point in the analysis. A Monte Carlo method was implemented to calculate this. The random uncertainty is sampled once for each data point, and the systematic uncertainty is sampled once for each sample (i.e. each time the Monte Carlo analysis is performed). The observed values are then adjusted accordingly, and a Langley fit is obtained, yielding values of I_0 and τ . This analysis is then performed 100000 times, which produces a distribution of derived I_0 and τ . This separates out the random and systematic components of the uncertainty, and allows for the “true” uncertainty in both I_0 and τ to be obtained. This is important, since otherwise the uncertainty would be overestimated.

The uncertainties (shown on Figure 3.17) have some wavenumber dependent asymmetry. The errors are assumed Gaussian (in the absence of evidence to the contrary); to overcome this asymmetry two distributions were set up for the random and systematic uncertainties; which of these is used in the Monte Carlo algorithm is determined by a random 50/50 selection. Given a sufficiently large number of samples (in this case 10^5), this should sample from each roughly the same number of times.

In a similar way, this approach is also applicable to the calculation of the Ångström parameters $\log(\beta)$ and $-\alpha$ (Section 3.3.5). In this instance, each data point has a

stated uncertainty (see Section 3.4.5.2), which is all assumed to be random in this case as no breakdown of the random and systematic components of the instrument uncertainty was available.

3.4: CAVIAR field campaigns

This section provides details of the field campaigns from which the results in this thesis were derived. These field campaigns were part of the CAVIAR (Continuum Absorption at Visible and Infrared wavelengths and its Atmospheric Relevance) consortium, led by the University of Reading. CAVIAR involved theoretical studies, laboratory observations and observations of the Sun through the atmosphere during two field campaigns. These measurements were performed by Marc Coleman, Tom Gardiner and Nigel Swann (National Physical Laboratory) and Liam Tallis (University of Reading).

This thesis focuses on observations from one of these field sites. While data from the Jungfraujoch site (Section 3.4.2) exists, it was found during the PhD that the calibration of this data was suspect, and the low water vapour absorption make it difficult even in principle to obtain continuum absorption spectra outside of foreign continuum in the bands. The Camborne campaign (Section 3.4.1) therefore provides the basis of the work in Chapters 4 through 6. Section 3.4.3 focuses more on the setup of the Fourier transform spectrometer used in both the Camborne and Jungfraujoch field campaigns, its calibration and the uncertainty budget.

Section 3.4.4 presents some of the additional work undertaken in this thesis to assess the calibration and uncertainty in the instrument. Section 3.4.5 presents details of the supplementary measurements used to construct atmospheric profiles and obtain the non-continuum optical depth, which is subtracted from the total optical depth derived from the FTIR measurements to obtain the continuum optical depth.

3.4.1: Camborne campaign

The first of the two field campaigns took place at Camborne, Cornwall, UK in July-September 2008. This site is located at 50.2128° N, 5.2948° W, and is located away from major sources of industrial pollution. Due to its proximity to the sea, it is likely that depending on the prevailing conditions the majority of aerosol is marine aerosol. The site is a UK Met Office synoptic station, and a radiosonde launch site (see

Section 3.4.5.1). When conditions permitted (i.e. during daytime, with no clouds obscuring the sun), scans were taken using the FTS to obtain spectral irradiance (see Section 3.4.3), and observations were taken simultaneously using the Microtops sunphotometer (see Section 3.4.5.2). Radiosondes were launched twice daily by the Met Office; additional launches were also made during the campaign. 22 August and 18 September had additional observations from the FAAM (Facility for Airborne Atmospheric Measurements) aircraft; these were not used in this analysis however (see Section 3.4.5.4).

While it was expected that there would be a significant number of days with sufficiently low aerosol and clear skies over this period, this was not the case in practice. Only two days permitted observations over a range of zenith angles sufficient to perform a Langley analysis; these were 22 August 2008 and 18 September 2008. The observations of 18 September 2008 are preferred here, since the observations of 22 August 2008 exhibited a spectral drift not present in other days of observations (see Section 3.4.4). Some spectra from other days are suitable for an analysis using the radiative closure method. Table 3.2 shows the (relevant) days on which usable spectra were taken, the temporal coverage of the FTS measurements, timings of relevant radiosonde launches and the range of aerosol optical depths across the day as observed by the sunphotometer. More information is available in *Tallis et al.* [2011].

Experiment number	Day(s)	Type of measurement	Time coverage	Radiosonde timings (UTC)	Range of AOD (9800 cm ⁻¹ channel)
CAV15	14-25 July 2008	UHTBB calibration/TSARS measurements	n/a	n/a	n/a
CAV18	11 August 2008	TSARS measurements	n/a	n/a	n/a
CAV19	12 August 2008	Solar measurements	2 meas. at 15:05 UTC	n/a	n/a

CAV20	13 August 2008	Solar measurements	21 meas. from 12:10- 14:21 UTC	11:00	0.608 (1 measurement)
CAV21	19 August 2008	Solar measurements	12 meas. from 12:09- 12:33 UTC	11:00, 15:00	0.348-0.092
CAV22	20 August 2008	TSARS measurements	n/a	n/a	n/a
CAV23	22 August 2008	Solar measurements	44 meas. from 09:32 to 17:32 UTC	05:00, 09:00, 11:00, 16:00	0.085-0.033
CAV25	18 September 2008	Solar measurements	21 meas. from 07:14 to 13:10 UTC	09:00, 11:00, 12:00	0.078-0.036
CAV26	18 September 2008	TSARS measurements	n/a	n/a	n/a
CAV27	23 September 2008	Solar measurements	2 meas. at 08:32- 08:33 UTC	11:00	0.077-0.058
CAV28	24 September 2008	Solar measurements	4 meas. from 07:45- 08:02 UTC	n/a	n/a

CAV29	24 September 2008	TSARS measurements	n/a	n/a	n/a
-------	-------------------------	-----------------------	-----	-----	-----

Table 3.2: *Table showing details of the calibration and Camborne field campaigns, sorted by date.*

3.4.2: Jungfrauoch campaign

In addition to the Camborne campaign, an additional field campaign took place at the Sphinx Observatory at the Jungfrauoch in the Swiss Alps (46.5475° N, 7.9852° E). This campaign took place from July-August 2009. This campaign aimed to support the Camborne measurements, by observing in spectral regions not possible in the Camborne campaign. This was possible due to the high altitude of the field site, above the majority of the atmospheric water vapour and aerosol. Like the Camborne campaign, some measurements were taken co-incident with flights by the FAAM aircraft. Unlike Camborne however, radiosonde measurements were not possible at the observatory, making the atmospheric profile difficult to ascertain.

Various aspects of the calibration were found to be an issue for this campaign. It was judged that a retrieval of the foreign continuum from the Jungfrauoch data would not be possible within the scope of this thesis after some exploratory analysis. While calibration is not inherently required to use the Langley method, the low water vapour concentrations and relatively low solar zenith angles meant that the Langley-derived absorption was negative in parts of the spectrum, since there was not enough atmospheric absorption for it to be detectable by the instrument. In addition, there were some issues with the use of intensity limiting apertures in this campaign (due to the low absorption in this spectral region at this height, the detector can become saturated); in principle a simple correction factor (an intensity limiting aperture should reduce the intensity by a number which does not vary spectrally, in this case by a factor of 2) should retrieve the correct spectrum, but this was found not to be the case. Because of these issues, the Jungfrauoch spectra were deemed unlikely to yield any useful information and are therefore not discussed any further.

3.4.3: Details of the CAVIAR FTIR

The following section describes the setup of the Fourier transform spectrometer used in the two campaigns. This section is covered in more detail in *Gardiner et al.* [2012], with Section 3.4.3.5 covered in part in *Menang et al.* [2013].

3.4.3.1: The Bruker 125 FTS and optical setup

The spectrometer used in this campaign is a Bruker IFS 125 M. This spectrometer has a high maximum resolution (0.00035 cm^{-1}), with broad spectral coverage possible depending on the chosen beam splitter and detector. Two detector/beam splitter combinations were used in the campaign. For the purposes of this thesis one of these setups provides spectral coverage in the region of interest; this was using a calcium fluoride beam splitter with an indium antimonide detector. This provides spectral coverage over the region $\sim 800 - 12500\text{ cm}^{-1}$. The detector response peaks at around 6000 cm^{-1} , perhaps the most important region for this work. The spectra are usually truncated to $2000 - 10000\text{ cm}^{-1}$ in this thesis; this is where the spectrometer response is believed to be the best and covers the region where the continuum uncertainty is greatest.

The spectrometer is controlled using the OPUS software mentioned in Section 3.2.4.3. This is the standard proprietary software that comes with the spectrometer and handles both acquisition of interferograms and the electronic processing of these into usable spectra in cm^{-1} .

The spectrometer is reliant on several optical mirrors to reflect the solar radiation into the laboratory and the spectrometer optics. These optics track the sun over the course of a day using a quadrant detector and feedback loop. The radiation is reflected by a set of gold mirrors, shown in Figure 3.8 (from *Gardiner et al.* [2012]). Radiation from a source a) (either the Sun or the calibration source, see Section 3.4.3.2) is collected by the tracker optics in b). The radiation is then focused through two apertures inside the FTIR. The external mirrors are subject to wear and tear (see Section 3.4.3.2 and 3.4.4.2). Figure 3.9 shows the internal optical setup of the FTIR instrument (also from *Gardiner et al.* [2012]). Aperture A3 limits the instrument FOV; A4 is a non-limiting aperture designed to capture any stray light in the system to ensure this does not affect a measurement.

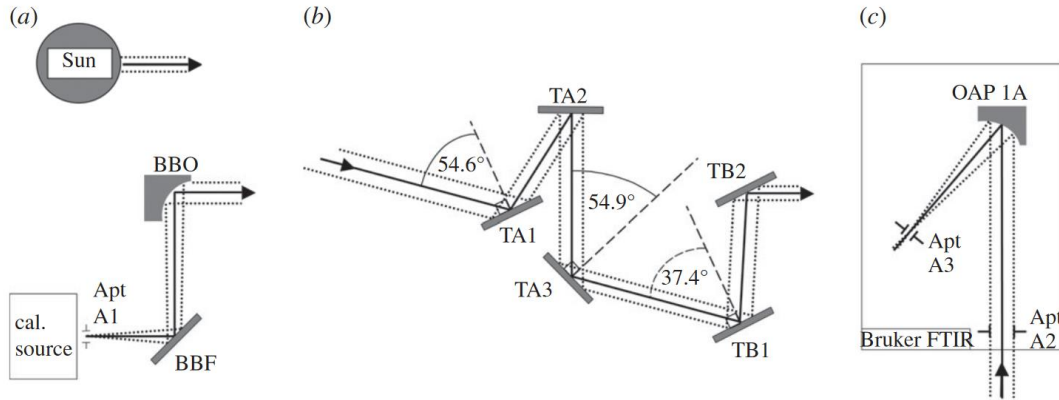


Figure 3.8: Optical setup of the FTS at the field sites. a) shows the input into the FTIR, b) the set of tracker optics and c) the internal optical setup of the spectrometer. From Gardiner et al. [2012].

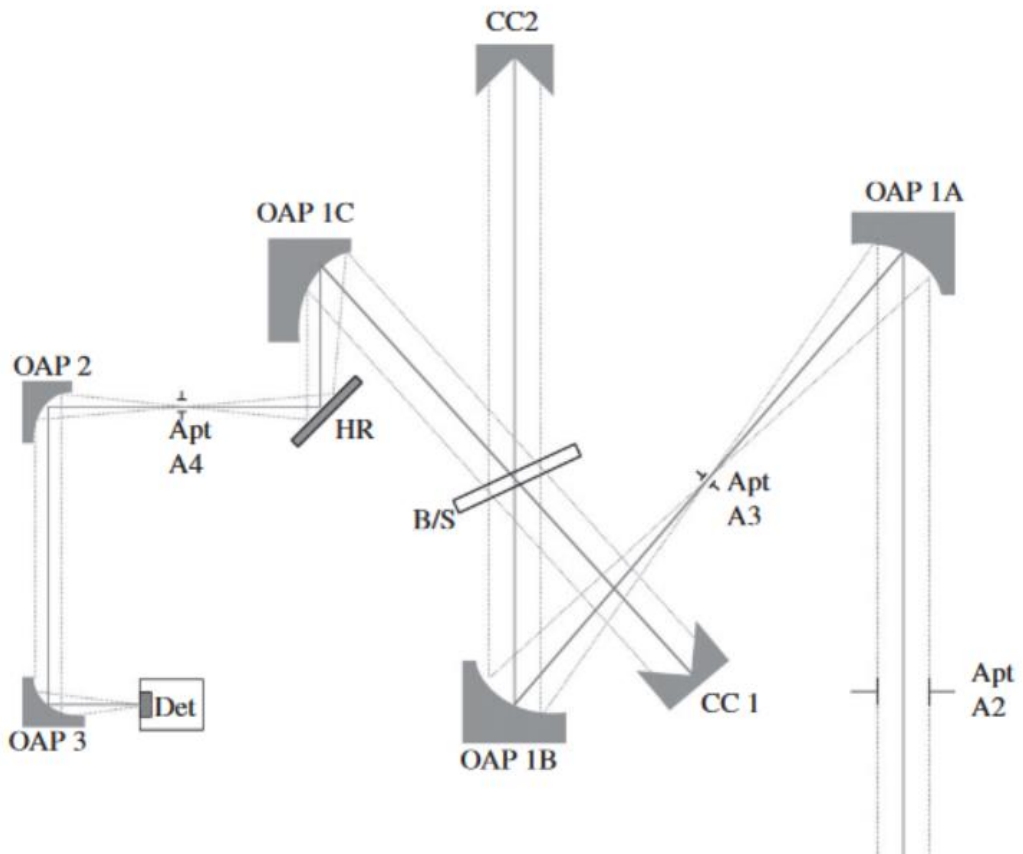


Figure 3.9: Internal optical setup of the FTIR instrument. OAP indicates off-axis parabolic mirrors used to reflect the radiation, B/S the beam splitter, Apt AX an aperture and Det the detector. CC1 and CC2 are the cube corner mirrors along each arm of the spectrometer. Note that the right hand side of the figure is the same as in c) of Figure 3.8. From Gardiner et al. [2012].

The input is aligned by the operator; this introduces a random error into the measurement (see Section 3.4.3.4). Uncertainty also arises from the apertures, external optics and other sources, also described in Section 3.4.3.4. The internal aperture A3 limits the field of view to ensure that only the centre of the solar disc is sampled.

The maximum resolution is 0.0035 cm^{-1} ; in practice this was not attainable, since taking a measurement takes a given amount of time. This time is increased if the scanning mirror is moved the entire length of the arm, which meant that changes in the atmosphere (e.g. clouds) could affect a measurement. The spectra in this thesis are at 0.03 cm^{-1} ; zero filling increases the number of data points above this. Each spectrum in this thesis is a composite of 2-8 scans of the interferometer, typically 8. This number was chosen to find a good balance between signal to noise and ensuring the atmosphere remained constant throughout a measurement.

To assess whether the atmosphere remains constant during a measurement, one can use the direct current (DC) voltage seen by the instrument as a function of time. This DC voltage is indicative of the overall signal incident on the detector; this will be reduced if there is a large change in water vapour or if a sub-visible cloud passes through the field of view. If there is scatter in this DC voltage during a scan (see e.g. Figure 3.10), then the measurement is rejected. This threshold is taken to be small; in this case a 1% change in the DC voltage was sufficient for a scan to be rejected.

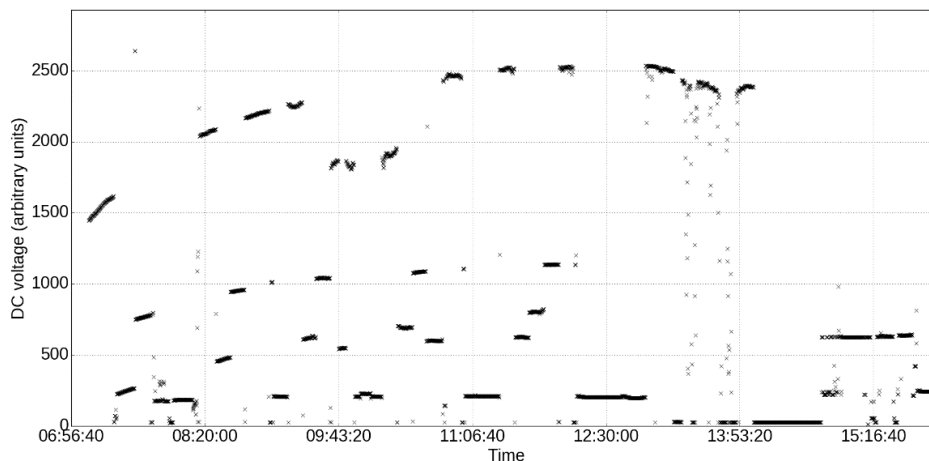


Figure 3.10: DC scan voltage as a function of time for 18 September 2008. The top curve shows measurements relevant to this thesis, other points are either baseline, measurements with scatter (that are thus rejected) or measurements taken using optical filters and/or a different beam splitter/detector setup that did not produce results relevant to this thesis.

3.4.3.2: Calibration procedure

The FTIR detector measures the interferogram as a function of optical path length (see Section 3.2.3); the path length is in arbitrary units but converted to cm using the wavenumber of the helium neon laser used to measure the interferometer displacement. When transforming the interferogram into a spectrum in cm^{-1} , the signal strength is also in arbitrary units. In addition, there is an angle and humidity dependent correction for mirror reflectivity, which is a multiplicative factor applied to this signal. The signal with a mirror reflectivity correction is suitable for Langley analysis to derive optical depth, but not compatible with the closure method and does not provide information on the solar spectral irradiance (see Chapter 4). An absolute calibration to a reference source is therefore required.

In this case, the calibration source is the Ultra High Temperature BlackBody (UHTBB) source at NPL (e.g. *Woolliams et al. [2006]*). This is a blackbody source at 3050 K, which is comparable to the equivalent temperature of the Sun's surface when considering the total wavenumber-integrated intensity reaching the surface. The UHTBB is extremely stable, to within $\sim 1\text{K}$. The blackbody was measured with a radiometer traceable to SI to ensure the stability throughout FTIR calibration.

Gardiner et al. [2012] demonstrate that the radiance S_v reaching the FTIR from the Sun is given by:

$$(3.23) \quad S_v = \eta_{cal} \frac{V_s}{V_c} B_v \pi \alpha_{solar}^2$$

where η_{cal} is the optical efficiency of mirrors BBO and BBF from a) in Figure 3.8, V_s and V_c are the measured values by the FTS (in arbitrary units) from the Sun and calibration respectively, B_v is the blackbody radiance observed at aperture A1 in Figure 3.8 and α_{solar} is the solar half-angle divergence, i.e. the angular divergence of the solar beam as it enters the FTIR aperture. This details the calibration for a given spectrum. An additional multiplicative factor converts the signal from radiance to irradiance. Figure 3.11 shows the calibration spectrum used to convert FTIR signal into spectral irradiance.

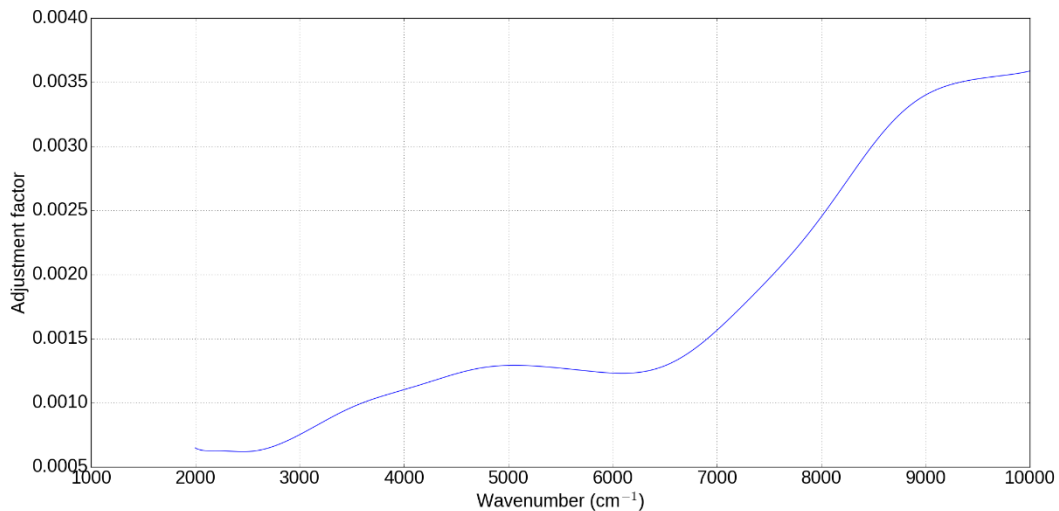


Figure 3.11: Calibration function derived from the UHTBB measurements. This is a direct multiplicative factor to the observed solar signal to obtain spectral irradiance, following Equation 3.23.

There is an additional calibration to the external optics as described in Figure 3.12. Measurements of the mirror reflectance were taken before and after the Camborne campaign using the National Reference Reflectometer [*Williams, 1999*]. These measurements are presented in Figure 3.12. These cover the region 4000-6600 cm⁻¹ at both low and high humidity; this is sufficient to cover the region of interest for the continuum measurements. Outside this spectral region, these need to be extrapolated due to insufficient data. This is done using a simple linear fit to the edges of the

reflectivity function. The correction is dependent on the angle of incidence of the radiation upon the mirror. The uncertainty arising from the use of a linear fit is included in the uncertainty budget; this is low at lower wavenumbers below ~ 4000 cm^{-1} (since the reflectivity tends toward 1), but higher in the higher wavenumbers (beyond 6600 cm^{-1}) where there are no measurements.

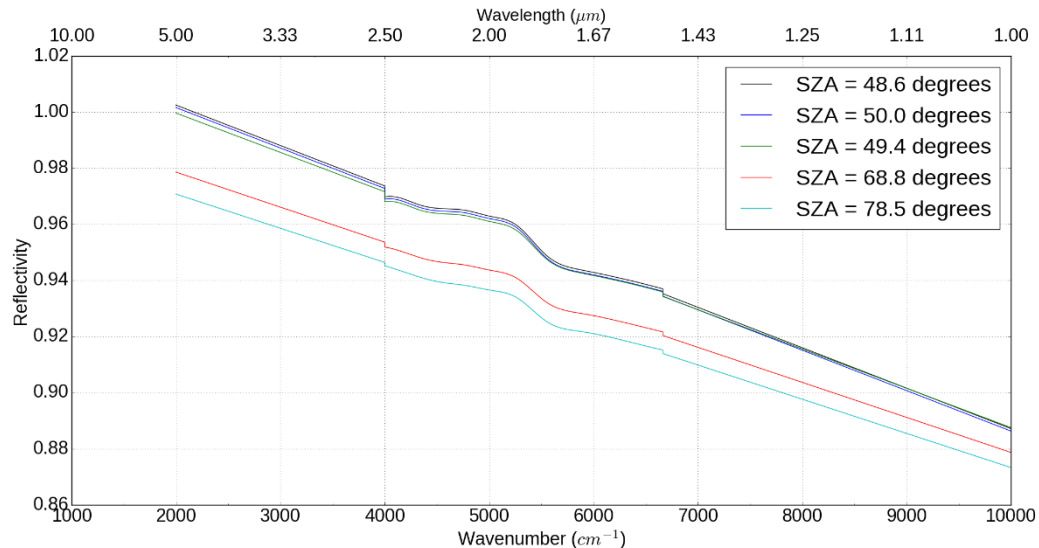


Figure 3.12: Mirror reflectivity function for different solar zenith angles. The region within 4000 - 6600 cm^{-1} is where the reflectivity is measured; outside this range is where the reflectivity is extrapolated.

The final major adjustment to the calibration is an adjustment to account for solar limb darkening. The solar disk is not uniform; the edges are significantly darker since the radiation has to travel through more of the solar atmosphere to reach Earth. As the temperature of the sun decreases with distance from the centre of the disk (in the photosphere), it follows that towards the edges one can only observe the lower temperature photons that are emitted from higher levels in the Sun, rather than higher temperature photons in the centre of the solar disk. An additional correction was applied, using the model of *Hestroffer and Magnan* [1998]. This correction is important, as the non-uniformity of the solar disk can introduce uncertainties on the order of 12% [*Gardiner et al.*, 2012]. The use of such a correction introduces an additional source of uncertainty; more details can be found in *Gardiner et al.* Since the measurements were taken close to solar minimum, the effect of sunspots is mitigated significantly, and thus solar variation is not considered as a contributor to the measurement uncertainty.

To assess the stability of the calibration over the course of the measurement campaign, a Transfer Standard Absolute Radiance Source (TSARS, e.g. *Pegrum et al.* [2004]) instrument was measured periodically, using the same optical setup as for the solar scans. The instrument is a simple integrating sphere, illuminated by external lamps. The source is known to be stable over short time periods (~5 hours) as measured by a filter radiometer at 800 nm [*Gardiner et al.*, 2012]. Less clear however is the stability of the instrument in the spectral region of interest, and the use of the TSARS as an adjustment to the calibration factors in e.g. *Menang et al.* [2013], contrary to the recommendation in Section 3(e) of *Gardiner et al.* [2012]. This is discussed in more detail in Section 3.4.4.1.

Figure 3.13 shows an uncalibrated measurement with the FTS; Figure 3.14a shows the calibration curve used to convert this into spectral irradiance and Figure 3.14b then shows the mirror reflectance correction used to further correct the spectrum (by dividing through by mirror reflectivity R). Figure 3.15 shows the final calibrated spectrum.

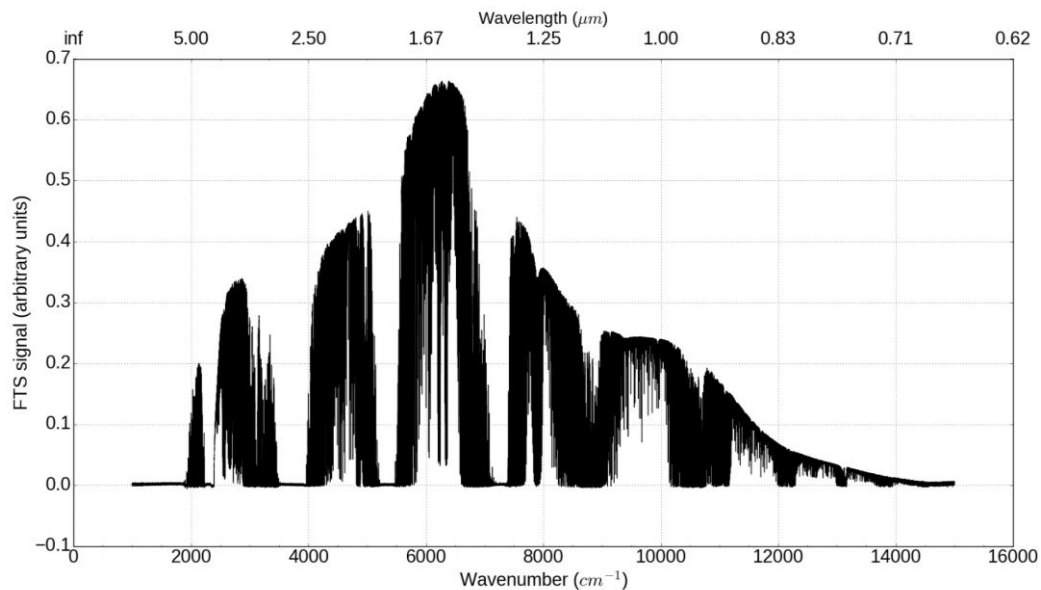


Figure 3.13: *Uncalibrated spectrum as measured directly by the FTIR at 10:51, 18 September 2008.*

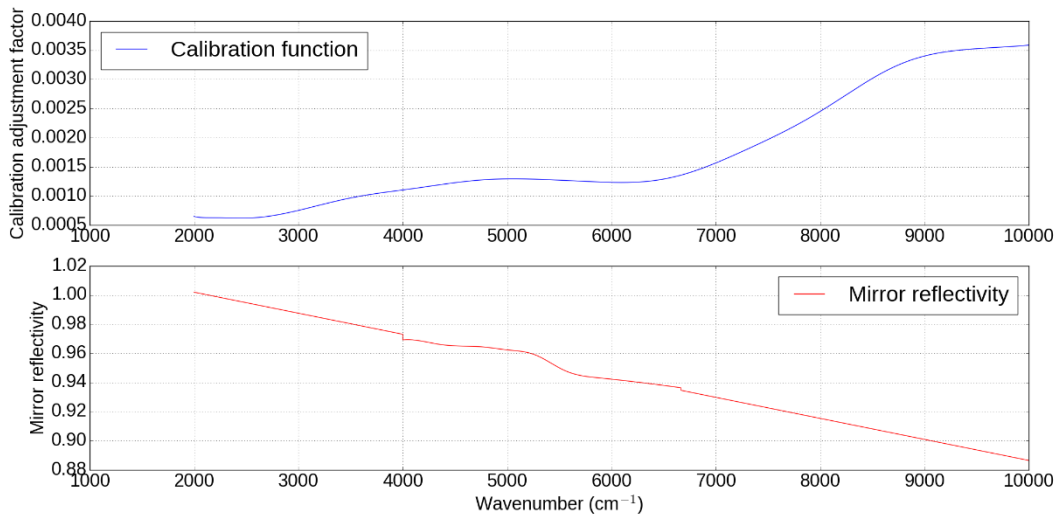


Figure 3.14: UHTBB calibration curve (upper plot) and mirror reflectivity correction function (lower plot) used to convert the spectrum from Figure 3.13 to that in Figure 3.15.

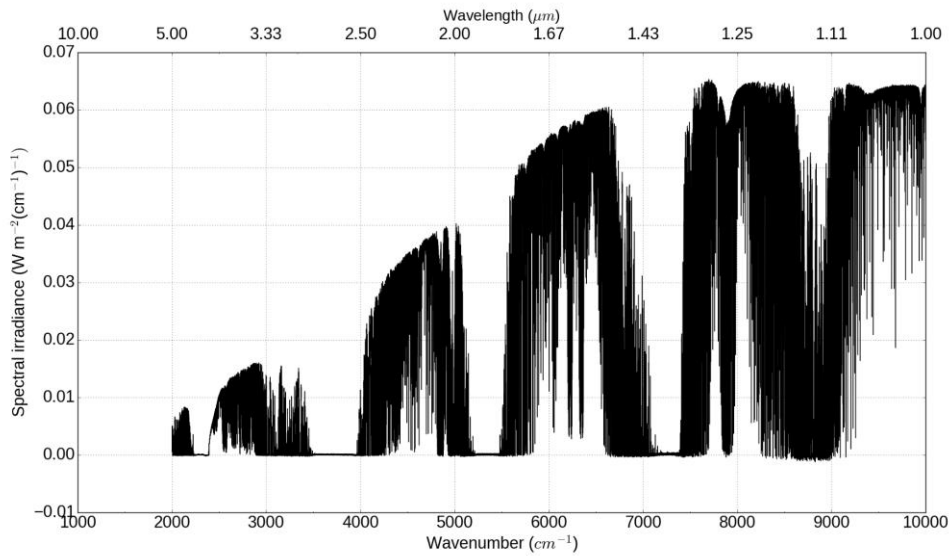


Figure 3.15: Final calibrated spectrum derived from Figs 3.15 and 3.16 (for 10:51, 18 September 2008).

3.4.3.4: FTIR uncertainty budget

The uncertainty budget for the FTIR measurements is made up of contributions from four primary sources; the external optics, the calibration to the UHTBB, uncertainties inherent to a solar measurement, and uncertainties within the FTIR system itself.

Table 3.3 shows the different contributions to the overall uncertainty budget. Figure 3.16 shows the relative contribution of each of these types of uncertainty as a

function of wavenumber, from *Gardiner et al.* [2012]. This reference provides a more exhaustive account of how these uncertainties were calculated.

Type	Source	Systematic or random?	Uncertainty (%)
Optics			
	Mirror ageing	Systematic	~1%, varies spectrally
	Humidity correction	Random	0.2%
	Alignment	Random	3%
	Apertures	Systematic	10 ⁻² %
UHTBB			
	Combined	Systematic	Varies spectrally
Solar measurements			
	Uniformity of solar disk	Random	0.4%
	Incident angle (reflectivity)	Systematic	1%
	Limb darkening	Random	0.04%
	Clouds	Random	1%
FTIR			
	Aperture	Systematic	10 ⁻² %
	Response	Systematic	1%
	Ice adsorption	n/a	n/a (0.1% in small region about 3300 cm ⁻¹)

	Calibration	Systematic	1%
--	-------------	------------	----

Table 3.3: Relative contribution of each of the four main types of uncertainty broken down into the constituent parts. Values are constant spectrally unless otherwise specified.

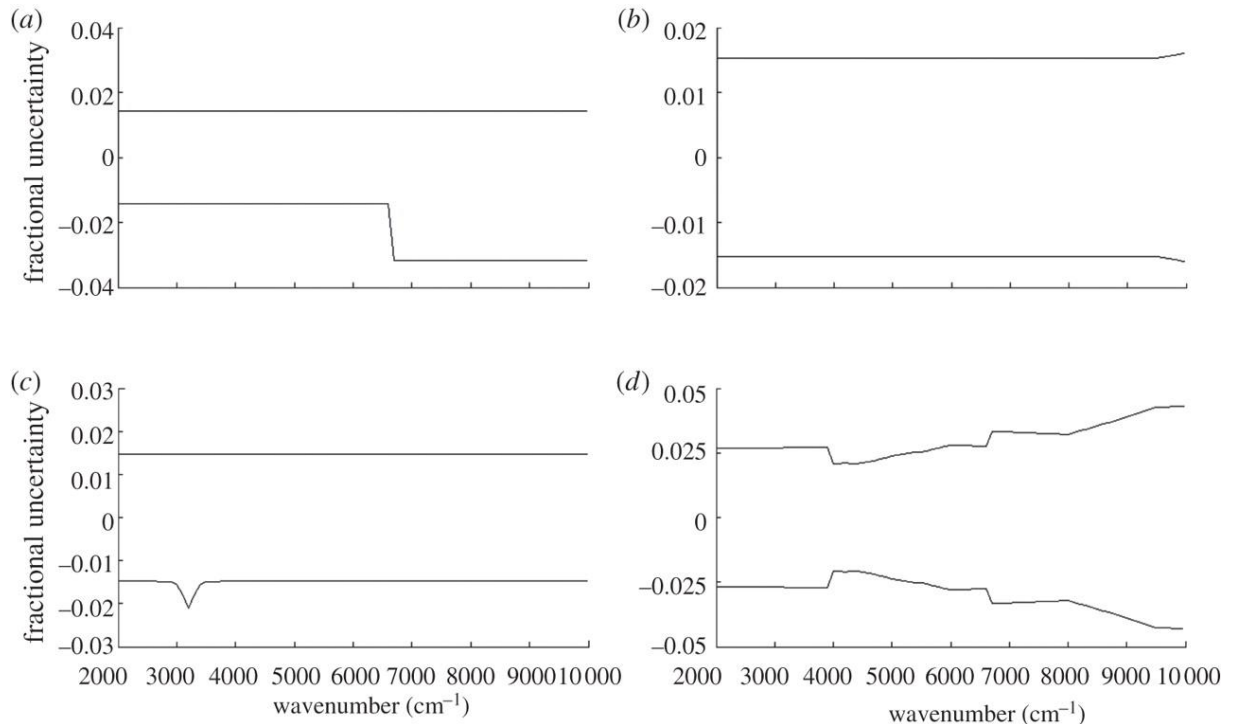


Figure 3.16: Fractional measurement uncertainty ($k = 1$) arising from the UHTBB (a), solar source (b), FTIR (c) and external optics (d) contributions. From Gardiner *et al.* [2012].

The uncertainties are either *random*, i.e. vary from measurement to measurement, or *systematic*, meaning that at least across the course of a day should remain constant. The division of errors from Table 3.3 was not considered in Gardiner *et al.* [2012]; this work was part of the PhD and necessary for the Monte Carlo analysis (see Section 3.3.7), since some types of error considered in Gardiner *et al.* [2012] are themselves partly random and partly systematic. Figure 3.17 shows the relative contribution of the random and systematic components to the measurement uncertainty. These are of roughly the same magnitude, which has consequences for the uncertainty in the Langley fits, since random effects contribute more to the uncertainty in the slope (optical depth), whereas systematic effects contribute more to uncertainty in the intercept (solar spectral irradiance).

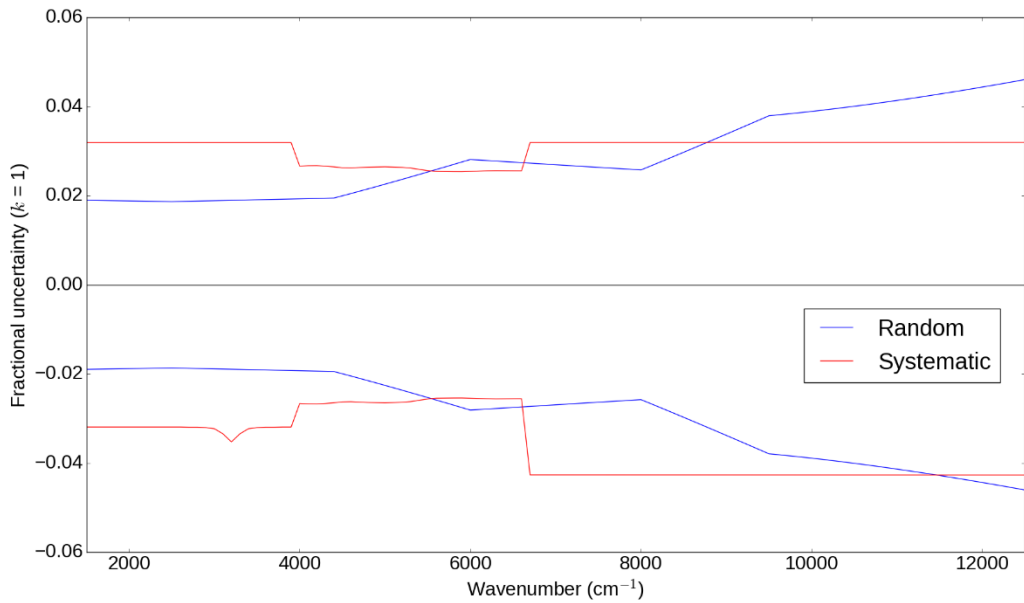


Figure 3.17: FTIR measurement uncertainty ($k = 1$) split into the contribution from random and systematic sources as a function of wavenumber.

Figure 3.18 shows the final uncertainty budget for an individual scan of the FTIR instrument. The small peak in the negative uncertainty at $\sim 3200 \text{ cm}^{-1}$ is a feature where ice can form inside the detector housing, as described in *Gardiner et al.* [2012]. Figure 3.19 shows an example spectrum from 18 September 2008, alongside this uncertainty (shown here at $k = 2$, 95% confidence interval). This uncertainty varies from 3.3% to 5.9% ($k = 1$). The increase at $\sim 6600 \text{ cm}^{-1}$ indicates the regime where the mirror reflectivity measurements are extrapolated rather than measured.

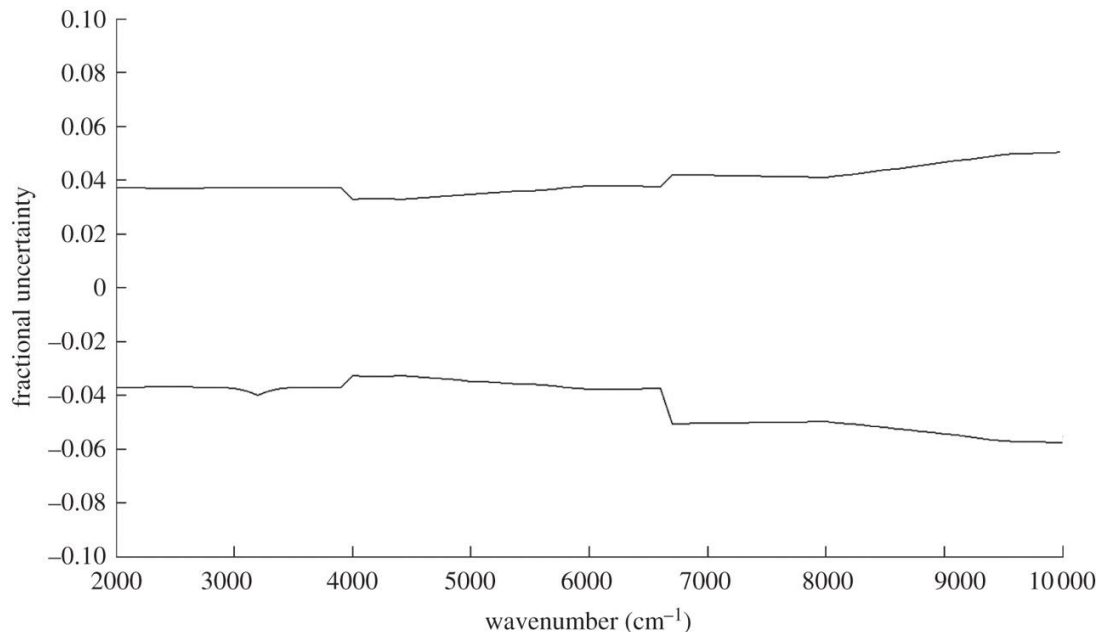
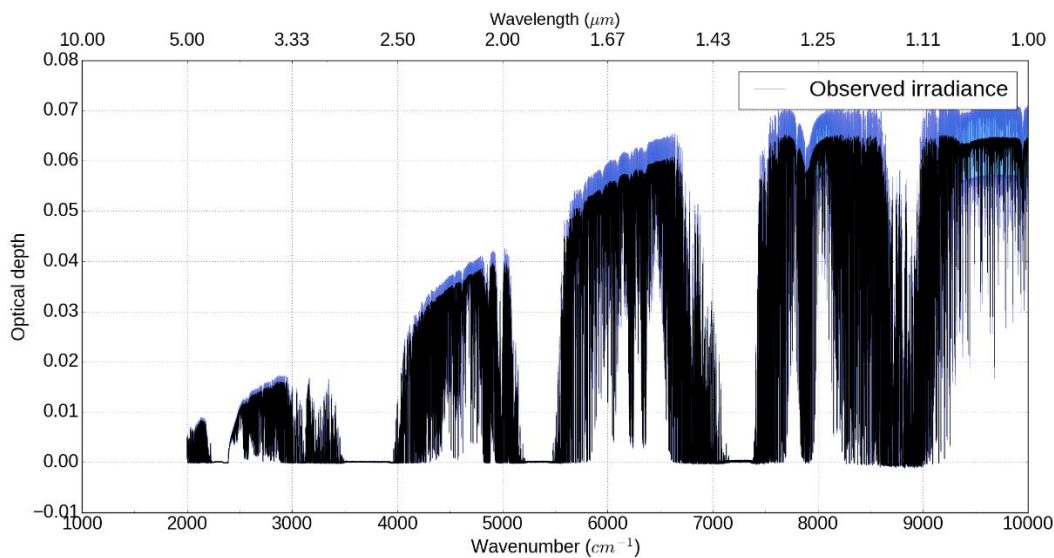


Figure 3.18: Overall FTIR uncertainty budget, from Gardiner et al. [2012].**Figure 3.19:** Spectrum from 11:24, 18 September 2008 with associated $k = 2$ uncertainties (blue shaded regions).

3.4.3.5: Smoothing and filtering of FTIR data

The FTIR data is subject to spectral filtering, to ensure that the derived continuum absorption in Chapter 5 is determined correctly, without contamination from e.g. incorrectly calculated absorption line positions. Data points that exceeded a given threshold (typically optical depth > 0.1) in *either* the observed data or the simulated data from a LBL code were rejected, to ensure that retrievals were only made in microwindows. This value was variable depending on the measurement day and the specific window, since each window and day has a different “baseline” depending on atmospheric conditions and spectral properties of the window.

Noise was detected in the optical depth measurements (see e.g. Figure 3.20); many of the instances of this noise coincided with lines in the solar spectrum (as measured in Chapter 4). This effect was present both in the Langley-derived spectra and the closure-derived spectra, indicating that it is not due to misattributed solar line positions in the chosen top of atmosphere spectrum. This may be due to some instrumental or physical effect involving a shift in the solar line positions. Regions $\sim 0.1 \text{ cm}^{-1}$ around solar lines are therefore filtered out to remove this effect, since it may have a small effect on the derived continuum even with filtering, if the offset is not equal either side of the baseline.

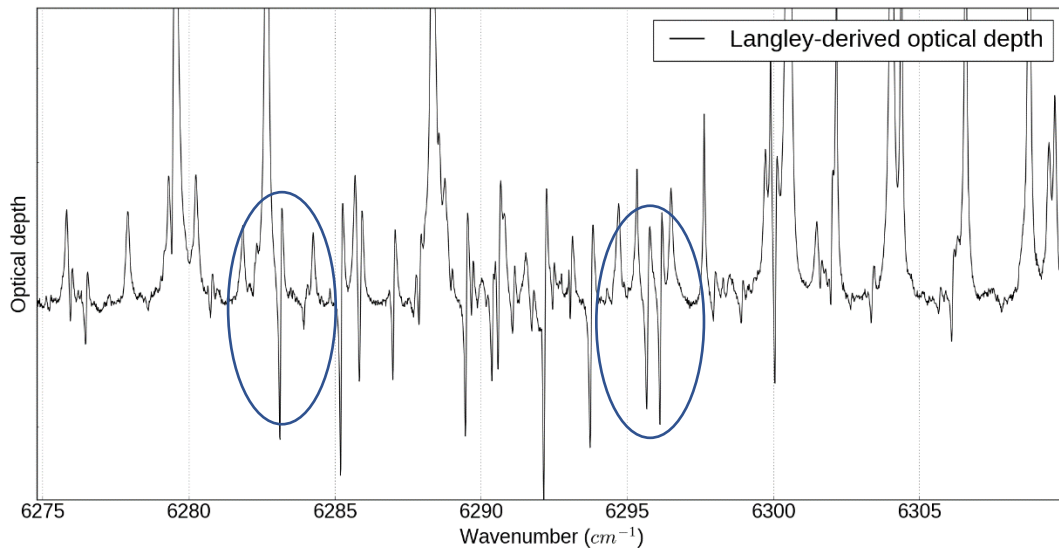


Figure 3.20: Noise detected in Langley measurements of optical depth arising (potentially) from shifting solar lines throughout a day (e.g. circled regions).

The data were then smoothed using a moving average filter over 15 cm^{-1} , to smooth out the effect of any weak solar or atmospheric lines with uncertain positions. If there is an offset, the residual of this offset should be 0, given sufficient smoothing and assuming the magnitude of the offset is equal either side of the baseline. Given the high resolution of these measurements, this step is necessary to derive a useful continuum without extremely high instrumental noise, since it is unlikely that the line-by-line code will be able to perfectly match up atmospheric line positions and broadening with the measurements. This smoothing also helps filter out any solar lines not accounted for by the solar filter, or indeed any other sources of high frequency spectral noise. This technique is suitable due to the low spectral variation of the continuum absorption.

3.4.4: Updates to calibration since *Gardiner et al.* [2012]

A significant portion of my PhD was spent on reassessing the instrument calibration relative to the calibration described in *Gardiner et al.* [2012], which was used in the work of *Menang et al.* [2013]. Together with the use of the Monte Carlo uncertainty evaluation method (Section 3.3.7), this led to a more confident uncertainty estimate with a proper consideration of the influence of random and systematic uncertainty upon the results.

3.4.4.1: TSARS stability

The largest change in the instrument calibration resulting from my PhD is the removal of the TSARS correction present in *Tallis et al.* [2011] and *Menang et al.* [2013]. The spectral drift present in the 22 August 2008 solar observations was also present in measurements of the TSARS on August 20. This was corrected for by multiplying the spectra by an adjustment factor (i.e. effectively recalibrating the instrument relative to the UHTBB calibration), determined from the ratio of the TSARS measurements at a given time close to the solar observations to the TSARS measurements at calibration.

This is problematic, since it assumes that a) the TSARS instrument is stable across the measurement campaign, which is not necessarily the case and b) that the TSARS is trustworthy enough to take priority over the UHTBB calibration, which was recommended not to be the case by *Gardiner et al.* [2012]. Figure 3.21 shows the ratio of the TSARS measurements over the measurement campaign relative to the TSARS measurements during calibration, i.e. the adjustment factors used in *Menang et al.* [2013]. In an ideal case, the TSARS measurements would be stable or slowly varying throughout the measurement campaign; however Figure 3.21 shows that this is clearly not the case. It is difficult to determine whether this drift is a result of the TSARS stability itself, or changes in the FTIR response. To assess whether the TSARS was generally stable enough for such an adjustment, observations during the calibration campaign were reanalysed.

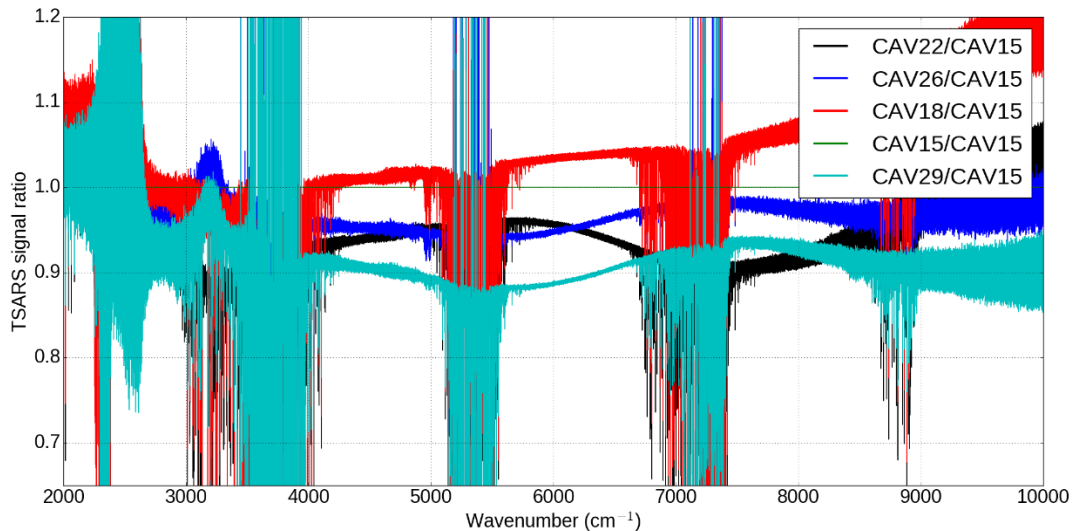


Figure 3.21: Ratio of TSARS measurements relative to a TSARS measurement from the pre-campaign calibration (CAV15). The black line (CAV22, corresponding the measurements of 22 August 2008) shows a spectral feature at 6600 cm^{-1} not present in the other spectra (a decrease in intensity on the high-wavenumber side of the window). See Table 3.2 for dates.

There was a relative dearth of measurements of the TSARS during the calibration phase before the Camborne measurements (CAV15 in Table 2); additional measurements would have helped assess its stability and allowed it to be a more useful source. There was one day during this calibration phase where TSARS measurements were made using the detector and optics used for the continuum measurements; the data from this day is shown in Figure 3.22. The observed signal from the TSARS is not particularly stable; it tends to vary both in amplitude and spectrally over the course of the calibration campaign (Figure 3.22). It additionally appears very sensitive to the alignment of the instrument optics, as shown in Figure 3.22; upon realignment, the intensity changed by up to 20%. This evidence was enough to reject the use of the TSARS as a calibration transfer as used in Tallis *et al.* [2011] and Menang *et al.* [2013]

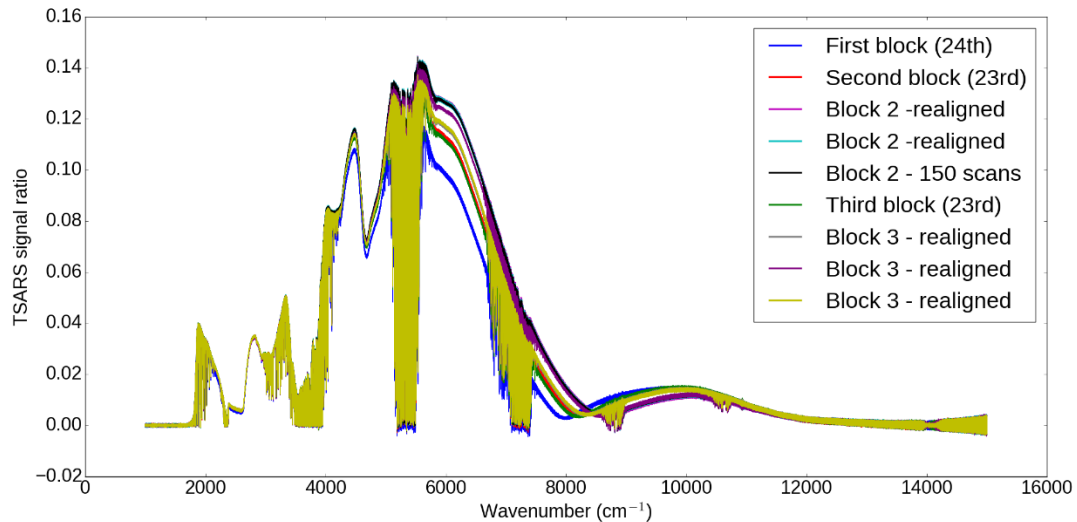


Figure 3.22: *Variability of TSARS measurements over a day, taken in 3 distinct blocks of several measurements.*

Due to the lack of a stable calibration transfer source (Section 3.4.4.1), it was decided that an additional source of uncertainty should be introduced to model the uncertainty in our calibration transfer. This was estimated as as 1% across the spectrum, after discussions with Tom Gardiner and Marc Coleman. This uncertainty was estimated based on experience using the FTS and the TSARS, and serves to make the uncertainty budget more conservative to account for the lack of calibration transfer. This 1% uncertainty does not significantly impact the uncertainty in the derived spectra, but adds additional uncertainty into the spectrum. This uncertainty is relatively small, since the solar spectra appear to be stable across the field campaign (with the exception of the 22 August 2008 observations). However, the need for such an uncertainty estimate emphasises the need for a more robust assessment of the calibration during the campaign, from a stable source. Chapter 7 goes into more detail on how this could be the case for a future measurement campaign.

3.4.4.2: Mirror reflectance calibration

As described in Section 3.4.3.1, the spectrometer is reliant on a set of tracker optics to divert the solar beam into the spectrometer. Since these mirrors are exposed to the elements, they become “used” over time, which results in a loss of reflectivity. An algorithm was written by Marc Coleman and Tom Gardiner at NPL and used in previous studies such as *Menang et al.* [2013]. This code was rewritten during my PhD and incorporated into my own retrieval software. It was found however that it

was not possible to reconcile my results with those of *Menang et al.* I later discovered a bug in the software in the *Menang et al.* software that removed this reflectivity correction, contrary to what was written in *Menang et al.* This results in a large offset out toward $\sim 10000 \text{ cm}^{-1}$ in the *Menang et al.* SSI that meant it was not reconcilable with other spectra (see Chapter 4). The application of this correction mitigates this significantly, with excellent agreement between various reference spectra and the updated CAVIAR spectrum in the 7000-10000 cm^{-1} region.

3.4.4.3: Phase correction

The issues with the spectra of 22 August 2008 and the corresponding TSARS spectrum (see Figure 3.21) motivated some work during my PhD on reassessing the phase correction used to transform the interferograms into spectra. It was hoped that adjustments to phase correction could remove some of the low frequency noise that seemed to adjust the shape of the spectrum, for example at $\sim 6600 \text{ cm}^{-1}$ in Figure 3.21 in the 22 August 2008 scans (this problem did not affect any of the other days). This was additionally motivated by the lack of documentation or ability to access the source code of the OPUS software used in the phase correction. *Chase* [1982] shows that the Mertz method can introduce significant spectral errors when using single-sided interferograms, such as those produced by the FTS in this work. These errors can be significantly mitigated using the Forman method (referred to as the symmetrisation-convolution method in the reference).

It was not immediately obvious that such an effect would arise from looking at the interferograms, which did not seem particularly different by eye to the CAV26 interferograms. A Mertz phase correction (see Section 3.2.4.3) was applied to these interferograms, and compared with the spectra directly taken from the OPUS software.

An attempt was made to perform the same analysis but using a convolution in interferogram space (the Forman method); however this was not completed as the focus of the PhD was changed shortly after attempting this.

Figure 3.23 shows the two spectra obtained via the two different phase correction methods, and Figure 3.24 the ratio of these spectra. The high frequency differences between these spectra could be explained by additional undocumented steps taken during the OPUS phase correction. The factor of ~ 4 difference between the phase

correction performed by myself and that from OPUS may be due to some electronic filtering or additional gain in the software that was not present in my own software.

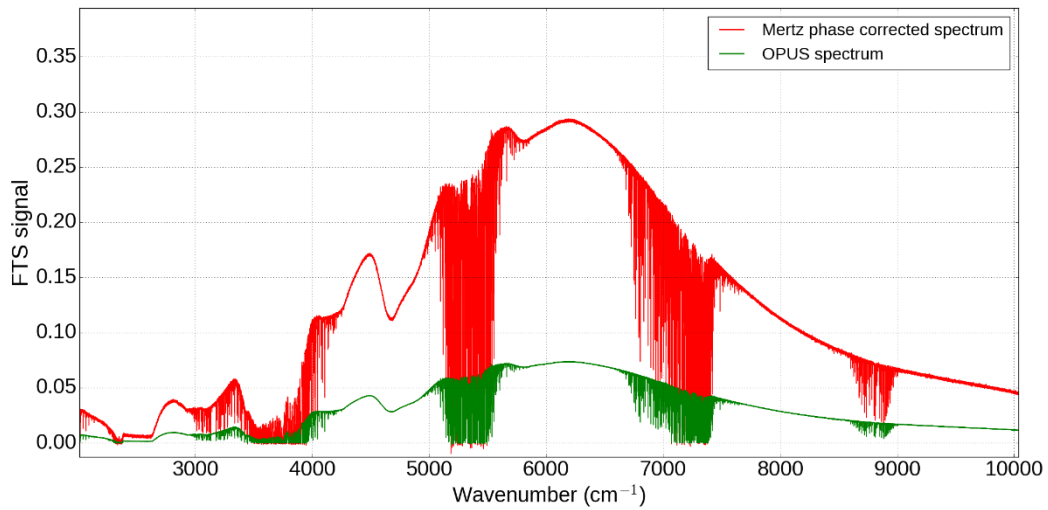


Figure 3.23: Spectra derived from the OPUS software (green) vs that from my own phase correction algorithm (red).

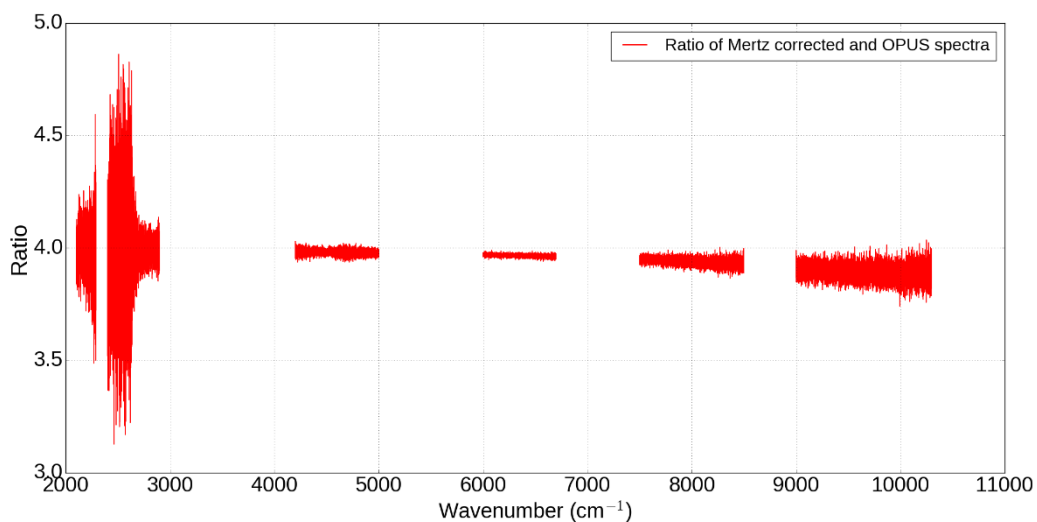


Figure 3.24: Ratio of the two spectra shown in Figure 3.23.

Future work would investigate this in more detail, as described in Chapter 7. However, it was decided to postpone this work during my PhD, to focus on the solar work presented in Chapter 4, given the advances in the literature that developed during my PhD.

3.4.5: Supplementary measurements

This section provides details about the additional measurements and data inputs used to characterise the atmospheric optical depth and assess the stability of the atmosphere across the course of a day.

3.4.5.1: Radiosonde ascents

Vertical profiles of atmospheric temperature, water vapour and pressure are necessary to determine the optical depth from spectral line absorption using a line-by-line code such as the RFM (Section 2.3.6). During the Camborne campaign, radiosonde ascents were performed at several times through each measurement day, both by the local UK Met Office synoptic site (twice daily, at 11:15 and 23:15) and specifically for the CAVIAR campaign. There was reasonable temporal coverage for the two days when Langley analysis was possible: four ascents on 22 August 2008 (05:00, 09:00, 11:15 and 16:00) and three on 18 September 2008 (09:00, 11:15 and 12:00), which covered the range of useful FTS observations for both days.

Additional radiosonde ascents were performed on other days, although these are less important since Langley analysis was not possible due to lack of temporal coverage with the FTS, and the observed AOD was generally higher on these days. Figure 3.25 shows the measured vertical profiles for 22 August 2008 at 11:15 (solid lines) and 18 September 2008 at 12:00 (dashed lines). Both days show similar temperature and pressure, but with somewhat different water vapour distributions. The sonde measurements go up to 15 km: regions above this are filled in using values from the US Standard atmosphere. The vast majority of the continuum comes from the troposphere (since this is where water vapour is concentrated), so this does not significantly affect the retrieval, but allows for some stratospheric lines to be resolved and included in the line-by-line simulations.

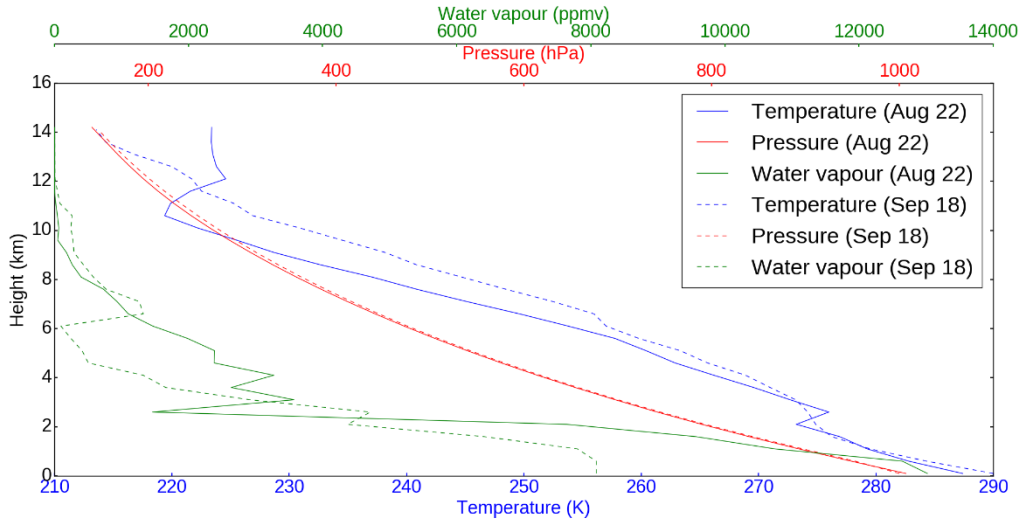


Figure 3.25: Vertical profile of temperature, water vapour and pressure for 22 August 2008, taken at 11:15 (solid lines) and 18 September 2008, taken at 12:00 (dashed lines) up to the highest point at which there were radiosonde measurements

Figure 3.26 shows the same profile, but extended up to the top of the atmosphere (only shown for 12:00 18 September 2008 in this case).

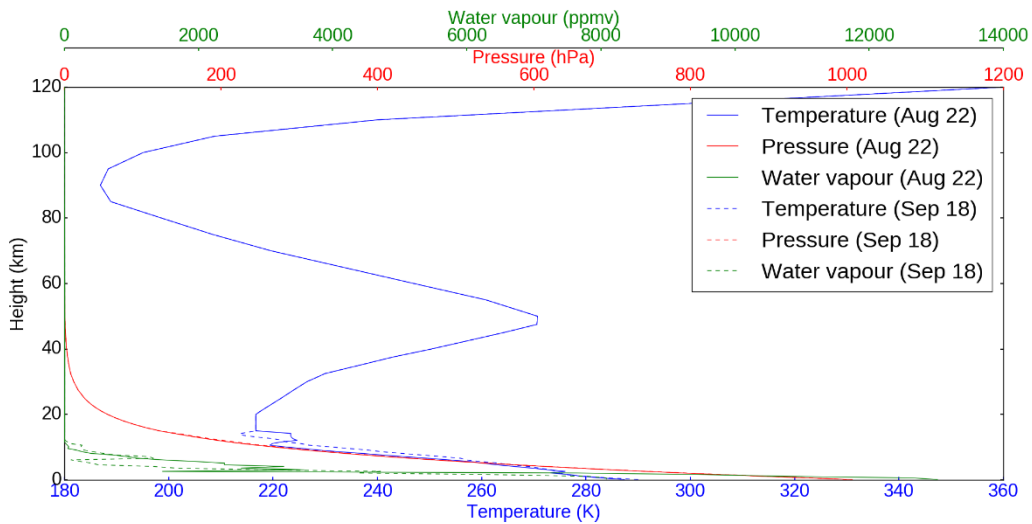


Figure 3.26: Vertical profile of temperature, water vapour and pressure for CAV25 (18 September 2008), taken at 12:00 (dashed lines) and CAV23 (22 August 2008, solid lines)

The radiosonde in question was a Vaisala RS92-SGP [Vaisala, 2013]. The atmospheric profiles are corrected for relative humidity bias using the correction of Miloshevich *et al.* [2009]. The stated uncertainty in the temperature profiles is ~0.5

°C, 5% in relative humidity and 1 hPa in pressure. An incorrectly reported value of one of these variables at a given level will result in an incorrect estimation of the broadening and strength of a given spectral line. In practice, the uncertainty from the LBL simulations is derived from sensitivity tests, with ~5% variations in each of these variables (in the RFM, this uses absolute humidity). This is conservative, given the stated uncertainty in the radiosonde manual. This does however allow us to account for additional sources of uncertainty, such as the uncertainty in the line broadening and strength in HITRAN, since this is not rigorously defined (see Section 2.3.6.2). Additionally, the radiosonde profile is not a true representation of the ray path to the spectrometer; the sonde ascends steadily with its horizontal motion, guided by the prevailing wind. This introduces additional uncertainty into the simulation.

Since the measurement is confined to microwindows between spectral lines, it is mostly the broadening which contributes to the continuum uncertainty. These uncertainties are small compared to those from aerosol scattering and the inherent measurement uncertainty from the FTS.

3.4.5.2: Microtops sunphotometer measurements

Coincident with the FTS observations were observations of aerosol optical depth using a Microtops II handheld sunphotometer [*Solar Light Company, 2001*]. This instrument uses 5 channels with a narrow FOV (2.5°), allowing for measurements of the solar disk. This should therefore provide an estimation of the AOD within the FOV of the spectrometer; while the sunphotometer has a larger FOV, there is unlikely to be significant amounts of diffuse radiation entering the instrument. The sky has a solid angle of 2π sr; integrating over the FOV of the sunphotometer gives a solid angle of 0.0005π sr. It is important to emphasise that the sunphotometer cannot discern between radiation that is unscattered and radiation that is forward scattered within the FOV of the instrument; both are treated in this case as not contributing to the AOD.

The wavelength channels are at 0.38, 0.44, 0.675, 0.936 and 1.02 μm ; the 1.02 μm channel is the most useful indicator of the AOD in the spectral region of interest. The AOD from these measurements is then extrapolated into the wavenumbers of interest via one of the two methods described in Section 3.3.5. Figure 3.27 shows AOD over

time for the two most relevant days of measurement, 22 August 2008 and 18 September 2008. There is variation in both days, with a maximum at around 0.08 in both, dropping off to about 0.04 at noon. This could potentially indicate some zenith angle-dependent bias. These numbers are small in absolute terms (they have very little effect on the derived SSI), but are large enough to cause issues for a continuum derivation or a Langley analysis in mostly transparent spectral window regions. These numbers are smaller in the wavenumbers of interest however, since the aerosol extinction drops off with decreasing wavenumber. The uncertainty of the sunphotometer is not explicitly stated in the Microtops user manual, although literature values (e.g. *Ichoku et al.* [2002]) estimate an optical depth uncertainty of $\sim \pm 0.02$ in the lower wavenumber channels and ± 0.01 or less in the higher wavenumber channels.

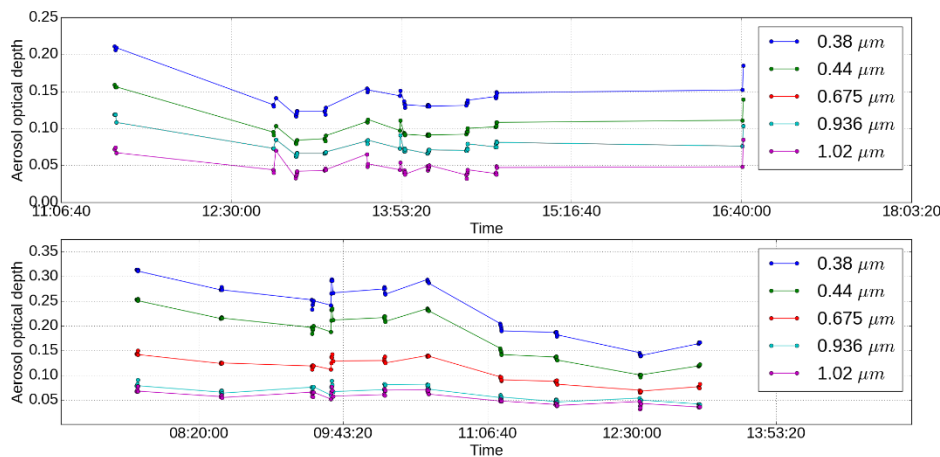


Figure 3.27: AOD over time for 22 August 2008 (upper panel) and 18 September 2008 (lower panel) for each of the 5 wavelength channels.

The aerosol measurements from 22 August 2008 have less variation between the wavenumber channels than those of 18 September 2008; this means that the AOD drops off less quickly with decreasing wavenumber, leading to larger AOD in the spectral region of interest than that of 18 September 2008. This, along with the problems due to spectral drift shown in the 22 August 2008 solar measurements are the major reasons why the observations of 18 September 2008 are preferred.

One problem with this however is the large (relative) temporal variation in AOD from the start to the end of the day on 18 September 2008. Figure 3.28 shows the temporal variation of the AOD from the spectrometer, the combined aerosol +

continuum absorption derived using the FTS, the integrated water vapour from the HATPRO instrument (see Section 3.4.5.3) and water vapour absorption derived from the line-by-line code in a microwindow and in a water vapour spectral line. This temporal variation in AOD (the drop off from start to end) is not seen in the spectrometer measurements (which lie mostly flat), and given the constancy of the water vapour amount (especially given the assumption that the continuum strength is lower than the AOD), this variation cannot be explained by the AOD. Given the robust calibration and checking used to ensure that the FTIR scans were not affected by changing conditions, the robustness of the Microtops measurements was called into question.

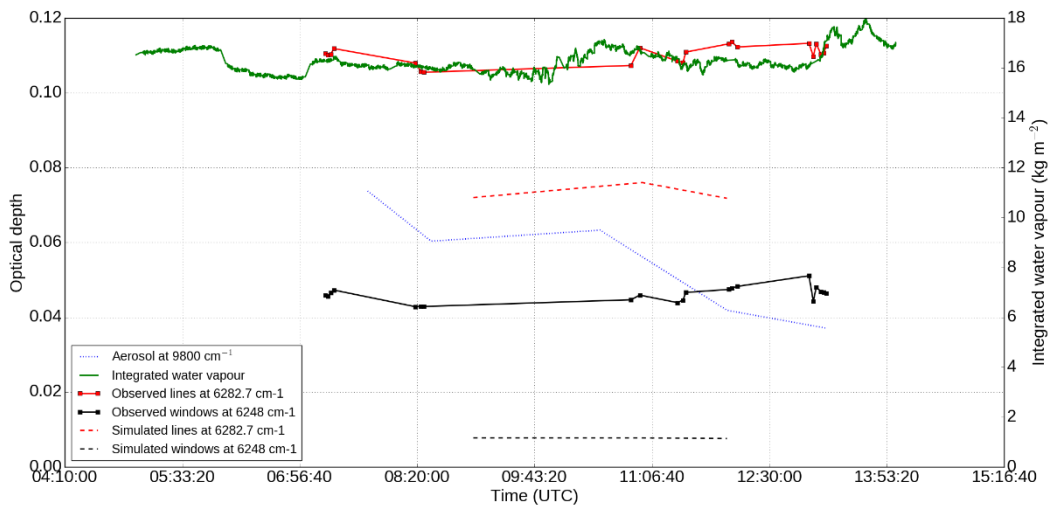


Figure 3.28: Time variation of water vapour from the HATPRO, simulated and observed water vapour optical depths from a microwindow and a line in the $1.6 \mu\text{m}$ window and aerosol optical depth at 10000 cm^{-1} . All values are taken for 18 September 2008. The uncertainty in the aerosol is $\sim \pm 0.01$, and on the FTS measurements is $\sim \pm 0.005$.

It was decided that the best way to treat the AOD would be to use a daily average, given the lack of reconcilability between the time-resolved FTIR and Microtops measurements. The variation in AOD is represented as an increased uncertainty in the aerosol optical depth used to derive the continuum. This is achieved via sensitivity tests of the Mie scattering code using the range of extinction at $1 \mu\text{m}$. Chapter 7 explains in more detail how this procedure could have been improved, and what observations may be necessary to do this.

Figure 3.29 shows the AOD used to derive the continuum using the Langley method for both 22 August 2008 and 18 September 2008. This was derived ultimately using the Mie scattering code, since this allowed for a more conservative estimate of the uncertainty and a physical extrapolation of the aerosol optical depth.

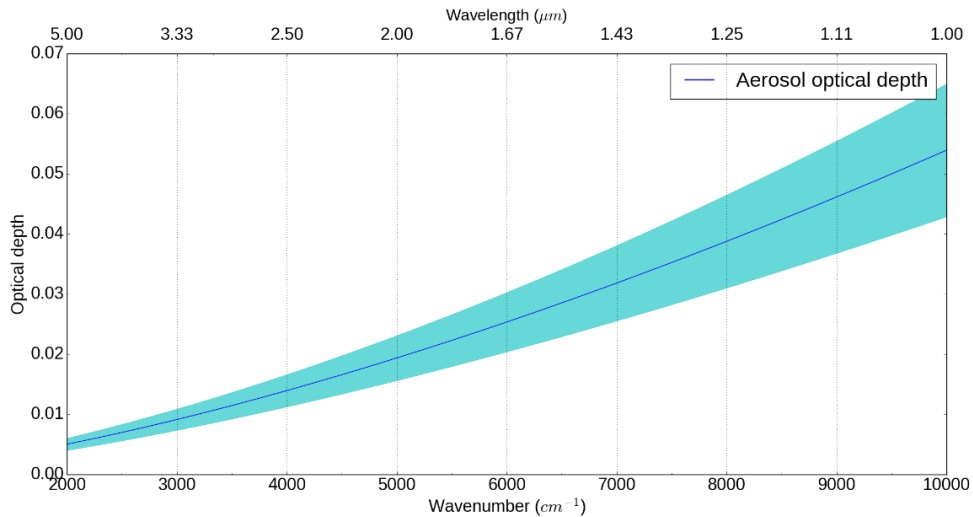


Figure 3.29: Final AOD values used to derive the water vapour continuum using the Langley method, with corresponding uncertainties.

3.4.5.3: HATPRO microwave radiometer

In addition to the radiosonde measurements, atmospheric water vapour was also measured using a HATPRO [Rose and Czekala, 2009] microwave radiometer. This was used to measure integrated water vapour across the course of the day. This is used as a cross-check to the radiosonde measurements, to ensure that there are no changes across the course of a day not picked up by the radiosonde, or spikes in the measurements over small time scales (e.g. during an FTS scan). This is shown for 18 September 2008 in Figure 3.28.

3.4.5.4: FAAM aircraft data

During the Camborne and Jungfraujoch campaigns, the Facility for Airborne Atmospheric Measurements (FAAM) aircraft was launched, making coincident measurements of temperature, water vapour and pressure, as well as aerosol measurements from the Passive Cavity Aerosol Spectrometer Probe (PCASP) instrument. In general, these measurements were not used however. The atmospheric profile derived from the aircraft are more uncertain and not as representative of the measurement conditions as the radiosonde profiles, since the aircraft takes a much

longer time to measure this profile compared to a radiosonde. There were dropsondes released from the aircraft, but these were not co-located with the radiosonde or the spectrometer and thus are not as robust as the sonde ascents.

The PCASP observations could ostensibly provide information about aerosol size distribution and number concentration for use in the Mie scattering code, although not aerosol composition (which is required for determining aerosol optical depth). After some exploratory work it was determined that this data would not be useful, due to the difficulties in implementing it into the model. The data proved to be very noisy and did not provide any insight into how the FTS spectra might be affected by aerosol, unlike the sunphotometer measurements. In addition, the PCASP measures aerosol that has been dried as it enters the inlets of the instrument. This would necessitate a correction for ambient relative humidity based on assumptions to provide meaningful results for this work.

3.4.5.5: Model reanalyses

ECMWF and Met Office reanalysis data exists for the Camborne site, and was used previously as a cross-check with the radiosonde ascents (e.g. *Tallis et al.* [2011]). This data was available for the entire measurement campaign but is not as useful as the radiosonde data due to the lower vertical and temporal resolution. As such, these data were used as a cross-check to ensure that the radiosonde values were reasonable (i.e. did not differ significantly from the reanalysis), but not included in any analysis.

Chapter 4:

Accurate measurements of NIR solar spectral irradiance between 4000-10000 cm⁻¹

4.1: Introduction

This Chapter consists of an analysis of the measurements described in Chapter 3; in this case to observe the (top of atmosphere) solar spectral irradiance (SSI). This work was published in *Geophysical Research Letters* [Elsey *et al.*, 2017], and is reproduced here as the bulk of Chapter 4 of this thesis (Section 4.2). The Supplementary to this work has been merged into the body of the text where appropriate to aid the narrative flow of the Chapter. Additional references to other Chapters of the thesis have been inserted as appropriate. Figure and Section headings have been changed for consistency with the format used in the rest of the thesis, and references are merged into the References section at the end of the thesis. The SSI data is available as Supplementary to the paper; a link has been provided to this in the body of the text. Spellings have been changed from American English to British English where appropriate. Minor edits have been made to improve the readability of the Chapter, and to fix some minor issues with the paper. Some of the methods described in Section 4.2.3 are repetitions of those presented in Chapter 3; these are left as is to not disrupt the flow of the manuscript.

The end result of this chapter is an updated version of the CAVIAR solar spectrum derived in *Menang et al.* [2013]. This work was motivated by the updates to the uncertainty budget and calibration detailed in Chapter 3, the work of *Thuillier et al.* [2015] and *Bolseé et al.* [2014], and the need to accurately constrain SSI to observe atmospheric optical depth via the closure method.

The work contained within the paper was performed and written up by myself (Jon Elsey) over the course of my PhD, with guidance and comments from the co-authors Keith Shine (UoR), Tom Gardiner and Marc Coleman (NPL). I was both lead author and corresponding author on this work and led the responses to the reviewers' comments. Revisions to this paper were also performed by myself, with valuable

advice and discussion from the co-authors. All figures and data were generated by myself. The original measurements used in this work were taken by Tom Gardiner, Marc Coleman and Liam Tallis in 2008 during the CAVIAR project, on which Keith Shine was the Principal Investigator.

The published manuscript, alongside a plain-language summary can be found via the following reference.

4.2: Paper manuscript

Elsey, J., Coleman, M. D., Gardiner, T., & Shine, K. P. [2017]. Can measurements of the near-infrared solar spectral irradiance be reconciled? A new ground-based assessment between 4,000 and 10,000 cm^{-1} . *Geophysical Research Letters*, 44, 10,071–10,080. <https://doi.org/10.1002/2017GL073902>

In addition to the published paper, Section 4.3 of this Chapter presents some additional work comparing this analysis with more recent results.

Can measurements of the near-infrared solar spectral irradiance be reconciled? A new ground-based assessment between 4000-10000 cm⁻¹

Jonathan Elsey¹, Marc D. Coleman², Tom Gardiner², Keith P. Shine¹

¹ Department of Meteorology, University of Reading, Earley Gate, Reading, RG6 6BB, UK

² National Physical Laboratory, Teddington, Middlesex, TW11 0LW, UK

Corresponding author: J. Elsey, (j.elsey@pgr.reading.ac.uk)

Key Points:

- In light of continuing disagreement in observations of near-infrared solar spectral irradiance (SSI), we present a new SSI with full uncertainty evaluation
- This SSI shows good agreement with the commonly-used ATLAS3 SSI at shorter wavelengths, but is ~7% lower at longer wavelengths
- This discrepancy is significant since the near-infrared contains several strong water vapour bands, which influence the atmospheric energy budget

Abstract

The near-infrared solar spectral irradiance (SSI) is of vital importance for understanding the Earth's radiation budget, and in Earth observation applications. Differences between previously published solar spectra (including the commonly-used ATLAS-3 spectrum) reach up to 10% at the low-wavenumber end of the 4000-10000 cm⁻¹ (2.5 – 1 μm) spectral region. The implications for the atmospheric sciences are significant, since this spectral region contains 25% of the incoming total solar irradiance. This work details an updated analysis of the CAVIAR SSI, featuring additional analysis techniques and an updated uncertainty budget using a Monte Carlo method. We report good consistency with ATLAS3 in the 7000-10000 cm⁻¹ region where the calibration of ATLAS3 is more certain, but ~7% lower in the 4000-7000 cm⁻¹ region, in general agreement with several other analyses.

4.2.1 Introduction

The top of atmosphere incoming solar spectral irradiance (SSI) is identified by the Global Climate Observing System as an “essential climate variable” [Bojinski *et al.*, 2014]. It is the primary driver of meteorological processes, through absorption and scattering of radiation [Stephens *et al.*, 2012]. It is therefore essential to ensure that this quantity is well constrained.

Observations of SSI have been performed over the last 50 years (for example, the pioneering airborne study of Arvesen *et al.* [1969]). Many recent SSI measurements (primarily from space-based instruments) have focused on ultraviolet wavelengths, since these are difficult to measure on Earth due to absorption by oxygen and ozone in the stratosphere and mesosphere (e.g. Fligge *et al.* [2001]), and the large variation in the UV over the 11-year solar cycle [Fröhlich and Lean, 2004]. There has been a comparative dearth in measurements of spectral region between 4000-10000 cm⁻¹ (2.5-1 μm, henceforth referred to as the near-infrared (NIR)), due to the difficulty in maintaining the stability or sensitivity of space-borne spectroradiometers. About 25% of the Sun’s energy reaches Earth in this spectral region, which makes it important for quantifying the global energy budget, particularly since it is home to several strong water vapour, CO₂ and other absorption bands. Many meteorological models use the semi-empirical spectrum from Kurucz and Bell [1995], e.g. Walters *et al.* [2014]. Such solar models derive directly the line structure and spectral envelope, and tie these to observations. The Kurucz and Bell spectrum shows a similar absolute level to the ATLAS3 (ATmospheric Laboratory for Applications and Science) spectrum from Thuillier *et al.* [2003]. This is an issue however, as recent measurements report a NIR SSI which is up to 8% lower than ATLAS3 (see Section 4.2.2 for details).

This controversy has primarily manifested itself in the solar physics literature, but it is of significant importance for the understanding of atmospheric processes, as SSI is a vital input into radiative transfer schemes used in climate and weather models, and in passive remote sensing systems such as MODIS (MODerate Imaging Spectroradiometer, [Thome *et al.*, 2001; Platnick and Fontenla, 2008]). For example, Menang and Shine [2013] found that using different NIR SSI from recent observations leads to ~8% differences in atmospheric absorption and heating rates. It

is therefore important to measure the SSI as accurately as possible from a number of independent sources. This work presents an update to the CAVIAR (Continuum Absorption in the Visible and Infrared and its Atmospheric Relevance) SSI [Menang *et al.*, 2013], in an attempt to reconcile these differences.

4.2.2 Current state of measurements

Most modern measurements of SSI are either performed at ground sites, or using airborne or space-based instrumentation. The first such campaign was the pioneering study by *Arvesen et al.* [1969], using an aircraft-based spectrometer measuring across the spectrum from the ultraviolet to the near-IR. Typically however, these efforts have largely focused on the visible and ultraviolet parts of the spectrum. A major step forward in measuring the NIR SSI from space was the ATLAS3 spectrum from *Thuillier et al.* [2003], which presented SSI out to 2.4 μm . This was developed using measurements from the SOLSPEC (SOLAR SPECTrometer) instrument, and was used to constrain the SSI derived from semi-empirical models of the photosphere (e.g. *Fontenla et al.* [2006]). Figure 4.1 shows the fractional deviations of some recent spectra (including ATLAS3) from the result presented in Section 4.2.5 of this work and the associated coverage factor $k = 2$ (95% confidence) uncertainty limits of each. There is consistency between CAVIAR2, ATLAS3 and the other spectra shown between 7000-10000 cm^{-1} (1.4-1 μm) but this is not the case from 4000-7000 cm^{-1} (2.5-1.4 μm). This emphasises the lack of consensus between ATLAS3 and alternative sources, where deviations vary between 5-10% over large portions of the spectrum, and exceed the quoted $k = 2$ measurement uncertainties. There is however better agreement between several of the other spectra, the impact of which will be discussed later.

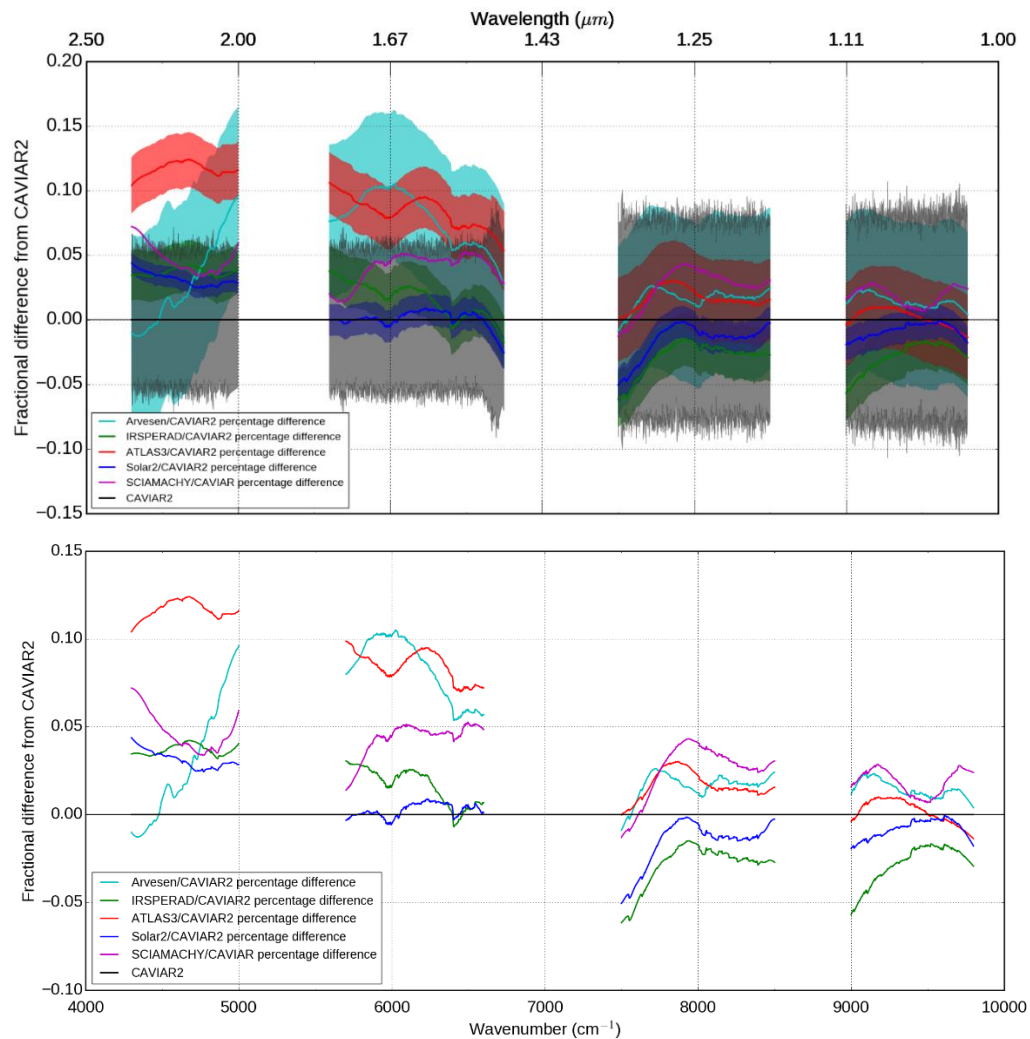


Figure 4.1: Fractional deviation of various solar spectra from the CAVIAR2 spectrum derived in this work, with and without uncertainties (upper and lower panels respectively). The shaded regions (upper panel) show the reported $k = 2$ uncertainties associated with each spectrum. The gaps are regions in which water vapour absorption is too high to retrieve the spectrum from the ground. These spectra have been smoothed over 15 cm^{-1} , to remove the effect of solar lines which are present in the original CAVIAR2 high-resolution measurements.

Aside from ATLAS3, of particular interest here are the spectra obtained from Thuillier *et al.* [2014], henceforth referred to as Solar2, and that from Bolsée *et al.* [2014]. The Solar2 spectrum was obtained using SOLSPEC (an updated version of the instrument used for ATLAS3). This spectrum was taken using measurements made immediately after the instrument was launched into space, and therefore closest in time to its absolute calibration (performed using a 3000 K blackbody). This

spectrum was ~8% lower than ATLAS3 between 2.5-1.6 μm . A reanalysis of this data (Solar2rev) was presented in *Thuillier et al.* [2015], and was in better agreement with ATLAS3; *Thuillier et al.* [2015] state that they believe ATLAS3 to be more reliable than either spectrum. This adjustment of Solar2 was justified by readings of the low-power tungsten ribbon lamp used to assess calibration drift in-flight; the signal obtained using this lamp reached an “equilibrium” state two years after launch, closely matching the signal observed during pre-flight calibration. [*Thuillier et al.*, 2015] note that they “have no clear explanation” for the drift and note that “it is most likely due to some temperature effect and/or the outgassing of the instrument” (see *BenMoussa et al.* [2013] for details on how this may occur). The justification used by *Thuillier et al.* [2015] to favour ATLAS3 over Solar2 has caused controversy (*Weber* [2015]; *Bolsée et al.* [2016]). This represents an issue with the reliance on space-based measurements of SSI, since the calibration and optical setup of these instruments is more difficult to reliably assess compared to those on the ground. Space-based measurements do in principle provide the best form of SSI measurement, as neither use of a radiative transfer model (RTM) or measurements with varying solar zenith angle (SZA) are required; achieving this in practice however is extremely difficult. This is illustrated by the disagreements in the processing of the SOLSPEC data. Also, as shown in *Harder et al.* [2010], SIM (Spectral Irradiance Monitor) measurements (used for example in *Coddington et al.* [2015]) are 8% lower than ATLAS3 at wavelengths higher than 1.5 μm ; the SIM spectrum is adjusted in this region to agree with ATLAS3. The authors stated justification for this adjustment is that the uncertainty in SIM is higher than that in ATLAS3. Hence, the data from SIM is not independent from ATLAS3 (and is therefore not shown in Figure 4.1). SSI data from the SCIAMACHY (Scanning Imaging Absorption Spectrometer for Atmospheric Chartography/Chemistry) satellite instrument [*Weber*, 2015] is also lower than ATLAS3 at 1.6 μm , with a spectral shape broadly consistent with Solar2. *Weber* [2015] shows that the SCIAMACHY spectra are all consistent with one another in this region, contrary to the claims of *Thuillier et al.* [2015].

There is agreement between the airborne spectrum of *Arvesen et al.* [1969] and ATLAS3 at ~1.6 μm , with better agreement with CAVIAR2 toward 2.5 μm . The degree of this agreement changes strongly with wavenumber however, and at 2.4 μm

there is no agreement between ATLAS3 and *Arvesen et al.* even within the $k = 2$ uncertainties. The *Arvesen et al.* analysis uses the Langley method, but the variation with solar zenith angle was derived from measurements made on different days and at markedly different locations. Thus, the effect of varying water vapour may have large implications for their derived SSI, particularly in the band regions of strong absorption. The *Arvesen et al.* measurements also predict a total solar irradiance (TSI) of 1390 W m^{-2} , above the 1360 W m^{-2} from contemporary sources [*Kopp and Lean, 2011*]. Accounting for this difference by normalizing the Arvesen data to 1360 cm^{-1} would bring their values closer toward agreement with CAVIAR2 between $2.5\text{-}1.4 \mu\text{m}$, assuming that the $1390 \rightarrow 1360 \text{ W m}^{-2}$ adjustment factor was applied evenly across the spectrum. It is important to emphasise here that, within the uncertainties, there is consistency between *Arvesen et al.* and CAVIAR2 in the entire $4000\text{-}10000 \text{ cm}^{-1}$ range.

Bolsée et al. [2014] presented an additional set of measurements from a ground-based spectrometer at the Izaña field site (henceforth referred to as IRSPERAD (InfraRed SPectroRADiometer)). This spectrum (see Figure 4.1) was found to be in modest agreement at $1.6 \mu\text{m}$ with the lower (Solar2) values of the solar irradiance reported in *Thuillier et al.* [2014]. At lower wavenumbers, these also agreed with the similar ground-based measurements of *Menang et al.* [2013], using an absolutely calibrated high-resolution spectrometer.

There are several drawbacks with the use of ground-based instruments. However, these can be mitigated through the careful use of various techniques such as the Langley method, or the use of a radiative transfer code, provided they are applied in relatively transparent regions between major atmospheric absorption bands. *Thuillier et al.* [2015] suggests that the use of ground-based methods could lead to incorrect SSI values because of “residual atmosphere absorption and aerosol scattering that consequently can make ground measurements necessarily lower than the space measurements”. We demonstrate here that this is not the case. Aerosol scattering is the most important source of extinction in the micro-windows in between individual spectral lines in this region, typically contributing up to 90% of the overall optical depth in the centre of the $1.6 \mu\text{m}$ window. However, the absolute value is small (on the order of 0.03 optical depths), and therefore has minimal effect on SSI retrievals. In our case, any changes in aerosol optical depth are automatically accounted for in

the Langley method if the atmospheric state is constant throughout a day of measurements, or incorporated into the uncertainty budget from the Monte Carlo method (see Section 4.2.4 for more details).

Scattering by water vapour and other gases also affects the observed radiation. This Rayleigh scattering can be calculated easily in the NIR. *Bucholtz* [1995] shows that for a mid-latitude summer atmosphere (comparable to the conditions in this work), the Rayleigh scattering optical depth is 8.67×10^{-3} at $1 \mu\text{m}$, reducing to 1.315×10^{-3} at $1.6 \mu\text{m}$. This is less than 5% of the overall optical depth in the centre of this window and does not significantly vary over the course of a day; any impact on the derived SSI will be minimal.

Similarly, absorption due to water vapour in the atmospheric windows has minimal effect on SSI. *Menang et al.* [2013] demonstrated that even for a 20% systematic change in absolute humidity over the course of a day, the effect on the derived SSI in the windows is less than 1%.

It is important to emphasise that if the optical depth contributions from any of these effects are constant throughout a day, then they will be removed by the Langley method (see Section 4.2.4.1). Variability can be detected via changes in the observed direct current voltage by the FTS detector (see Section 3.4.3.1) and filtered out, or can be included within the statistical uncertainty estimates. The estimates presented in the last paragraph apply to the sea-level Camborne field site used here and in *Menang et al.* [2013]; the high-altitude field site used by *Bolsée et al.* [2014] is less affected. We also note that the optical depth from aerosol and Rayleigh scattering is strongly wavenumber dependent, and is largest at the higher wavenumbers ($7000\text{--}10000 \text{ cm}^{-1}$) where we show that the various spectra agree well (Figure 4.1).

An additional advantage of ground-based measurements is the high spectral resolution that can be achieved. For example, *Gardiner et al.* [2012] (see Section 3.4.3.2) presents a calibration method suitable for measurements of the Sun at the 0.03 cm^{-1} resolution presented in this work. By contrast, SOLSPEC has a resolution of 4 cm^{-1} at $1 \mu\text{m}$. The optical alignment of a ground-based setup can also be constantly monitored and adjusted, in a way which is generally difficult on a satellite. There is also more scope for assessing the calibration drift of a ground-based instrument.

The lack of agreement in the near-IR SSI amongst the various datasets (both space and ground-based) is clearly a serious issue. Accepting that there are advantages and disadvantages of all observing systems, there is nevertheless a requirement that they should agree within their respective uncertainties, and that agreement between independent measurements gives the most confidence in any result. This is clearly not the case at present. We present an improved and extended analysis of the high spectral resolution CAVIAR SSI values from *Menang et al.* [2013], in light of the ongoing controversy, using an updated calibration and assessment of the uncertainty budget, and an additional method of deriving SSI.

4.2.3 Analysis methods

Section 4.2.5 will focus on two methods of deriving SSI from a ground-based setup; the Langley method and the radiative closure method. These methods have their own distinct advantages and disadvantages, and together provide a quasi-independent assessment of SSI even when using the same observations. To increase the confidence in these methods, it is ideal to use measurements from as many days as possible and to constrain the atmospheric state to minimise the effect of changes throughout a day, particularly in the case of the Langley method.

The irradiance reaching the surface from the Sun is described by the Beer-Bouguer-Lambert law

$$(4.1) \quad I(\nu) = I_0(\nu) \exp(-m(\theta)\tau(\nu))$$

where ν is spectral wavenumber, I is the irradiance measured at the surface, I_0 is SSI, τ is the atmospheric optical depth (including absorption and scattering), and m is the airmass factor as a function of SZA θ .

4.2.3.1 Langley method

The Langley method is a commonly used method of measuring both τ (calibrating sun photometers for example), and SSI (e.g. *Arvesen et al.* [1969], *Menang et al.* [2013] and *Bolsée et al.* [2014]). The method is based on Equation (4.1). The second-order effects of atmospheric refraction and the Earth's curvature are neglected here. The technique is not suitable for measuring in spectral regions where there is strong absorption.

From Eq. (1), by taking the natural logarithm of both sides, we obtain;

$$(4.2) \quad \ln(I(\nu)) = \ln(I_0(\nu)) - \tau(\nu)m(\theta)$$

Assuming constant SSI and τ , Eq. (2) describes a linear relationship between the logarithm of the observed intensity and the airmass factor allowing an estimate of τ from the gradient of the slope, and $\ln(I_0)$ from the intercept. Since data points are taken at discrete intervals throughout a day, an ordinary least squares fit is performed to the data. Assuming τ is constant throughout the day, the derived SSI is independent of τ . It is desirable to take measurements over a wide range of airmass factors, and as the technique relies on the assumption of constant τ , it is preferable to have at least one day of mostly clear skies. There should also be supplementary atmospheric measurements to monitor any variations in τ .

4.2.3.2 Radiative closure method

The radiative closure method also exploits Equation (4.1). In this case, we calculate SSI from the measured irradiance and independent estimates of τ . Here, τ is calculated using the Reference Forward Model (RFM) [Dudhia, 2017], using line parameters from the HITRAN2012 spectroscopic database [Rothman *et al.*, 2013], continuum absorption from MT_CKD 2.5 [Mlawer *et al.*, 2012], and atmospheric profiles from coincident radiosonde ascents (see Section 4.2.4.3). It is necessary to focus on atmospheric windows between strong absorption bands. In contrast to the Langley method, one can derive the SSI with a single observation provided there are clear skies. However, the reliance on an RTM (and knowledge of the atmospheric state) introduces additional uncertainty into the final value. For high-resolution measurements, any error in the strength or position of spectral lines in the RTM could result in incorrect SSI, necessitating filtering (see Section 4.4). The Langley-derived values are preferred to those from the closure method, since the lack of reliance on a model means that there is less uncertainty. However, the closure-derived spectra provide an important consistency check.

4.2.4 Experimental methods

We use measurements taken during a field campaign between August-September 2008 at Camborne, UK (50.219° N, 5.327° E). These used an absolutely calibrated sun-pointing Fourier transform spectrometer (FTS) at 0.03 cm⁻¹ resolution over the

region 2000-10000 cm^{-1} (5-1.6 μm). The pre-campaign calibration phase took place at the National Physical Laboratory (NPL), UK (see *Gardiner et al.* [2012]). Our analysis focuses primarily on measurements of 22 August and 18 September 2008; these days had clear-sky conditions over sufficient SZA for use of the Langley technique. More details are presented in Chapter 3.4.

4.2.4.1 Calibration

The spectrometer calibration is discussed by *Gardiner et al.* [2012]. To produce a reliable SSI, measurements must be radiometrically calibrated against an irradiance source of comparable magnitude. Our spectrometer was calibrated against the Ultra High Temperature Blackbody (UHTBB), based at NPL which is capable of reaching temperatures around 3000 K, and is directly traceable to the International System of Units [*BIPM*, 2006]. While this system is not directly comparable to the effective temperature of the Sun's surface, the attenuation experienced in the UHTBB system is minimal, whereas the solar signal travels through the atmosphere. The integrated intensity measured by the spectrometer during solar measurements is therefore comparable to that of the UHTBB, giving similar behaviour and minimizing potential detector response issues.

The UHTBB is not transportable; as such a transfer source was used in the field to assess calibration drift. The spectra from *Menang et al.* [2013] include a correction from this transfer source; however as a result of further analysis of the stability of this source this correction was not applied in this work (see Chapter 3.4.4.1).

In addition, the instrument relies on an external optical setup which is exposed to the elements [*Gardiner et al.*, 2012]. This results in a loss of mirror reflectivity over time, which must be corrected for, but this was not done in *Menang et al.* [2013]. Measurements of mirror reflectivity were taken before and after the measurement campaign, with the reflectivity values after the campaign taken as representative of the mirror reflectivity during the campaign. Hence, the reflectivity adjustment is likely an overestimate, which could potentially result in an overestimate of the derived SSI. The potential for this overestimate is accounted for in the uncertainty budget.

4.2.4.2 Spectrometer measurement uncertainty

The uncertainty in the FTS setup comes primarily from four sources. The first arise from the calibration procedure (including the calibration checks from the transfer source). The second are from the solar source and atmospheric path itself (particularly the non-uniformity of the solar disc, and the effect of sub-visible cirrus). The third are uncertainties arising from the external optics, and the fourth is the uncertainty from the spectrometer itself, including optical alignment. The combined ($k = 1$) measurement uncertainty varies with wavenumber, between around 3.3% in the region where the tracker optics had been directly measured before and after the campaign with a reference reflectometer and up to a maximum of 5.9% outside of this region. *Gardiner et al.* [2012] present a detailed assessment of the measurement uncertainties, with additional work since *Gardiner et al.* presented in Chapter 3.4.3.4.

4.2.4.3 Atmospheric state analyses

Data were obtained from Vaisala RS92-SGP radiosonde [*Vaisala*, 2013] launches from Camborne, analyses from the UK Met Office, and Microtops sunphotometer measurements [*Solar Light Company*, 2001]. These include estimates of aerosol optical depth (AOD), temperature, pressure and water vapour profiles of the atmosphere. All other relevant gases are considered to be well mixed. These are necessary for quantification of the SSI from the closure method, since in conjunction with an RTM they provide values of the atmospheric optical depth. More information is presented in Figure 4.2. The AOD values for the relevant spectral region are calculated from the sunphotometer measurements using the Ångström exponent method [*Schuster et al.*, 2006]. More information is presented in Chapter 3.4.5.

4.2.4.4 Filtering of observed spectra

To focus on the higher quality data, several filtering methods were used to remove regions of strong absorption, not only in the bands but also in areas of strong absorption within windows, such as individual water vapour lines. These filters also mitigate or remove the effect of sub-visible clouds and other time-varying extinction sources. This filtering follows the procedure of *Menang et al.* [2013] and is discussed in Chapter 3.4.3.5.

4.2.5 Results and discussions

The results presented here have been normalised to 1 astronomical unit. The Langley-derived spectrum from 18 September 2008 is our best estimate of the SSI (as discussed in *Menang et al.* [2013]), and is referred to as CAVIAR2.

The uncertainty in CAVIAR2 is obtained using a Monte Carlo uncertainty evaluation method (see Figures 4.2 and 4.3). The Langley method uses multiple measurements, which each have a random component which varies from measurement to measurement, and a systematic component which is in principle the same for all the measurements across a day (see *Gardiner et al.* [2012]).

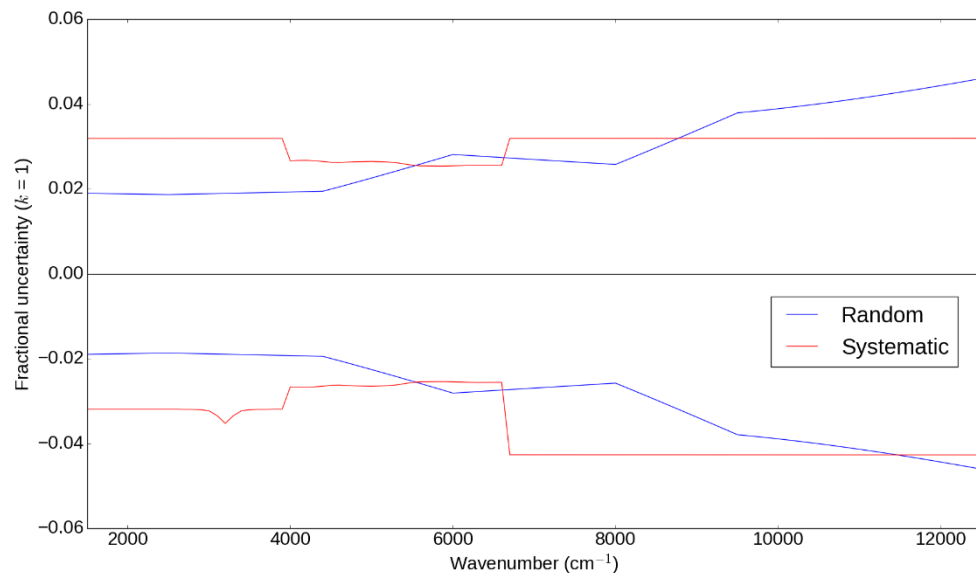


Figure 4.2. Spectral variation of uncertainty in a given spectrum, split into the random and systematic components. The large jump in the negative systematic uncertainty compared to the positive at 6600 cm^{-1} is primarily due to the absence of mirror reflectivity measurements beyond this point, with the consideration that the overall reflectivity cannot exceed 100%. See *Gardiner et al.* [2012] for more details.

The use of a Monte Carlo method allows the different effects of the random and systematic components of the uncertainty in a given measurement upon the Langley results to be rigorously assessed in a statistical manner. The fractional uncertainty used to adjust a given spectrum is drawn from a normal distribution based on the experimental uncertainties shown in Figure 4.2 (discussed in detail in *Gardiner et al.* [2012]). Figure 4.3a shows the probability density functions for the random and

systematic components of uncertainty for a given wavenumber. The systematic distribution is generated either from the positive or negative values randomly for each sample. Points from these distributions are then selected randomly and are used to perturb the observed spectra (black points in Figure 4.3b), with a systematic perturbation affecting each spectrum equally (red points, note the log scale), and a random perturbation added to each spectrum individually to get the final perturbed values (blue points).

These blue points are used to derive SSI by performing an ordinary least squares fit (blue line) and then calculating SSI (i.e. the irradiance at zero airmasses) using the intercept of this line. This process is repeated 50000 times (20 examples of this are shown in Figure 4.3c) and results in a histogram of derived SSI (Figure 4.3d). The mean and standard deviation of this histogram give the observed SSI and its uncertainty. It is important to emphasise that these generated uncertainties do not act as an adjustment to the absolute value of the final spectrum, since given enough samples the mean result should be indistinguishable from the fit to the original data. Gardiner et al. [2012] presents more information about the sources of measurement uncertainty.

The distinction between random and systematic uncertainties is not considered in the treatment of *Menang et al.* [2013], which leads to a less rigorous assessment of the overall uncertainty as the random effect (which will mostly average out across a day provided there are enough samples) is treated as the same for all spectra. The spectra presented in the Figures use the resolution of the Monte Carlo simulations (1 cm^{-1}); a spectrum at full resolution (0.03 cm^{-1}) is available in the Supplementary material to the online version of this paper (<http://dx.doi.org/10.1002/2017GL073902>), with fractional uncertainties interpolated from the Monte Carlo derived uncertainty (which varies smoothly with wavenumber). The lower spectral resolution does not affect the envelope of the spectrum.

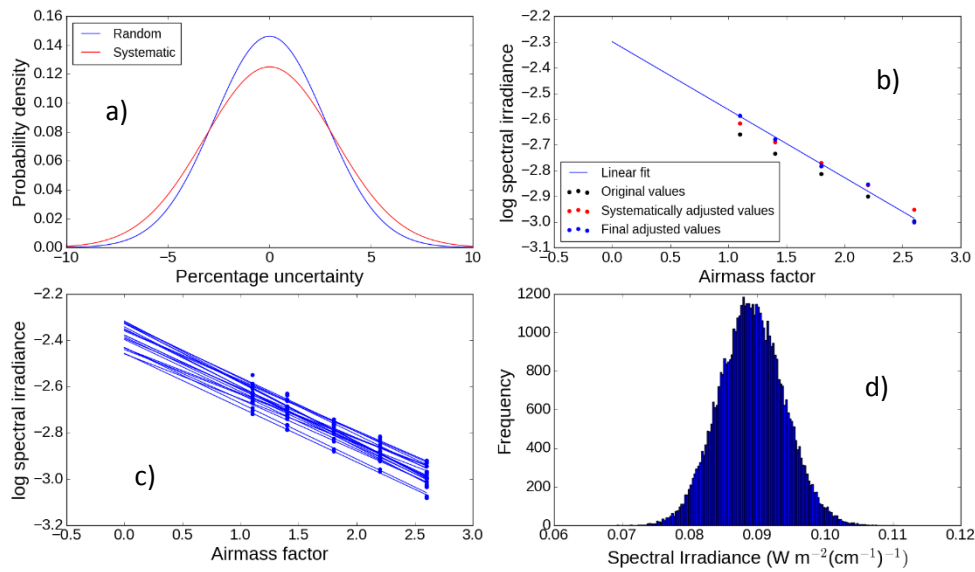


Figure 4.3: Schematic of the Monte Carlo method used to derive the SSI and its uncertainty using the Langley method, at each wavenumber. The example shown is an idealised case.

The uncertainty in the closure method is obtained using the measurement uncertainty from *Gardiner et al.* [2012], with an additional uncertainty due to the use of the RTM. The use of supplementary data introduces an additional source of uncertainty into the final value of the SSI in this case. The uncertainty in the AOD is determined from the statistical fit of the data points (with an optical depth uncertainty of ± 0.01) in the Ångström extrapolation (see Figure 4.4). This is in contrast to the Mie scattering code used for the AOD extrapolation in Chapter 5 (see Chapter 3.4.5), which was implemented after the publication of this paper and is more important for determining the water vapour continuum absorption described in Chapter 5 than SSI. The AOD in the higher (1.02 μm) wavelength channel is most representative of conditions in the spectral region of interest, and generally does not vary significantly throughout the course of the day. The exception is toward the end of 22 August, and the corresponding spectra were not used to derive the SSI, due to the large change in AOD (see Figure 4.4). In the closure method for deriving SSI, these data were used to perform an Ångström extrapolation (e.g. *Schuster et al.* [2006]) to longer

wavelengths, with ordinary least squares fitting used to derive the Ångström coefficients.

The uncertainty in the radiosonde measurements is variable with height, although typically the ($k=1$) uncertainty in temperature is ~ 0.25 K, that in pressure is around 0.5 hPa, and that in relative humidity is around 2.5% [Vaisala, 2013]. For the purposes of this work, the optical depth uncertainty comes from a combination of the AOD uncertainty and the model uncertainty. This model uncertainty included sensitivity analyses performed with variation of $\sim 3\%$ in pressure and temperature. This is above the stated uncertainty given by the radiosonde manufacturer. However, this uncertainty as input into the RTM provides a surrogate for uncertainty in the lineshape and line broadening in the model, and that of the HITRAN 2012 database itself. This effect is mostly negligible and only affects weak lines because regions around strong spectral lines are in any case filtered out.

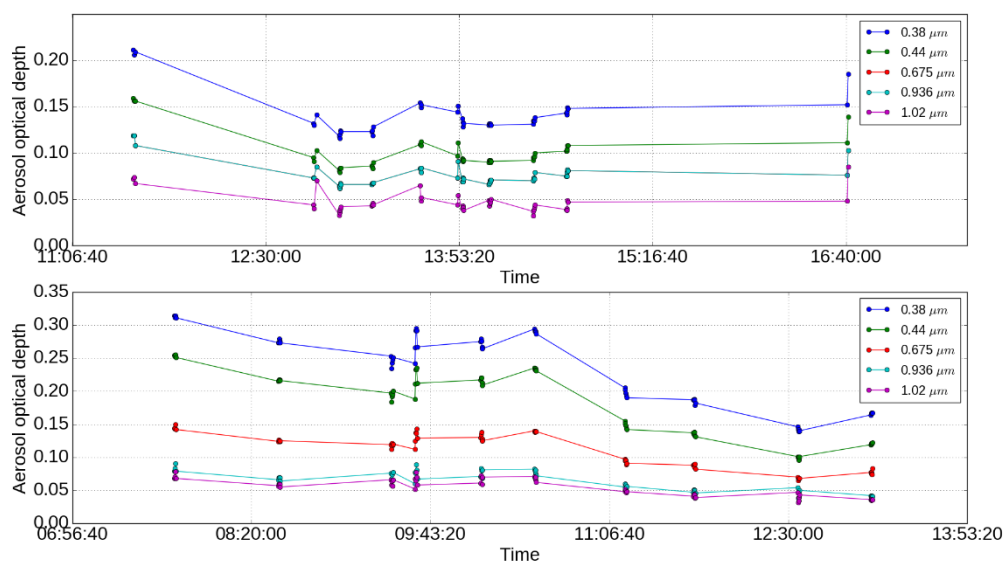


Figure 4.4. Time series of aerosol optical depth (AOD) at 5 wavelengths across the two main measurement days (22 August (upper plot) and 18 September (lower plot) 2008) measured using a hand-held Microtops Sunphotometer [Solar Light Company 2001].

In addition, the effect of uncertainty in the relatively weak water vapour continuum (see Chapter 5) is considered. Some recent laboratory studies differ by more than a factor of 100 in the centre of the $1.6 \mu\text{m}$ window (e.g. Shine *et al.*, [2016]). It is

important to include this uncertainty, since continuum absorption is second only to aerosol scattering as a source of extinction in the microwindows between individual water lines, even considering the large uncertainty. The upper limit of the uncertainty in the SSI from the closure method includes the optical depth including the highest values of the continuum observed in the laboratory in both the 2.5 and 1.6 μm windows, using the nominal temperature scaling from *Shine et al.* [2016c]. This effect remains a second-order effect given its low optical depth contribution even in the regions which are mostly transparent. The continuum does not affect the SSI derived using the Langley method provided water vapour amounts remain constant.

Figure 4.5 shows the mean of the closure-method spectra from two days' worth of measurements (averaging 44 spectra from 22 August and 21 spectra from 18 September), alongside CAVIAR2 from 18 September 2008, and their associated $k = 2$ uncertainties. There is a high level of consistency between the spectra derived using these two quasi-independent methods. Given the fact that the measurements are taken on differing days with differing meteorological conditions, the agreement between these spectra indicates that neither the methodology nor the atmospheric state bias the results.

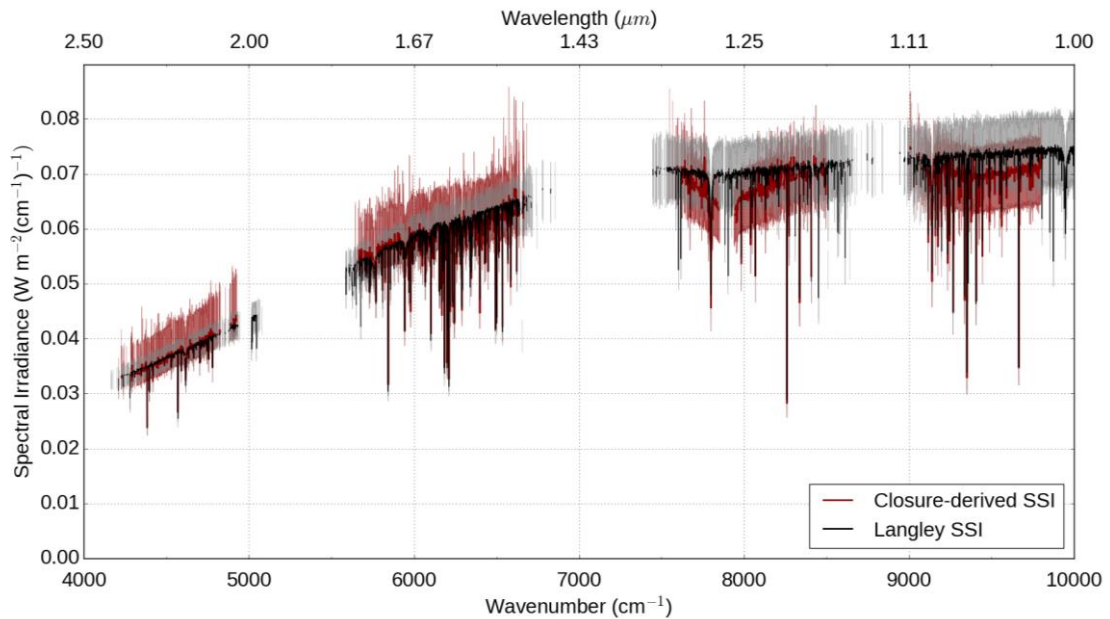


Figure 4.5: Derived CAVIAR spectra using both the Langley method and the mean of radiative closure method over two days of measurements, and their associated $k = 2$ uncertainties. The gray shaded region indicates the uncertainty in the Langley-derived values, and the red that in the closure-derived values. The feature at 8000 cm^{-1} in the closure-derived spectra is an oxygen continuum band not modelled in the RFM.

Figure 4.6 shows CAVIAR2 alongside ATLAS3 and Solar2. Our measurements in the $7000\text{--}10000\text{ cm}^{-1}$ region are consistent with both ATLAS3 and Solar2. Our confidence in the space-based instruments is good in this region, and the uncertainties in CAVIAR2 are relatively large. The quoted values lie very close to one another even without considering the larger uncertainties. This is in contrast with *Menang et al.* [2013], in which there was an underestimation of the SSI in this region relative to ATLAS3, due to the missing mirror reflectivity correction and the use in CAVIAR of the TSARS transfer standard, which was found to be too variable to use as a reliable calibration transfer for its use in CAVIAR2 (see Figure 4.7). The level of consistency between ATLAS3 and CAVIAR2 in this region is indication that any differences are not a systematic effect across the spectrum. There is also broad consistency between the fine structure of the two spectra; however the higher spectral resolution of CAVIAR2 means that a direct comparison is not possible. Figure 4.7 shows the ratio and absolute values of the CAVIAR and CAVIAR2 spectra. The envelopes differ due to the additional mirror reflectivity correction and

lack of TSARS correction. The apparent differences in some line strengths in Figure 4.7 are due to different filters used in the two spectra; these do not affect the envelope.

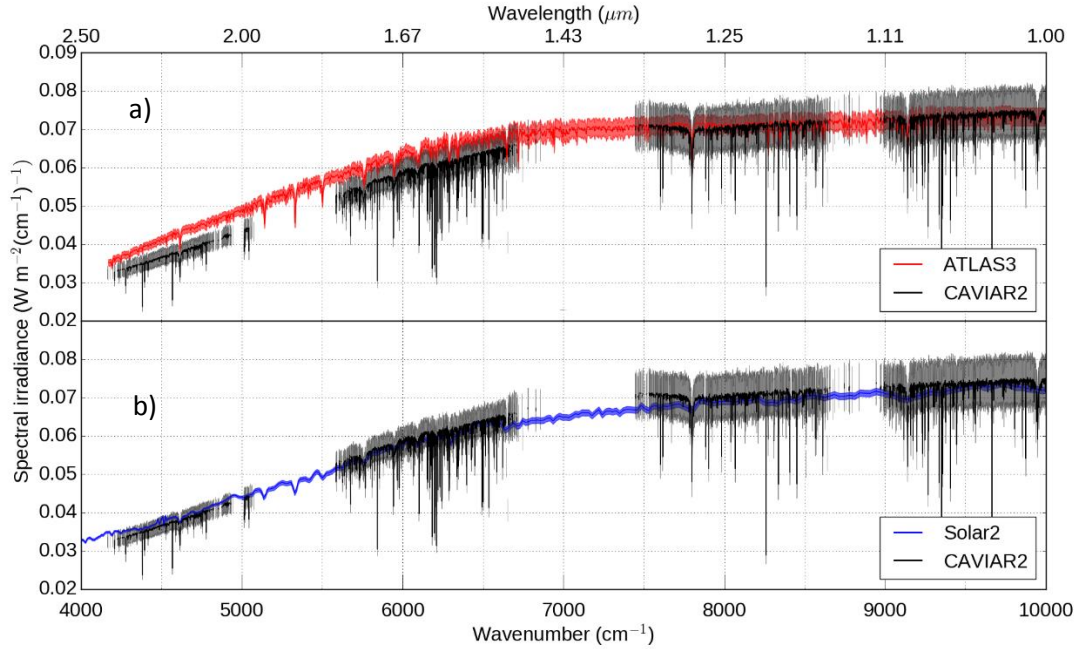


Figure 4.6: Derived spectra from this work and the ATLAS3/Solar2 spectra, with associated $k = 2$ uncertainties.

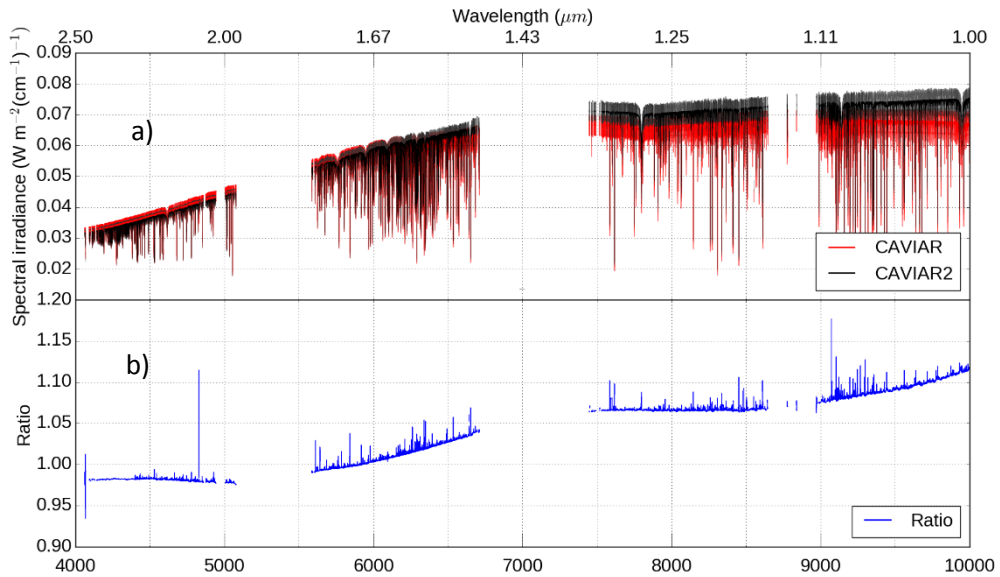


Figure 4.7: Comparison of CAVIAR [Menang et al., 2013] against CAVIAR2. Figure 4.7a shows the absolute level (and corresponding uncertainties) of the two spectra, while Figure 4.7b shows the ratio of the two spectra.

Given the 1-3% uncertainty quoted in *Thuillier et al.* [2003], there is poor agreement between the spectrum derived in this work and ATLAS3 between 4000-7000 cm^{-1} . There is good agreement between this work, IRSPERAD and Solar2 in this region (as shown in Figure 4.1). This weight of data provides a clear indication that the NIR SSI is well represented by these spectra, since there is agreement not only between several independent ground-based spectra but also from the initial SOLSPEC measurements used to derive Solar2. There is also some consistency between this and the unexplained 8% difference between the NIR SSI from SIM relative to ATLAS3 (see Section 4.2.2). Relative to the other spectra (e.g. in Figure 4.1), CAVIAR2 appears to show larger values in the region starting at $\sim 6700 \text{ cm}^{-1}$ and ending at $\sim 7700 \text{ cm}^{-1}$. This is likely to be due to a combination of the mirror reflectivity correction (which is an extrapolation beyond 6600 cm^{-1}), and the stronger water vapour absorption since these data are on the edges of the windows where any effects due to changing water vapour start to become more significant [*Menang et al.*, 2013]. Nevertheless, the uncertainty budget accounts for these effects and consistency within these uncertainties is maintained for all the spectra (the increased uncertainty brings it into consistency with ATLAS3 in this narrow region).

4.2.6 Conclusions

The uncertainty in near-infrared observations of the SSI is an important issue in atmospheric and solar sciences. We have presented an improved reanalysis of the high-resolution CAVIAR ESS from *Menang et al.* [2013], with updated uncertainty estimates and calibration, incorporating additional analysis methods and data. This reanalysis shows excellent agreement with various spectra in the 7000-10000 cm^{-1} ($1.4 - 1 \mu\text{m}$) region (Figure 4.1). In the 4000-7000 cm^{-1} ($2.5 - 1.4 \mu\text{m}$) region we show good agreement with *Bolsée et al.* [2014] and Solar2 (*Thuillier et al.* [2014]), but significant ($\sim 7\%$) differences from the ATLAS3 spectrum of *Thuillier et al.* [2003] and the revised Solar2rev spectrum from *Thuillier et al.* [2015]. We demonstrate that our results are fundamentally consistent with the spectrum of *Arvesen et al.* [1969] within the $k = 2$ uncertainties, which has varying levels of agreement with our work and ATLAS3 across the 4000-7000 cm^{-1} region. We believe that our dataset is significant evidence in favour of the former sets of measurements in this spectral region due to our more robust calibration, agreement with the various solar spectra in the high-frequency end of the NIR (in contrast with

Menang et al. [2013]), our rigorous uncertainty budget, and the agreement between various sets of measurements at different sites with different calibration and methodology.

We question the arguments expressed in *Thuillier et al.* [2015] regarding the uncertainty of the ground-based methods. We find no evidence that residual atmospheric absorption could lead to a significant bias in our derived SSI. In addition, the optical depth due to aerosols and Rayleigh scattering is highest toward 1 μm , where there is much better agreement between the spectra. Their argument also does not resolve the reason for differences between the various space-based measurements. Given the range of NIR measurements and our detailed assessment of the uncertainty in our measurements, we question whether ATLAS3 should be regarded as a reference spectrum at wavelengths greater 1.3 μm .

The measurements presented in this work are taken close to solar minimum. However, in the near-IR the variation due to solar cycles contributes on the order of 0.25% at 1.6 μm [*Lean and DeLand*, 2012; *Coddington et al.*, 2015], well below the 7% difference between this work and ATLAS3. The 27 day solar variability also has little effect, since there were only 5 sunspots observed on 22 August and none on 18 September. [*SIDC*, 2017]

These results have significant implications on our understanding of the total solar irradiance. Using the stated values of ATLAS3 and CAVIAR2 and integrating over the region 4000-10000 cm^{-1} (interpolating the absolute level in the band regions, with lines from *Kurucz and Bell* [1995]), we find that as a central estimate CAVIAR2 is $\sim 16 \text{ W m}^{-2}$ (4.5 %) lower than ATLAS3. This is less than the 8% of *Menang et al.* [2013], primarily because of the better consistency beyond 8000 cm^{-1} . As pointed out in *Weber* [2015], a reduction in SSI in the NIR can be accounted for not only by uncertainties elsewhere in the spectrum, but also by uncertainties in TSI measurements. While there must fundamentally be consistency between measurements of TSI and SSI, constraining the SSI in this narrow region to the TSI would require reduced uncertainty in both the TSI and SSI. Given the robust nature of our uncertainty budget, and the lack of overlap in the $k = 2$ uncertainties of the CAVIAR and ATLAS3 spectra, this indicates that the ATLAS3 uncertainty budget may require re-assessment. Indeed, *Thuillier et al.* [2003] note that their calculated

variance (based on their uncertainty estimate) is smaller than the observed variance from their measurements, and likely implies some unknown source of uncertainty.

We stress that we do not believe that there is fundamental inconsistency between the TSI from current spectral observations and CAVIAR2 within the uncertainties.

Accounting for the ($k = 1$) uncertainties in Solar2 [Thuillier *et al.*, 2009] from the far UV out to $1\mu\text{m}$ leads to a 6 W m^{-2} uncertainty in this spectral region. Applying the same analysis in the near-IR using the ATLAS3 uncertainty from $7000\text{-}10000\text{ cm}^{-1}$ and the CAVIAR2 uncertainty between $4000\text{-}7000\text{ cm}^{-1}$ (i.e. using the lowest uncertainty limits for measurements which we believe are accurate in the respective spectral regions) gives a further 8 W m^{-2} . Thus, without even accounting for any uncertainty in TSI measurements (believed to be $\sim 0.5\text{ W m}^{-2}$ [Kopp and Lean, 2011]), accounting for the $k = 2$ uncertainties, or any uncertainties in wavelengths longer than $2.5\mu\text{m}$ (which contributes 50 W m^{-2} to the TSI), the differences in the TSI budget are almost reconciled.

It is clear that more measurements of the SSI are required, from as wide a range of sources as possible. The TSIS-1 mission was launched in late 2017 [Science.nasa.gov, 2017], which includes a version of SIM with a new calibration method. This involves the use of both a tunable laser and a cryogenic radiometer, which should provide greater accuracy in both the irradiance scale and the spectrometer response. No data is yet publically available from this mission at the time of writing. In addition, further ground-based and airborne measurements are also required. These should involve the use of a high-intensity calibration source, and a robust calibration transfer. One such possibility is the use of radiatively-calibrated lasers at specifically chosen frequencies, such that the spectral response of the spectrometer can be measured quickly and efficiently in the field. For a system set up as in the one in Gardiner *et al.* [2012], it would be also useful to track the reflectance change in the tracker optics over time, rather than once before and once at the end of the campaign. In addition, while it is not strictly necessary (since the Langley method filters out the non-time-varying components of the atmosphere, and is affected minimally by non-time-varying components in the micro-windows), an ideal system would be set up at high altitude, to minimise the effect of atmospheric aerosols and gaseous absorption. Such measurements would be useful not least as a cross-check to the space-based measurements, but also for long-term monitoring of the SSI across

solar cycles. Any such measurement campaigns should particularly focus on a rigorous uncertainty budget, in accordance with the Guide to the Expression of Uncertainty in Measurement [JCGM, 2008].

4.3: Additional analysis

Following the publication of *Elsey et al.* [2017], *Meftah et al.* [2017] published a new reference SSI from 0.165-3 μm (3333-60606 cm^{-1}), based on a revised analysis of measurements taken by the SOLAR/SOLSPEC instrument. These measurements are taken over the period 2010-2016 and used to make a composite. The low variability in the IR over solar cycles relative to the pre-flight calibration uncertainty means that this can be directly compared with the 2008 solar minimum CAVIAR observations. These measurements are taken at a lower spectral resolution, and are combined with high resolution measurements to present a high-resolution reference spectrum, known as SOLAR-ISS. It is the belief of *Meftah et al.* that these measurements have a higher accuracy than ATLAS3.

The SOLAR-ISS spectrum shows a difference relative to ATLAS3 of $\sim 4\%$ in the NIR region, with a peak difference of $\sim 6.5\%$ at 4760 cm^{-1} . A comparison of ATLAS3 to SOLAR-ISS and CAVIAR2 is shown in Figure 4.8, alongside the $k = 2$ uncertainties. The envelopes of SOLAR-ISS and CAVIAR2 overlap within the uncertainties. There are regions where there is no overlap; these mostly correspond to solar lines missing from SOLAR-ISS (CAVIAR2 has a higher resolution). Within these uncertainties the spectra agree well (this agreement can be seen more explicitly in Figure 4.9). The relatively small uncertainties in SOLAR-ISS and ATLAS3 mean there is no consistency between $4000\text{-}7000\text{ cm}^{-1}$. There is however much better agreement between $7000\text{-}10000\text{ cm}^{-1}$, as with CAVIAR2. This lack of consistency between ATLAS3 and SOLAR-ISS, and the agreement between SOLAR-ISS and CAVIAR2 provides additional strong evidence for the lower SSI in the $4000\text{-}7000\text{ cm}^{-1}$ region.

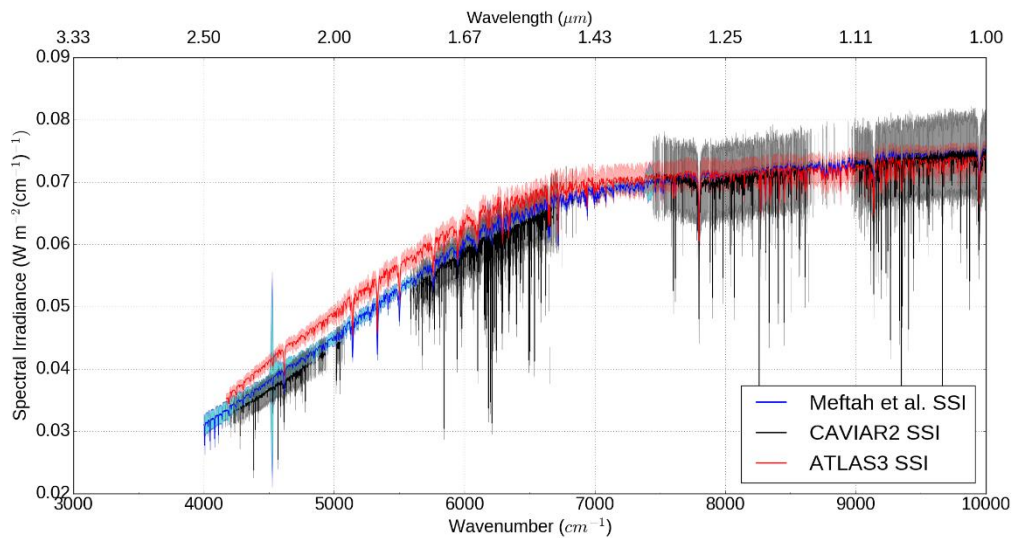


Figure 4.8: Comparison of the SOLAR-ISS spectrum (blue), ATLAS3 (red) and CAVIAR2 spectrum (black), with corresponding $k = 2$ uncertainties (shaded regions).

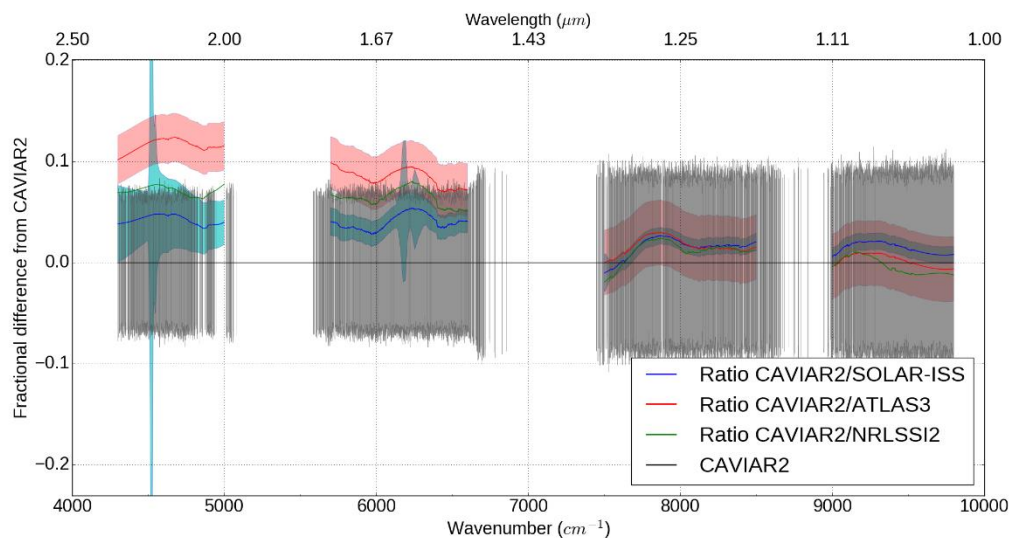


Figure 4.9: Plot showing fractional difference from CAVIAR2 (this work) for the SOLAR-ISS spectrum [Meftah et al., 2017], ATLAS spectrum [Thuillier et al., 2003] and NRLSSI2 spectrum [Coddington et al., 2016], with corresponding $k = 2$ uncertainties (shaded regions). Uncertainties are not shown for NRLSSI2 (see text).

Of particular note in the climate modelling community is the SSI of Coddington et al. [2016], hence the NRLSSI2 (Naval Research Laboratory Solar Spectral

Irradiance-2) spectrum. This paper presented a climate data record of monthly and daily values of solar irradiance (total and spectral) from 1882-2016, and yearly solar irradiance from 1610-2016. This dataset is updated quarterly with preliminary values, and is updated at the end of the year with final values. The 4000-10000 cm^{-1} component of this data record is obtained from SORCE-SIM observations [Harder *et al.*, 2005]; at lower wavenumbers the semi-empirical Kurucz and Bell [1995] spectrum is used. The SIM data, as discussed in Section 4.2.2, is forced to agree with the ATLAS3 spectrum in this region, so it is not independent of ATLAS3. These observations are then scaled by observations of sunspots to obtain the variability over time. An additional composite SSI was published in Haberreiter *et al.* [2017]. As with NRLSSI2, this composite uses SIM for its absolute level in the NIR region, and is therefore not considered further here.

The NRLSSI2 spectrum is a useful tool for climate modelers requiring solar irradiance values at a given time. Matthes *et al.* [2017] recommend NRLSSI2 alongside the SATIRE-S (Spectral And Total Irradiance REconstructions for the Satellite era [Ball *et al.*, 2014] semi-empirical spectrum as the recommended SSI in to the Coupled Model Intercomparison Project Phase 6 (CMIP6). These two spectra are averaged arithmetically to obtain the recommended spectrum and are plotted independently here.

Figure 4.10 shows these spectra relative to CAVIAR2, and Figure 4.9 shows the ratio, alongside the SOLAR-ISS and ATLAS3 spectra. The SATIRE-S and NRLSSI2 spectra do not have spectroscopic uncertainties; these are therefore not included in the plots. Some uncertainty is included in the NRLSSI2 datafiles, however it is unclear if this is uncertainty due to the spectroscopy (in which case it is negligibly small) or due to uncertainty in the algorithm used to construct the solar cycle variability dataset. The NRLSSI2 and SATIRE-S spectra are similar in absolute level in the NIR region, yet systematically above the best estimate of CAVIAR2, and barely consistent within the $k = 2$ uncertainties between 4000-5000 cm^{-1} , and is on the edge of the uncertainty limits between 6000-7000 cm^{-1} . This is in part due to the lack of uncertainties in NRLSSI2 and SATIRE-S, but also indicates that the central values are potentially too high, if one were to take the CAVIAR2 SSI as being indicative of the true value. This is consistent with the forcing of the SIM dataset to agree with ATLAS3 (and thus the interdependence of NRLSSI2 on

ATLAS3 to some extent). The differences between NRLSSI2 and ATLAS3 could be attributed to the scaling of NRLSSI2 to agree with the commonly accepted quiet-Sun TSI value of $\sim 1360 \text{ W m}^{-2}$. There appears to be no agreement in parts of the 4000-7000 cm^{-1} region between NRLSSI2 and SOLAR-ISS within the $k = 2$ uncertainties of the SOLAR-ISS measurements.

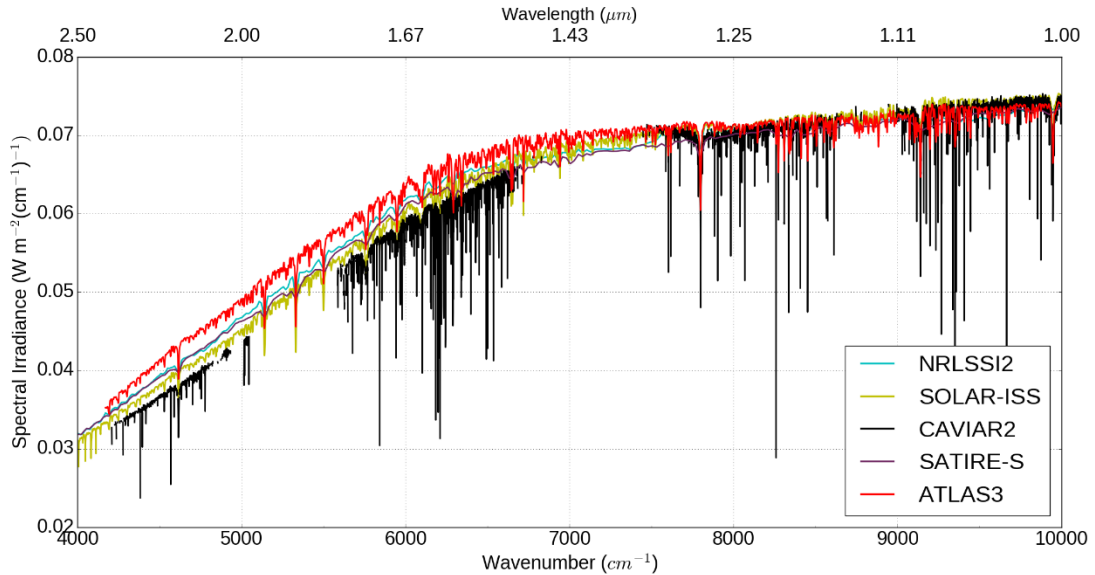


Figure 4.10: Comparison of the NRLSSI2 spectrum (green), SATIRE-S spectrum (dark blue), CAVIAR2 spectrum (black), ATLAS3 (red) and NRLSSI2 (light blue) spectra, shown here without uncertainties.

SOLAR-ISS shows lower spectral irradiance than ATLAS3 in the NIR, leading to a reduced integrated irradiance relative to ATLAS3. The integrated TSI observed over the 0.165-3 μm (60606.06- 3333.33 cm^{-1}) region, when including a 28 W m^{-2} contribution from 3-160 μm (3333.33-62.5 cm^{-1}) from SATIRE-S gives a TSI of 1372 W m^{-2} , $\sim 11 \text{ W m}^{-2}$ above the best estimate of TSI of $\sim 1360 \pm 0.5 \text{ W m}^{-2}$ [Kopp, 2016]. The authors point out that their integrated irradiance is still above that observed from TSI measurements despite the higher spectral accuracy. The authors also challenge the use of TSI measurements to correct the ATLAS3 spectrum in Thuillier *et al.* [2003], which had a TSI of $\sim 1390 \text{ W m}^{-2}$ when accounting for contributions outside of its spectral region of interest. A uniform correction of $\sim 1.4\%$ across the spectrum was applied to agree with a target of 1367.7 W m^{-2} (the previous recommended value), without any justification as to how this energy was spread throughout the spectrum. The integrated difference between CAVIAR2 and SOLAR-ISS (4000-10000 cm^{-1}) is $\sim 7.5 \text{ W m}^{-2}$, interpolating CAVIAR2 linearly between the

water vapour bands. Taking the CAVIAR2 values in this region and SOLAR-ISS outside would go a significant way to achieving the desired TSI target. The use of a TSI argument should not be leaned upon too heavily however, as this difference could just as easily be made up in another part of the spectrum, not observed in CAVIAR2.

Additional work is required to reconcile these SSI, in particular observations with realistic uncertainty estimates, since given a rigorously estimated uncertainty budget no two spectra should disagree within these uncertainties. Nevertheless, *Meftah et al.* [2017] provide additional compelling evidence for a lower SSI in the 4000-7000 cm^{-1} region, and reinforces the conclusions of *Elsey et al.* [2017]. Since the NIR SSI is influential in determining atmospheric energy balance due to the presence of strong water vapour bands in this region, these results should be considered in climate modelling experiments such as CMIP6.

Since *Elsey et al.* [2017], *Menang* [2018] presented an assessment of near-infrared heating rates from various different SSI, including ATLAS3, CAVIAR2, IRSPERAD and SOLAR-ISS, showing a difference in absorbed irradiance of $\sim 6 \text{ W m}^{-2}$ (5% of the total) between CAVIAR2 and ATLAS3. This difference translates to a difference in tropospheric heating rates of $\sim 0.1 \text{ K day}^{-1}$; an increase of around 10%.

Chapter 5:

Observations of the near-IR water vapour continuum in the atmosphere

5.1: Introduction

This chapter uses the FTS measurements described in Chapter 3 to derive the water vapour continuum absorption (hereafter simply ‘continuum’). As discussed in Chapter 2.4, the continuum is modelled in the atmosphere using the MT_CKD model. The effectiveness of MT_CKD in modelling the near-infrared continuum is however uncertain, due to the paucity of observations and the disagreement between these. Compounding this issue is the lack of observations at atmospheric temperatures, meaning that the accuracy of the MT_CKD continuum is dependent on assumptions made about the temperature scaling of the self-continuum, which is itself the subject of ongoing study.

The results presented in this chapter cover the wavenumber region 2000-10000 cm^{-1} , and are a more detailed analysis of the results briefly reported in *Menang* [2012]. As with Chapter 4, the results presented here are a combination of derivations using the Langley method and the radiative closure method described in Chapter 2, with observations primarily from 22 August 2008 and 18 September 2008.

Since the FTS observations from Camborne are made through the atmosphere, any such continuum derived using them (subject to corrections from gaseous absorption and other sources of smoothly varying extinction) should provide a useful check to MT_CKD, and within the bounds of uncertainty provide upper and lower limits to the strength of the continuum in these conditions. Atmospheric measurements of the continuum in this spectral region have been published before (e.g. *Reichert and Sussmann* [2016]). However, the conditions at the Zugspitze field site used in that study are not suitable for derivation of the self-continuum due to the lack of water vapour. The Reichert study also lacks radiometric calibration, instead using a Langley method along with a medium-temperature blackbody to generate a calibration function. The Camborne measurements therefore represent a unique

retrieval of the water vapour continuum from absolutely calibrated measurements of solar radiation.

Retrieving the continuum using the Camborne measurements is more challenging than the SSI derived in Chapter 4, since the gradient of the Langley fit is far more sensitive to small changes in optical depth due to non-continuum components (such as aerosol changes). These aerosol changes are difficult to assess in turn, due to the lack of external validation for the Microtops sunphotometer measurements. This chapter will dedicate particular attention to assessing the consistency between the FTS spectral measurements and the aerosol measurements from the Microtops.

Another challenge is extrapolating these aerosol measurements from the visible and near-visible channels of the Microtops to the desired near-infrared values.

Atmospheric absorption needs to be modelled accurately, meaning that the atmospheric temperature, pressure and water vapour need to be measured using radiosondes. Since the continuum in the atmosphere is a combination of a foreign component and a self-component, it is only possible to derive a combined total continuum absorption coefficient. Derivation of the relative contribution is not straightforward, from the small number of measurements available here and the relatively constant water vapour partial pressures over the campaign.

As with the SSI derivation, sharp focus is placed on the derivation of a rigorous uncertainty budget. Due to the difficulty in deriving the continuum in these conditions, the upper and lower limits of this uncertainty budget are especially important since these provide the upper and lower bounds of absorption.

5.2: Laboratory measurements and MT_CKD

As discussed briefly in Chapter 1, there have been many recent attempts to derive the continuum in various laboratories, with significant disagreement between measurements of the self-continuum, particularly at room temperature. In the 1.6 and 2.1 μm windows, these differences are greater than an order of magnitude with no agreement between the uncertainties. *Shine et al.* [2016c] presents a detailed account of these.

As discussed in Chapter 2, the continuum is parameterised in most radiative transfer models by the CKD (Clough-Kneizys-Davies) and more recently the MT_CKD

(Mlawer-Tobin_CKD) models [Mlawer *et al.*, 2012]. These are lineshape models (at least in the window regions, see Chapter 2.4 for more details), which adjust the primarily Lorentzian lineshape of water vapour lines using a χ -factor derived mostly from measurements at wavenumbers in the mid and far-infrared ($< 2000 \text{ cm}^{-1}$). The continuum is assumed to be due to a combination of far-wing contributions beyond the standard Lorentzian and collision-induced absorption between water vapour and other molecules; the χ -factor is determined accordingly. An additional spectrally dependent correction is then made to the spectrum to scale it to match selected³ observations. At the time of writing however, the lack of agreement and sparsity of observations in the $2.1 \mu\text{m}$ and $1.6 \mu\text{m}$ windows makes this approach less viable in these windows.

It is therefore key to determine the absorption strength from observations in the $2000\text{-}10000 \text{ cm}^{-1}$ spectral region, in order to improve MT_CKD and to more accurately determine the near-infrared window absorption in radiative transfer models. Throughout this chapter reference will be made simply to “MT_CKD” to denote the continuum derived from this model, in this case the most recent version at the time of writing (MT_CKD 3.2). Other versions of MT_CKD will be specified (for example MT_CKD 2.5, which is still used in many radiative transfer models).

The most recent attempts to observe the continuum in the laboratory will be discussed below. This primarily focuses on the laboratory FTS measurements from the CAVIAR project [Ptashnik *et al.*, 2011a, 2012], laboratory spectra from the Institute for Atmospheric Optics in Tomsk [Ptashnik *et al.*, 2013, 2015] the cavity ring-down spectroscopy measurements of Mondelain *et al.* [2013, 2014] and the calorimetric interferometry measurements of Bicknell *et al.* [2006]. There is also some discussion of the atmospheric measurements of Reichert and Sussmann [2016], although these are taken at high altitude and thus focus more on the foreign-continuum.

The foreign-continuum component could still be significant; CAVIAR measured a foreign continuum that contributes $\sim 40\%$ of the total in the $1.6 \mu\text{m}$ window for a typical mid-latitude atmosphere (more so in drier atmospheres, less in moister ones) [Ptashnik *et al.*, 2012]. MT_CKD on the other hand has a foreign contribution of

³ The process by which observations are selected for use in successive versions of MT_CKD is generally unexplained, aside from a passing reference in the code itself.

~10% in all of the NIR windows. The Camborne measurements presented in this thesis may therefore be dominated by self-continuum, or be made up of roughly equal contributions from the self and foreign continua in these windows. Due to the difficulty in separating out the foreign and self-continua, it is not possible to assert this for the Camborne measurements. A future campaign (see Chapter 7) may be able to deduce this by taking measurements over a wider range of water vapour concentrations.

5.2.1: CAVIAR and TomsK continua

5.2.1.1: Self-continuum

Ptashnik et al. [2011a, 2012] (hereafter the CAVIAR continuum) presented separate foreign and self-continua using observations taken by an FTS set up at the Rutherford Appleton Laboratory. These measurements ranged from 472-293 K, at vapour pressures between 0.015 and 5 atm between 2500-10000 cm^{-1} . The wide range of temperatures enables assessment of the temperature dependence of the self-continuum. Figure 5.1 (from *Shine et al.* [2016c], redrawn from *Ptashnik et al.*, [2011a]) shows the CAVIAR continuum in relation to MT_CKD 2.5 at each of the temperatures used in the CAVIAR measurements.

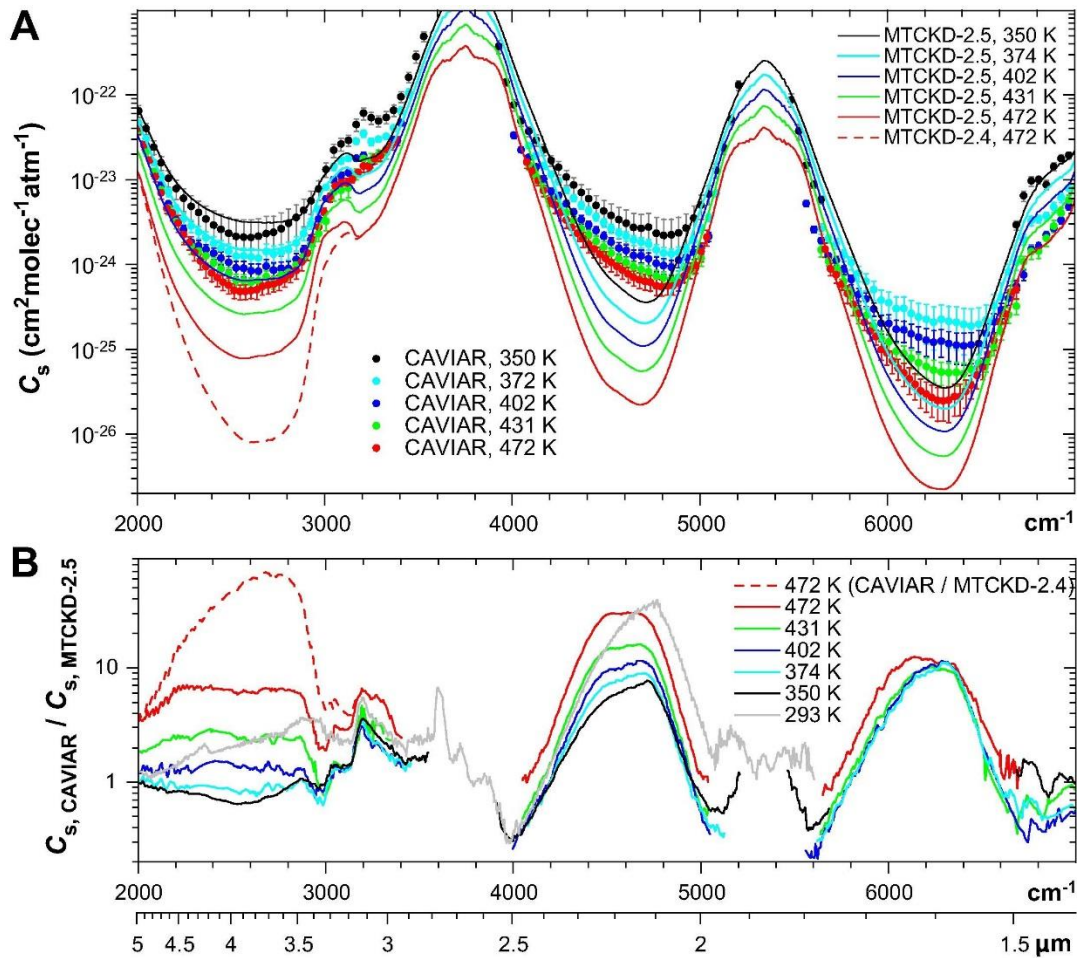


Figure 5.1: Laboratory observations of the water vapour self-continuum from CAVIAR at different temperatures (dotted points), compared to MT_CKD 2.5 model observations at the same temperatures (solid lines) (A), and the ratio of these values (B). From Shine et al. [2016c].

The MT_CKD 2.5 values are ~ 10 x weaker than the CAVIAR measurements in the centres of the 2.1 and 1.6 μm windows; the exact difference varies since the temperature dependence implied by the CAVIAR measurements is different to that of MT_CKD. The uncertainties in the room-temperature measurements are somewhat large ($\sim 70\%$), to the extent that no measurements were reported at room temperature in the 1.6 μm window. The uncertainties in the high temperature measurements are smaller ($\sim 15\text{-}20\%$ in the 2.1 μm window and $\sim 25\text{-}30\%$ in the 1.6 μm window). Nevertheless, within these uncertainties the measurements “unambiguously show that self-continuum absorption at the centres of all near-IR windows is typically an order of magnitude stronger than MT_CKD” [Ptashnik et al., 2011a]. Due to the large uncertainty, there are no measurements at atmospheric

temperatures (< 293 K), and the room temperature measurements at $1.6 \mu\text{m}$ are not included on Figure 5.1.

Further sets of FTS measurements [Ptashnik *et al.*, 2013] were taken at the Institute for Atmospheric Optics in Tomsk, Russia (henceforth Tomsk continuum). These measurements look at the self-continuum, and report values in excess of both the CAVIAR measurements and MT_CKD when corrected for temperature. Due to the longer gas path cell, these measurements are taken at a lower temperature than the CAVIAR measurements (290 and 318 K). The baseline of the spectrometer is adjusted based on measurements at 9300 cm^{-1} ; it is assumed (justifiably due to the extremely weak signal) here that the continuum is negligible. Within the measurement uncertainties, they agree well with the CAVIAR observations at wavenumbers lower than 5000 cm^{-1} . These uncertainties are smaller than the CAVIAR uncertainties due to the better baseline stability and longer path length.

Ptashnik *et al.* [2015] repeated these measurements; these presented a $\sim 1.5\text{x}$ weaker continuum than the 2013 Tomsk measurements in the 4700 and 6600 cm^{-1} windows. This was predominantly due to the choice of baseline; in this case the MT_CKD values in the window at 2500 cm^{-1} were used. This was motivated partly due to the large continuum values from Ptashnik *et al.* [2013]; MT_CKD represents some of the lower observed values in this window and as such was chosen as a conservative estimate. It also allows for the continuum to be measured relative to MT_CKD in these windows, and where MT_CKD is more directly derived from measurements.

The Tomsk and CAVIAR datasets present values which are roughly an order of magnitude stronger than MT_CKD in the $2.1 \mu\text{m}$ window at room temperature. The Tomsk measurements have a self-continuum 2 orders of magnitude stronger in the $1.6 \mu\text{m}$ window. The disagreement between these FTS measurements and MT_CKD is strongest within the centres of these two windows. Toward the edge of the windows and in the bands however there is much better agreement (Figure 5.3).

5.2.1.2: Foreign continuum

The other important contribution to the continuum comes from interactions between water vapour and air (i.e. predominantly N_2 and O_2). Measurements were made of the foreign continuum during CAVIAR [Ptashnik *et al.*, 2012] in the 2.1 and $1.6 \mu\text{m}$ windows, by subtracting the self-continuum contribution from their total observed

continuum absorption coefficients. As with the self-continuum therefore, the uncertainties increase with decreasing temperature (due to the uncertainty in the subtracted self-continuum), despite the experimentally-observed lack of temperature dependence. Figure 5.2 shows the CAVIAR foreign continuum over the range 2000-10000 cm^{-1} , demonstrating the consistency with varying temperature (figure from *Ptashnik et al.* [2012]). Also plotted on this figure are the MT_CKD foreign continuum values, which are significantly weaker than the CAVIAR values. This indicates that, independent of the self-continuum, there is significant evidence for a strengthening of the foreign continuum within MT_CKD. *Ptashnik et al.* [2012] suggest that this increased foreign continuum at $\sim 2500 \text{ cm}^{-1}$ may be due to *bimolecular absorption*, a strengthening of the N_2 fundamental band via $\text{N}_2\text{-H}_2\text{O}$ interactions. This does not explain the behaviour in the other near-infrared spectral windows. The effect of a strengthened foreign continuum and the consistency with the continuum of this work is explored further in Chapter 6.

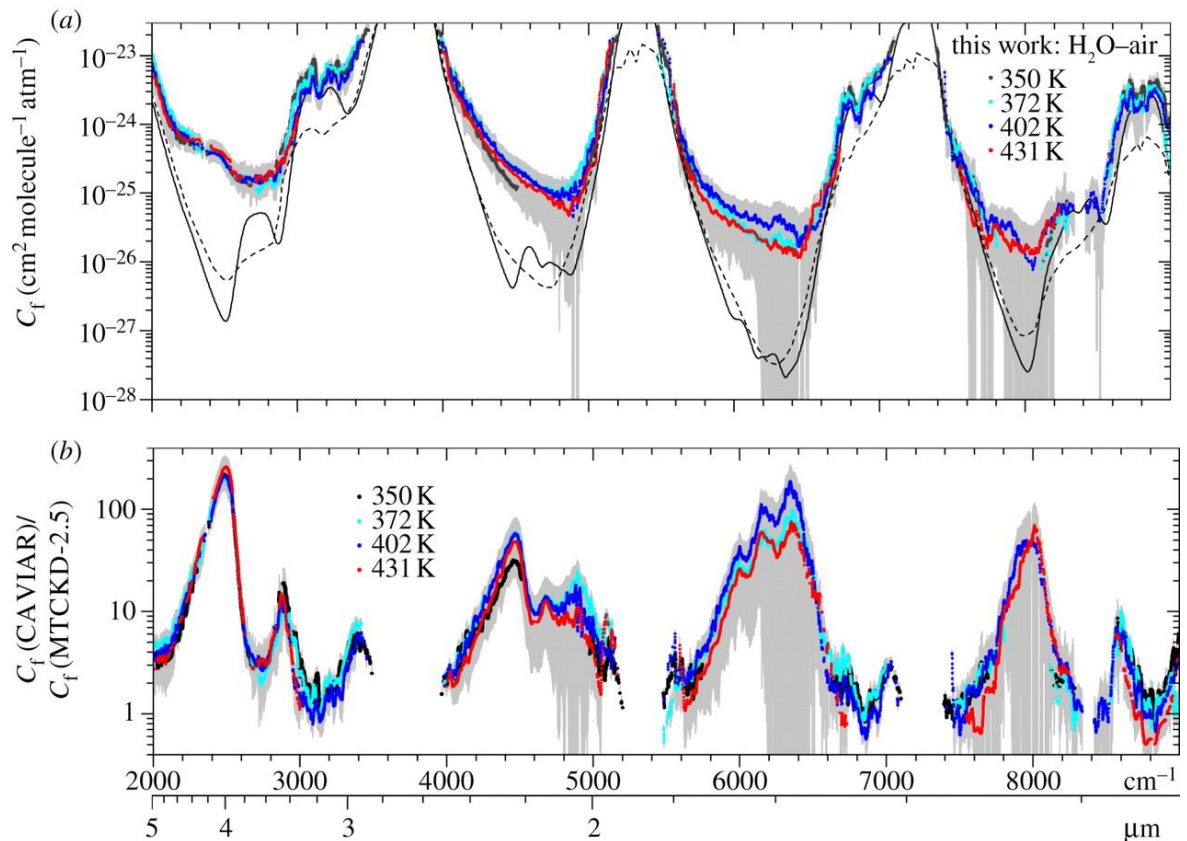


Figure 5.2: Foreign continuum derived from laboratory measurements by Ptashnik *et al.* [2012], (coloured lines) at different temperatures relative to MT_CKD (solid black line) and the Tipping and Ma $\text{H}_2\text{O-N}_2$ far-wing model (see e.g. Shine *et al.* (2013)). The changes between the observed foreign continuum at different temperatures are small, this can be explained by the uncertainties (grey shaded regions) and the need to subtract the self-continuum from the total, or by some weak temperature dependence of the foreign-continuum. Figure from Ptashnik *et al.* [2012].

Another important result from Ptashnik *et al.* [2012] was that the foreign continuum plays a significant role in atmospheric conditions, contributing up to 50% of the total continuum absorption in the 1.6 and 2.1 μm windows. This is in contrast to MT_CKD, where the self-continuum dominates over the foreign in atmospheric conditions. If the inferred CAVIAR self-continuum at atmospheric temperatures is an overestimate (see Section 5.2.2), then the relative importance of the foreign continuum would increase in these conditions. Thus, the foreign continuum is an important component of the atmospheric absorption that should be taken into equal consideration with the self-continuum. This is explored further in Chapter 6.

5.2.2: Grenoble CRDS continua

5.2.2.1: Self-continuum

The other major set of continuum observations in this region are the cavity ring-down spectroscopy (CRDS) and optical feedback cavity enhanced absorption spectroscopy (OF-CEAS) measurements of *Mondelain et al.* [2013, 2014] in Grenoble. The results of *Mondelain et al.* [2014] are considered more robust, henceforth referred to as the Grenoble continuum. These measurements use a laser based technique to measure at specific wavenumbers within the 1.6 and 2.1 μm windows, predominantly at room temperature with additional OF-CEAS measurements at various different temperatures between 296 and 323 K. Their reported continuum values are significantly lower (at room temperature) than those of any of the sets of FTS measurements. The reason for the discrepancy between the two is not known; there are however some explanations which might cause this (see Section 5.2.4).

These measurements are however in reasonable (~50%) agreement with MT_CKD (at room temperature, see Figure 5.1) within this region, although this is not the case at higher temperatures. In the 2.1 μm window there are observations in 4 wavenumbers towards the bands and only one in the centre of the window, but there are observations at 10 wavenumbers in the middle of the 1.6 μm window. Additional sets of measurements [*Richard et al.*, 2017; *Lechevallier et al.*, 2018] were presented in the 2.1 μm window which are in general agreement with the *Mondelain et al.* [2014] results. *Lechevallier et al.* [2018] present values in this window compared with MT_CKD 3.2, showing that the increase in continuum strength in this region relative to MT_CKD 2.5 is consistent with their measurements.

The agreement between MT_CKD and the Grenoble measurements is not an indicator of the accuracy of either, given the disagreement between the CRDS and FTS measurements and the lack of a physical basis for the MT_CKD χ -factors and weak interaction terms (see Chapter 2).

5.2.2.2: Foreign continuum

Mondelain et al. [2015] presented a foreign continuum measurement at one wavenumber (4250 cm^{-1}) at 298 K. This was done using the cavity ring-down technique as with the self-continuum measurements. Their reported values were a

factor of ~4.5 stronger than MT_CKD in this region, and a factor of ~2 weaker than those of CAVIAR (see Figure 5.3).

5.2.3: Other measurements

There also exist combined self and foreign-continuum measurements from *Bicknell et al.* [2006]. These are measured using a calorimetric interferometric method, but are isolated to specific wavenumbers within the relevant windows. This method is not a direct measurement; it is a relative measurement that must be scaled to known absorption, in this case CH₄ lines at ~2.2 μm. The lack of significant documentation and limited wavelength regions make analysis of these measurements in context a challenge, yet they are one of the few extant measurements of H₂O continuum absorption in the near-IR spectral region. These measurements give absorption coefficients that are generally stronger than the Grenoble values and MT_CKD, but significantly weaker than the Tomsk and CAVIAR FTS measurements at room temperature (Figure 5.1).

5.2.4: Synthesis

5.2.4.1: Self-continuum

Figure 5.3 (from [*Shine et al.*, 2016c]) shows the best estimates of the different laboratory spectra at room temperature in the spectral windows of interest (showing here self-continuum absorption coefficient) with their uncertainties. Also plotted is the MT_CKD 2.5 continuum, showing the differences between the FTS and CRDS measurements and MT_CKD. It should be noted that the agreement between the CRDS measurements and MT_CKD is not the case at higher temperatures (see Section 5.2.6).

In addition to the 1.6 and 2.1 μm windows mentioned previously, there are also measurements in the 4 μm window, from CAVIAR, an FTS study by *Baranov and Lafferty* [2012] focusing on the 4 μm window, older measurements by *Burch and Alt* [1984] using a grating spectrometer, and OF-CEAS measurements by *Richard et al.* [2017] and *Lechevallier et al.* [2018] at selected wavenumbers. These are shown on Figure 5.4 (from *Lechevallier et al.* [2018]).

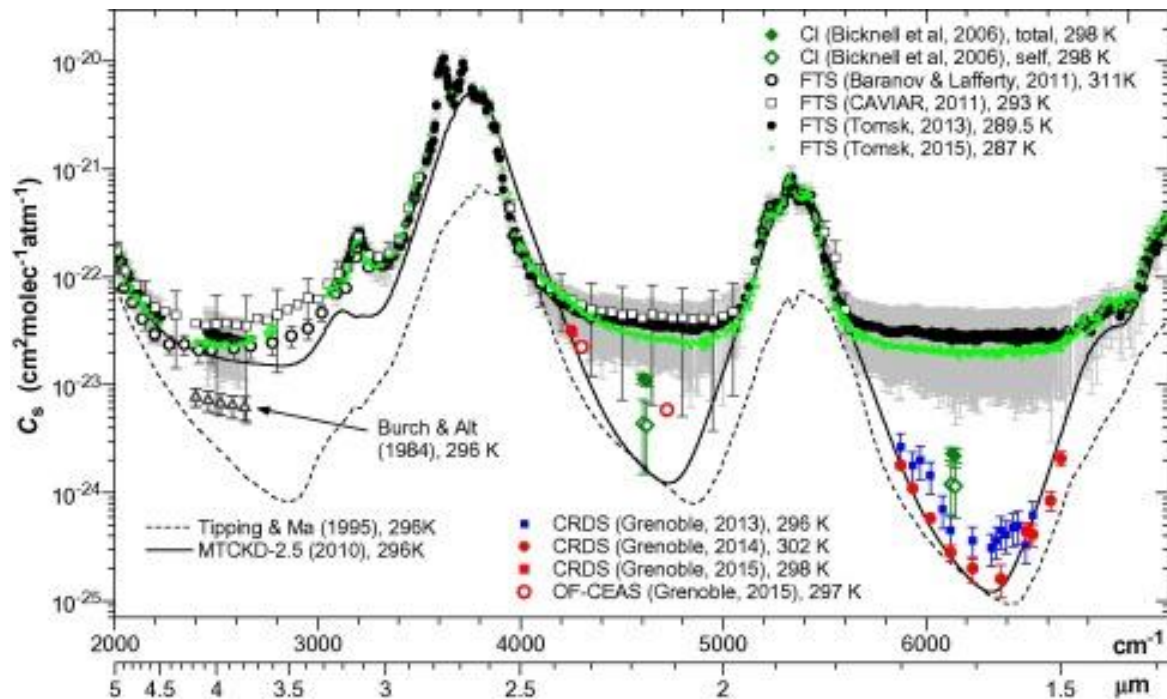


Figure 5.3: Comparison of observed self-continuum absorption coefficient C_s for the various laboratory spectra at room temperature. While higher temperature measurements exist for CAVIAR in the 1.6 μm window, the uncertainties were too large to allow for useful observations at room temperature. From Shine et al. [2016c].

The data on Figure 5.3 in the 4 μm window seem to agree well, aside from the older *Burch and Alt* measurements. The latest Grenoble OF-CEAS measurements (Figure 5.4) however show a marked decrease in the observed self-continuum relative to the FTS measurements, as is the case between the Grenoble and CAVIAR measurements in the 2.1 and 1.6 μm windows. Possible reasons for this are presented in Section 5.2.5. MT_CKD 2.5 agrees well with the CAVIAR and *Baranov and Lafferty* FTS measurements in this window (Figure 5.3); however as with the other windows this agreement should not be taken as evidence for or against a given continuum, due to the semi-empirical nature of MT_CKD.

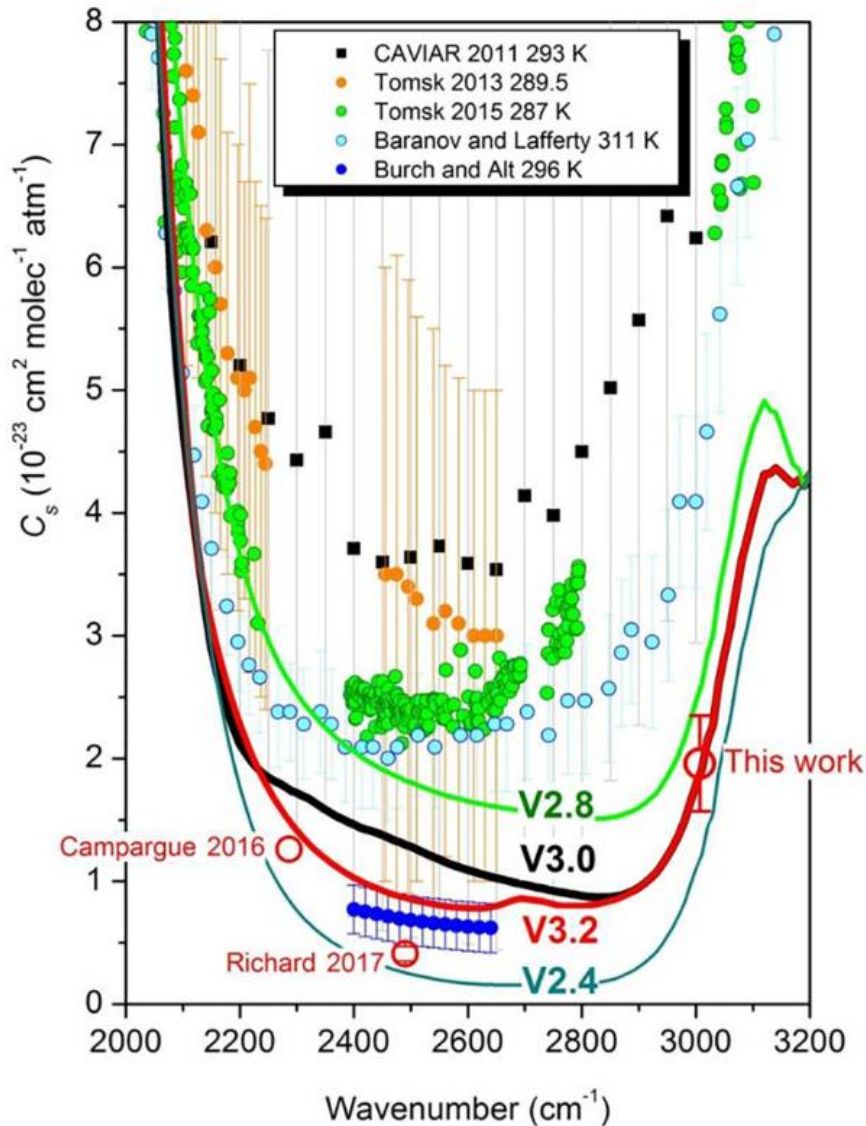


Figure 5.4: Comparison of observations of the self-continuum at room temperature (exact temperature shown in legend) in the $4\ \mu\text{m}$ window. “This work” refers to the source of the figure [Lechevallier et al., 2018]. The solid lines (“V 2.4” through “V3.2”) are various versions of the MT_CKD continuum model at 296 K. The OF-CEAS results are at $\sim 296\ \text{K}$.

5.4.2.2: Foreign continuum

Figure 5.5 shows a comparison between the CAVIAR data, Grenoble data and MT_CKD (from Shine et al. [2016c]). There are several measurements in the $4\ \mu\text{m}$ window, from CAVIAR and from Baranov and Lafferty [2012]. Independent of temperature, the Baranov and Lafferty [2012] and CAVIAR measurements agree, and significantly exceed MT_CKD in this window.

It is difficult to make robust comparisons to an observation set that does not include significant spectral or temperature coverage, as is the case with the Grenoble CRDS foreign continuum. Nevertheless, both datasets showed a marked increase in the 2.1 μm window relative to MT_CKD. The room temperature Grenoble measurements and the CAVIAR measurements at 402 K agree within their stated errors, which provides significant evidence that the foreign continuum is at most weakly temperature dependent across the range of conditions measured.

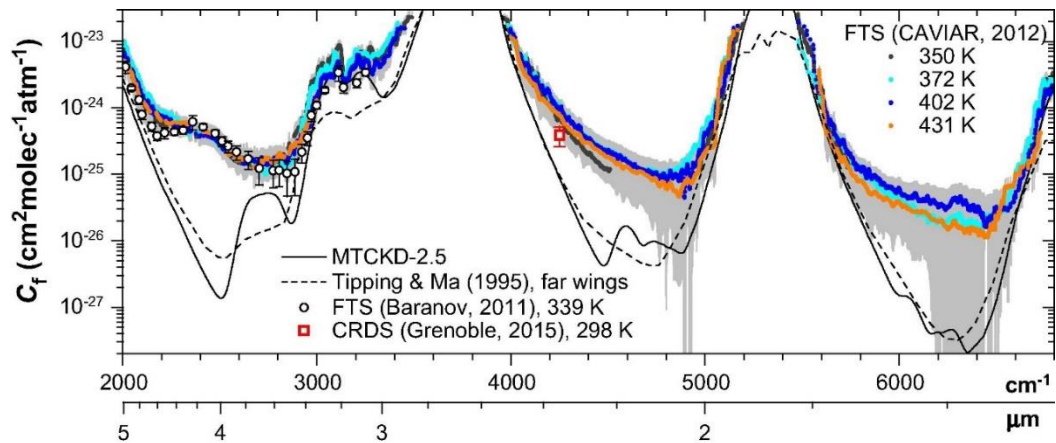


Figure 5.5: Retrievals of the foreign continuum in the 4, 2.1 and 1.6 μm windows. CAVIAR values are in colour (solid lines), with uncertainties (grey shaded regions). The Grenoble measurement (square point at 4200 cm^{-1}) agrees within the uncertainties with CAVIAR; both exceed MT_CKD significantly. From Shine et al., [2016c].

There is a dearth of broadband measurements of the foreign continuum; there are even fewer observation datasets than there are for the self-continuum, despite their relatively equal importance in the atmosphere (assuming the CAVIAR values are accurate). The relative importance and dearth of measurements are strong motivators for the work presented in Chapter 6, where the continuum derived in this work will be compared with that the available laboratory measurements.

5.2.5: Discussion of observation techniques

As with the difference between ground-based and space-based spectra in the SSI work, a lot of the debate arises from the use of the associated measurement techniques (in this case Fourier transform spectroscopy and cavity ring-down spectroscopy/optical feedback cavity enhanced absorption spectroscopy), both of

which have their advantages and disadvantages. While FT spectroscopy has a much wider spectral range than the laser methods, the observed spectrum is heavily dependent on the choice of baseline. Laser methods are much more sensitive on the other hand, and provide a more precise assessment of the absorption. However, the use of lasers limits the number of wavenumbers that can be chosen within a window to observe. *Shine et al.* [2016c] recommend the use of laser methods due to their ability to measure weak absorption more precisely, notably at room temperature.

The cavity ring-down technique relies on an accurate assessment of the reflectivity of the dielectric mirrors used to reflect the laser beam within the cavity. Recent studies (e.g. *Serdyukov et al.* [2016]) show that when the cavity cell is injected with water vapour, these mirrors can experience an increase in reflectivity on the order of ~1%. Given the high (~0.99) reflectivity of these mirrors, this can significantly impact measurements of radiation; and as pointed out in *Serdyukov et al.* [2016], the higher the reflectivity, the larger impact this effect has on the final results. The mirror reflectivity is not specified in either of *Mondelain et al.* [2013, 2014], so the exact influence an increase in reflectivity cannot be determined. However, an increase in the reflectivity would lead to a longer ring-down time, which would go some way to explaining the lower absorption relative to the Bicknell and CAVIAR measurements. There may also be some unaccounted for surface effects, since the size of the gas cell is much smaller in the CRDS measurements compared to the FTS measurements. While these provide qualitative reasons why this *may* have been the case, it is not reasonable to assert that this is the case.

An important caveat is the requirement for measurements from *independent* sources using the same technique. This is the case for the FTS measurements (from CAVIAR and Tomsk), but not the case for the CRDS measurements. There exist measurements (unpublished) by Joe Hodges at NIST using the cavity ring-down technique; one example is a measurement presented in Figure 5.8. This shows an absolute level significantly above the Grenoble CRDS measurements, with very small uncertainties. This is concerning given the small (claimed) uncertainties in the CRDS measurements; while they are clearly precise they may not be accurate if there is no agreement within the uncertainties with independent measurements in the same conditions (or indeed measurements with a different method, provided they have estimated their uncertainties correctly). This is particularly the case when

measurements taken using the same instrument in the same laboratory do not agree within their uncertainties, for example the self-continuum of *Mondelain et al.* [2013, 2014].

The difference in these continua could have profound impacts on modelling of the atmospheric energy budget and in remote sensing. A self-continuum on the order of the Tomsk FTS measurements would indicate that the continuum would have a significant effect on these; however a continuum on the order of MT_CKD and the CRDS measurements would have minimal effect.

5.2.6: Temperature dependence of the observed self-continuum

Another subtlety involved is the lack of a well-constrained self-continuum temperature dependence. Given the fact that most of these measurements are taken at above room temperature, any uncertainty in this temperature dependence and deviation from the nominal temperature dependence included in MT_CKD will have a significant effect on the atmospheric continuum. This especially motivates the need for continuum measurements in atmospheric conditions, since most of the continuum comes from the lower troposphere, with typical temperatures well below room temperature.

Figure 5.6 shows the observed temperature dependence of the self-continuum in the 2.1 μm window a) at the low frequency edge (4250 cm^{-1}), b) in the centre of the window (4301 cm^{-1}) and c) at the high-frequency edge (4723 cm^{-1}) for the CAVIAR, Tomsk [*Ptashnik et al.*, 2013] and Grenoble [*Mondelain et al.*, 2014] measurements, along with the MT_CKD temperature dependence. The dashed line shows the temperature dependence expected from an exponential fit ($\exp(D_0/kT)$) with D_0 the dimer dissociation energy. In the $1000/T$ vs. $\log_{10}(C_s)$ space chosen for the graph, the measurements should lie on a straight line if they have this temperature dependence.

Within the uncertainties, the CAVIAR and Grenoble measurements appear to agree well with this fit, however the Tomsk measurements do not. The Grenoble and high-temperature CAVIAR measurements in Figure 5.6 agree well, assuming this temperature dependence.

This temperature dependence is itself an assumption however; it is entirely possible that deviations from this fit are physical, e.g. due to a change in a dominance of

quasi-bound dimers at high temperature to true-bound dimers at low temperature [Ptashnik *et al.*, 2011b]. A change in this temperature dependence could result in the central values of the room-temperature CAVIAR and Tomsk measurements being consistent with the high temperature CAVIAR measurements.

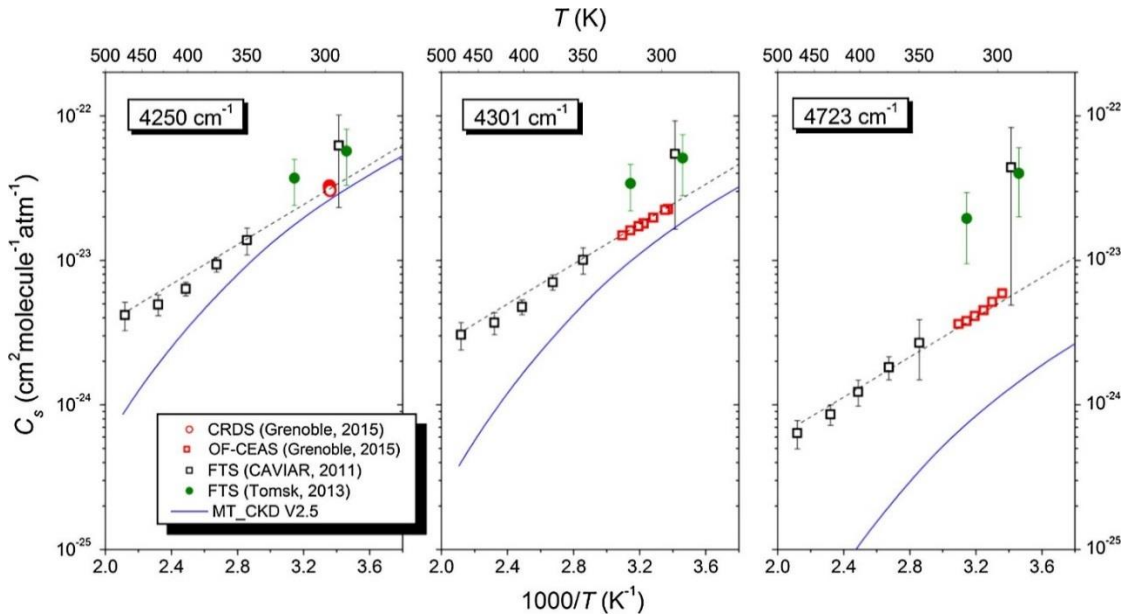


Figure 5.6: Observed temperature dependence in the 2.1 μm window at three wavenumbers at the edges and centre of the window. The uncertainties in the CRDS measurements are smaller than the symbol size. (From Shine *et al.* [2016c])

Figure 5.7 shows the observed temperature dependence in the 1.6 μm for these same sets of measurements, again at the low frequency edge (5875 cm^{-1} , first frame), b) in the centre of the window (6121 cm^{-1} , second frame) and c) at the high-frequency edge (6665 cm^{-1} , third frame) along with the temperature dependence assumed by MT_CKD. At the low ν edge of the window, there is reasonable agreement between this temperature dependence and the observed temperature dependence for the various datasets, excluding the Ptashnik *et al.* [2013] Tomsk measurements.

Also shown on Figure 5.7 are the measurements of Bicknell *et al.* [2006]; however these are only shown in the centre of the window. These measurements are of both the self and foreign continuum; this makes it difficult to isolate the contribution from the self-continuum, given the uncertainty in the strength of the foreign continuum (see Section 5.4.2.2). This middle frame shows reasonable consistency between the CAVIAR and Bicknell *et al.* measurements (if the assumed temperature dependence is correct), but not with the Grenoble measurements, which indicate a much weaker

temperature dependence than MT_CKD or the other sets of observations. The third frame again shows no consistency between CAVIAR and Grenoble.

In all three of these frames, the Tomsk measurements are inconsistent unless there is significant deviation from the assumed exponential temperature dependence at lower temperatures. The CAVIAR data seems consistent in Figure 5.6 and the first two frames of Figure 5.7, but there is some deviation in Figure 5.7. The Grenoble measurements are mostly internally consistent (i.e. lie on a straight line), despite the lack of consistency in the final two panels of Figure 5.7.

A lack of theoretical understanding and additional data make the exact temperature dependence in the centre of this window difficult to ascertain; there is no compelling reason to assume that it will be the same as the temperature dependence in the 2.1 μm window. Equally however, there is no reason to assume it will be different. The Ptashnik *et al.* [2011a] FTS measurements indicate reasonably consistent temperature dependences between these two windows at high temperature.

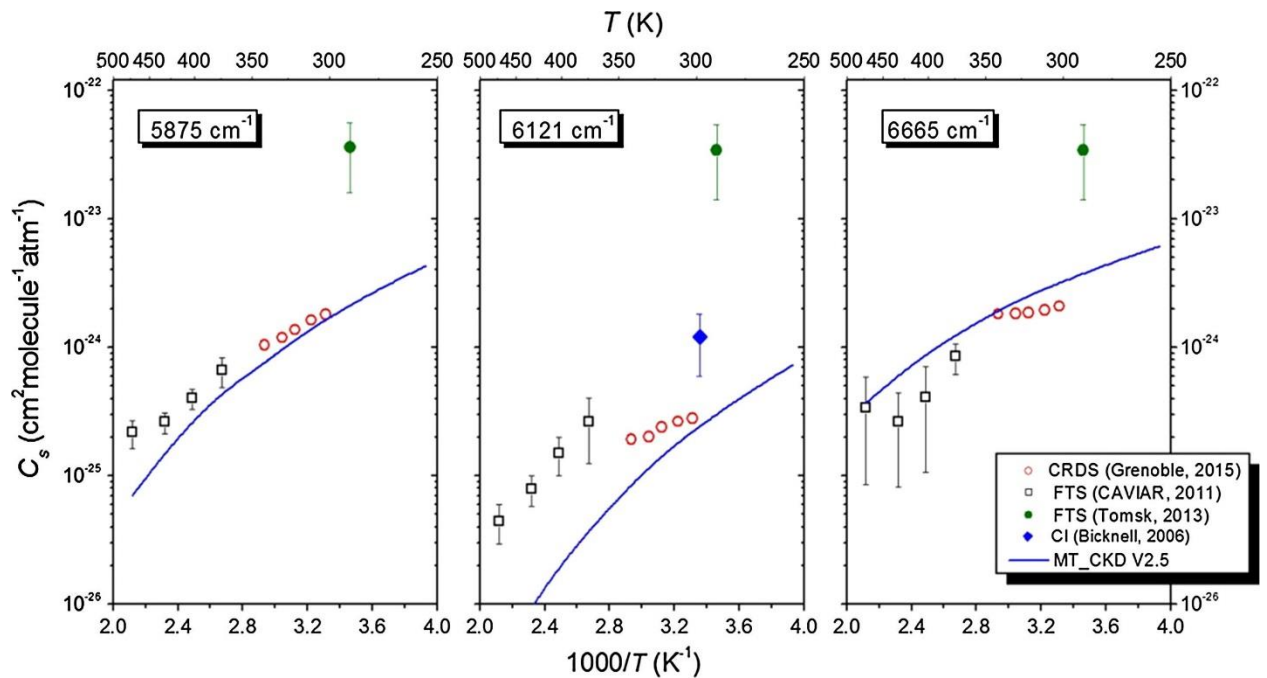


Figure 5.7: Temperature dependence against self-continuum absorption coefficient, this time for the edges and centre of the 1.6 μm window. The CRDS uncertainties are again smaller than the symbol size. (From Shine *et al.* [2016c]).

Additionally, there have been some recent (unpublished) measurements taken at the National Institute of Standards and Technology (NIST) using the cavity ring-down technique. These are shown on Figure 5.8 and appear consistent with the temperature

dependence of the CAVIAR measurements, but less so with the Grenoble measurements. These measurements do not have a detailed uncertainty analysis. Nevertheless; they provide some indication that the CAVIAR temperature dependence could be extrapolated down to lower temperatures.

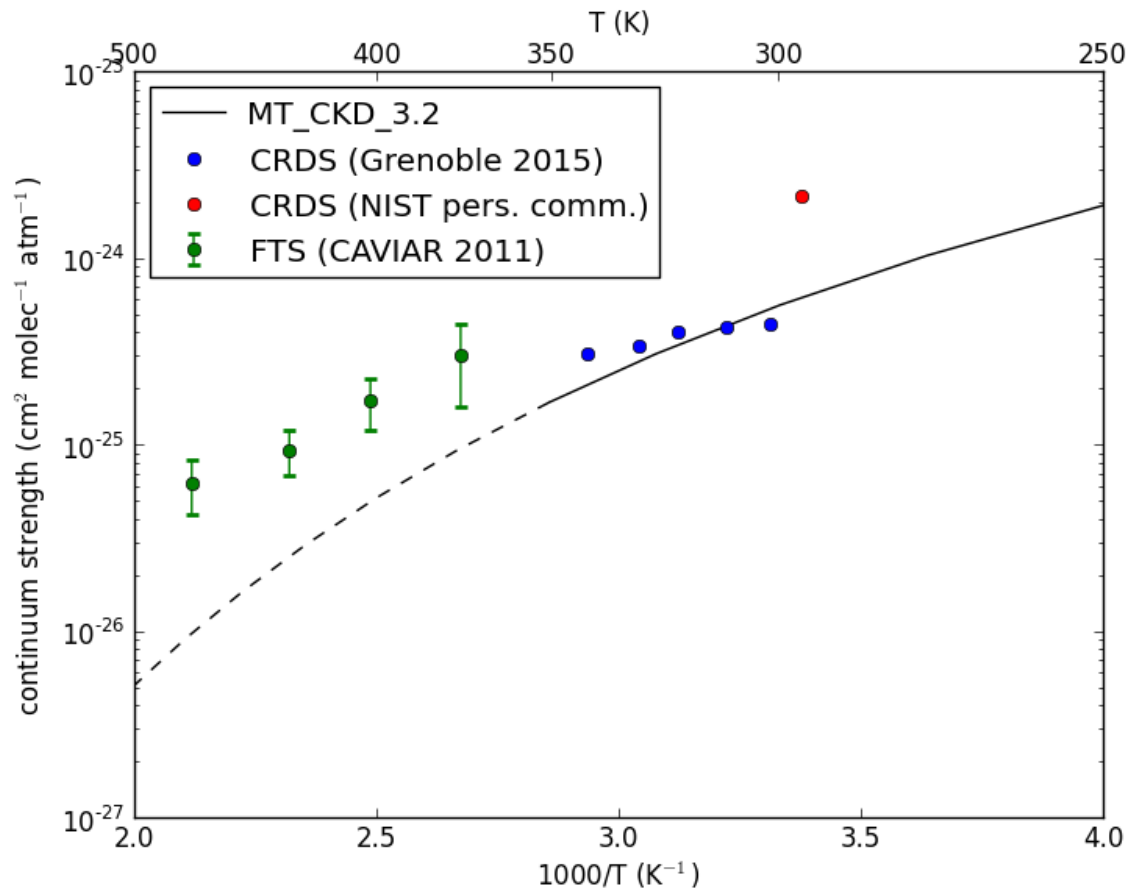


Figure 5.8: Similar to Figure 5.7, but including the NIST data point (all observations at $\nu = 6121 \text{ cm}^{-1}$). Stated uncertainties in the Grenoble and NIST measurement are smaller than the symbol size. (With thanks to Joe Hodges and Keith Shine).

5.2.7: Atmospheric observations of the near-IR continuum

Reichert and Sussmann [2016] presented continuum values derived from measurements taken at the high altitude Zugspitze site in the German Alps (47.42° N, 10.98° E; 2964 metres above sea level). This was done using a spectrometer calibrated using a combination of Langley-derived top of atmosphere irradiance, a medium-temperature (~1970 K) blackbody and an assumed SSI from a radiative transfer model [Reichert *et al.*, 2016]. There are several issues with these

measurements and with the calibration process however, particularly for the stated aim of measuring continuum absorption in the 2.1 and 1.6 μm windows. These are expressed more fully in *Shine et al.* [2016a, 2016b], on which I was a co-author, and will be discussed in the following paragraphs.

These measurements, unlike the previous measurements mentioned in this Chapter, were taken in the atmosphere using the Sun as a radiation source. These are ostensibly the most immediately comparable measurements to the ones presented in this thesis. However, there are a number of significant differences which make comparison between these two datasets challenging. The Zugspitze work is taken at high altitude, meaning that the vapour pressure is significantly lower, so it is expected that the foreign-continuum will dominate over the self-continuum. This makes it difficult to compare with the CAVIAR field measurements since this is mostly either self-continuum (in the 2.1 μm window) or a combination of the two (in the 1.6 μm window); these are very difficult to separate without making some significant assumptions about the relative effect of each of these components (in the absence of measurements over a wide range of conditions).

While a high altitude site makes it more difficult to measure the effect of water vapour due to the lower vapour pressures (most of the water vapour is concentrated in the lower troposphere), this also means that the observation site is above the atmospheric boundary layer. This means that the effect of aerosol scattering is strongly reduced, which aids the analysis of the measurements and reduces the measurement uncertainty. These measurements were also taken near the winter solstice, in contrast to the measurements in this work. This means that the atmospheric path is longer due to the larger zenith angles, which mitigates the lower water vapour concentrations. However, the effect of atmospheric refraction becomes more pronounced at these higher zenith angles, which introduces additional uncertainty. The lower water vapour concentration does not allow for easy measurement in the windows; however this also allows for measurements to be taken at band centre, since unlike in the Camborne measurements these are not saturated.

The large airmass factors involved also present an issue for Langley extrapolation for the calibration procedure, since a long extrapolation must be made from the data points at the lowest observed airmass (~ 6 airmasses, *Reichert et al.* [2016]) to zero

airmass. The *Reichert and Sussmann* results are primarily derived using the closure technique, making the calibration of their instrument of primary importance.

Figure 5.9 shows the *Reichert* results against two versions of the MT_CKD model (2.5 and the BPS-MT_CKD 2.0 model developed at GFDL (e.g. *Paynter and Ramaswamy* [2014]) which brings the MT_CKD 2.5 model more in agreement with the *Mondelain et al.* [2013, 2014] values in the 2.1 and 1.6 μm windows. These values are only shown where the uncertainty at $k = 2$ (95% confidence interval) does not exceed the central value, i.e. the uncertainties do not overlap with an absorption coefficient of zero. These show that it was not possible to derive combined self + foreign continuum coefficients in the centres of these windows in their measurement conditions.

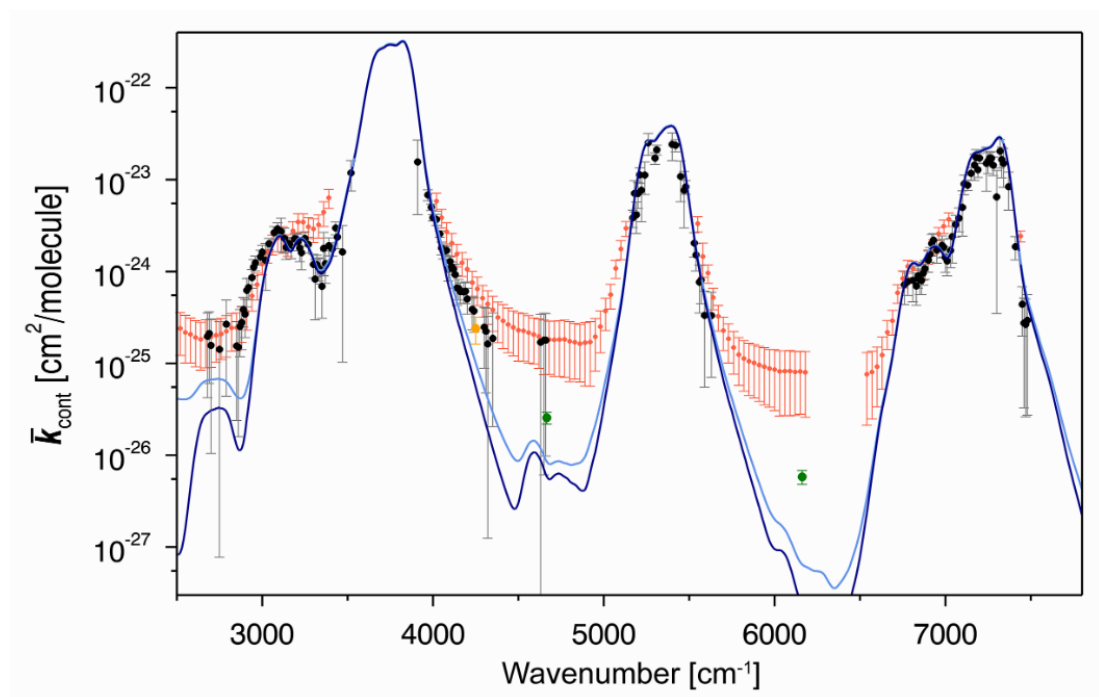


Figure 5.9: Absorption coefficients (in black) from *Reichert and Sussmann* [2016], alongside MT_CKD 2.5 (light blue line), the BPS-MT_CKD 2.0 model (darker blue), the *Bicknell et al.* measurements (green points) and the *Ptashnik et al.* [2013] measurements (red points). Points are only shown where the continuum values exceed the $k = 2$ uncertainties. Figure from *Reichert and Sussmann* [2016].

Nevertheless, the *Reichert* papers are significant advances in our understanding of the in-band continuum in the atmosphere, and physical values are presented in the

2.1 μm window and band edges. These values seem to be in good agreement with the *Ptashnik et al.* [2013] values, although the large uncertainties mean they are also consistent with MT_CKD. Perhaps more important for atmospheric studies is the calibration method described in *Reichert et al.* [2016]; as our understanding of the SSI becomes more robust, the calibration method could be used readily in the field to get absolute measurements of radiation and absorption without needing to go to the lengths described in Chapter 3 and *Gardiner et al.* [2012].

An additional, unpublished set of atmospheric continuum measurements was presented by *Mlawer et al.* [2014]. These do not include uncertainties, which makes them difficult to reconcile either with the work presented in Section 5.3 or the previous laboratory measurements. Since these results are unpublished, and there were significant difficulties in e.g. removing the effects of aerosols, these results are not included in the comparisons presented in this thesis.

5.3: Derivation of continuum using Camborne measurements

5.3.1: Introduction

The FTS measurements of 22 August 2008 and 18 September 2008 are used here to derive an estimate of the continuum absorption in the atmosphere. Optical depths are derived using both the Langley method and the radiative closure method using the CAVIAR2 SSI from Chapter 4. The continuum is hence derived using this total atmospheric optical depth via:

$$(5.1) \quad \tau_{cont} = \tau_{total} - \tau_{H_2O} - \tau_{gas} - \tau_{Rayleigh} - \tau_{aerosol} - \tau_{other}$$

In this case, extinction due to clouds is considered negligible due to the spectra being taken only during clear skies, and the DC voltage filtering removing any scans where invisible clouds could have passed through the FOV of the instrument. Here, τ_{H_2O} is the *line* absorption due to water vapour, and τ_{gas} the line absorption due to other atmospheric gases. τ_{other} in this case refers to other sources of continuum absorption (e.g. from CO_2), or collision-induced absorption such as that of O_2 at $\sim 8000 \text{ cm}^{-1}$. $\tau_{aerosol}$ is the aerosol optical depth, referred to in various other places in the thesis as

AOD. The values of τ_x used to generate τ_{cont} come from either models or observation as discussed below.

Figure 5.10 shows a schematic of how the various pieces of data described in Chapter 3 are put together to derive the continuum.

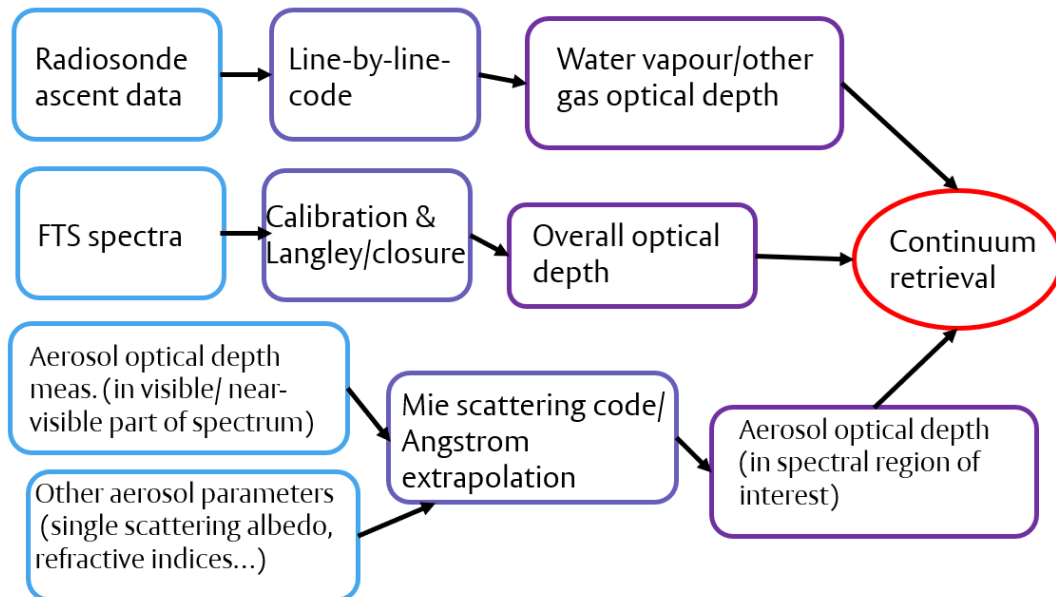


Figure 5.10: Schematic of the continuum derivation process. The Ångström extrapolation is not used in itself, but is used as a constraint on the Mie scattering calculations.

As described in Section 3.3.3, the Langley-derived optical depth spectra are preferred, since they have a smaller uncertainty than the closure-derived spectra, as no prescribed SSI is required (which has uncertainties). The spectra from 18 September are considered more robust, since the AOD is smaller (in the spectral region of interest, see Chapter 3.4.5.2), and there are spectral features in the spectra of 22 August which are spurious (see Chapter 3.4.4.1 and Figure 3.21). The closure-derived spectra from 18 September are used as a cross-check to the Langley-derived values. The closure and Langley-derived spectra from 22 August are used to compare to the 18 September spectra; differences in water vapour concentrations between the two days mean that they are not directly comparable without making some assumptions about the relative effects of the foreign and self-continuum. This will be explored further in Chapter 6.

5.3.2: Retrieval of continuum optical depth from observed optical depth

The following section describes the process used to derive the continuum optical depth from the Langley-derived optical depths (see Chapter 3.3.2). Each component in Equation (5.1) is considered in turn and is subtracted from the total observed optical depth to derive the continuum. This is then subject to smoothing to present a best-estimate Langley-derived continuum. The subsections describe how each of these components of the overall optical depth are derived, with reference to the relevant Sections in Chapter 3 as necessary.

5.3.2.1: Observed optical depth

As described in Chapter 2.13, the NIR region is home to many spectral lines; these are primarily due to water vapour, but with some localised bands due to e.g. CO₂ and CH₄. The absorption in the atmosphere is saturated in much of this region (particularly within the strong water vapour bands); the spectrometer therefore observes no radiation in these regions. This means that the spectrometer cannot measure beyond a certain optical depth.

Figure 5.11 shows the observed optical depth in the 2000-10000 cm⁻¹ spectral region. The observed optical depths are only presented at points where a) a Langley analysis was possible (see Chapter 3.3.2 and 3.4.3), and b) where the total optical depth at that wavenumber in either the model or the observations did not exceed 0.5. This is to ensure that misattribution of spectral lines (either positioning or strength) does not affect the derived continuum. The observations show the same band-window structure as the atmospheric optical depth (black line on Figure 5.11) derived from the model simulations; however since the observations include aerosol extinction, Rayleigh scattering and continuum absorption the baseline (i.e. the lower envelope of the data points) is higher.

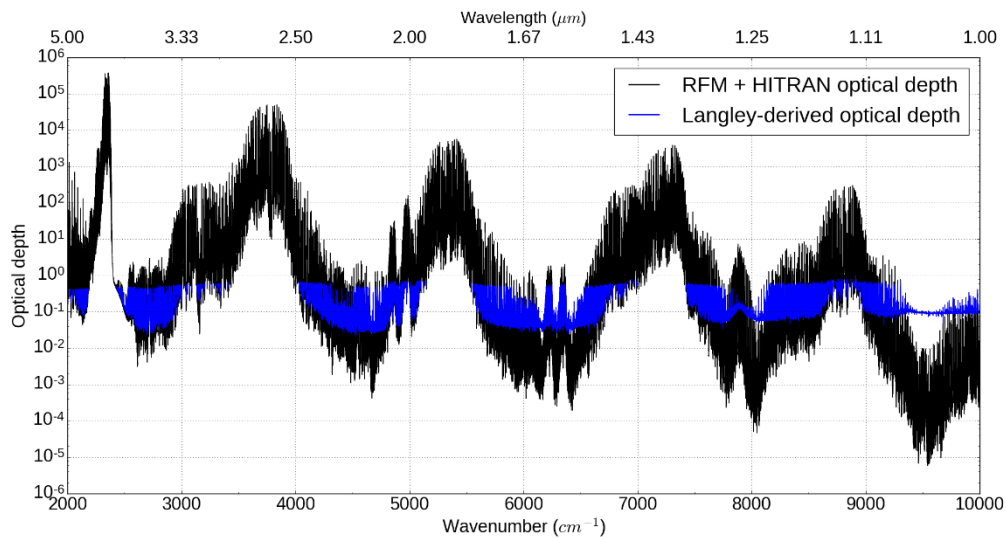


Figure 5.11: Observed optical depth from the Langley analysis of 18 September 2008 in the NIR spectral region (blue), alongside the modelled optical depth (black). The observed optical depth is only shown where it or the modelled optical depth is less than 0.5.

The following sections discuss the process by which the continuum is extracted from the total optical depth in a small spectral region. This process is applied to all of the wavenumbers in the 2000-10000 cm^{-1} interval.

5.3.2.2: Optical depth from gaseous absorption

As described in Chapter 2.3.3 and 2.3.6, absorption (optical depth) by atmospheric gases is determined from a line-by-line code, with atmospheric parameters determined from radiosonde ascents, and contemporary CO_2 and CH_4 concentrations (Chapter 3.4.5.1) as input. These optical depths are subtracted from the observed optical depths, which in principle should leave only continuous absorption (i.e. absorption that does not vary sharply with wavenumber, such as via Rayleigh scattering, water vapour continuum and aerosol extinction). In practice, this is not necessarily the case, since there will be mismatch between line positions, broadening and strength from the spectrometer compared to those from HITRAN/RFM, which is particularly the case given the high spectral resolution of the FTS observations. Sensitivity tests were performed using the range of uncertainty in the radiosonde (in temperature, water vapour mixing ratio and pressure) to model such an offset within the uncertainty budget. This effect is additionally mitigated via smoothing of the final continuum spectrum (see Chapter 3.4.3.5).

Optical depths will be compared within the two atmospheric windows of most interest; the 1.6 and 2.1 μm windows. Figure 5.12 shows a comparison of the modelled (line-by-line) optical depth spectrum with the Langley-derived optical depth from 18 September 2008 within the 1.6 μm window. While the baselines are significantly different due to the lack of aerosol or continuum in the model run, the main spectral features are consistent between them, both in terms of lineshape and position as well as intensity.

There is additional noise in the observed optical depth spectrum shown in Figure 5.12; this noise matches up with positions of solar lines (see Chapter 3.4.3.5), indicating that this may be due to shifting solar lines throughout the day, or some instrumental issue. These are filtered out, so do not affect the derived continuum.

This feature is present both in the Langley-derived spectra and the closure-derived spectra (not shown), indicating that it is not due to incorrect line positions in the *chosen* SSI (since this is not required in the Langley method). These artefacts should have little impact on the derived continuum since this is subject to smoothing; to further mitigate this a filter of $\sim 0.1 \text{ cm}^{-1}$ either side of a solar line (obtained from the CAVIAR2 SSI from Chapter 4) is applied to remove these effects (see Section 3.4.3.5).

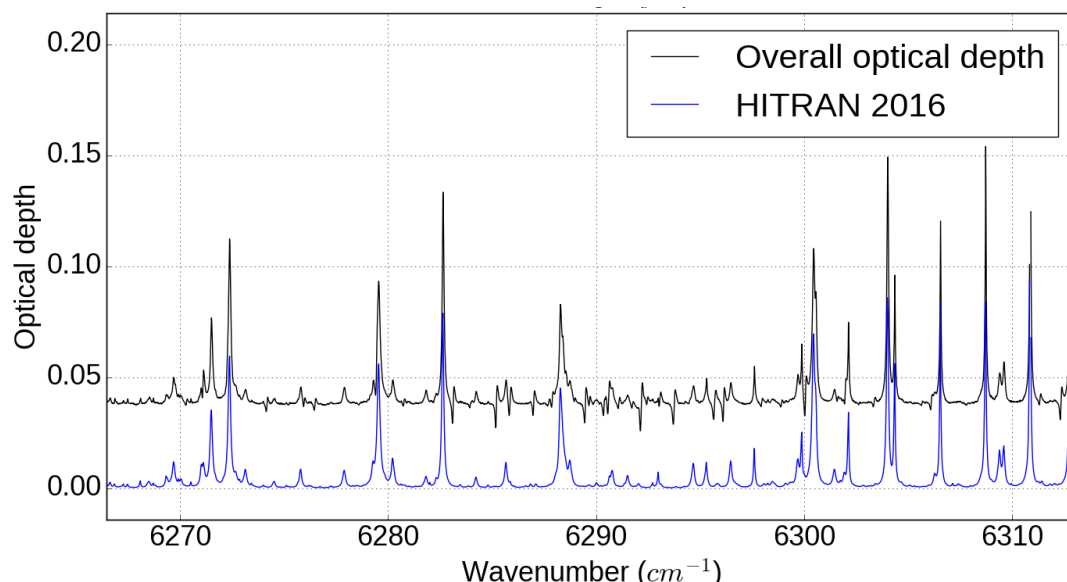


Figure 5.12: Total observed optical depth from 18 September 2008, via the Langley method, and derived optical depth from a line-by-line simulation using HITRAN 2016 using radiosonde data for the atmospheric profile. This plot shows a localised set of water vapour lines in the 1.6 μm window.

Figure 5.13 shows the same within part of the 2.1 μm window. In this case, two of the lines are somewhat stronger than those in Figure 5.12, as can be seen in the feature at $\sim 4682\text{ cm}^{-1}$ where the tip of a (relatively) strong water vapour line has been filtered out. This prevents incorrect derivation of continuum optical depth, which could happen when subtracting a very large optical depth from a model run from a markedly smaller optical depth from the observations in regions where the atmospheric absorption is saturated. In this part of the window, the noise is less obvious.

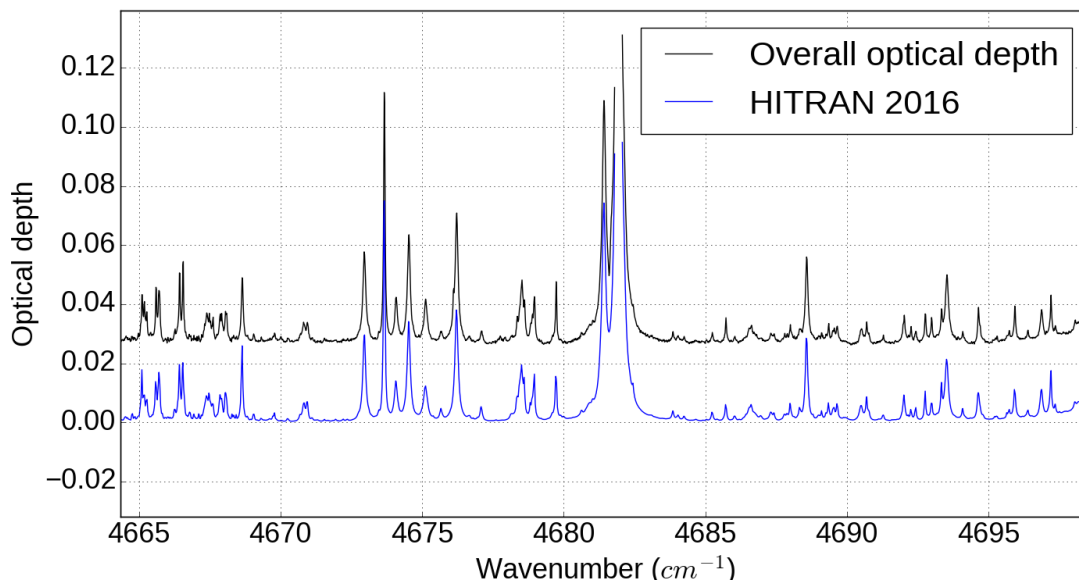


Figure 5.13: Total observed optical depth from 18 September 2008, via the Langley method, and derived optical depth from a line-by-line simulation using HITRAN 2016, using radiosonde data for the atmospheric profile. This plot shows a localised set of water vapour lines in the 2.1 μm window.

5.3.2.3: Optical depth from Rayleigh scattering

Rayleigh scattering is a second-order effect in the near-IR due to its strong wavelength dependence; however it is not entirely negligible. In this study, mid-latitude summer Rayleigh optical depths from *Bucholtz* [1995] are used, and subtracted directly from the optical depth observed by the spectrometer. This is described in more detail in Chapter 3.3.4. The Rayleigh scattering optical depth is shown in Figure 3.6.

5.3.2.4: Optical depth from aerosol extinction

By far the largest source of uncertainty in the calculation of τ_{cont} is the contribution of aerosol extinction. While most important in the visible and UV spectral regions, aerosol extinction is still perhaps the dominant contributor to optical thickness in the near-IR atmospheric windows. It is especially difficult to separate from the continuum signal since like the continuum, the spectral behaviour of aerosol extinction is generally smooth. In addition, most methods of measuring aerosol extinction use channels in the visible or near-visible part of the spectrum; therefore these measurements have to be extrapolated into the near-infrared. In this work, the only source of direct aerosol measurements are concurrent measurements taken using the Microtops sunphotometer in 5 different channels between 0.436-1.020 μm .

The Langley method assumes constant optical depths for all components; however as seen in Figure 3.28 $\tau_{aerosol}$ changes throughout the course of a day. While this has little effect on the y-intercept of a Langley fit (the absolute changes are small, and therefore the SSI is almost entirely unaffected), the gradient is much more sensitive to these changes. This variation is not evident when looking at the derived optical depth from the FTS spectra, which led to concerns about the accuracy of the Microtops instrument (see Section 3.4.5.2). Figure 3.28 shows the observed time variation of $\tau_{aerosol}$ from the Microtops measurements at 1.02 μm alongside the observed time variation of the optical depth from the spectrometer at 1.02 μm with the line and Rayleigh contributions removed (i.e. $\tau_{cont} + \tau_{aerosol}$). The time-dependent mismatch between the FTS spectra and the Microtops measurements was the primary motivation for using the daily average of the Microtops optical depths rather than time-varying values.

Another notional method of assessing $\tau_{aerosol}$ independent of the sunphotometer is to take the spectral values measured at $\sim 9500 \text{ cm}^{-1}$ by the FTS. The continuum in this region as measured in the laboratory is vanishingly small; in e.g. *Ptashnik et al.* [2013] it is assumed to be zero. While this may not be the case in these lower-temperature conditions, it is at least a useful exercise to determine what kind of near-IR $\tau_{aerosol}$ arises from assuming all the extinction in this window to be due to aerosol (after removing Rayleigh scattering). The raw optical depth derived in this window is relatively large (around 0.1, see Figure 5.11); this is possibly because this window is

right on the edge of the range of the detector used in the spectrometer (see Chapter 3.4.3.1).

This in turn leads to large implied aerosol values that result in negative continuum values in the near-IR windows. The spectral variation of this implied aerosol scattering would then be derived using the Mie scattering model. In practice, this method is not used, since it leads to unphysical values of the continuum absorption in the other near-infrared windows and does not account for other possible contributors to the optical depth in the 1.02 μm window (e.g. continuum absorption) or spectrometer issues. Chapter 7 describes ways in which this could be improved in a future experiment. For example, using a spectrometer with greater sensitivity in the near-visible part of the spectrum could better quantify the extinction at these wavelengths and improve consistency between the Microtops measurements and the FTS. This would act as a better constraint on $\tau_{aerosol}$ in the spectral regions of interest to this work.

As discussed in Chapter 3.3.5 and 3.4.5.2, a Mie scattering code was used to quantify the spectral behaviour of the aerosol extinction in the spectral region of interest, as it is more physically-based than the Ångström extrapolation. This was done using the average AOD measured across the day, since as will be shown in Figure 5.22 the derived τ_{cont} (using the closure method) are not consistent if a time-varying $\tau_{aerosol}$ correction is applied. Figure 5.14 shows the aerosol optical depth used for 18 September.

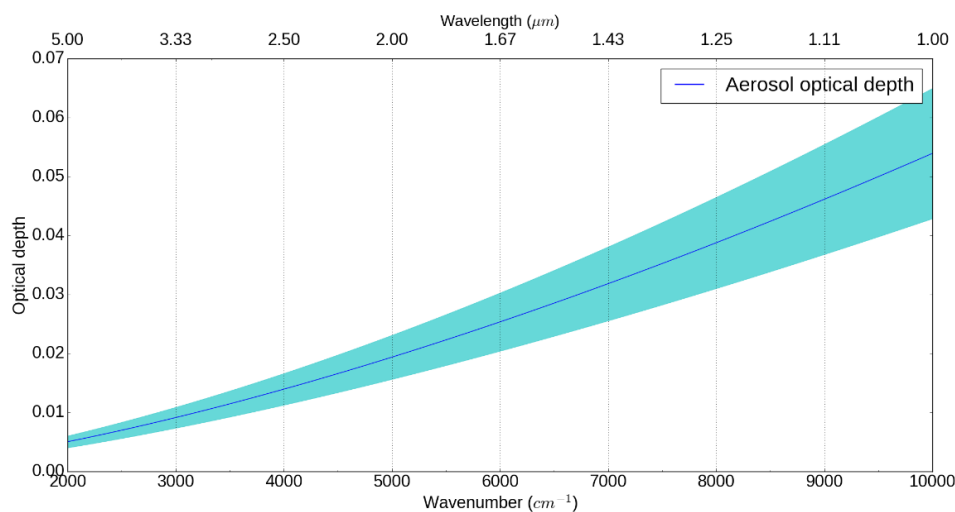


Figure 5.14: $\tau_{aerosol}$ for 18 September derived from the Mie scattering calculations assuming an optical depth from the Microtops at 1 μm , with $k = 1$ uncertainties.

5.3.2.5: Continuum absorption

Figure 5.15 shows a step-by-step schematic of the continuum derivation process in a small spectral region in the 1.6 μm window, beginning with the derived optical depth and subtracting each component of the optical depth in turn. In this case, τ_{other} in Equation (5.1) is assumed negligible. Figure 5.15 shows the case inside the 1.6 μm window for the Langley analysis of 18 September 2008. A comparison of the closure-derived to the Langley-derived continuum for both 18 September 2008 and 22 August 2008 is presented in Section 5.5.1.

The derived continuum in Figure 5.15 has a smooth baseline, with large peaks and troughs, which are caused by mismatches in spectral line positions between the model simulations and the spectrometer output (see Section 5.3.2.2). These are mitigated by smoothing over 15 cm^{-1} , as shown in Figure 5.16. This smoothing introduces minimal change in the baseline (and therefore the derived continuum). These results are examined in more detail in Section 5.5.

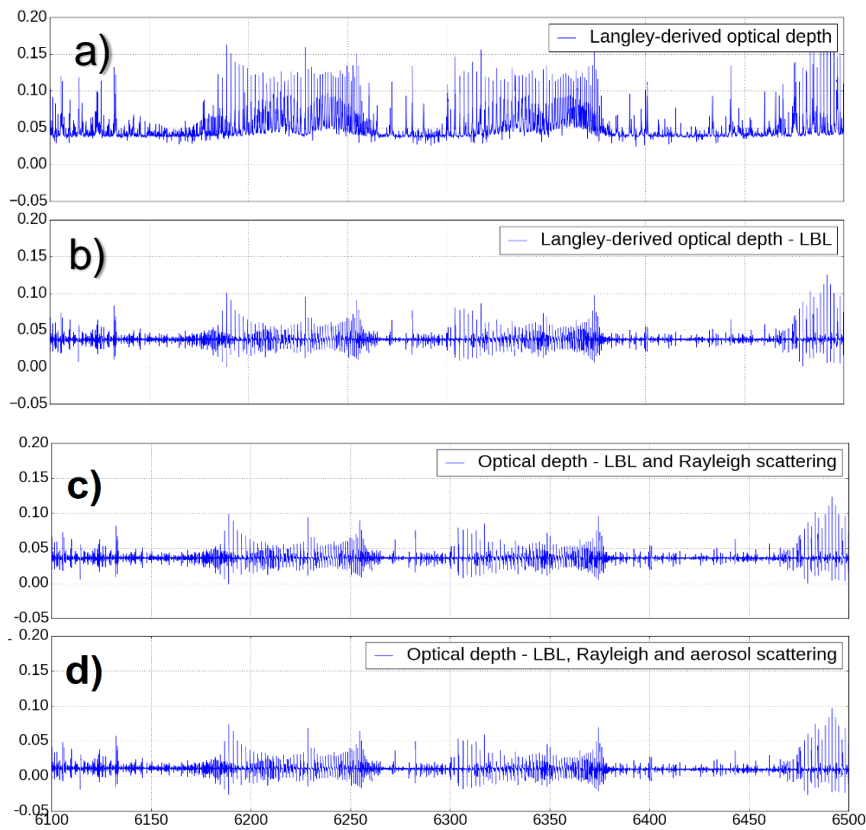


Figure 5.15: Derivation process of the continuum absorption as seen in the 1.6 μm window. The observed total optical depth is shown in (a), from which contributions from the line-by-line code (b), Rayleigh scattering (c) and aerosol (d) are subtracted to obtain the derived continuum (d). The final continuum is then smoothed (see Figure 5.16).

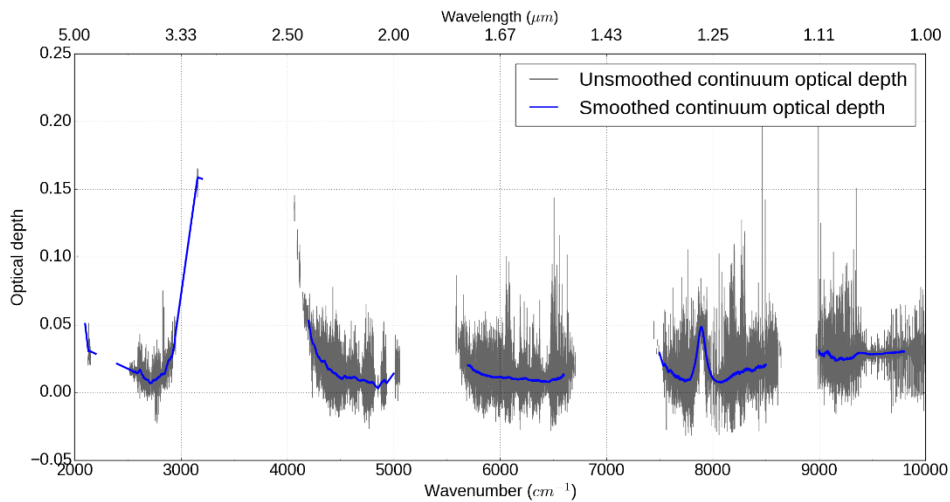


Figure 5.16: *Derived continuum from the Langley analysis of 18 September 2008, both smoothed and unsmoothed between 2000-10000 cm^{-1} .*

5.4: Uncertainty budget

The uncertainty budget is a combination of uncertainty from the observations themselves, the ancillary observations used to generate the other contributors to the total extinction, uncertainties in the radiative transfer model and line database, and in the case of aerosol extinction the assumptions used in determining the near-infrared spectral behaviour. These are all combined to determine the final uncertainty in the continuum. The experimental uncertainties were presented in Section 3.4.3.4. The uncertainty in aerosol scattering was presented in Section 3.4.5.2, using the method discussed in Section 3.3.5.2. When using the closure method, an additional uncertainty is introduced through the use of an assumed SSI. In this case, the uncertainty is that of the CAVIAR2 spectrum derived in Chapter 4.

Figure 5.17 shows the relative contribution of each component of the uncertainty budget. The contributions from aerosol and the measurement are larger than the model uncertainty within the 1.6 μm window. Note that these uncertainties are added in quadrature: the line by line uncertainty is therefore dominant in the edges of the windows (where the lines are strongest), and the aerosol/observational uncertainties dominate in the centres. For part (a) of this Figure, the line-by-line uncertainty (discussed in Chapter 3.4.5.1) has been smoothed over 15 cm^{-1} for visual clarity. The relative contribution of the line-by-line uncertainty in between microwindows is therefore exaggerated, and underestimated where individual lines are located. Part

(b) of this Figure shows the relative contribution inside the 2.1 μm window, indicating that the LBL uncertainty is significantly smaller than the aerosol and measurement uncertainty within microwindows without this smoothing.

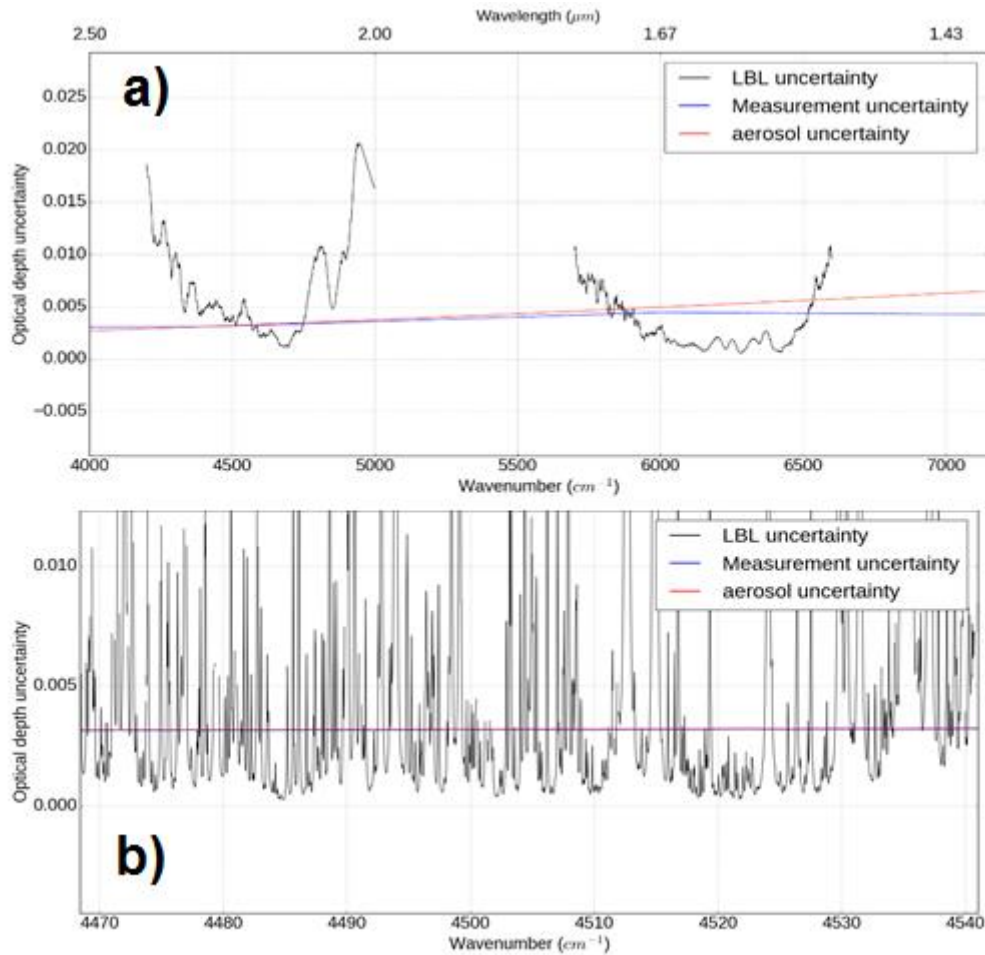


Figure 5.17: Contribution of each part of the uncertainty budget (in this case for 18 September 2008): these are added in quadrature to obtain the final uncertainty. Part (a) shows the uncertainty across the 1.6 and 2.1 μm windows. The uncertainty in the line-by-line simulations is smoothed here as a visual aid; this smoothing is not applied when calculating the uncertainty in practice. Part (b) shows the uncertainty in a small part of the 2.1 μm window, without smoothing.

5.4.1: Observational uncertainties

The observational uncertainties are derived in the same manner as Chapter 4, as described in Chapter 3 and in *Gardiner et al.* [2012]. Again, a Monte Carlo method (Section 3.3.7) is used to derive the uncertainty in the Langley fit, this time focusing

on the slope rather than the intercept. The uncertainty in the closure-derived optical depth is a composite of the uncertainty in optical depth derived from the measurement and SSI, and the statistical spread of the observations which are added in quadrature.

5.4.2: Uncertainties in the model-derived optical depth

The uncertainty in the model-derived optical depth is a combination of uncertainty inherent within the radiative transfer model, uncertainty in the spectroscopic quantities within HITRAN, and uncertainty in water vapour, temperature and pressure from the radiosonde ascent used to construct the atmospheric profiles.

The uncertainty from HITRAN is not well-quantified (see Section 2.3.6.2); each line has an “uncertainty parameter” associated with it which provides a range of uncertainties within which the true value lies. Different contributors of data to the HITRAN database (whether experimental or theoretical) may have different definitions of what these uncertainty parameters may mean, since they are ultimately arbitrary. The lack of strong quantification means that these are not included in this work. Additional uncertainty from the broadening and strength of lines is included via sensitivity tests using 5% uncertainty in the radiosonde-derived atmospheric parameters (see Section 3.4.5.1).

The uncertainty in the model is obtained via sensitivity tests using the stated uncertainty in the radiosonde observations. These differences in temperature, pressure and WV will result in different amounts of absorption and broadening between model runs taken using these adjusted parameters. Most of this uncertainty is within spectral lines; since these are predominantly filtered out, only the far-wing effects are important for deriving continuum within the microwindows (see Figure 5.17 (b)). This uncertainty is rather small and is almost negligible when compared with the uncertainty from the observations and from the aerosol within these microwindows. The uncertainty in other atmospheric extinction (e.g. absorption due to non-measured gases, Rayleigh scattering etc.) is more difficult to quantify, since these values are either taken from standard atmospheres (in this case the US Standard atmosphere), or from observations (in the case of well-mixed gases like CH₄ and CO₂), or otherwise calculated without direct observations (Rayleigh scattering). These are assumed to be minor effects however and are only important in narrow

spectral regions. They should not contribute significantly to the uncertainty, and are therefore neglected.

5.4.3: Uncertainties in aerosol measurements

Using the Mie scattering code to generate uncertainties is challenging. The lack of well-defined input parameters (since they are coming from climatological values, which have a broad range) means that the uncertainty budget needs to be derived in a more *ad hoc* manner. This is discussed in more detail in Section 3.3.5.2. Due to the large number of parameters controlling aerosol extinction and the wide ranges thereof, it is difficult to determine the exact range of the uncertainties. The best estimate of the uncertainties used here is presented in Figure 3.29, derived via sensitivity tests using the Mie scattering code for the range of parameters in *Dubovik et al.* [2002].

5.5: Results and analysis

5.5.1: Best estimate of the derived continuum

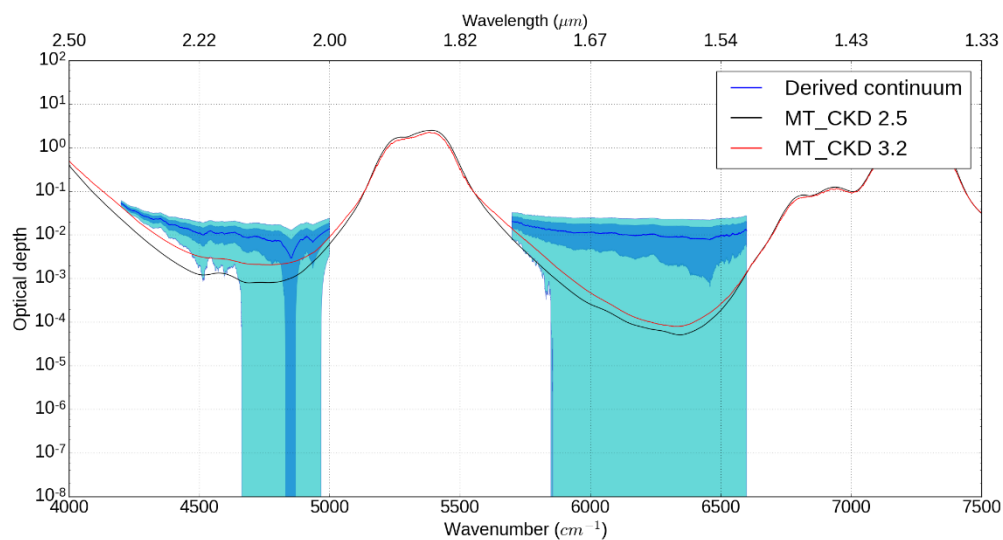


Figure 5.18: Best estimate of the water vapour continuum (Langley analysis of 18 September 2008) in the 1.6 and 2.1 μm windows (blue line, $k = 1$ uncertainties in blue and $k = 2$ uncertainties in cyan) compared with MT_CKD 2.5 (black) and 3.2 (red).

Figure 5.18 shows the final best estimate of the continuum (from the Langley analysis of 18 September 2008), with the corresponding best estimate of the uncertainty ($k = 1$ in blue and $k = 2$ in cyan) on those values, focusing on the two windows of interest. Relative to MT_CKD, the central values are significantly stronger; a factor of ~ 10 in the $2.1 \mu\text{m}$ window and a factor of ~ 100 in the centre of the $1.6 \mu\text{m}$ window. Of particular interest is the spectral shape of the derived continuum; this is similar to the behaviour from the FTS self-continuum measurements from the laboratory (e.g. Ptashnik et al. 2011), in that the strength (at least in logarithmic space) appears to be reasonably constant across the window. This increase in strength also appears consistent with the relative strengths of the FTS laboratory measurements and MT_CKD at room temperature (see Chapter 6 for a more detailed analysis).

It is important to emphasise that MT_CKD has no uncertainties associated with it, which makes any assertions about consistency with MT_CKD difficult to make. A lack of consistency between a given measurement analysis and MT_CKD is indicative that the model requires strengthening, assuming that there are no systematic errors unaccounted for in the experiment and that the uncertainty budget is reasonably characterised. Agreement between a given measurement and MT_CKD does not provide compelling evidence for a given continuum being correct; this can only be determined through comparison of the relevant experimental data.

The $k = 1$ (67% confidence interval) uncertainty limits appear to be inconsistent with MT_CKD in this instance. This is despite the large uncertainty introduced from the range of plausible aerosol values, and the relative contribution of the measurement uncertainty. This indicates that the value is *likely* not to be consistent with MT_CKD. However, the overlap between the two in their $k = 2$ uncertainties (aside from in the low-wavenumber edge of the $2.1 \mu\text{m}$ window) means that the two are not necessarily inconsistent (unlike the room temperature FTS measurements). This is not unexpected, given the challenges faced in measuring the continuum in atmospheric conditions. The central values in all of the windows here are above zero; this is in contrast to the values of *Reichert and Sussmann* [2016] which showed predominantly negative values in the $1.6 \mu\text{m}$ window. The significantly lower $k = 2$ uncertainties in the low wavenumber edge of the $2.1 \mu\text{m}$ window are indicative of a stronger continuum than predicted by MT_CKD in this region.

These values are significantly lower than the values presented in Figure 7.15 of *Menang* [2012]. This is in significant part due to the updated calibration procedure used in this thesis. The *Menang* results also do not include a detailed uncertainty estimate; the detailed assessment of the uncertainty budget in this thesis indicates that *Menang* [2012] was over-optimistic in their assessment of the uncertainty.

Figure 5.19 shows the ratio of the Camborne-derived continuum optical depth to that of MT_CKD 2.5 and 3.2, with the corresponding uncertainty. The continuum strength is $\sim 4x$ stronger than MT_CKD 3.2 in the 2.1 μm window, and about 20x stronger in the centre of the 1.6 μm window; this is somewhat consistent with the CAVIAR self-continuum measurements of *Ptashnik et al.* [2011] but does not show enough of an increase to account for the Tomsk FTS values discussed in Section 5.2.1. These results indicate that MT_CKD significantly underestimates atmospheric absorption in these windows. Chapter 6 will present more detailed analyses of these measurements in relation to the laboratory spectra and discuss the relative contribution of the foreign and self-continuum.

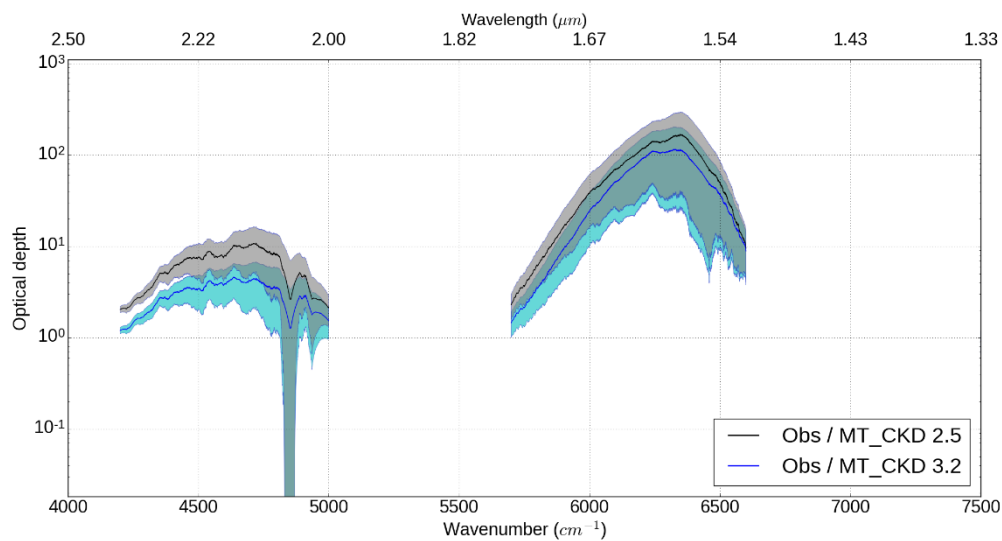


Figure 5.19: Ratio of the Langley-derived continuum derived from 18 September 2008 to MT_CKD 3.2 and 2.5, with corresponding $k = 1$ uncertainties. The $k = 2$ uncertainties are not shown, but overlap with zero.

Figure 5.20 shows the derived continuum optical depth across the 2000-10000 cm^{-1} range, compared with MT_CKD 2.5. In this case, the dark blue line shows the central values, the medium blue the $k = 1$ uncertainties and the cyan the $k = 2$ uncertainties.

Within the regions of interest, the $k = 2$ uncertainties overlap with the MT_CKD uncertainties.

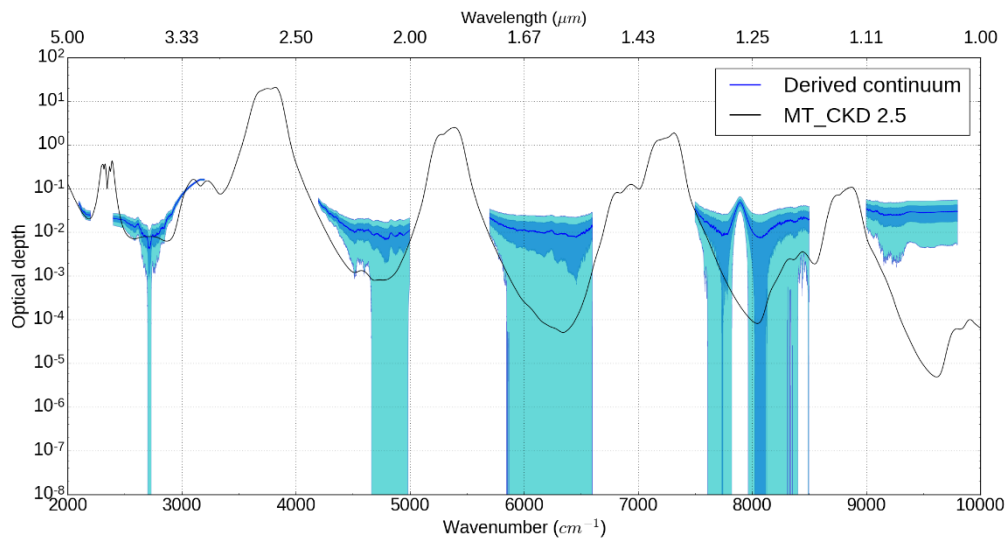


Figure 5.20: Langley-derived continuum optical depth from 2000-10000 cm^{-1} for 18 Sept 2008. The blue shaded regions are the $k = 1$ uncertainties, the cyan regions the $k = 2$ uncertainties.

There are a few features in this Figure that are noteworthy. The continuum in the window at 1.25 μm is also significantly stronger than the MT_CKD water vapour continuum; however the presence of a strong O_2 continuum band which is not present within the RFM is important, since it strengthens the absorption in the centre of this window and means that the two cannot be compared directly.

The derived continuum in the window at $\sim 4 \mu\text{m}$ appears to be in reasonable agreement with MT_CKD in the centre of the window; this is not the case towards the edges of the bands either side. This agreement with MT_CKD also indicates agreement with the laboratory spectra of *Baranov and Lafferty* [2012], and with the CAVIAR [*Ptashnik et al.*, 2012] data (shown on Figure 5.3). This is in contrast to the CRDS measurements of *Lechevallier et al.* [2018] (shown on Figure 5.5), which are lower by roughly an order of magnitude.

The observed optical depth at $\sim 9500 \text{ cm}^{-1}$ is very large relative to MT_CKD; the reason for this is unknown. It was speculated that the feature at 1 μm may be due to an underestimation of the required correction or the uncertainty in the mirror reflectivity (see Section 3.4.3.2). This was motivated by the mirror reflectivity correction being an extrapolation beyond 6600 cm^{-1} , which in this case would lead to

an overestimation of the signal. However, the following demonstrates that this is unlikely to be the case. An adjustment of the mirror reflectivity would lead to a systematic change in the observed irradiances at a given wavenumber. This adjustment would be the same for each observation, which means that the gradient in the Langley analyses would be mostly unaffected, even when considering the shift into logarithmic space (see Figure 5.21). This also applies when calculating the uncertainty budget in the optical depth, since the separation of the systematic and random component filters out the systematic effect in the uncertainty budget.

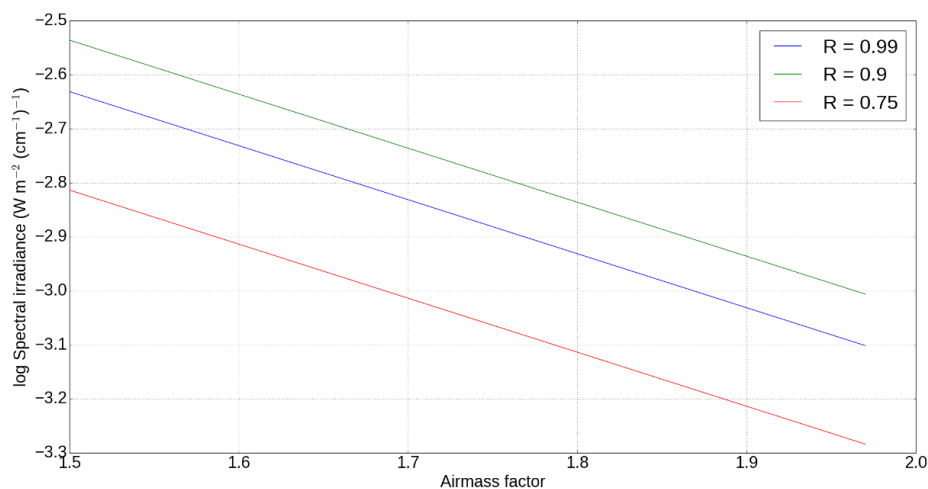


Figure 5.21: *Idealised Langley plots of a set of dummy observations adjusted by a mirror reflectivity factor R , demonstrating the lack of change in gradient even when accounting for the shift into logarithmic space.*

Therefore, the only possible effect that the mirror reflectivity could have on this is if the reflectivity changed over the period of a single day, e.g. via uncertainty in the angular dependence of the mirrors. However, the angular dependence was not observed to be particularly important from the NRR observations (see Chapter 3). This may have changed as the mirrors became aged; any ageing effects and imperfections may not be uniform across the mirrors, which may change this angular dependence. This was not considered particularly likely however.

A more compelling reason is that this is likely in part due to aerosol scattering. The uncertainty in the observations across the day and the discrepancy between the FTS spectra and the aerosol measurements certainly seem to indicate that the aerosol scattering is not correctly accounted for at these wavenumbers. This effect is less

pronounced with decreasing wavenumber and should be mostly unimportant in the 2.1 μm window (see Figures 5.14 and 5.17). The lack of well-constrained aerosol is a significant contributor to the uncertainty in the derived continuum (in contrast to the SSI, on which it has a minimal effect); ways in which this could be mitigated in a future campaign are discussed in Chapter 7.

Figure 5.22 shows the closure-derived continuum for various times across 18 September 2008 with a time-varying aerosol correction applied, to show how the offset between the FTS spectra and the Microtops measurements affects the continuum retrieval. As the observations were taken over short measurement periods (a few minutes) with long gaps (around an hour) between them, they are here averaged over these short periods. Again, the results are smoothed over 15 cm^{-1} . As discussed previously (Section 3.4.5.2), the aerosol measurements across the day showed a marked decrease that was not found in the FTS spectra; this manifests itself as an increase in continuum optical depth throughout the day. The constancy of the integrated water vapour and meteorological conditions throughout the day (Figure 3.28) indicate that it is very unlikely that the continuum is getting stronger during the course of the day, and certainly not by a factor of two. This throws further doubt on the observed time variation in τ_{aerosol} . As will be discussed in Section 5.5.2.1, the use of a day-averaged τ_{aerosol} leads to a much more consistent continuum derivation.

Also of interest here is the pattern observed at $\sim 7500\text{ cm}^{-1}$ towards the edge of the band in the 1.25 μm window, and at the low-wavenumber edge of the 1.6 μm window. It appears here that the continuum optical depth is *decreasing* at these wavenumbers into the bands in the early (07:45-10:30 UTC) retrievals, but not in the later (12:00-13:10 UTC) retrievals. The cause of this is unknown, but it is likely due to some experimental effect and should be accounted for in the uncertainty budget.

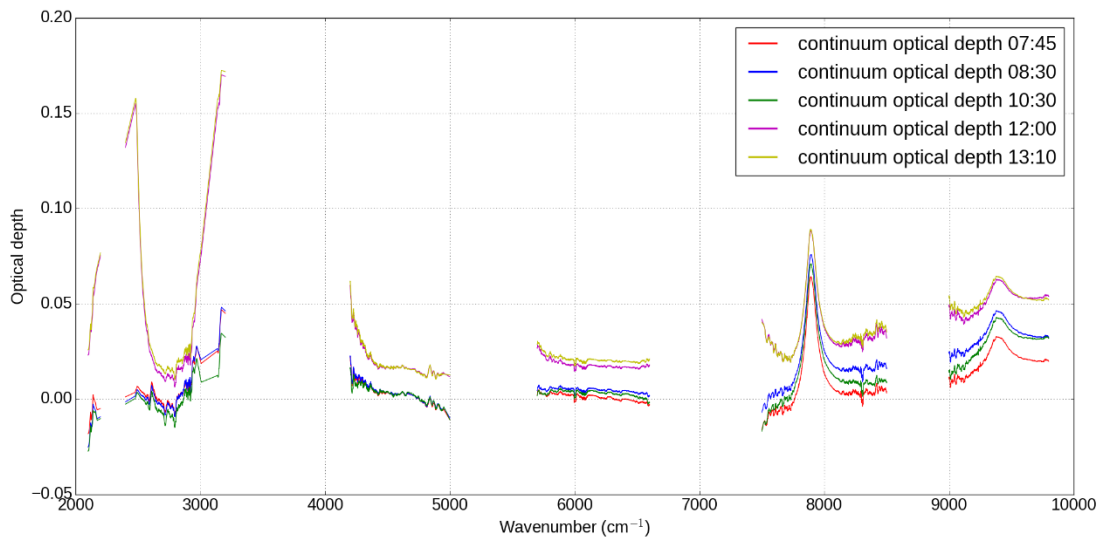


Figure 5.22: Continuum optical depth derived over 18 September 2008 at different times of the day using the closure spectra. Means are taken over observations taken over a short (~ 30 minute) time period. The uncertainties ($\sim \pm 0.04$) are large in the closure measurements however, meaning that they are generally consistent despite the differences.

5.5.2: Comparison of Langley and closure-derived continuum absorption

A key consistency check is a comparison between the Langley and closure-derived spectra; the methods are quasi-independent, since no reference is made to an SSI in the Langley method, and in principle no radiometric calibration is necessary. This is split into two sections, one for each day during which a Langley analysis was possible.

5.5.2.1: 18 September 2008

Figure 5.23 shows the closure-derived continua for 18 September 2008, using the average of the Microtops measurements across the day at $1 \mu\text{m}$ (extrapolated using the Mie code) to derive a representative $\tau_{aerosol}$ correction as in Figure 5.15. Using the same $\tau_{aerosol}$ correction in this manner significantly mitigates the spread shown in Figure 5.22; the central values of these data are very close to one another, although they do agree within the rather large uncertainties. This agreement is a strong indicator that the aerosol is not changing significantly throughout the day.

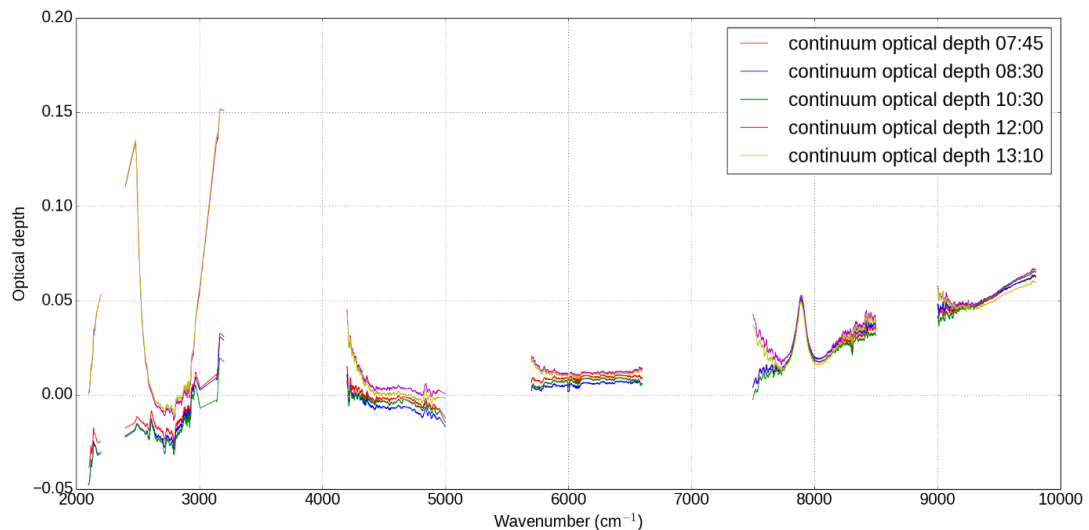


Figure 5.23: *Individual closure-derived continuum absorption from the observations of 18 September 2008, using a time-averaged AOD correction (as opposed to the time-dependent AOD correction used in Figure 5.22).*

The best estimate of the closure-derived continuum (average of these 21 observations) is presented in Figure 5.24 (a), alongside the Langley-derived spectrum. This shows the averaged continuum across the day. The continua are barely distinguishable on this Figure, indicating that they are in extremely close agreement. Figure 5.24 (b) shows the residual of these two continua, demonstrating how consistent the two are in these two windows. The difference is on the order of $\sim 1\%$ as an average across the two windows. The uncertainties in the closure-derived continuum are larger, since in this case the systematic uncertainty is not directly removed via the Monte Carlo technique, and the uncertainties in the chosen SSI are incorporated into the uncertainty budget as well. The average AOD across the day (i.e. the mean of all of the Microtops AODs measured across 18 September) was used to adjust all spectra equally (as in Figure 5.15); this led to consistent optical depths across the day (rather than the banded structure seen in Figure 5.22), which is consistent with the constant water vapour observed from the HATPRO and radiosonde ascents (see Figure 3.28).

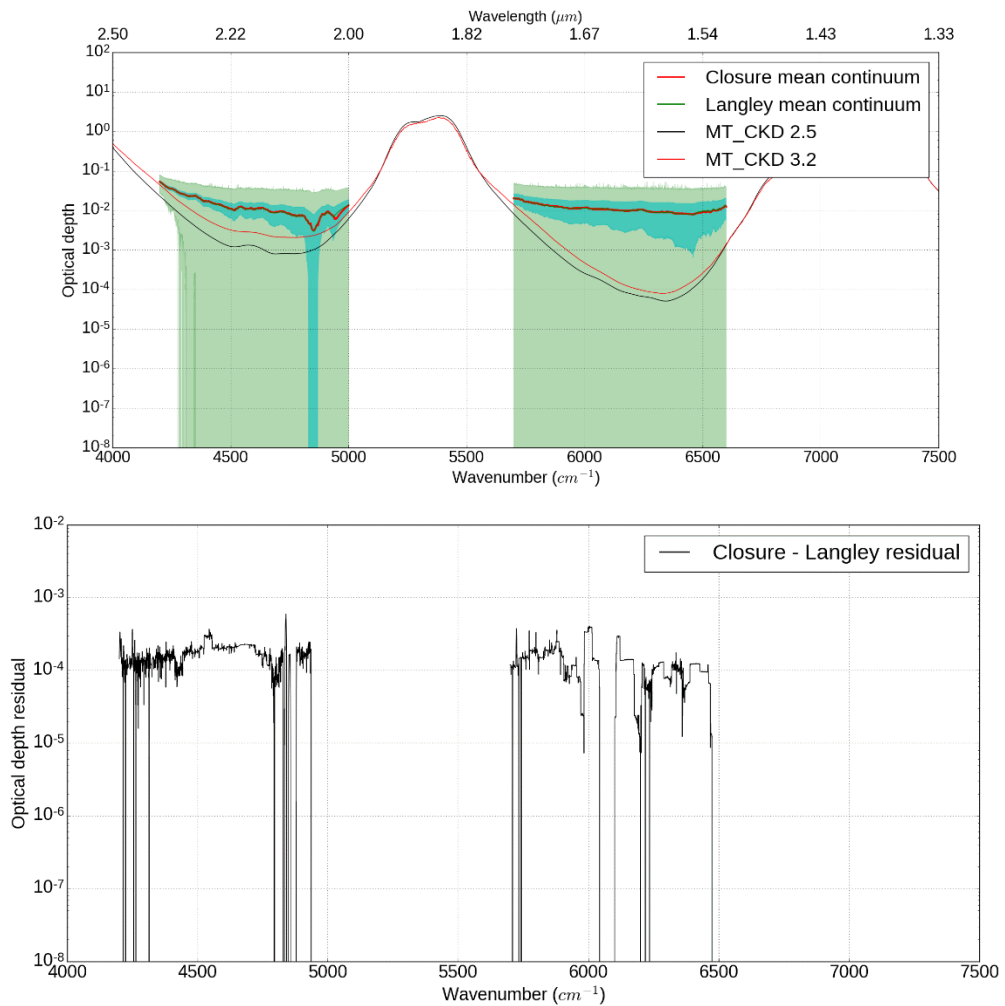


Figure 5.24: (upper panel): Best estimate of closure-derived continuum absorption (black) alongside the best estimate of the Langley-derived continuum absorption (blue), with $k = 1$ uncertainties (shaded regions) from 18 September 2008. The green line and blue line are almost indistinguishable due to the extremely close agreement. (lower panel): Residual of the closure minus Langley-derived continuum optical depth. These points lie two orders of magnitude below the points on Figure 5.24 (upper).

This strong agreement is a useful confirmation of the retrieval, since the atmospheric optical depths are derived in two quasi-independent ways from the same data. Since the Langley method relies on the assumption that the optical depth is constant during the day, whereas the closure-derived spectra do not, this supports the view that the conditions across the day were not changing significantly enough to affect the Langley analysis.

5.5.2.2: 22 August 2008

The observations of 22 August 2008 are not favoured, as explained in Chapter 3.4.4. Nevertheless, these can in principle provide a consistency check with the 18 September 2008 observations. Figure 5.25 shows the derived continuum optical depth in the 2.1 and 1.6 μm windows from both the closure and Langley methods. In much of the spectrum, these optical depths are negative, like the observations of *Reichert and Sussmann* [2016] (Figure 5.9). This limits the usefulness of the Langley-derived 22 August continuum as a cross-check.

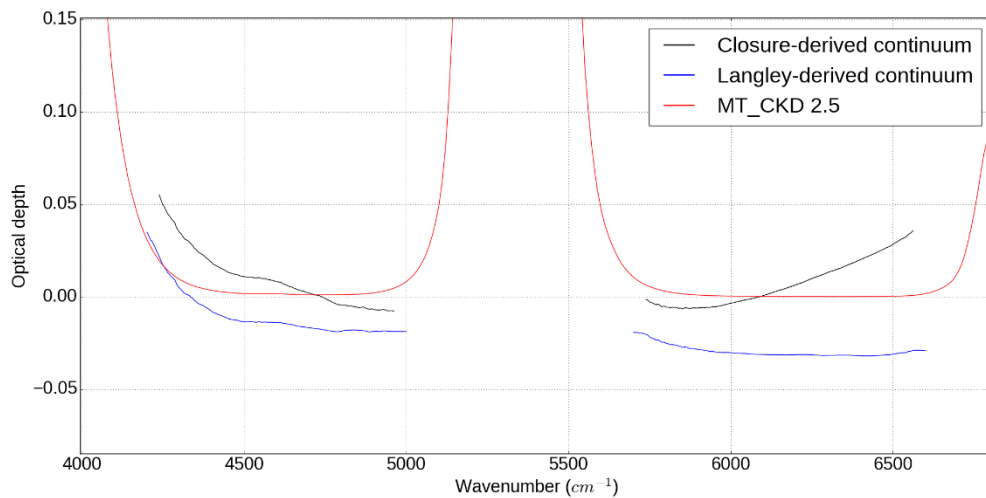


Figure 5.25: Closure and Langley-derived continuum absorption from 22 August 2008 in the 2.1 and 1.6 μm windows. These are shown on an absolute scale, since the derived continuum optical depths are negative at some wavenumbers.

Figure 5.26 shows an example Langley plot at 6000 cm^{-1} ; the difference in irradiance from one observation to another (with increasing airmass) is extremely small, due to the low optical depth. There is also significant scatter, which is indicative of changing conditions across the day. When performing the Langley fit, this therefore gives very low or even negative optical depth.

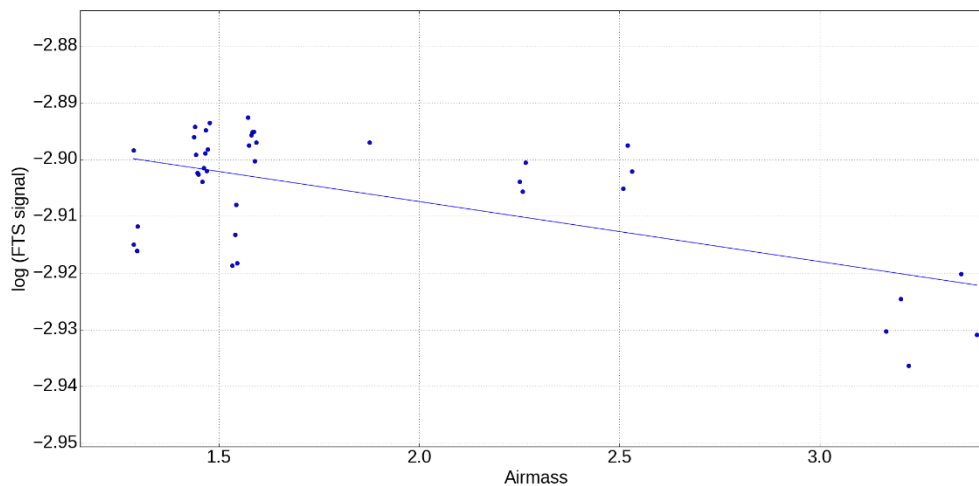


Figure 5.26: Example Langley plot at 6000 cm^{-1} using the observations of 22 August 2008.

The closure-derived spectra are also negative in much of the region of interest. Part of this is due to the difference in spectral shape from the 18 September observations. The offset in the closure-derived spectra varies with wavenumber; this is attributable to the difference in spectral shape between the 18 September observations and the 22 August observations, as can be seen in Figure 3.21. The low optical depth may be also due to an underestimate of the chosen SSI; however given the evidence presented in Chapter 4 this is unlikely to be the case. There may also be issues with the Microtops aerosol measurements; although without the ability to cross-check the results it is not possible to determine whether there is some systematic offset.

5.6: Conclusions

In this Chapter an estimate of the water vapour continuum absorption was successfully derived using the FTS observations of 18 September 2008. This estimate was obtained from two different methods (Langley and closure), with very close agreement between the central values of the two retrievals. This built on the previous analysis presented in *Menang* [2012], but with a rigorously derived uncertainty budget and new calibration. This work presents the first derivation (to the author's knowledge) of the near-IR atmospheric continuum in these windows at mean sea level with a well-constrained uncertainty budget, and the first to be derived using a radiometrically calibrated spectrometer. This is a significant step in our

understanding of the strength of the continuum in these windows. The lack of any similar robust measurements is an indicator of the difficulty in taking such measurements.

The results show general agreement with the FTS self-continuum observations in the laboratory from *Ptashnik et al.* [2011a]. They demonstrate that MT_CKD underestimates the total continuum in the 2.1 and 1.6 μm windows, which could be evidence of the self-continuum being stronger (as in the CAVIAR laboratory measurements), an increased contribution from the foreign continuum or both. Therefore, it is unclear how much of the offset can be made up by changing the assumptions made by MT_CKD about the relative strength of the self and foreign continuum. This will be the subject of a more detailed analysis in Chapter 6.

There is good agreement with MT_CKD (and therefore *Ptashnik et al.* [2015] and *Baranov and Lafferty* [2012]) in the 4 μm window. These results will be compared in more detail in Chapter 6.

There are however numerous problems with the experiment. The data from 22 August 2008 were ultimately not suited for a continuum retrieval, due to the unexplained spectral features in this work, which were not possible to remedy (see Section 3.4.4.3). The aerosol measurements on 18 September were not reconcilable with the FTS spectra, without some additional unexplained contribution to the optical depth or a systematic error in the sunphotometer measurements. This led to a more conservative estimate of the uncertainty, which limits the strength of any conclusions made, since the $k = 2$ uncertainties overlap zero optical depth. The lack of alternative days for Langley analysis means that the continuum is only derived in one set of conditions, which makes it not possible to retrieve the relative contribution from the self and foreign continuum. The derived continuum in the 1.02 μm window is considerable; while there are few laboratory retrievals in this window, these values are unexpectedly large. Chapter 7 includes a discussion on how this experiment could be improved, particularly with regards to the calibration of the FTS instrument, additional assessment of aerosol optical depth and ways of mitigating the large measurement uncertainty.

Chapter 6:

Comparison of atmospheric Langley-derived and laboratory continua

6.1: Introduction

This Chapter will assess how the spectrum derived in Chapter 5 fits into the broader literature discussed in Section 5.2. It is not possible to directly compare with the results of *Reichert and Sussmann* [2016] in the 1.6 μm window since no values are presented there in that work, but it is possible to compare values in the 2.1 and 4 μm windows. This analysis is presented in Section 6.2.

Of particular interest is a comparison of the Langley-derived spectra from this work and the laboratory-derived CAVIAR self-continuum of *Ptashnik et al.* [2011a] and foreign continuum of *Ptashnik et al.* [2012], and the Grenoble CRDS and OF-CEAS measurements of e.g. *Mondelain et al.* [2013, 2014]. This analysis is presented in Sections 6.3 and 6.4. Since the continuum derived in this work is a combined self + foreign continuum, it is difficult to directly compare it to either the self or foreign laboratory continua individually. This analysis here instead attempts to assess the strength of the foreign or self-continuum given an assumed value for the other component (i.e. taking an experimental or MT_CKD value of the self or foreign continuum). This procedure is explained in more detail in Section 6.3 and in Figure 6.6.

This procedure was possible via separating the foreign continuum from within the MT_CKD code and implementing it into the RFM. The self-continuum can then be retrieved as the difference between the total continuum and the foreign for a given path. This foreign or self-continuum can then be scaled by the atmospheric measurements. This is explained in more detail in Section 6.3. Figure 6.1 shows the self and foreign continuum from MT_CKD for the atmospheric path obtained at 12:00 GMT on 18 September 2008. The self-continuum dominates in these conditions within the windows, while the foreign continuum dominates in the bands.

This is not observed to be the case in e.g. *Ptashnik et al.* [2012]. Due to the difficulty in separating out the self and foreign continuum, this work cannot by itself resolve this discrepancy. However, given the robustness of the CAVIAR-lab foreign continuum measurements, if there was some agreement with the observed self-continuum measurements, it would provide some additional evidence toward those measurements being representative of the self/foreign partitioning.

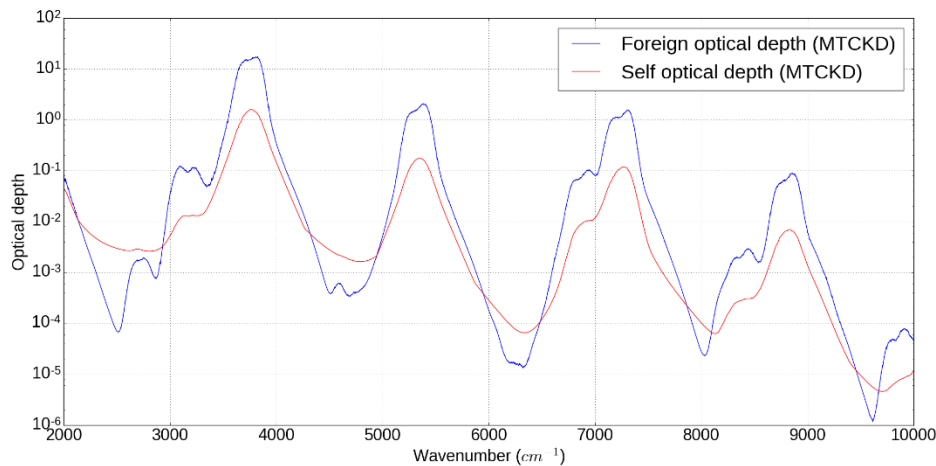


Figure 6.1: *MT_CKD* total column optical depth separated into a contribution from the self-continuum (red) and foreign continuum (blue) for atmospheric conditions on 12:00, 18 September 2008.

Section 6.3 presents figures similar to Figure 5.6 (showing the temperature dependence of the self-continuum at selected wavenumbers), but updated with the data from the Langley-derived 18 September 2008 spectra, assuming a nominal atmospheric temperature. This is again performed as a ratio to *MT_CKD*, assuming a foreign continuum from either *MT_CKD* or from laboratory measurements.

6.2: Comparison with other atmospheric spectra

Due to the difficulties in taking measurements of the continuum in the atmosphere, the only published dataset of the near-IR continuum with which to compare is *Reichert and Sussmann* [2016]. They presented mean continuum coefficients at 10 cm^{-1} intervals in the region 2500-7500 cm^{-1} ; however due to the extremely large uncertainties, robust values in the windows are only quoted between 2500-5000 cm^{-1} . The authors also present values that are a direct ratio to *MT_CKD* 2.5; these are compared here in Figure 6.2, shown alongside the equivalent data from this work

(i.e. the 18 September 2008 Langley-derived spectrum divided by a model run with MT_CKD 2.5 using the conditions of 18 September 2008 as model input).

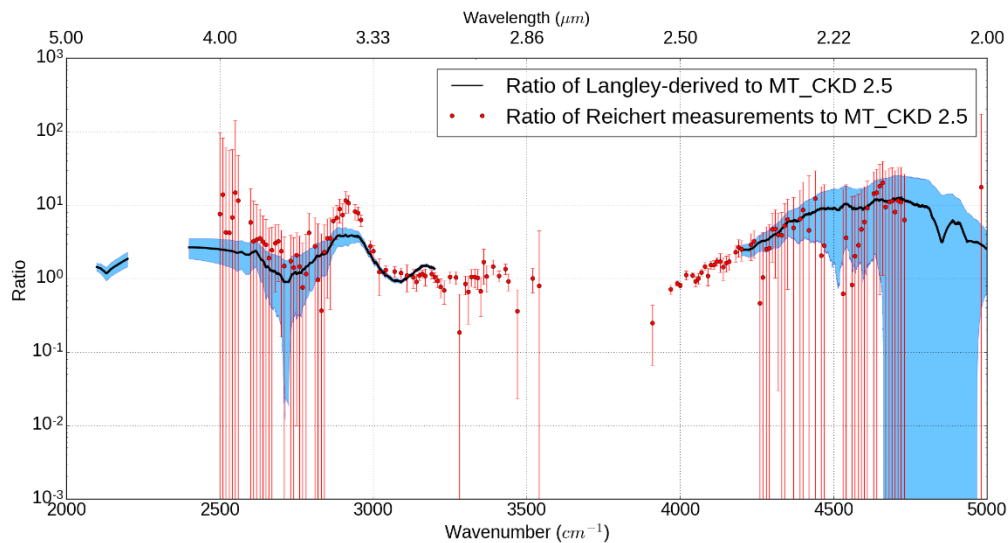


Figure 6.2: Data points from Reichert and Sussmann [2016] as a ratio to MT_CKD 2.5 (red), compared with the corresponding data from this work (blue). The error bars and shaded regions correspond to the $k = 2$ uncertainties.

This analysis shows agreement within the uncertainties between the ratios of the two spectra across most of the 2.1 and 4 μm windows. There is disagreement on the edges of the 4 μm window; on the high wavenumber end of this window the spectra do not agree within their uncertainties.

The low-wavenumber end of the spectrum is that with the most certainty in the absolute level, since the effect of aerosol extinction is lowest at lower wavenumbers. This agreement is the case despite the significantly different conditions between Reichert and Sussmann and this work; their observations are at a high altitude field site, rather than at near sea level. A typical integrated water vapour (IWV) observed during their campaign was ~ 2 mm, compared to the ~ 17 mm in this work. Therefore, it is reasonable to presume that the majority of the Reichert and Sussmann continuum is foreign continuum; indeed the authors estimate that this makes up 80-95% of their observed continuum.

Figure 6.3 shows the same ratio, but this time taking only the foreign continuum, making the assumption that the self-continuum is well-represented by MT_CKD and subtracting the MT_CKD self-continuum from the total Langley optical depth. The Langley foreign continuum is estimated by subtracting the MT_CKD self-continuum

from the total observed continuum optical depth, and then taking the ratio. This ratio is performed to MT_CKD 3.2 since we did not have a version of MT_CKD 2.5 with the foreign and self-continua separated; the Reichert ratios are taken direct from the Supplementary to their paper (which used MT_CKD 2.5) since I did not have access to their atmospheric profiles. The agreement is retained, and improved in some portions of the spectrum, e.g. at $\sim 2700\text{ cm}^{-1}$.

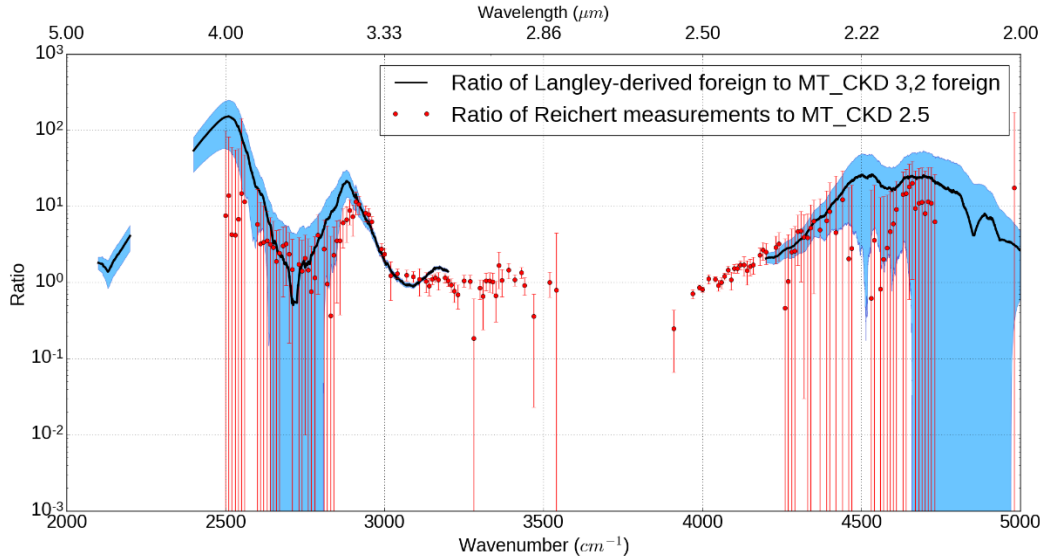


Figure 6.3: Data points from Reichert and Sussmann [2016] as a ratio to MT_CKD 2.5 (red), compared with the foreign continuum from this work divided by the MT_CKD 3.2 foreign (blue). The error bars and shaded regions correspond to the $k = 2$ uncertainties.

The absolute values of these spectra appear to agree well with MT_CKD, particularly in the $4\ \mu\text{m}$ window, where there is also excellent agreement between MT_CKD and most of the available laboratory spectra (see Figure 5.3). In the centre of the windows, the uncertainties in the Reichert and Sussmann data are significantly larger, and less confidence can be placed in these results. Nevertheless, the central values agree within the respective uncertainties in most cases, and appear to suggest a factor of 10 strengthening of the MT_CKD foreign continuum is required in the centre of the $2.1\ \mu\text{m}$ window. This will be examined further in Sections 6.3 and 6.4.

Reichert and Sussmann derive a mean continuum coefficient via:

$$(6.1) \quad k_{cont} = \frac{\int_{h_{obs}}^{\infty} k_{cont}(T, n_{wv}, n_{air}) n_{wv} dh}{\int_{h_{obs}}^{\infty} n_{wv} dh} = \frac{\tau_{cont}}{m\ IWV}$$

where k_{cont} is the mean continuum coefficient, h_{obs} is the height from which the observer is taking measurements, n_{wv} and n_{air} the number densities of water vapour and air respectively, m is the airmass factor, and IWV is the integrated water vapour of the path in molecules cm^{-2} . Given the Langley-derived observations are by definition at one airmass, it is possible to perform the same analysis for the Langley-derived continuum from this work, using the observed IWV from the HATPRO (see Section 3.4.5.3). These results are shown in Figure 6.4, compared to the corresponding values from *Reichert and Sussmann*. Note the linear scale, rather than the logarithmic scale of Figures 6.2 and 6.3.

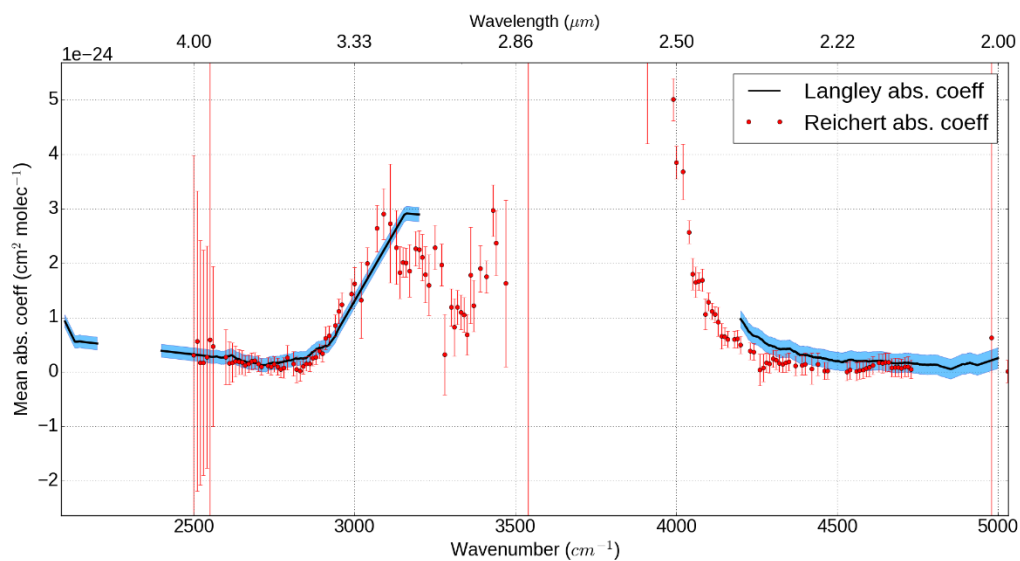


Figure 6.4: Mean continuum absorption coefficients from *Reichert and Sussmann* [2016] compared to those derived from this work (blue). The error bars and shaded regions correspond to the $k = 2$ uncertainties.

There is good agreement between the data; however this may be due to competing biases. This may be due to the significantly different water vapour paths and altitudes (leading to a different ratio of foreign to self-continuum in either case), calibration methods and atmospheric conditions (meaning that any deviation from the MT_CKD temperature dependence would cause a bias one way or the other).

6.3: Temperature dependence of the self-continuum

This section assesses the temperature dependence in the self-continuum as obtained from the Langley-derived CAVIAR-field measurements. To do this, a representative temperature must be chosen, corresponding to the conditions in the atmosphere at the time of measurement. Since the temperature, pressure and water vapour volume mixing ratio do not change significantly over the course of 18 September 2008, this can be estimated by calculating the contribution to the continuum at each layer within MT_CKD/RFM. The cumulative sum of these contributions is shown below in Figure 6.5, summing from the surface upward. This figure shows that in the windows over 90% of the continuum comes from the lowest 2 km of the atmosphere. Looking at the temperature profile of this region from the radiosonde data gives a temperature range of ~ 290-275 K. This temperature range was therefore chosen to be representative of the self-continuum for the Langley-derived data. The continuum obtained by estimating the self-continuum at 280 K is henceforth referred to as the Langley-estimated self-continuum.

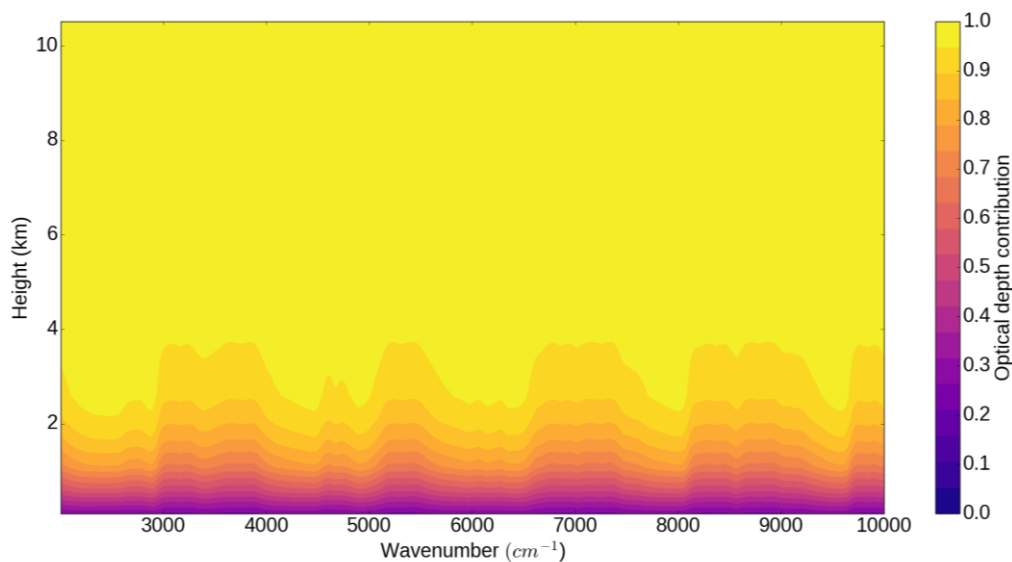


Figure 6.5: *Cumulative fractional contribution to the total continuum optical depth from the surface upward to 10 km as a function of wavenumber. The lowest point of the yellow shaded region indicates the height below which 95% of the continuum absorption originates.*

It is necessary to assume a foreign continuum when calculating the Langley-estimated self-continuum. This is done both the MT_CKD foreign continuum and the CAVIAR-lab foreign continuum. This assumption is reasonable; these are the two extant datasets of foreign continuum, and since there is little experimental evidence to suggest that the foreign continuum has any significant temperature dependence, the elevated-temperature CAVIAR foreign continuum can be used. By making this assumption, the Langley-estimated self-continuum can be obtained as detailed in Figure 6.6 by removing the atmospheric foreign continuum component.

Given that the ratio of two absorption cross-sections is the same as the ratio of two optical depths (provided the optical depths are obtained in the same conditions), this process allows the derivation of a scaling factor which is applied to the MT_CKD continuum plotted on e.g. Figure 5.20 in atmospheric conditions. Selecting a wavenumber and applying this scaling yields the Langley-estimated self-continuum at that wavenumber, which can then be plotted as on Figures 5.6-5.7. It is important to note that this process can be “mirrored” i.e. the Langley-estimated foreign continuum can be obtained by removing the impact of the self-continuum. This however relies on an additional assumption about the temperature dependence of the self-continuum; in this case an extra step is included to scale C_{lab}^{self} to the representative atmospheric temperature.

Section 6.4 will use this to compare laboratory observations of the foreign continuum with the Langley-estimated foreign continuum by removing the self-continuum obtained from a) extrapolation of the CAVIAR-lab self-continuum b) directly from MT_CKD and c) using the room temperature Tomsk measurements of *Ptashnik et al.* [2015].

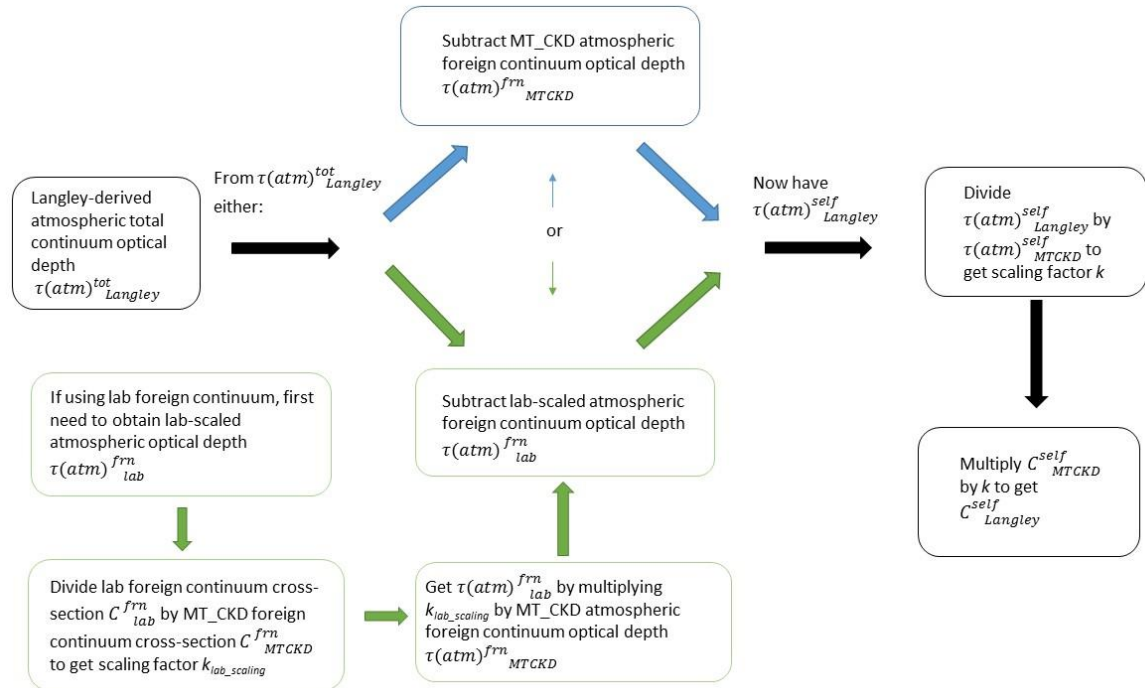


Figure 6.6: Schematic of the steps taken to convert the Langley-derived optical depth into a Langley-estimated self-continuum. The blue and green lines show the two different methods; either using the MT_CKD foreign continuum (blue), or using a laboratory foreign continuum (which first must be scaled to atmospheric conditions, which is done as a ratio to MT_CKD). The black lines show the remainder of the process, ending with the estimation of the Langley self-continuum cross section. This process can be done with the self and foreign continua swapped around, in which case the Langley-estimated foreign continuum would be derived from the laboratory or MT_CKD self-continuum.

Figures 6.7 shows this case at 4723 cm^{-1} (in the centre of the $2.1\text{ }\mu\text{m}$ window). Figures 6.8-6.10 show the case at various points in the $1.6\text{ }\mu\text{m}$ window. These wavenumbers were chosen to highlight some of the additional data available, including unpublished data from NIST (courtesy of Joe Hodges), and new data from Tomsk using a photoacoustic method (*Kapitanov et al.* [2018], paper in Russian).

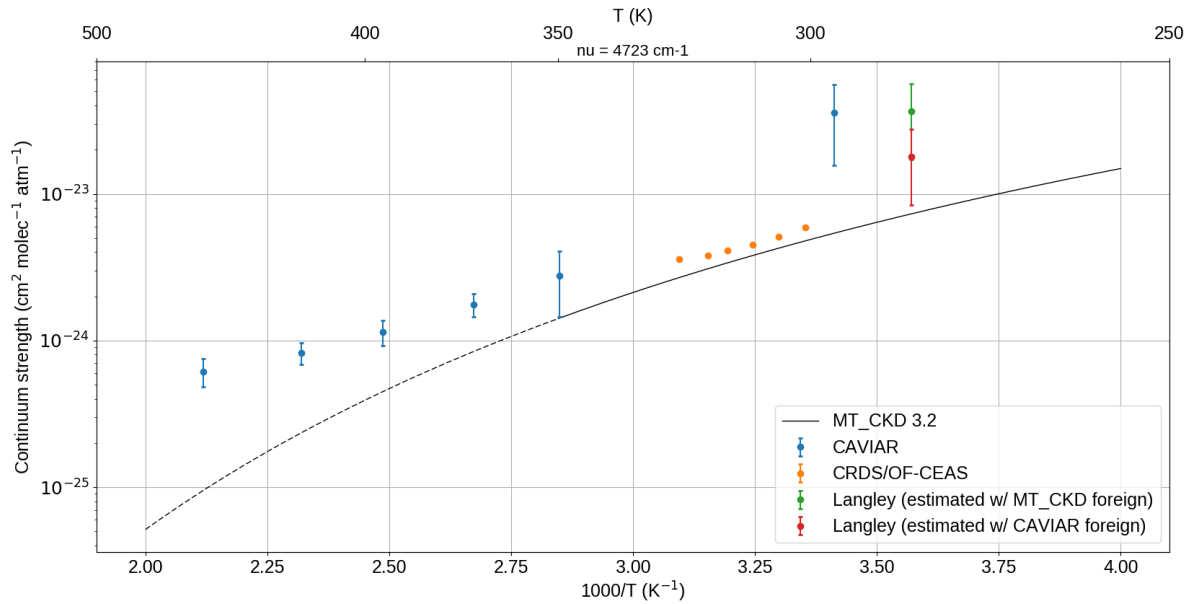


Figure 6.7: Temperature dependence of the self-continuum from various sources, including the Langley-estimated self-continuum at 4723 cm^{-1} . Uncertainties quoted at $k = 1$.

The Langley-estimated (using CAVIAR foreign continuum) self-continuum in the $2.1 \mu\text{m}$ window appears to be consistent with the observations from both the CRDS/OF-CEAS measurements (orange) and the CAVIAR-lab data (blue), if the data point at room temperature is ignored in the latter. This indicates that the temperature dependence may well be well-represented by the negative exponential fit (straight line in on the graph). The situation using the MT_CKD foreign continuum appears to be somewhat worse, but is still consistent with CAVIAR within the $k = 2$ uncertainties ($k = 1$ shown on plot, as $k = 2$ overlap zero). Nevertheless, this data appears to agree with the Grenoble and CAVIAR-lab self-continua, with significantly better agreement if the CAVIAR foreign continuum is used.

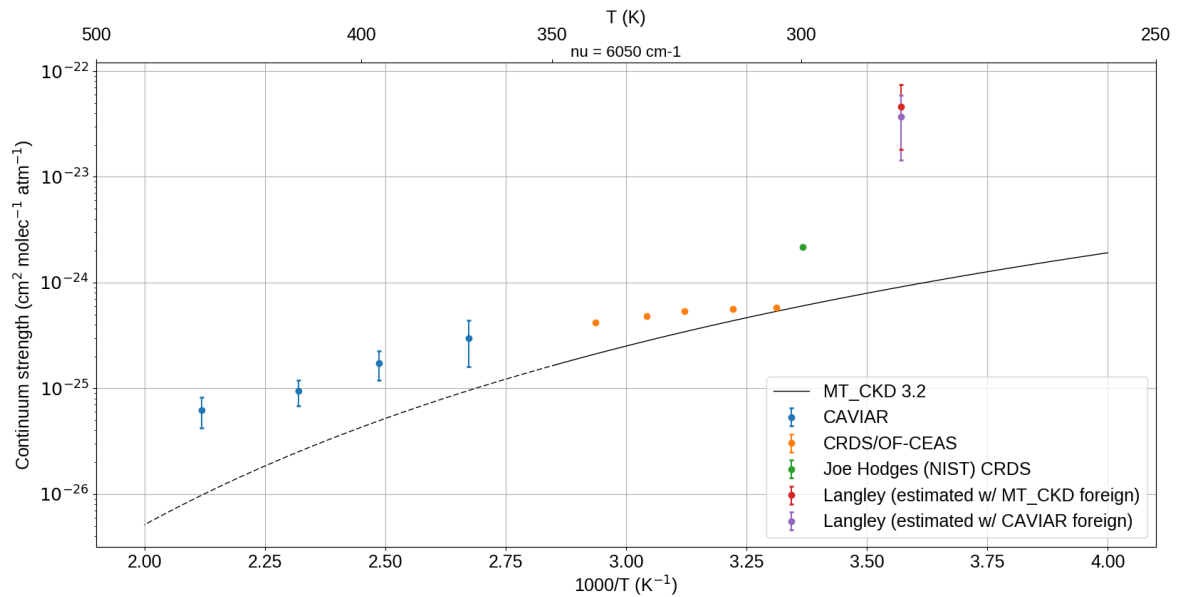


Figure 6.8: Temperature dependence of the self-continuum from various sources, including the Langley-estimated self-continuum at 6050 cm^{-1} .

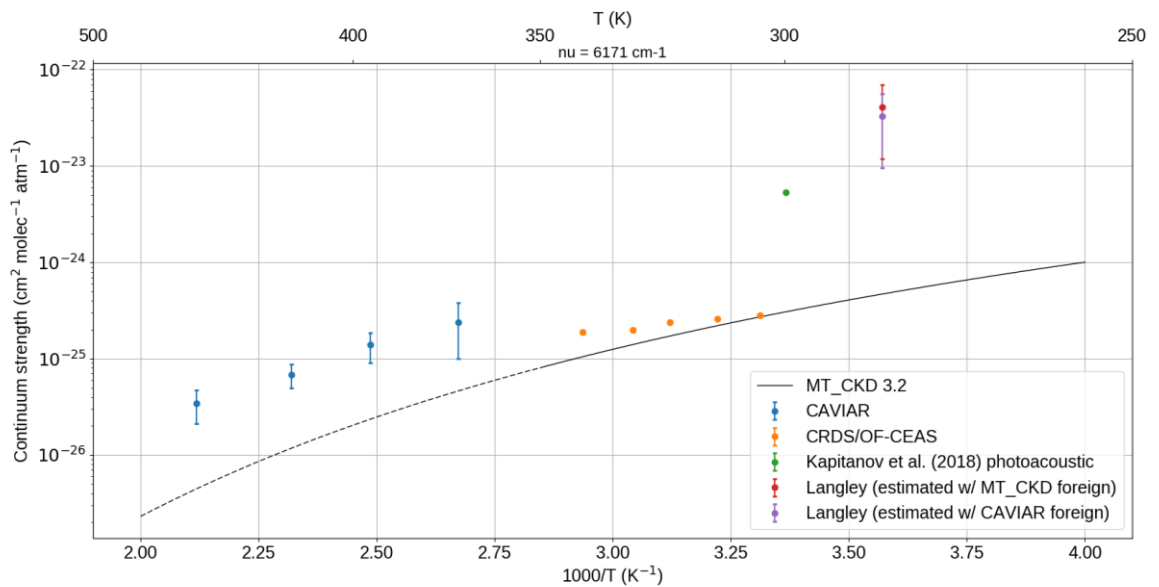


Figure 6.9: Temperature dependence of the self-continuum from various sources, including the Langley-estimated self-continuum at 6171 cm^{-1} .

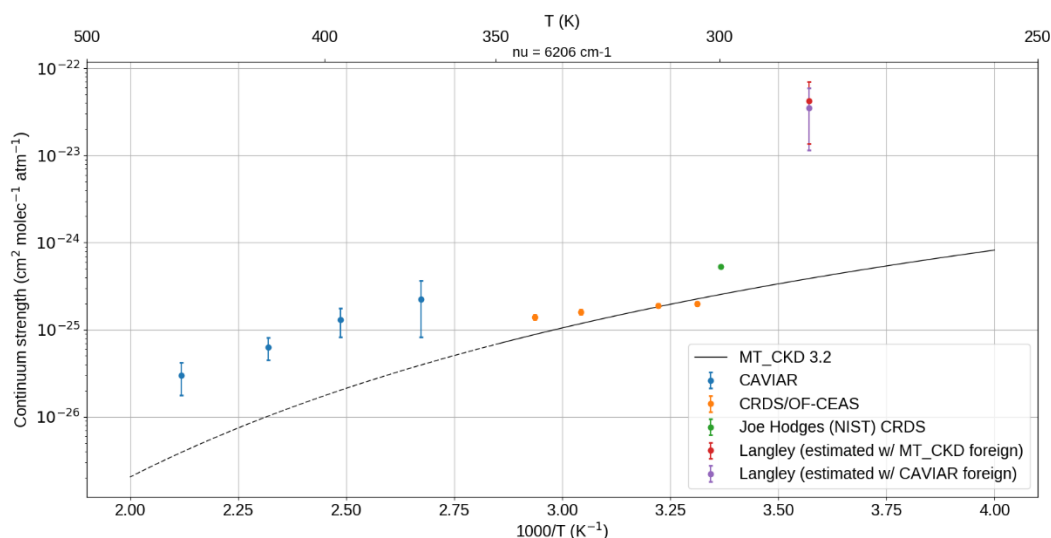


Figure 6.10: Temperature dependence of the self-continuum from various sources, including the Langley-estimated self-continuum at 6206 cm^{-1} .

The situation in the $1.6\text{ }\mu\text{m}$ window is less clear. The Langley-derived self-continuum appears to be significantly stronger than the CAVIAR and OF-CEAS measurements, as well as the additional data (NIST CRDS data from Joe Hodges at $6050/6206\text{ cm}^{-1}$ and photoacoustic data from Tomsk at 6171 cm^{-1}). Nevertheless, the $k = 2$ uncertainties are large (again, $k = 1$ shown since $k = 2$ uncertainties extend below zero), and a straight line fit through these data would show consistency in this case. The NIST CRDS data points do not report uncertainties, but the central values appear to be reasonably close to the CAVIAR-lab data, and certainly appear stronger than the very weak values which would be implied by extrapolation of the Grenoble measurements in temperature. The *Kapitanov et al.* value has small uncertainties, but could yet be consistent with an extrapolation of the CAVIAR-lab data.

The lack of consistency in the self-continuum between the lab data and the Langley data could mean that the derived continuum optical depth was too strong in this window (in Chapter 5), or could mean that the foreign continuum was too small in both MT_CKD and the CAVIAR-lab measurements. This assumes a straight line temperature dependence however; in reality this may change due to e.g. a change in the regime from bound to quasi-bound dimers (e.g. *Ptashnik et al.* [2011b]).

6.4: Self and foreign continuum at atmospheric temperatures

6.4.1: Self-continuum

Figure 6.11 shows an updated version of Figure 5.3, showing only the Grenoble, MT_CKD, CAVIAR-lab and CAVIAR-field (Langley-estimated using MT_CKD foreign continuum) data for clarity. In addition, the CAVIAR-lab data has been extrapolated from high temperature to 280 K. This was performed by taking a linear fit through the CAVIAR-lab data points at each number, and (by assuming that the temperature dependence is a negative exponential, i.e. is a straight line on the previous Figures) taking the value of the derived straight line at 280 K as the “new” CAVIAR-lab coefficient.

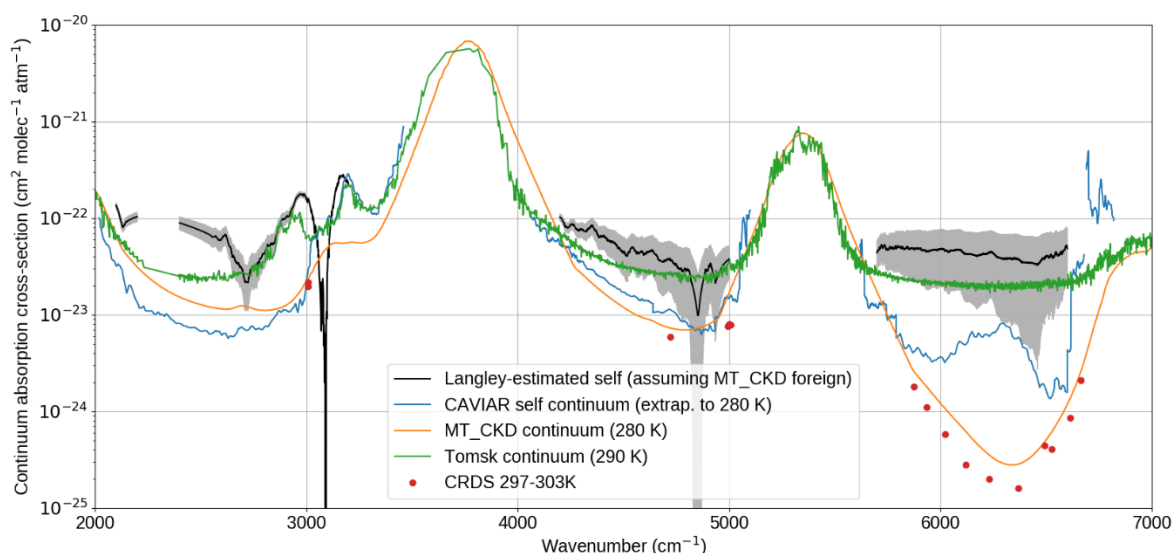


Figure 6.11: *Self-continuum from 2000-7000 cm⁻¹ from MT_CKD (orange line), CAVIAR-lab (blue), CAVIAR-field estimated using the MT_CKD foreign-continuum (black), TomsK continuum (green) and various OF-CEAS and CRDS observations from Grenoble (red). Uncertainties shown at $k = 1$.*

Figure 6.12 shows the same case, but with the Langley-estimated self-continuum obtained using the CAVIAR-lab foreign continuum.

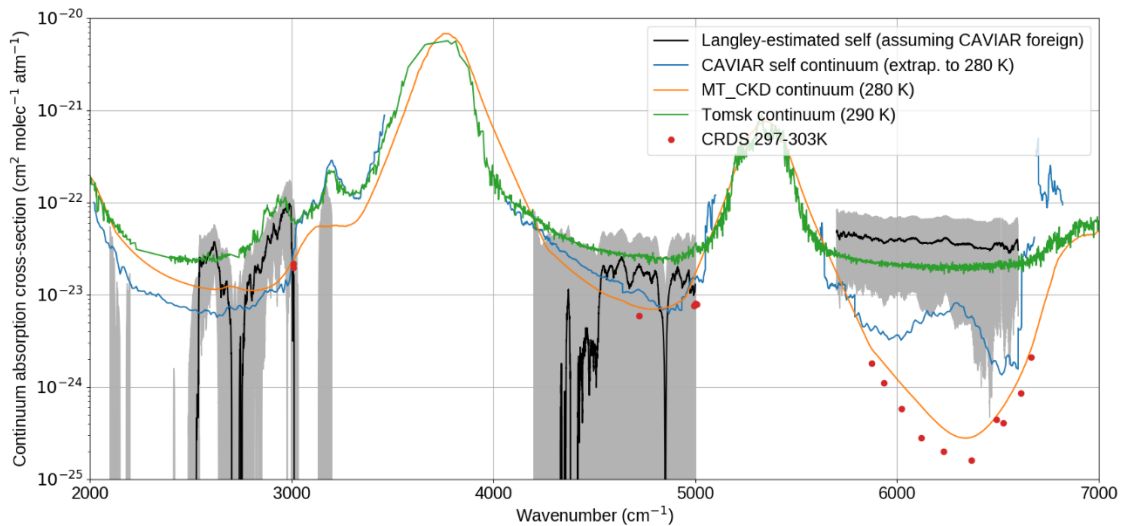


Figure 6.12: Self-continuum from 2000-7000 cm^{-1} from MT_CKD (orange line), CAVIAR-lab (blue), CAVIAR-field estimated using the CAVIAR-lab foreign-continuum (black), Tomsk continuum (green) and various OF-CEAS and CRDS observations from Grenoble (red). Uncertainties shown at $k = 1$.

This analysis shows that, contrary to the CAVIAR room temperature continuum shown Figure 5.3 (which was directly measured rather than extrapolated from higher temperature measurements, but with large uncertainties), the CAVIAR-lab data is generally consistent with the CRDS data in the 2.1 μm window, providing the assumption about the temperature dependence is robust. Note that the CAVIAR self-continuum is at lower temperature than the CRDS measurements (which have not been extrapolated in temperature), this explains some of the discrepancy. Assuming the CAVIAR-lab foreign continuum leads to a significant decrease in the Langley-estimated self-continuum in the 2.1 μm window, compared to using the MT_CKD foreign continuum. In the high-wavenumber edge of the window, this appears to improve the agreement with the extrapolated CAVIAR-lab self-continuum, but less so at the lower-wavenumber edge (although there is still consistency within the uncertainties).

The significantly lower values of the foreign continuum in the 1.6 μm window relative to the 2.1 μm window lead to a small decrease when using the CAVIAR-lab foreign continuum compared to the MT_CKD foreign continuum. This gives an implied self-continuum in this window that exceeds even the Tomsk values, although these are still consistent with the extrapolated CAVIAR-lab measurements within the

$k = 1$ uncertainties in a small window of the spectrum. There is consistency within the $k = 2$ uncertainties with all of the spectra, since these uncertainties are large. This may indicate that the Tomsk self-continuum is accurate, or that there are problems with the Langley-estimated continuum (which should be covered within the uncertainty budget).

6.4.2: Foreign continuum

Figure 6.13 shows foreign continuum in the 2000-7000 cm^{-1} range, showing the data from MT_CKD, CAVIAR-lab, CAVIAR-field (Langley-estimated using the MT_CKD self-continuum) and *Reichert and Sussmann*. Note that *Reichert and Sussmann* is, at least in part, a combined self + foreign continuum. For the purposes of Figure 6.13, it is assumed that since the foreign continuum is dominant in the conditions present in *Reichert and Sussmann* (estimated to be 80-95% of the total optical depth), the foreign continuum this is the only contributor to the total.

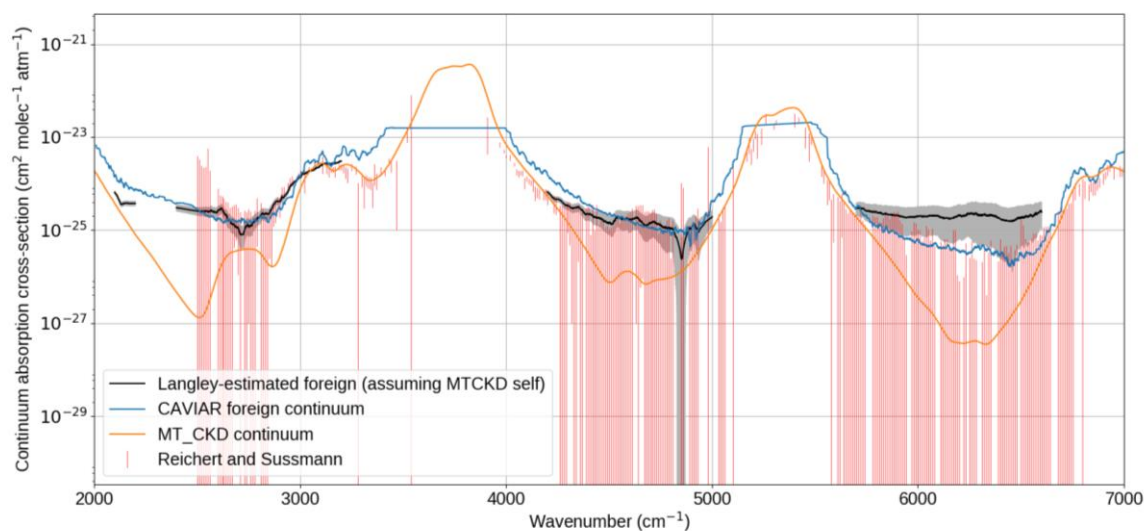


Figure 6.13: Foreign continuum from 2000-7000 cm^{-1} from MT_CKD (orange), CAVIAR-lab (blue), CAVIAR-field estimated using MT_CKD self (black) and *Reichert and Sussmann* (red).

Figure 6.14 shows the same case with the CAVIAR-field foreign continuum estimated using the CAVIAR-lab self-continuum.

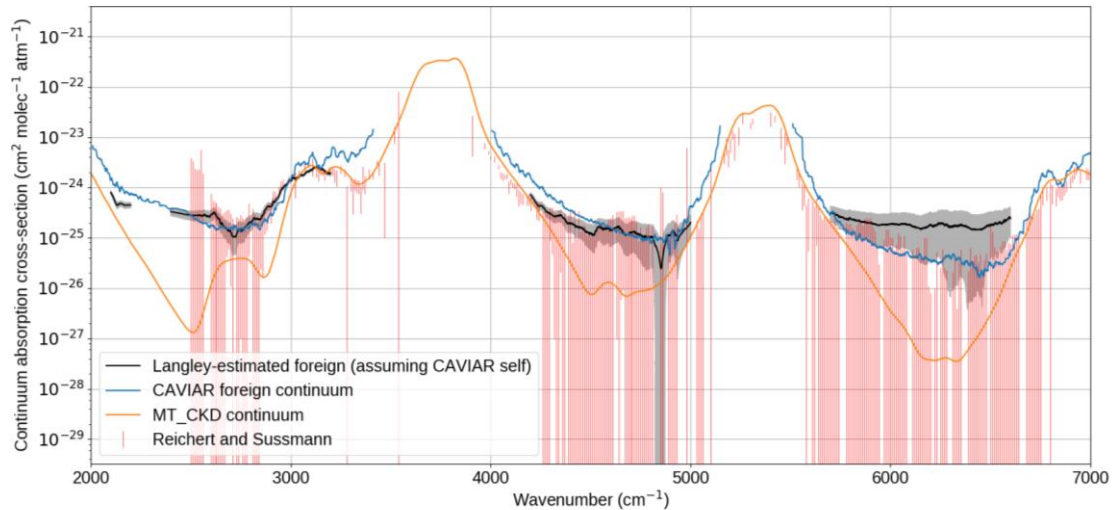


Figure 6.14: Foreign continuum from 2000-7000 cm^{-1} from MT_CKD (orange), CAVIAR-lab (blue), CAVIAR-field estimated using MT_CKD (black) and Reichert and Sussmann (red).

The differences in these spectra appear small. This, as is seen in Section 6.4.1, is due to the small differences between the MT_CKD and CAVIAR-lab spectra at 2.1 μm when extrapolated to 280 K. Additionally, because the self-continuum at 1.6 μm implied by the Langley-estimated continuum greatly exceeds that of the CAVIAR-lab data (Section 6.4.1), the difference in the estimated foreign continuum between using these two is small. Nevertheless, there appears to be some agreement between the foreign continuum across the spectrum between Reichert and Sussmann, CAVIAR-lab and CAVIAR-field within the uncertainties.

Finally, this CAVIAR-field foreign continuum is estimated using the Tomsk continuum, shown in Figure 6.15.

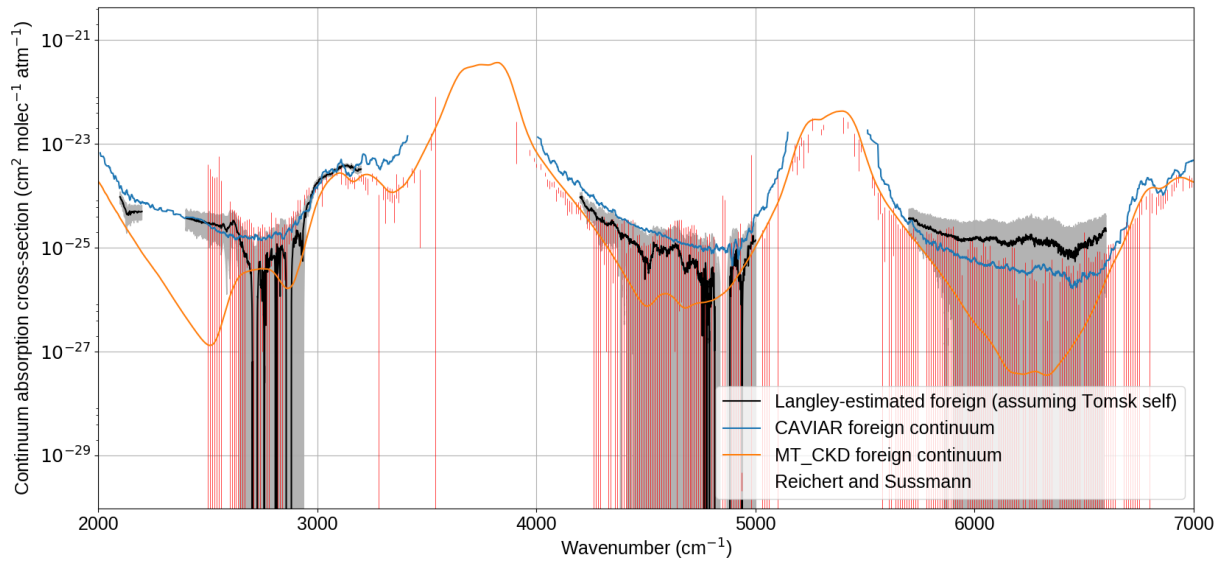


Figure 6.15: Foreign continuum from 2000-7000 cm^{-1} from MT_CKD (orange), CAVIAR-lab (blue), CAVIAR-field estimated using the Tomsk self-continuum (black) and Reichert and Sussmann (red).

Using the Tomsk continuum here pushes the Langley-estimated foreign continuum below the CAVIAR-lab foreign continuum, although is still consistent within the uncertainties. Given the belief that the Tomsk data are too high in both of these windows, this provides evidence that the foreign continuum is closer to the level of the CAVIAR-lab data than MT_CKD, with particularly good agreement at 2.1 μm .

6.4.3: Combined continuum

Figure 6.16 shows the ratio of the combined self and foreign continuum of CAVIAR-lab and CAVIAR-field to MT_CKD. This data appears to show that the two are consistently larger than MT_CKD by a factor of 5 or so in the 2.1 μm window, but either a factor of 10 (CAVIAR-lab) or 100 (CAVIAR-field) in the 1.6 μm window. Within the uncertainties, the ratios of the total continua are consistent. Since the

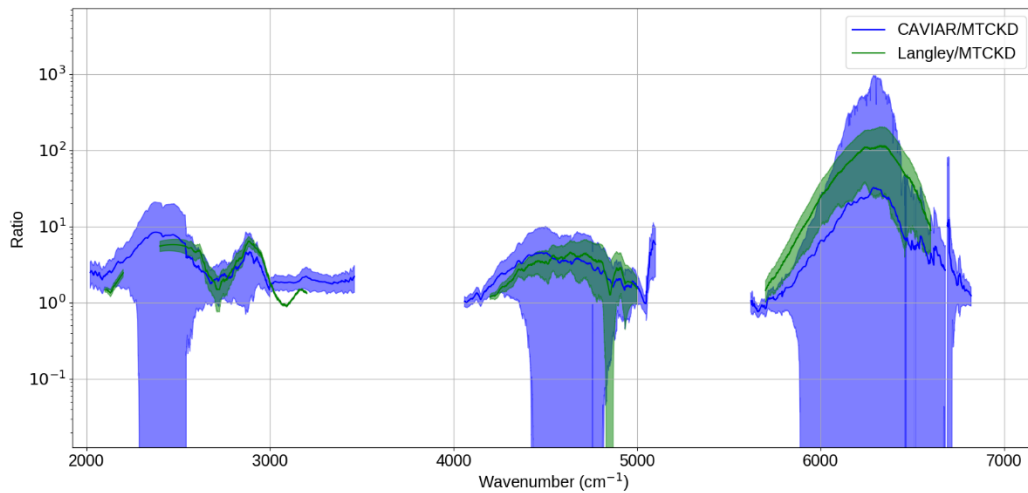


Figure 6.16: Ratio of the CAVIAR-field (green) and CAVIAR-lab (blue) total continuum to MT_CKD. Uncertainties quoted at $k = 1$.

6.5: Conclusions

In this Chapter, the foreign and self-continuum have been estimated in atmospheric conditions. This has been done with a direct comparison to the CAVIAR laboratory data of *Ptashnik et al.* [2011a; 2012], and by looking at the atmospheric-derived spectra of *Reichert and Sussmann* [2016]. This analysis appears to show a Langley-estimated continuum consistent with the CAVIAR-lab data in the 2.1 μm window, but significantly stronger at 1.6 μm . This is particularly the case for the foreign continuum, where the CAVIAR-lab and MT_CKD data at 280 K are close. There is also some agreement within the uncertainties between the Langley-estimated continuum and the continuum of *Reichert and Sussmann*. However, the large uncertainties, and assumptions made in performing this analysis, it is not possible to make any strong conclusions based on this work. Nevertheless, this data implies that the MT_CKD continuum is not a good representation of the total continuum, particularly in the 1.6 μm window, and that this strengthening is likely to be due to an underestimation of the foreign continuum.

Chapter 7:

Summary of results and future work

7.1: Introduction

This Chapter will present the conclusions based on the work done in Chapters 3, 4, 5 and 6, bringing together elements from each. This is presented in Section 7.2. Section 7.3 presents some ideas about how the results of this thesis could be improved upon in a future campaign, and how our understanding of solar spectral irradiance and the water vapour continuum could be improved.

7.2: Conclusions

7.2.1: Solar spectral irradiance (Chapter 4)

Chapter 3 presented an updated calibration of the FTS instrument used in this work. This is especially important for the work presented in Chapter 4, since observations of solar spectral irradiance require an absolutely calibrated instrument. The result of this calibration was a new high resolution SSI from 2000-10000 cm^{-1} (named CAVIAR2), which showed significantly better agreement with satellite observations in the 7000-10000 cm^{-1} region (in which there is high confidence in the satellite observations) than the previous estimate of *Menang et al.* [2013], but significantly lower values (~10%) in the 4000-7000 cm^{-1} region than the space-based ATLAS3 observations of *Thuillier et al.* [2003], while agreeing well with analyses by *Bolsée et al.* [2014], *Thuillier et al.* [2014] and *Meftah et al.* [2017]. Preliminary results from the Total and Spectral Solar Irradiance Monitor (TSIS-1) [*Pilewskie et al.*, 2018] are beginning to become available.

Given the weight of evidence for a lower SSI, I recommend the use of an SSI with this lower level of near-infrared irradiance for modelling purposes, such as for inclusion in CMIP6. The recommended NRLSSI2 spectrum [*Coddington et al.*, 2015] relies on measurements by the SIM [*Harder et al.*, 2005], which in the near-IR is adjusted by a factor of ~10% to agree with ATLAS3. I question the validity of this adjustment and recommend a reconsideration of the near-IR calibration of this

spectrum. The wavelength-integrated difference between ATLAS3 and CAVIAR2 approaches 16 W m^{-2} in this spectral region, which must be made up for by a corresponding increase elsewhere in the spectrum. It is worth noting however that the ATLAS3 integrated irradiance is significantly higher than the recommended TSI of 1360 W m^{-2} (e.g. *Kopp* [2016]; *Dudok de Wit et al.* [2017]). The preliminary TSIS-1 measurements agree with this TSI within the uncertainties when integrated across the spectrum ($1359.46 \pm 1.51 \text{ W m}^{-2}$), including a contribution from the SATIRE-S solar model below 200 nm and above 2360 nm.

The spectral resolution (0.03 cm^{-1}) of the CAVIAR2 spectrum is well in excess of that currently achievable by a space-based measurement system. While this can only provide information on solar lines within the atmospheric windows, this can be a useful tool to compare with theoretical and semi-empirical spectra such as *Kurucz and Bell* [1995]. A high-altitude field site would allow for even more of these spectral lines to be observed, and in the future perhaps even monitored. This provides a role for ground-based measurements even in the era of satellite observations, particularly for looking at variation of solar irradiance over time, since it is easier in principle to assess calibration drift from a ground-based instrument. Additionally, given a well-characterised uncertainty budget, any two measurement systems should agree within these uncertainties regardless of whether they are space or ground-based.

7.2.2: Water vapour continuum (Chapters 5 and 6)

Chapter 5 presented the first published observations of the near-infrared water vapour continuum in the atmosphere with radiometrically calibrated observations and a robust uncertainty budget. These observations were primarily from Langley-derived spectra of 18 September 2008, with consistency checks with closure-derived spectra of 18 September (these methods are quasi-independent). While the $k = 2$ uncertainties of this data overlap with the MT_CKD 2.5 and 3.2 continuum (and with zero absorption), the central value is significantly higher, a factor of 5 greater than MT_CKD 3.2 (and a factor of 10 greater than MT_CKD 2.5) in the $2.1 \mu\text{m}$ window and a factor of 100 greater than both MT_CKD 3.2 and 2.5 in the $1.6 \mu\text{m}$ window. This demonstrates that MT_CKD may be unsuited in its current state for modelling absorption in these windows. The results also show good agreement with MT_CKD

in the 4 μm window, where most observations agree. It is worth reiterating that MT_CKD is tied to measurements at these lower wavenumbers; and is not necessarily representative of the situation in the wavenumbers of interest in this work. The only way to ensure an accurate continuum is for there to be agreement between various different sets of measurements from different sources within the uncertainties, which is not the case for the 2.1 and 1.6 μm windows on which this work focuses.

In the 4 μm window, and most other near-IR windows at room temperature, the Grenoble CRDS measurements are significantly lower, and do not agree within the uncertainties. The differences between the FTS data and CRDS data across the spectrum appear to be systematic, with the FTS data larger and (Grenoble) CRDS data lower. The reason for this is unknown; it is unclear what would cause a systematic increase in optical depth in the FTS data across the spectrum. Section 5.2.5 does discuss a recent study [*Serdyukov et al.*, 2016] which may explain a systematic decrease in the CRDS data, but this is by no means conclusive.

There is an unexpectedly large extinction feature in the 1.02 μm window. This may be some continuum feature not observed in the laboratory but may also be due to atmospheric aerosol.

Less success was had with the observations of 22 August 2008. This was primarily due to spectral features that were not present in the observations of 18 September 2008. An attempt was made to correct for these features via phase correction, but this was not successful. This was mitigated somewhat in *Menang* [2012] due to the use of the TSARS as a calibration factor; however this overrides the blackbody calibration and is not recommended by *Gardiner et al.* [2012].

Other days of spectra were available; however these were few and far between, and often suffered from large aerosol optical depths, making the continuum retrieval extremely uncertain and not useful as a cross-check.

In Chapter 6, an assessment was made of the relative impact of the foreign and self-continuum in atmospheric conditions. Assuming a foreign or self-continuum from MT_CKD or laboratory data, an estimated foreign and self-continuum was derived from the Langley-derived continuum from Chapter 5. These results indicate that the foreign continuum in MT_CKD is an underestimate in the 2.1 and 1.6 μm windows,

in line with the CAVIAR foreign continuum of *Ptashnik et al.* [2012]. It is however difficult to make any judgements about which of the self-continua are likely to be correct, since there are large uncertainties in the spectrum obtained from this work.

7.3: Future work

This section details future work that could be undertaken to improve our understanding of both solar spectral irradiance and the water vapour continuum. This is broken down into two parts; Section 7.3.1 considers solar spectral irradiance, and Section 7.3.2 the water vapour continuum.

7.3.1: Solar spectral irradiance

There appears to be some consensus on a lower value of near-infrared SSI from 4000-7000 cm^{-1} from several measurements (e.g. this work, *Meftah et al.* [2018], *Thuillier et al.* [2014], *Bolseé et al.* [2014]), yet the large uncertainties make this inconclusive. The best method of reducing this uncertainty is to make measurements from a variety of space, aircraft and ground-based spectrometers, with a detailed intercomparison of the various data.

It is important not just to look at the absolute value of SSI, but also to determine its change over time, including time periods longer than the lifetime of space-based spectrometers. This can currently only be done using ground-based measurements, preferably at high altitude. Ideally this would cover a wide spectral range (~100-5000 nm), allowing for high spectral and temporal resolution datasets for use in GCMs and radiation models over time without relying on semi-empirical spectra or reanalysis data, and potentially observe any long-term trend in SSI at any wavelength. This should be combined with additional theoretical work, to compare solar atmosphere models with the high resolution measurements to determine the exact positions and strengths of solar lines.

Characterising the NIR SSI is an important task in itself, but also has implications for our understanding of the continuum. If the SSI was known with great accuracy and precision, then it becomes possible to calibrate sun-pointing spectrometers to the SSI, which would allow for absolute measurements of downwelling radiation and atmospheric extinction. This could be used to derive the near-infrared continuum

absorption, as was attempted by *Reichert and Sussmann* [2016]. This could also be used to assess the calibration drift for radiometrically calibrated instruments without having to use a transfer standard source such as the TSARS. The ability to calibrate a spectrometer without needing access to a high temperature blackbody would allow for many more field sites to make calibrated measurements of atmospheric radiation, which would open up many avenues for e.g. deriving the NIR continuum absorption in different conditions.

7.3.2: Water vapour continuum

Understanding of the water vapour continuum cannot be obtained from either atmospheric or laboratory experiments alone. A combination of the two, ideally in conditions that allow for synthesis of the two methods is required. Laboratory measurements allow for controlled experimental conditions, but do not necessarily capture the complex processes that affect the absorption in the atmosphere. It is therefore a necessity to confirm any laboratory measurements by direct atmospheric observations, as has been done in this thesis. Sections 7.3.2.1 and 7.3.2.2 detail how future experiments could improve our understanding of the continuum, both in the near-IR windows on which this work focuses and also elsewhere in the spectrum. Section 7.3.2.3 discusses further steps once the continuum has been rigorously derived in the laboratory.

7.3.2.1: Laboratory experiments

Since the results presented in Section 7.2 are by no means conclusive, and more atmospheric measurements of the continuum are necessary, an important question to answer is how a similar such field experiment might be improved in the future, and how we could use both field and laboratory experiments to improve our understanding of the continuum.

One important aspect is for new laboratory measurements of the continuum. The lack of reconcilability between the Grenoble and CAVIAR observations is a significant problem for modelling groups such as MT_CKD attempting to create a useful product for climate and weather models. Ideally, these measurements should come from as many independent groups as possible, using a variety of methods. While measurements at room temperature are possible, these are not necessarily representative of atmospheric conditions. Any future project should aim to measure

at as many different temperatures and pressures as possible, to fully capture the range of plausible atmospheric conditions and allow for better direct comparison with atmosphere-derived spectra.

One such project is the ASPIC (Advanced Spectroscopy for improved characterisation of the near-Infrared water vapour Continuum) project, being undertaken by the University of Reading and the Rutherford Appleton Laboratory, which aims to build on the CAVIAR measurements using a similar FTS setup. This project includes several advances in spectroscopy and optics since the CAVIAR experiments.

The first of these is the use of a new super-continuum laser source. This laser is used as a broadband light source and has a much higher intensity than the lamp used in the CAVIAR laboratory experiment [Ptashnik *et al.*, 2011a] and is more spatially coherent. This allows for even more reflections, which allows for a larger path length. The increase in intensity and spatial coherence should allow for a much higher sensitivity than the CAVIAR FTS measurements, rivalling that of the CRDS measurements but with a much larger cell (mitigating the potential effect of e.g. water adsorption on the dielectric mirrors or other surface effects) and significantly greater spectral coverage.

The other advancement in ASPIC is the use of a new optical cavity and multipass cell. This, combined with the use of the super-continuum laser allows for many more reflections (and therefore a much larger path length, and therefore more absorption) than available in CAVIAR (210 m in ASPIC compared to ~20 m in CAVIAR).

A pilot study was run in 2015, the results of which showed good agreement with the CAVIAR lab measurements in the 2.1 μm window (Figure 9 of Shine *et al.* [2016c]), although no measurements were possible in the 1.6 μm window due to a lack of baseline stability. This baseline stability will be significantly improved in ASPIC due to the new cavity and light source.

An additional aspect is the use of an NIR (1.5-1.6 μm) laser, to probe directly in the centre of the 1.6 μm window and compare with the results from the FTS measurements.

ASPIC should be able to probe down to temperatures approaching those found in the lowest levels of the atmosphere (270-315 K); given measurements of the foreign

continuum in this project it will therefore be possible to compare the new ASPIC results with the results derived in this thesis.

This project, while capable of deriving the continuum in conditions close to atmospheric conditions will not on its own be definitive. Additional measurements from other groups are necessary, especially using different methods such as CRDS, and taking into account advances in spectroscopy, and the controlled laboratory setup may not be able to capture some of the more complex physical processes that occur in the atmosphere (which contribute to the continuum). A brief overview of experimental advances is presented in *Shine et al.* [2016c].

7.3.2.2: Considerations for future field campaigns

During my PhD several aspects of the experiment proved difficult to manage and contributed to a more conservative estimate of the uncertainty than otherwise may have been the case. One challenge not directly related to the experiment itself was the time (almost 10 years) between the field campaign and the analysis performed in this work. The ability to make supplementary measurements, or to have regular access to the FTS software and measurements would have been useful particularly during the phase correction portion of the work.

While the overall calibration of the instrument is considered robust, and the uncertainty budget plausible, there were several aspects of the calibration that could have been improved. An assessment of the mirror reflectivity over time during the campaign would have been extremely useful. In this case, the mirrors were considered “used” as soon as they entered the field. In reality however, the degradation of these mirrors would have likely taken place gradually, meaning that a time-dependent mirror reflectivity calibration would be necessary.

The TSARS calibration transfer standard was one of the more disappointing aspects of the campaign. Its stability was lower than expected, and it did not provide a particularly useful calibration check. A future campaign might use a more stable source, such as a laser. While this would not provide the necessary spectral coverage, a set of lasers in each window would be able to provide a stable calibration transfer source which can be used to accurately assess the change in the FTS calibration over time. This could in principle be done in each of the infrared windows provided one had a set of lasers which could sample a few points within each window. This,

alongside a detector more suited for observations at shorter wavelengths (higher wavenumbers) beyond 7000 cm^{-1} , which would allow for us to more effectively probe the continuum in these windows, which is subject to even fewer sets of observations than the NIR windows. As was discussed in Section 7.3.1, a stronger constraint on the NIR SSI would allow for an instrument to be calibrated in situ.

An attempt was made to improve the calibration of the instrument using a different phase correction procedure to that done natively by the OPUS FTS software, since there were spectral features (e.g. Figure 5.27) which *may* have been caused by the phase correction. This was also motivated by the “black box” nature of the OPUS software; the source code is not editable by the end user. However, this was unsuccessful, and put on hold due to the new literature regarding the near-infrared solar spectral irradiance, which was deemed to be a more important immediate problem. A future campaign could mitigate this problem by using open source, modifiable software rather than OPUS to perform the numerical filtering necessary to turn interferograms into usable spectra. This could be done using the TCCON (Total Carbon Column Observing Network, e.g. *Wunch et al.* [2011]) I2S (Interferogram 2 Spectra) software for example, which is open source.

The observations of 22 August 2008 could have been corrected for by some normalised factor using the TSARS observations. However, this would have overwritten the blackbody calibration and introduced significant additional uncertainty into the continuum derivation.

The most significant contributor to the experimental uncertainty was the uncertainty introduced from the Microtops sunphotometer measurements and the extrapolation of these measurements into the spectral region of interest. Over the course of the project, there were several reasons to question the effectiveness of the Microtops to measure aerosol throughout the day, given that these changes were not picked up by the much more sensitive high-resolution Fourier Transform spectrometer.

Part of the problem may have been the handheld nature of the sunphotometer. Since this relies on a user to take a measurement by pointing the photometer at the Sun, there is the potential for additional error. While it is unlikely that this caused the systematic offset shown in Chapter 5, it cannot be ruled out entirely.

A future measurement campaign would best take place at a site with dedicated in situ aerosol measurement systems, such as an AERONET (AErosol RObotic NETwork, e.g. *Russell et al.* [2010]) site. The closest AERONET site to the Camborne field site in 2008 is at Chilbolton, over 200 miles away, making a cross-comparison with the observed Camborne AOD highly uncertain and dependent significantly on the prevailing wind.

Ideally, the site should be as far away as possible from any source of aerosols, such as industry, agriculture or marine sites. Satellite observations of aerosols are more ubiquitous than they were in 2008. An experimental campaign performed today could use one of these products to observe aerosol optical depth over a similar area to the campaign site as a cross-check to the in-situ measurements. This was considered for the work done in this PhD, but no suitable aerosol product was found that could explain the observations. Satellite observations use atmosphere windows to measure AOD; this adds an element of circularity too, since a continuum must be assumed to isolate the aerosol signal.

For these reasons, a site such as Mauna Loa in Hawaii would be a good place for such a field campaign. This site is in a remote location away from industrial and agricultural sources of aerosol, and its position 3300 metres above sea level make it ideal for removing the effects of aerosol.

The spectral behaviour of AOD in this work was obtained via a Mie scattering code. This is in principle the best way to derive aerosol spectral behaviour. However, the uncertainties were quite large in this work, for several reasons. Since no (useful) observations of the relevant parameters (size distribution, refractive index...) were available, these were estimated from a range of typical parameters and constrained somewhat using the observed Ångström exponent. An updated field campaign might again use a research aircraft, among other aerosol observing systems to obtain these quantities. The FAAM aircraft used for the Camborne experiment measured aerosol properties, but this was done using an inlet which dried the aerosol as it entered. This is less useful for assessing the radiative impact (as is necessary for a continuum retrieval); a future campaign might measure ambient rather than dry aerosol properties.

An important aspect of the work (see Chapters 5 & 6) is distinguishing the foreign continuum from the self-continuum. This is in principle possible by taking measurements over a wide range of measurement conditions. This was not the case in the CAVIAR campaign, although it was expected that there would be more usable measurement days than there were in practice. There were observations from the Jungfraujoch observatory, which has significantly lower water vapour concentrations. These would not have covered a sufficient range of water vapour to determine the relative contribution however, since the concentrations are so low that information could only be reliably attained in the band regions, even if the calibration were robust. Additionally, the Jungfraujoch experiment took place over a year after the Camborne experiment; the calibration of the instrument had changed somewhat. Thus, the results may not have been directly comparable, although this would have been mitigated by the Langley method or a more robust field calibration standard than the integrating sphere used in the Jungfraujoch campaign.

For observing in the windows, an approach like that of *Reichert and Sussmann* [2016] and *Reichert et al.* [2016] may have been useful, using the calibration procedure from *Gardiner et al.* [2012] in the laboratory and cross-comparing with the Langley method-based calibration from *Reichert et al.* The *Reichert and Sussmann* experiment was performed in winter, so the solar zenith angles are sufficiently large to (ostensibly) observe in the bands despite the lower integrated water vapour. Observing over as wide a range of water vapour conditions as possible would be the most appropriate way to constrain the atmospheric continuum. As mentioned in Section 7.3.1, this requires a robust estimate of the near-infrared solar spectral irradiance, further motivating the need for new measurements of SSI.

Observations at the Jungfraujoch could have in principle resulted in a better constraint on the solar spectral irradiance, since the atmospheric optical depth is significantly lower, meaning that the observed irradiance is closer to the top of atmosphere irradiance. However, since there is good confidence that the conditions do not change much throughout the day for 18 September, and that a small change in optical depth does not significantly affect the intercept of a Langley plot, there is every reason to have confidence in the derived SSI from the Camborne experiment alone.

Sun-pointing ground-based measurements are not the only method of deriving the continuum in atmospheric conditions. An aircraft-based measurement with a high-resolution spectrometer could in principle derive the continuum for a much wider range of conditions than a ground-based measurement and allow for the derivation of a vertical profile of the continuum absorption. This has been done in the mid and far-infrared regions [Green *et al.*, 2012; Newman *et al.*, 2012] as part of the broader CAVIAR project. Such a campaign would require a high-quality calibration transfer assessment. This method, as with the Reichert *et al.* method requires knowledge of the solar spectral irradiance, since a Langley analysis is difficult with an aircraft measurement campaign (as in e.g. Arvesen *et al.* [1969])

It is possible to use a horizontal path to derive the continuum absorption in atmospheric conditions from a ground-based system. This allows for *in situ* assessment of the humidity and other atmospheric parameters in the beam path, making it more akin to a laboratory measurement than a sun-pointing measurement. It also removes the effect of clouds and aerosols which can contaminate a sun-pointing measurement. This would rely on a well-characterised source; e.g. Rieker *et al.* [2014] observe spectral properties of carbon dioxide and methane lines using a frequency comb method, which allows for high precision measurements over a range of wavenumbers (5990-6260 cm^{-1} in Rieker *et al.*) at very high spectral resolution. Such a method would not be without its problems however; the continuum is very weak, meaning that the path would need to be as long as possible in order to maximise the amount of absorption.

7.3.2.3: Further steps and incorporation into radiation models

Once the continuum has been robustly characterised in the laboratory and reconciled with atmospheric measurements, the next step is to incorporate this into radiation models. This should first involve direct incorporation into HITRAN and other spectroscopic databases. This would allow for direct incorporation into radiation models without the need for a separate model such as MT_CKD and make it easier for model developers to track any changes in the continuum absorption as new experimental data is acquired. This step should be made in conjunction with theoretical work, to explain the causes of the continuum and reconcile the various hypotheses about this, particularly reconciling the dimer and far-wing explanations of the continuum. Additionally, such work should go into developing a more

sophisticated understanding of the temperature dependence (e.g. by assessing the effect of a transition between bound and quasi-bound dimers with temperature and how this affects absorption characteristics). An immediate step that could be taken after this work is to repeat the analysis of Chapter 6 with an updated temperature dependence. Any updated continuum model should be put into line-by-line codes and GCM/weather prediction radiation schemes, with intercomparison between the two to ensure that the effect is being modelled correctly in the lower-resolution GCM radiation schemes.

Any such work should take place alongside impact studies, looking at how a more complete model of the continuum affects the surface-atmosphere energy partition, and the changes in the hydrological cycle this causes. This is particularly important in a warming climate due to the water vapour feedback. Finally, the impact on remote sensing should be considered. Tests should be run to assess how much the updated continuum affects retrievals of various properties. In principle, this could lead to a reanalysis of old data, if this effect was significant.

Bibliography

- Allen, M. R., and W. J. Ingram (2002), Constraints on future changes in climate and the hydrologic cycle, *Nature*, 419(6903), doi:10.1038/nature01092.
- Arvesen, J. C., R. N. J. Griffin, and B. D. J. Pearson (1969), Determination of extraterrestrial solar spectral irradiance from a research aircraft, *Appl. Opt.*, 8(1), 2215–2232, doi:10.1364/AO.8.002215.
- Atkins, P., J. de Paula, and J. Keeler (2017), *Atkins' Physical Chemistry*, 11th ed., Oxford University Press.
- Ball, W. T., N. A. Krivova, Y. C. Unruh, J. D. Haigh, and S. K. Solanki (2014), A new SATIRE-S spectral solar irradiance reconstruction for solar cycles 21--23 and its implications for stratospheric ozone, *Journal of the Atmospheric Sciences*, 4086–4101, doi:10.1175/JAS-D-13-0241.1.
- Banwell, C. N., and E. M. McCash (1994), *Fundamentals of Molecular Spectroscopy*, McGraw-Hill Education.
- Baranov, Y. I., and W. J. Lafferty (2012), The water vapour self- and water–nitrogen continuum absorption in the 1000 and 2500 cm^{-1} atmospheric windows, *Phil. Trans. R. Soc. A*, 370(1968), 2578–2589.
- Barber, R. J., J. Tennyson, G. J. Harris, and R. N. Tolchenov (2006), A high-accuracy computed water line list, *Mon. Not. R. Astron. Soc.*, 368(3), 1087–1094, doi:10.1111/j.1365-2966.2006.10184.x.
- Barber, R. J., J. Tennyson, G. J. Harris, and R. N. Tolchenov (2008), High accuracy computed water line list - BT2 (Barber+, 2006), *VizieR On-line Data Cat.*, 6119(February), 2008.
- BenMoussa, A. et al. (2013), On-Orbit Degradation of Solar Instruments, *Sol. Phys.*, 288(1), 389–434, doi:10.1007/s11207-013-0290-z.
- Bernath, P. F. (2005), *Spectra of Atoms and Molecules*, Oxford University Press.
- Bicknell, W. E., S. Di Cecca, M. K. Griffin, Search for low-absorption regions in the 1.6- and 2.1-micron atmospheric windows, *J. Dir. Energy*, 2(2), 151–161.
- Bignell, K., F. Saiedy, and P. A. Sheppard (1963), On the Atmospheric Infrared Continuum, *J. Opt. Soc. Am.*, 53(4), 466–479, doi:10.1364/JOSA.53.000466.

- BIPM (2006), *Le système international d'unités (SI) Brochure*,
https://www.bipm.org/utls/common/pdf/si_brochure_8_en.pdf. Accessed 16 September 2018
- Bojinski, S., M. Verstraete, T. C. Peterson, C. Richter, A. Simmons, and M. Zemp (2014), The concept of essential climate variables in support of climate research, applications, and policy, *Bull. Am. Meteorol. Soc.*, 95(9), 1431–1443, doi:10.1175/BAMS-D-13-00047.1.
- Bolsée, D. et al. (2014), Accurate Determination of the TOA Solar Spectral NIR Irradiance Using a Primary Standard Source and the Bouguer–Langley Technique, *Sol. Phys.*, 289(7), 2433–2457, doi:10.1007/s11207-014-0474-1.
- Bolsée, D., N. Pereira, E. Cuevas, R. García, and A. Redondas (2016), Comments to the Article by Thuillier et al. “The Infrared Solar Spectrum Measured by the SOLSPEC Spectrometer Onboard the International Space Station” on the Interpretation of Ground-based Measurements at the Izaña Site, *Sol. Phys.*, 291(8), 2473–2477, doi:10.1007/s11207-016-0914-1.
- Bucholtz, A. (1995), Rayleigh-scattering calculations for the terrestrial atmosphere., *Appl. Opt.*, 34(15), 2765–2773, doi:10.1364/AO.34.002765.
- Burch, D. E. (1982), *Continuum Absorption by H₂O*, Ford Aerospace and Communications Corp, Newport Beach, CA, Aeronautic Div.
- Burch, D. E., and R. L. Alt (1984), *Continuum Absorption by H₂O in the 700-1200 cm⁻¹ and 2400-2800 cm⁻¹ Windows*, Ford Aerospace and Communications Corp, Newport Beach, CA, Aeronautic Div.
- Chase, D. B. (1982), Phase Correction in FT-IR, *Appl. Spectrosc.*, 36(3), 240–244.
- Clough, S. A., F. X. Kneizys, and R. W. Davies (1989), Line shape and the water vapor continuum, *Atmos. Res.*, 23(3), 229–241, doi:https://doi.org/10.1016/0169-8095(89)90020-3.
- Clough, S. A., M. W. Shephard, E. J. Mlawer, J. S. Delamere, M. J. Iacono, K. Cady-Pereira, S. Boukabara, and P. D. Brown (2005), Atmospheric radiative transfer modeling: A summary of the AER codes, *J. Quant. Spectrosc. Radiat. Transf.*, 91(2), 233–244, doi:10.1016/j.jqsrt.2004.05.058.
- Coddington, O., J. L. Lean, P. Pilewskie, M. Snow, and D. Lindholm (2015), A Solar Irradiance Climate Data Record, *Bull. Am. Meteorol. Soc.*, (July), doi:10.1175/BAMS-D-14-00265.1.

- Daniel, J. S. (2004), Atmospheric water vapor complexes and the continuum, *Geophys. Res. Lett.*, *31*, 1–4, doi:10.1029/2003GL018914.
- Deangelis, A. M., X. Qu, M. D. Zelinka, and A. Hall (2015), An observational radiative constraint on hydrologic cycle intensification, *Nature*, *528*(7581), 249–253, doi:10.1038/nature15770.
- Dubovik, O., B. Holben, T. F. Eck, A. Smirnov, Y. J. Kaufman, M. D. King, D. Tanré, and I. Slutsker (2002), Variability of Absorption and Optical Properties of Key Aerosol Types Observed in Worldwide Locations, *J. Atmos. Sci.*, *59*(3), 590–608, doi:10.1175/1520-0469(2002)059<0590:VOAAOP>2.0.CO;2.
- Dudhia, A. (2017), The Reference Forward Model (RFM), *J. Quant. Spectrosc. Radiat. Transf.*, *186*, 243–253, doi:10.1016/j.jqsrt.2016.06.018.
- Dewitte, Steven, and Stijn Nevens. "The total solar irradiance climate data record." *The Astrophysical Journal* 830, no. 1 (2016): 25. doi:10.3847/0004-637X/830/1/25
- Dudok de Wit, T., G. Kopp, C. Fröhlich, and M. Schöll (2017), Methodology to create a new total solar irradiance record: Making a composite out of multiple data records, *Geophys. Res. Lett.*, *44*, 1196–1203, doi:10.1002/2016GL071866.
- Elsasser, W. M. (1938) Far infrared absorption of atmospheric water vapor. *Astrophys J* *87*:497–507
- Elsej, J., M. D. Coleman, T. Gardiner, and K. P. Shine (2017), Can Measurements of the Near-Infrared Solar Spectral Irradiance be Reconciled? A New Ground-Based Assessment Between 4,000 and 10,000 cm⁻¹, *Geophys. Res. Lett.*, *44*(19), 10,10-71,80, doi:10.1002/2017GL073902.
- Fligge, M., S. K. Solanki, J. M. Pap, C. Fröhlich, and C. Wehrli (2001), Variations of solar spectral irradiance from near UV to the infrared - Measurements and results, *J. Atmos. Solar-Terrestrial Phys.*, *63*(14), 1479–1487, doi:10.1016/S1364-6826(01)00020-7.
- Fontenla, J. M., E. Avrett, G. Thuillier, and J. Harder (2006), Semiempirical Models of the Solar Atmosphere. I. The Quiet and Active Sun Photosphere at Moderate Resolution, *Astrophys. J.*, *639*(1), 441–458, doi:10.1086/499345.
- Fontenla, J. M., J. Harder, W. Livingston, M. Snow, and T. N. Woods (2011), High-resolution solar spectral irradiance from extreme ultraviolet to far infrared, *J. Geophys. Res.*, *116*(July), D20108, doi:10.1029/2011JD016032.
- Forster, P. M., T. Richardson, A. C. Maycock, C. J. Smith, B. H. Samset, G. Myhre, T. Andrews, R. Pincus, and M. Schulz (2016), Recommendations for diagnosing effective

- radiative forcing from climate models for CMIP6, *J. Geophys. Res.*, *121*(20), 12,412–460,475, doi:10.1002/2016JD025320.
- Fröhlich, C., and J. Lean (2004), Solar radiative output and its variability: Evidence and mechanisms, *Astron. Astrophys. Rev.*, *12*(4), 273–320, doi:10.1007/s00159-004-0024-1.
- Gardiner, T. D., M. Coleman, H. Browning, L. Tallis, I. V. Ptashnik, and K. P. Shine (2012), Absolute high spectral resolution measurements of surface solar radiation for detection of water vapour continuum absorption, *Philos. Trans. R. Soc. A Math. Phys. Eng. Sci.*, *370*, 2590–2610, doi:10.1098/rsta.2011.0221.
- Gordon, I. E., L.S. Rothman, C. Hill, R.V. Kochanov, Y. Tan et al. (2017), The HITRAN2016 molecular spectroscopic database, *J. Quant. Spectrosc. Radiat. Transf.*, *203*, 3–69, doi:10.1016/j.jqsrt.2017.06.038.
- Grant, W. B. (1990), Water vapor absorption coefficients in the 8-13 microm spectral region: a critical review, *Appl. Opt.*, *29*(22), 3206, doi:10.1364/AO.29.003206.
- Green, P. D., S. M. Newman, R. J. Beeby, J. E. Murray, J. C. Pickering, and J. E. Harries (2012), Recent advances in measurement of the water vapour continuum in the far-infrared spectral region, *Phil. Trans. R. Soc. A*, *370*(1968), 2637–2655.
- Griffiths, P. R., and J. de Haseth (1986), *Fourier Transform Infrared Spectroscopy*, 2nd edition, Wiley.
- Haberreiter, M., M. Schöll, T. Dudok de Wit, M. Kretzschmar, S. Misios, K. Tourpali, and W. Schmutz (2017), A new observational solar irradiance composite, *J. Geophys. Res. Sp. Phys.*, *122*(6), 5910–5930, doi:10.1002/2016JA023492.
- Harder, J., G. Lawrence, J. Fontenla, G. Rottman, and T. Woods (2005), The spectral irradiance monitor: scientific requirements, instrument design, and operation modes, in *The Solar Radiation and Climate Experiment (SORCE)*, pp. 141–167, Springer.
- Harder, J. W., G. Thuillier, E. C. Richard, S. W. Brown, K. R. Lykke, M. Snow, W. E. McClintock, J. M. Fontenla, T. N. Woods, and P. Pilewskie (2010), The SORCE SIM solar spectrum: Comparison with recent observations, *Sol. Phys.*, *263*(1), 3–24, doi:10.1007/s11207-010-9555-y.
- Hestroffer, D., and C. Magnan (1998), Wavelength dependency of the solar limb darkening, *Astron. Astrophys.*, *333*, 338–342.
- Hogan, R. J., and A. Bozzo (2018), A Flexible and Efficient Radiation Scheme for the ECMWF Model, *J. Adv. Model. Earth Syst.*, *10*, doi:10.1029/2018MS001364.

- Ichoku, C., et al., Analysis of the performance characteristics of the five-channel Microtops II Sun photometer for measuring aerosol optical thickness and precipitable water vapor, *J. Geophys. Res.*, 107(D13), doi:10.1029/2001JD001302, 2002.
- Ineson, S., A. A. Scaife, J. R. Knight, J. C. Manners, N. J. Dunstone, L. J. Gray, and J. D. Haigh (2011), Solar forcing of winter climate variability in the Northern Hemisphere, *Nat. Geosci.*, 4(11), 753–757, doi:10.1038/ngeo1282.
- IPCC, 2014: Climate Change 2014: Synthesis Report. Contribution of Working Groups I, II and III to the Fifth Assessment Report of the Intergovernmental Panel on Climate Change [Core Writing Team, R.K. Pachauri and L.A. Meyer (eds.)]. IPCC, Geneva, Switzerland, 151 pp. Iqbal, M. (1983), *An Introduction to Solar Radiation*, 1st ed., Academic Press.
- Jaquinet-Housson, N. R. Armante, N.A. Scott, A. Chédin, L. Crépeau, et al., The 2015 edition of the GEISA spectroscopic database. *Journal of Molecular Spectroscopy*, Elsevier, 2016, 327, pp.31-72. doi:10.1016/j.jms.2016.06.007.
- Joint Committee For Guides In Metrology (2008), Evaluation of measurement data — Guide to the expression of uncertainty in measurement, *Int. Organ. Stand. Geneva ISBN, 50* (September), 134, doi:10.1373/clinchem.2003.030528.
- Kapitanov V.A., Osipov K.Yu., Ptashnik I.V. Photoacoustic measurements of the water vapor continuum absorption in the 1.6 μm window. *Optika Atmosfery i Okeana*. 2018. V. 31. No. 12. P. 995–1000 [in Russian].
- Kopp, G. (2016), Magnitudes and timescales of total solar irradiance variability, *J. Sp. Weather Sp. Clim.*, 6, A30, doi:10.1051/swsc/2016025.
- Kopp, G., and J. L. Lean (2011), A new, lower value of total solar irradiance: Evidence and climate significance, *Geophys. Res. Lett.*, 38(1), 1–7, doi:10.1029/2010GL045777.
- Kopp, G., K. Heuerman, D. Harber, and G. Drake (2007), The TSI Radiometer Facility: absolute calibrations for total solar irradiance instruments, *Metrologia*, 667709, doi:10.1117/12.734553.
- Kurucz, R L., Bell, B. (1995), 1995 Atomic Line Data, Kurucz CD-ROM No. 23. Cambridge, Mass.: Smithsonian Astrophysical Observatory.
- Kurucz, R. L. (2005), New atlases for solar flux, irradiance, central intensity, and limb intensity, *Mem. della Soc. Astron. Ital. Suppl.*, 8, 189–191.
- Lean, J. L., and M. T. DeLand (2012), How does the Sun’s spectrum vary?, *J. Clim.*, 25, 2555–2560, doi:10.1175/JCLI-D-11-00571.1.

- Lechevallier, L., S. Vasilchenko, R. Grilli, D. Mondelain, D. Romanini, and A. Campargue (2018), The water vapour self-continuum absorption in the infrared atmospheric windows: new laser measurements near 3.3 and 2.0 μm , *Atmos. Meas. Tech.*, *11*(4), 2159–2171.
- Lee, K. H., M. S. Wong, J. Nichol, and P. W. Chan (2015), Retrieval of aerosol size distribution from Microtops II sunphotometer in Hong Kong, *Aerosol Air Qual. Res.*, *15*(5), 1712–1719, doi:10.4209/aaqr.2015.01.0048.
- Liou, K. N. (2002), *An Introduction to Atmospheric Radiation*, Academic Press.
- Matthes, K., B. Funke, M. Anderson, L. Barnard, J. Beer, P. Charbonneau, M. Clilverd, T. Dudok de Wit, M. Haberreiter, and A. Hendry (2017), Solar forcing for CMIP6 (v3. 2), *Geosci. Model Dev.*, *10*(6), 2247–2302.
- Meeus, J. (1999), *Astronomical Algorithms*, 2nd ed., Willmann-Bell.
- Meftah, M. et al. (2017), SOLAR-ISS: A new reference spectrum based on SOLAR/SOLSPEC observations, *Astron. & Astrophys.*, 1–13, doi:10.1051/0004-6361/201731316.
- Menang, K. P. (2012), A High Resolution Extraterrestrial Solar Spectrum and Water Vapour Continuum at Near-Infrared Wavelengths from Ground-Based Spectrometer Measurements, PhD thesis, University of Reading.
- Menang, K. P. (2018), Assessment of the Impact of Solar Spectral Irradiance on Near-Infrared Clear-Sky Atmospheric Absorption and Heating Rates, *J. Geophys. Res. Atmos.*, *123*(12), 6460–6468, doi:10.1029/2018JD028342.
- Menang, K. P., and K. P. Shine (2013), The effect of chosen extraterrestrial solar spectrum on clear-sky atmospheric absorption and heating rates in the near infrared, *Radiat. Process. Atmos. Ocean Proc. Int. Radiat. Symp. (eds Cahalan RF, Fischer J) Date 6-10 August 2012 AIP Conf. Proc. 1531, 520, 520–523*, doi:10.1063/1.4804821.
- Menang, K. P., M. D. Coleman, T. D. Gardiner, I. V. Ptashnik, and K. P. Shine (2013), A high-resolution near-infrared extraterrestrial solar spectrum derived from ground-based Fourier transform spectrometer measurements, *J. Geophys. Res. Atmos.*, *118*, 5319–5331, doi:10.1002/jgrd.50425.
- Miloshevich, L. M., H. Vömel, D. N. Whiteman, and T. Leblanc (2009), Accuracy assessment and correction of Vaisala RS92 radiosonde water vapor measurements, *J. Geophys. Res. Atmos.*, *114*(D11), doi: 10.1029/2008JD011565.
- Mitsel, A. A., and K. M. Firsov (1995), A fast line-by-line method, *J. Quant. Spectrosc.*

- Radiat. Transf.*, 54(3), 549–557, doi:[https://doi.org/10.1016/0022-4073\(95\)00022-D](https://doi.org/10.1016/0022-4073(95)00022-D).
- Mlawer, E., et al. "Determination of Near-IR Water Vapor Self Continuum from Field Observations." The 13th Biennial HITRAN Conference (HITRAN13), Harvard-Smithsonian Center for Astrophysics, Cambridge, MA, USA, doi: 10.5281/zenodo.11107. Vol. 10. 2014.
<http://adsabs.harvard.edu/abs/2014hitr.confE...6M>
- Mondelain, D., A. Aradj, S. Kassi, and A. Campargue (2013), The water vapour self-continuum by CRDS at room temperature in the 1.6 μm transparency window, *J. Quant. Spectrosc. Radiat. Transf.*, 130, 381–391, doi:10.1016/j.jqsrt.2013.07.006.
- Mondelain, D., S. Manigand, S. Kassi, and A. Campargue (2014), Temperature dependence of the water vapor self-continuum by cavity ring-down spectroscopy in the 1.6 μm transparency window, *J. Geophys. Res. Atmos.*, 119(i), 5625–5639, doi:10.1002/2013JD021319.
- Mondelain, D., S. Vasilchenko, P. Čermák, S. Kassi, and A. Campargue (2015), The self- and foreign-absorption continua of water vapor by cavity ring-down spectroscopy near 2.35 μm , *Phys. Chem. Chem. Phys.*, 17(27), 17762–17770, doi:10.1039/C5CP01238D.
- Newman, S. M., P. D. Green, I. V Ptashnik, T. D. Gardiner, M. D. Coleman, R. A. McPheat, and K. M. Smith (2012), Airborne and satellite remote sensing of the mid-infrared water vapour continuum, *Philos. Trans. R. Soc. A Math. Phys. Eng. Sci.*, 370, 2611–2636, doi:10.1098/rsta.2011.0223.
- Norton, R. H., and R. Beer (1977), Errata: New Apodizing Functions For Fourier Spectrometry, *J. Opt. Soc. Am.*, 67(3), 419, doi:10.1364/JOSA.67.000419.
- Olivero, J. J., and R. L. Longbothum (1977), Empirical fits to the Voigt line width: A brief review, *J. Quant. Spectrosc. Radiat. Transf.*, 17(2), 233–236, doi:[https://doi.org/10.1016/0022-4073\(77\)90161-3](https://doi.org/10.1016/0022-4073(77)90161-3).
- Oyafuso, F. et al. (2017), High accuracy absorption coefficients for the Orbiting Carbon Observatory-2 (OCO-2) mission: Validation of updated carbon dioxide cross-sections using atmospheric spectra, *J. Quant. Spectrosc. Radiat. Transf.*, 203, 213–223, doi:10.1016/j.jqsrt.2017.06.012.
- Payne, V. H., E. J. Mlawer, K. E. Cady-Pereira, and J. L. Moncet (2011), Water vapor continuum absorption in the microwave, *IEEE Trans. Geosci. Remote Sens.*, 49(6 PART 2), 2194–2208, doi:10.1109/TGRS.2010.2091416.
- Paynter, D., and V. Ramaswamy (2014), Investigating the impact of the shortwave water

- vapor continuum upon climate simulations using GFDL global models, *J. Geophys. Res. Atmos.*, 119(18), doi: 10.1002/2014JD021881.
- Paynter, D. J., and V. Ramaswamy (2011), An assessment of recent water vapor continuum measurements upon longwave and shortwave radiative transfer, *J. Geophys. Res. Atmos.*, 116(20), 1–13, doi:10.1029/2010JD015505.
- Pegrum, H. M., E. R. Woolliams, N. P. Fox, L. van Riel, G. Otter, and M. Kowalewski (2004), Calibration of the NPL transfer standard absolute radiance source (TSARS) and its use with GOME 2-FM3 spectral radiance measurements, in *Sensors, Systems, and Next-Generation Satellites VIII*, vol. 5570, pp. 503–515, International Society for Optics and Photonics.
- Petty, G. W. (2005), *A First Course in Atmospheric Radiation*, Sundog Publishing, Madison, Wisconsin.
- Pilewskie, P., G. Kopp, E. Richard, O. Coddington, T. Sparn, and T. Woods (2018), TSIS-1: Continuity of the Total and Spectral Solar Irradiance Climate Data Record from Space., in *15th AMS Conference on Clouds and Radiation, Vancouver*.
https://ams.confex.com/ams/15CLOUD15ATRAD/video gateway.cgi/id/48608?recordid=48608&uniqueid=Paper347328&entry_password=176469 (Accessed 16 September 2018)
- Pincus, R. et al. (2015), Radiative flux and forcing parameterization error in aerosol-free clear skies, *Geophys. Res. Lett.*, 42(13), 5485–5492, doi:10.1002/2015GL064291.
- Platnick, S., and J. M. Fontenla (2008), Model calculations of solar spectral irradiance in the 3.7- μ m band for earth remote sensing applications, *J. Appl. Meteorol. Climatol.*, 47(1), 124–134, doi:10.1175/2007JAMC1571.1.
- Platnick, S. et al. (2017), The MODIS Cloud Optical and Microphysical Products: Collection 6 Updates and Examples from Terra and Aqua, *IEEE Trans. Geosci. Remote Sens.*, 55(1), 502–525, doi:10.1109/TGRS.2016.2610522.
- Ptashnik, I. V., R. A. McPheat, K. P. Shine, K. M. Smith, and R. G. Williams (2011a), Water vapor self-continuum absorption in near-infrared windows derived from laboratory measurements, *J. Geophys. Res. Atmos.*, 116, 1–16, doi:10.1029/2011JD015603.
- Ptashnik, I. V., K. P. Shine, and A. A. Viganin (2011b), Water vapour self-continuum and water dimers: 1. Analysis of recent work, *J. Quant. Spectrosc. Radiat. Transf.*, 112(8), 1286–1303, doi:10.1016/j.jqsrt.2011.01.012.
- Ptashnik, I. V., R. A. McPheat, K. P. Shine, K. M. Smith, and R. G. Williams (2012), Water

- vapour foreign-continuum absorption in near-infrared windows from laboratory measurements, *Philos. Trans. R. Soc. A Math. Phys. Eng. Sci.*, doi:10.1098/rsta.2011.0218.
- Ptashnik, I. V., T. M. Petrova, Y. N. Ponomarev, K. P. Shine, A. A. M. Solodov, and A. A. M. Solodov (2013), Near-infrared water vapour self-continuum at close to room temperature, *J. Quant. Spectrosc. Radiat. Transf.*, 120, 23–35, doi:10.1016/j.jqsrt.2013.02.016.
- Ptashnik, I. V., T. M. Petrova, Y. N. Ponomarev, A. A. M. Solodov, and A. A. M. Solodov (2015), Water vapor continuum absorption in near-IR atmospheric windows, *Atmos. Ocean. Opt.*, 28(2), 115–120, doi:10.1134/S1024856015020098.
- Rädel, G., K. P. Shine, and I. V. Ptashnik (2014), Global radiative and climate effect of the water vapour continuum at visible and near-infrared wavelengths, *Q. J. R. Meteorol. Soc.*, (April), 727–738, doi:10.1002/qj.2385.
- Reda, I., and A. Andreas (2008), *Solar position algorithm for solar radiation applications*, *Solar Energy, Volume 76, Issue 5, 2004*, pp. 577-589, ISSN 0038-092X, doi:/10.1016/j.solener.2003.12.003.
- Reichert, A., and R. Sussmann (2016), The Zugspitze radiative closure experiment for quantifying water vapor absorption over the terrestrial and solar infrared. Part III: Quantification of the near-infrared water vapor continuum under atmospheric conditions, *Atmos. Chem. Phys. Discuss.*, 2016, 1–13, doi:10.5194/acp-2016-323.
- Reichert, A., M. Rettinger, and R. Sussmann (2016), The Zugspitze radiative closure experiment for quantifying water vapor absorption over the terrestrial and solar infrared. Part II: Accurate calibration of high spectral resolution infrared measurements of surface solar radiation, *Atmos. Meas. Tech. Discuss.*, 2016, 1–16, doi:10.5194/amt-2016-127.
- Richard, L., S. Vasilchenko, D. Mondelain, I. Ventrillard, D. Romanini, and A. Campargue (2017), Water vapor self-continuum absorption measurements in the 4.0 and 2.1 μm transparency windows, *J. Quant. Spectrosc. Radiat. Transf.*, 201, 171–179, doi:https://doi.org/10.1016/j.jqsrt.2017.06.037.
- Rieker, G. B. et al. (2014), Frequency-comb-based remote sensing of greenhouse gases over kilometer air paths, *Optica*, 1(5), 290–298, doi:10.1364/OPTICA.1.000290.
- Rose, T., and H. Czekala (2009), RPG-HATPRO Radiometer Operating Manual, *Radiom. Phys. GmbH, Version, 7*.

- Rothman, L. S. et al. (2013), The HITRAN2012 molecular spectroscopic database, *J. Quant. Spectrosc. Radiat. Transf.*, *130*, 4–50, doi:10.1016/j.jqsrt.2013.07.002.
- Russell, P. B., R. W. Bergstrom, Y. Shinozuka, A. D. Clarke, P. F. Decarlo, J. L. Jimenez, J. M. Livingston, J. Redemann, O. Dubovik, and A. Strawa (2010), Absorption Angstrom Exponent in AERONET and related data as an indicator of aerosol composition, *Atmos. Chem. Phys.*, *10*(3), 1155–1169, doi:10.5194/acp-10-1155-2010.
- Salmi, T., V. Hänninen, A. L. Garden, H. G. Kjaergaard, J. Tennyson, and L. Halonen (2008), Calculation of the O - H stretching vibrational overtone spectrum of the water dimer, *J. Phys. Chem. A*, *112*, 6305–6312, doi:10.1021/jp800754y.
- Schneider, M., F. Hase, and T. Blumenstock (2006), Ground-based remote sensing of HDO/H₂O ratio profiles: Introduction and validation of an innovative retrieval approach, *Atmos. Chem. Phys.*, *6*(12), 4705–4722, doi:10.5194/acp-6-4705-2006.
- Von Schuckmann, K. et al. (2016), An imperative to monitor Earth’s energy imbalance, *Nat. Clim. Chang.*, *6*(2), 138–144, doi:10.1038/nclimate2876.
- Schuster, G. L., O. Dubovik, and B. N. Holben (2006), Angstrom exponent and bimodal aerosol size distributions, *J. Geophys. Res. Atmos.*, *111*(7), 1–14, doi:10.1029/2005JD006328.
- Science.nasa.gov (2017), NASA Webpage, Available from: <https://science.nasa.gov/missions/tsis-1>. Accessed 16 September 2018.
- Serdyukov, V. I., L. N. Sinitsa, and A. A. Lugovskoi (2016), Influence of gas humidity on the reflection coefficient of multilayer dielectric mirrors, *Appl. Opt.*, *55*(17), 4763–4768.
- Shillings, A. J. L., S. M. Ball, M. J. Barber, J. Tennyson, and R. L. Jones (2011), An upper limit for water dimer absorption in the 750 nm spectral region and a revised water line list, *Atmos. Chem. Phys.*, *11*(9), 4273–4287, doi:10.5194/acp-11-4273-2011.
- Shine, K. P., I. V. Ptashnik, and G. Rädcl (2012), The Water Vapour Continuum: Brief History and Recent Developments, *Surv. Geophys.*, *33*, 535–555, doi:10.1007/s10712-011-9170-y.
- Shine, K. P., M. Coleman, J Elsey, T Gardiner (2016a), Comment on “The Zugspitze Radiative Closure Experiment... Part II” by A. Reichert et al., *Atmos. Meas. Tech. Discuss.*, doi:10.5194/amt-2016-127-SC1, 201.
- Shine, K. P., J. Elsey, and I. V Ptashnik (2016b), Comment on “The Zugspitze Radiative Closure Experiment... Part III” by A. Reichert and R. Sussmann, *Atmos. Chem. Phys.*

- Discuss.*, doi:10.5194/acp-2016-323-SC1, 201.
- Shine, K. P., A. Campargue, D. Mondelain, R. A. McPheat, I. V. Ptashnik, and D. Weidmann (2016c), The water vapour continuum in near-infrared windows--Current understanding and prospects for its inclusion in spectroscopic databases, *J. Mol. Spectrosc.*, 327, 193–208, doi:10.1016/j.jms.2016.04.011.
- Solar Light Company (2001), Microtops II Ozone Monitor and Sunphotometer manual, Available from: <http://solarlight.com/wp-content/uploads/2014/05/MTPMAN-RevC.pdf> (Accessed 16 September 2018)
- Stephens, G. L., J. Li, M. Wild, C. A. Clayson, N. Loeb, S. Kato, T. L'Ecuyer, P. W. Stackhouse, M. Lebsock, and T. Andrews (2012), An update on Earth's energy balance in light of the latest global observations, *Nat. Geosci.*, 5(10), 691–696, doi:10.1038/ngeo1580.
- Takahashi, K. (2009), Radiative Constraints on the Hydrological Cycle in an Idealized Radiative–Convective Equilibrium Model, *J. Atmos. Sci.*, 66(1), 77–91, doi:10.1175/2008JAS2797.1.
- Tallis, L., M. Coleman, T. Gardiner, I. V. Ptashnik, and K. P. Shine (2011), Assessment of the consistency of H₂O line intensities over the near-infrared using sun-pointing ground-based Fourier transform spectroscopy, *J. Quant. Spectrosc. Radiat. Transf.*, 112(14), 2268–2280, doi:10.1016/j.jqsrt.2011.06.007.
- Tashkun, S. A. A., V. I. Perevalov, R. R. Gamache, and J. Lamouroux (2015), CDSD-296, high resolution carbon dioxide spectroscopic databank: Version for atmospheric applications, *J. Quant. Spectrosc. Radiat. Transf.*, 152, 45–73, doi:10.1016/j.jqsrt.2014.10.017.
- Tennyson, J. et al. (2014), Recommended isolated-line profile for representing high-resolution spectroscopic transitions (IUPAC technical report), *Pure Appl. Chem.*, 86(12), 1931–1943, doi:10.1515/pac-2014-0208.
- Thome, K., S. F. Biggar, and P. N. Slater (2001), Effects of assumed solar spectral irradiance on intercomparisons of earth-observing sensors, *Proc. SPIE 4540, Sensors, Syst. Next-Generation Satell. V, 4540*, 260–269, doi:10.1117/12.450668.
- Thuillier, G., M. Hers, P. C. Simon, D. Labs, H. Mandel, and D. Gillotay (2003), Observation of the solar spectral irradiance from 200 nm to 870 nm during the ATLAS 1 and ATLAS 2 missions by the SOLSPEC spectrometer, *Metrologia*, 35(4), 689–695, doi:10.1088/0026-1394/35/4/79.

- Thuillier, G. et al. (2009), SOLAR/SOLSPEC: Scientific objectives, instrument performance and its absolute calibration using a blackbody as primary standard source, *Sol. Phys.*, 257(1), 185–213, doi:10.1007/s11207-009-9361-6.
- Thuillier, G. et al. (2014), The Solar Irradiance Spectrum at Solar Activity Minimum Between Solar Cycles 23 and 24, *Sol. Phys.*, 289(6), 1931–1958, doi:10.1007/s11207-013-0461-y.
- Thuillier, G., J. W. Harder, A. Shapiro, T. N. Woods, J.-M. M. Perrin, M. Snow, T. Sukhodolov, and W. Schmutz (2015), The Infrared Solar Spectrum Measured by the SOLSPEC Spectrometer Onboard the International Space Station, *Sol. Phys.*, 290(6), 1581–1600, doi:10.1007/s11207-015-0704-1.
- Toledano, C., V. E. Cachorro, A. Berjon, A. M. De Frutos, M. Sorribas, B. A. De la Morena, and P. Goloub (2007), Aerosol optical depth and Ångström exponent climatology at El Arenosillo AERONET site (Huelva, Spain), *Q. J. R. Meteorol. Soc.*, 133(624), 795–807.
- Tran, H., D. Bermejo, J. L. Domenech, P. Joubert, R. R. Gamache, and J. M. Hartmann (2007), Collisional parameters of H₂O lines: Velocity effects on the line-shape, *J. Quant. Spectrosc. Radiat. Transf.*, 108(1), 126–145, doi:10.1016/j.jqsrt.2007.03.009.
- Trenberth, K. E., A. Dai, G. van der Schrier, P. D. Jones, J. Barichivich, K. R. Briffa, and J. Sheffield (2014), Global warming and changes in drought, *Nat. Clim. Chang.*, 4, 17–22, doi:10.1038/NCLIMATE2067.
- Turner, D. D., A. Merrelli, D. Vimont, and E. J. Mlawer (2012), Impact of modifying the longwave water vapor continuum absorption model on community Earth system model simulations, *J. Geophys. Res. Atmos.*, 117(4), 1–11, doi:10.1029/2011JD016440.
- Vaisala (2013), Vaisala RS92-SGP datasheet, Available from:
<http://www.vaisala.com/Vaisala Documents/Brochures and Datasheets/RS92SGP-Datasheet-B210358EN-F-LOW.pdf> (Accessed 16 September 2018)
- Varanasi, P., S. Chou, and S. S. Penner (1968), Absorption coefficients for water vapor in the 600–1000 cm⁻¹ region, *J. Quant. Spectrosc. Radiat. Transf.*, 8(8), 1537–1541, doi:https://doi.org/10.1016/0022-4073(68)90090-3.
- Vardavas, Ilias; Taylor, F. (2007), *Radiation and Climate*. International Series of Monographs on Physics, Oxford University Press, ISBN: 9780199697144
- Vigasín, A. A. (1985), On the spectroscopic manifestations of weakly bound complexes in rarefied gases, *Chem. Phys. Lett.*, 117(1), 85–88, doi:https://doi.org/10.1016/0009-

2614(85)80410-3.

- Walters, D. N. et al. (2014), The Met Office Unified Model Global Atmosphere 4.0 and JULES Global Land 4.0 configurations, *Geosci. Model Dev.*, 7(1), 361–386, doi:10.5194/gmd-7-361-2014.
- Weber, M. (2015), Comment on the Article by Thuillier et al. “The Infrared Solar Spectrum Measured by the SOLSPEC Spectrometer onboard the International Space Station,” *Sol. Phys.*, 290(6), 1601–1605, doi:10.1007/s11207-015-0707-y.
- Wild, M., and B. Liepert (2010), The Earth radiation balance as driver of the global hydrological cycle, *Environ. Res. Lett.*, 5(2), doi:10.1088/1748-9326/5/2/025203.
- Williams, D. C. (1999), Establishment of absolute diffuse reflectance scales using the NPL Reference Reflectometer, *Anal. Chim. Acta*, 380(2), 165–172, doi:https://doi.org/10.1016/S0003-2670(98)00480-2.
- Woods, T. N., F. G. Eparvier, J. Fontenla, J. Harder, G. Kopp, W. E. McClintock, G. Rottman, B. Smiley, and M. Snow (2004), Solar irradiance variability during the October 2003 solar storm period, *Geophys. Res. Lett.*, 31(10), 1–4, doi:10.1029/2004GL019571.
- Woolliams, E. R., N. P. Fox, M. G. Cox, P. M. Harris, and N. J. Harrison (2006), Final report on CCPR K1-a: Spectral irradiance from 250 nm to 2500 nm, *Metrologia*, 43(1A), 1–396.
- Wunch, D., G. C. Toon, J.-F. L. Blavier, R. A. Washenfelder, J. Notholt, B. J. Connor, D. W. T. Griffith, V. Sherlock, and P. O. Wennberg (2011), The Total Carbon Column Observing Network, *Philos. Trans. R. Soc. London A Math. Phys. Eng. Sci.*, 369(1943), 2087–2112, doi:10.1098/rsta.2010.0240.
- Zhao, M. et al. (2018), The GFDL Global Atmosphere and Land Model AM4.0/LM4.0: 2. Model Description, Sensitivity Studies, and Tuning Strategies, *J. Adv. Model. Earth Syst.*, 10(3), 735–769, doi:10.1002/2017MS001209.
- Zhong, W., S. M. Osprey, L. J. Gray, and J. D. Haigh (2008), Influence of the prescribed solar spectrum on calculations of atmospheric temperature, *Geophys. Res. Lett.*, 35(22), 3–7, doi:10.1029/2008GL035993.